Heinrich Heine
Universität
Düsseldorf

Advanced Molecular-Sensitive Imaging to Unravel Spatio-Temporal Hallmarks of CD95 Receptor Activation

Inaugural-Dissertation

zur Erlangung des Doktorgrades der
Mathematisch-Naturwissenschaftlichen Fakultät der
Heinrich-Heine-Universität Düsseldorf

vorgelegt von

Nina Maria Bartels
aus Reutlingen

Düsseldorf, Oktober 2022

Aus dem Institut für Experimentelle Medizinische Physik
der Heinrich-Heine-Universität Düsseldorf

Gedruckt mit der Genehmigung der
Mathematisch-Naturwissenschaftlichen Fakultät
der Heinrich-Heine-Universität Düsseldorf

Berichterstatter:

1. Prof. Dr. Cornelia Monzel
   Experimentelle Medizinische Physik
   Heinrich-Heine-Universität Düsseldorf
2. Prof. Dr. Claus Seidel
   Lehrstuhl für Molekulare Physikalische Chemie
   Heinrich-Heine-Universität Düsseldorf

Tag der mündlichen Prüfung: 30.06.2023

Eidesstattliche Versicherung

Ich versichere an Eides Statt, dass die Dissertation von mir selbständig und ohne unzulässige fremde Hilfe unter Beachtung der „Grundsätze zur Sicherung guter wissenschaftlicher Praxis an der Heinrich-Heine-Universität Düsseldorf“ erstellt worden ist.

Düsseldorf, 26.08.2023

Ort, Datum

Nina Maria Bartels

Abstract

Unraveling the spatio-temporal organization and dynamical interactions of receptors in the plasma membrane remains a key challenge for our mechanistic understanding of cell signal initiation. To study membrane receptors in their natural environment, integrated in a plasma membrane of human cells, requires minimally invasive and highly sensitive techniques. In biological sciences, fluorescence microscopy and spectroscopy techniques are powerful tools to study intact cells. However, each of these techniques exhibits particular spatio-temporal regimes of superior performance and few techniques are hitherto capable of relating measured intensities to molecular numbers and concentration. To solve these issues, the present work advances molecular-sensitive imaging techniques and establishes a generic concept to uncover molecular mechanisms of signal initiation.

A paradigm of a ligand-induced cell signal initiation process is the oligomerization of TNF (tumor necrosis factor) receptor CD95 in the signaling pathway for apoptosis (i.e. a coordinated natural form of cell death). A deregulation of the CD95 signaling mechanism was shown to be characteristic in some types of cancer leading to proliferation rather than cell death [1]. As the switch from signaling for death to life is hypothesized to occur via different CD95 activity states, the mechanism of molecular organization of CD95 on the cell membrane is of high interest, where the correct molecular configuration is yet to be defined.
Here, the proposed oligomerization models are scrutinized in live cells by establishing high-fidelity monomer and dimer controls as well as molecular sensitive imaging techniques such as confocal Photobleaching Step Analysis (cPBSA), a quantitative STED analysis, an advanced FRET approach, and using FCS. Thus, CD95 interactions are probed over the whole dynamic range from µs to hours, molecular to cellular scales and with particular focus on molecular concentrations.
The obtained results reveal a minimal model of signal initiation, where signaling dynamics scale with molecular concentrations. Suggested high oligomerization states are not observed. Instead, ligand coupling induces a switch of $6-15\,\%$ CD95 monomers to dimers/trimers evenly distributed in the plasma membrane. This suffices to trigger apoptosis efficiently.

As a result of the CD95 oligomerization study, the methods of choice were successfully advanced to tap their full potential for quantitative molecular imaging studies. In this course,

- STED images were subjected to a quantitative object and brightness analysis,
- a novel approach for robust PBSA is presented using a confocal setup and ubiquitous fluorescent proteins, and
- FRET is advanced towards a quantitative interpretation and high precision of oligomer studies.

Since a cell signal initiation is a transient and potentially localized process, this study highlights the importance of combining complementary techniques for a full understanding of this process.

Additionally, an excursion into (pre-)clinical research highlights the benefits of microscopy in this field with a microscopic study of therapeutic membrane receptors. In cancer immunotherapy, chimeric antigen receptor (CAR) T-cell therapy represents a major advancement in personalized treatment strategies, which has led to an exponential growth within this research field. CARs are genetically engineered to bind a specific tumor-associated antigen and start the T-cell activation pathway in order to fight the malignancies. In this study, multi-channel, time-lapse widefield microscopy is utilized in combination with bioimage data analysis to visualize and characterize the killing of cancer cells induced by novel CAR designs.
A time-lapse study of a novel 2^{nd} generation CAR generated against CD44v6 shows concentration dependent effect in the killing efficiency using varying effector-to-target ratios. In further studies, the agglomeration of CD19 CARs expressed in T- and NK cells into immunological synapses with the antigen-carrying target cells could be visualized. The specificity of this interaction was shown in comparison to non-specific effector and target cell combinations.
Overall, advanced fluorescence microscopy could contribute towards a more differentiated understanding of the CAR-induced killing mechanism and complement the clinical standard approaches.

Altogether, this thesis contributes towards a greater understanding of receptors in the cellular plasma membrane. To do so, it provides technical developments for quantitative molecular imaging. Based on these advancements, a general concept/approach to understand cell signal initiation mechanism is presented including the workflow and necessary tools along with statistical analysis. In particular an understanding of cell apoptosis signal initiation, which is essential for a multitude of vital processes during development, homeostasis, elimination of malignant cells is achieved.

Contents

I

Introduction

1 Cell Apoptosis and the CD95-Receptor

Cell death is a natural biological event in the development and life of all organisms. While it might be apparent, that cell death is involved in the immune system fighting injuries, pathogens or mutations, its function is less apparent but equally important in many more aspects. During the development of an organism, cell death is used to remove excess cells, shape tissues and support differentiation. During the development of our brain, 50 % or more of the newly formed neurons and neural connections are systematically eliminated to establish the complex functional network [2]. The balance, or homeostasis, between cell growth and death plays an evenly important role to secure the complex live of a mature multicellular organism. For instance, every day over 50 billion cells undergo programmed cell death in the human body [3]. Imbalance in cell death dynamics will lead to serious disorders and diseases.

1.1 Cell Apoptosis

There are different forms of cell death depending on the trigger mechanism. While necrosis is a non-physiological, inflammatory process caused by infections or injuries, apoptosis is one of the programmed forms of cellular death. This well-controlled process includes the cleavage of more than 500 cellular substrates [4], resulting in chromatin condensation, nuclear fragmentation, loss of the cytoskeleton [5] and a characteristic morphology of apoptotic cells. Apoptosis is indicated by cell rounding and shrinkage accompanied with cell blebbing into smaller fragments - the apoptotic bodies. These apoptotic bodies prevent the release of intracellular material which could potentially be toxic or infectious for the surrounding tissue.

Besides being notably a valuable tool for the immune system, apoptosis is also highly important for the development, regulation and function of the immune system itself [6, 7]. One example is the homeostatic control of the immune system via apoptosis: after the immune response, the number of antigen-reactive lymphocytes must be reduced

until the amount of lymphoid cells reaches the baseline level again. Generally, the immune system produces more cells than finally needed, and hence needs to eliminate the excess cells. This is achieved with apoptosis.
A more detailed insight in the immune system and its key players can be found in Part V.

Knowing the involvement of apoptosis in the immune system, it is not surprising that malfunction of apoptosis results in severe health conditions including autoimmune diseases and immunodeficiency [6]. Generally, diseases can be categorized into two groups: the absence of sufficient apoptosis can result in excessive growth of cells leading to tumor cells and, in consequence, cancer, whereas excessive apoptosis leads to the pathological loss of cells. A disease featuring too much apoptosis is for example the acquired immune deficiency syndrome (AIDS) [7]. Of course it is important to distinguish, that diseases exhibiting apoptosis malfunctioning can either be a direct effect of alterations to the apoptotic mechanism or be a secondary, indirect consequence of the disease [6].

1.1.1 Cell Apoptosis Pathways

The mechanism of apoptosis is highly complex and sophisticated, supporting a variety of different pathways and stimuli. In principle, it can be triggered via two pathways: the intrinsic or extrinsic pathway (see Figure 1.1). The intrinsic pathway can be activated by internal factors such as DNA damage, cell stress or the withdrawal of survival factors. The extrinsic pathway is initiated by the detection of extracellular death signals from other cells. In this case, signals are mediated by death receptor/death ligand systems. Both pathways have in common, that they eventually activate cysteine-dependent aspartate-directed proteases (caspases) which cleave cellular substrates leading to the biochemical and morphological changes that define apoptosis.

The intrinsic pathway is also known as mitochondrial pathway since pro-apoptotic BCL2 (B-cell lymphoma 2) family proteins such as BAD (BCL2 associated agonist of cell death protein) and BID (BH3 interacting-domain death agonist) activate mitochondria via changes in the mitochondrial outer membrane permeability (MOMP) to release cytochrome c into the cytoplasm. Free cytochrome c then couples to the apoptotic protease activating factor 1 (APAF1) to form the apoptosome which then binds to the initiator caspase procaspase-9. The activation of initiator caspases eventually starts the proteolytic cascade of caspase activation by cleavage (caspase-9) and activation of

effector caspases, namely caspase-3, caspase-6 and caspase-7.

The extrinsic pathway is initiated by proteins of the TNFR (Tumor Necrosis Factor Receptor) superfamily. These receptors are characterized by a common intracellular motif, the death domain (DD). After activation by their natural ligand of the TNF family, the death domain attracts intracellular adaptor proteins which, in turn, attract the initiator caspases procaspase-8 and procaspase-10. Together, these proteins form the so-called DISC (Death Inducing Signaling Complex). Similar to the intrinsic pathway, the activation of initiator caspases recruits the downstream effector caspases and with that starts the proteolytic activity.

Both pathways lead to active effector caspases (caspase-3, -6 and -7) cleaving cellular substrates - the "death substrates". The degradation of intermediate filaments around the nucleus (nuclear lamins) is involved in chromatin degradation and nuclear shrinkage/fragmentation. The cleavage of specific DNase inhibitors lead to DNA fragmentation and cleaved cytoskeletal proteins. The latter one is the cause for blebbing and fragmentation of the cell into apoptotic bodies which represent the characteristic morphological changes of apoptosis.

1.1.2 The TNFR Superfamily

The tumor necrosis factor (TNF) ligand and receptor superfamily (TNFSF) is a family of transmembrane proteins with important regulatory functions crucial for immune homeostasis. It plays an important role in cell proliferation, survival and – most prominently - cell death. For humans, the TNFSF is comprised of 19 ligands and 29 receptors [8–10].

The TNF receptors are characterized by the presence of a cysteine-rich domain (CRD) in the extracellular domain. TNF ligands also share a common structural motif on their extracellular domain, the TNF homology domain (THD), which binds to CRDs of TNF receptors to mediate a cellular response. The further signaling cascade classifies the TNFRs into three classes: (i) receptors with an intracellular death domain motif, transducing the signal via DD-binding partners, (ii) receptors with TRAF (TNF receptor–associated factors)-interaction motif (interacting with members of the TRAF-family) and (iii) decoy receptor without intracellular binding partners, working as ligand inhibitors. The first class of receptors (i) are also called death receptors (DRs) and are able to induce apoptosis via the extrinsic signaling pathway (compare Chapter 1.1.1). For several TNFRs, there are multiple ligands and binding partners able to

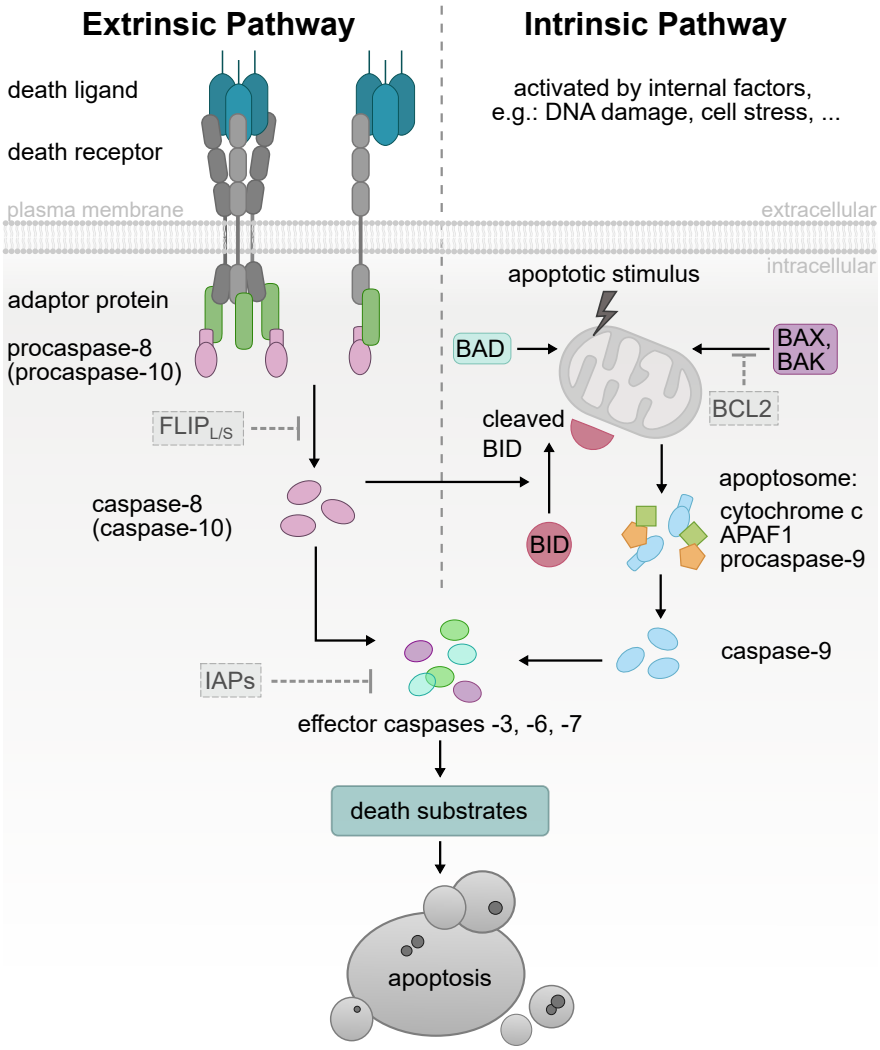

Figure 1.1: Illustration of the two main apoptosis signaling pathways. Apoptosis can be initiated by two alternative pathways: either through the extrinsic pathway via death receptors on the cell surface or through the intrinsic pathway via internal factors and the mitochondria. While death receptors recruit initiator caspases (procaspase-8, -10) directly via an adaptor protein to their death domain, mitochondria activate a large protein complex called apoptosome to recruit procaspase-9. Both pathways eventually activate effector caspases cleaving the death substrates, which eventually results in apoptosis. Inhibitors are illustrated with dashed lines. Further details can be found in Chapters 1.1.1 and 1.2.3.

induce and forward the signal.

The TNF receptors are expressed in many cell types of the human body but it particularly play an important role in the immune system [7, 11]. Hence, elucidating the TNFR signaling pathways is further important due to their potential therapeutic benefit for patients with various diseases, including cancer, autoimmunity, or infectious diseases [11, 12]. In this context, the TNF receptor Cluster of Differentiation 95 (CD95) is of particular interest, as it is exclusively activated by its ligand CD95L and solely interacts with one adaptor molecule, providing high control over its stimulation and signaling cascade. Other prominent DR examples, but with multiple interaction partners, are TNFR1 and DR4, which are activated by their ligands TNFα, LTα or TRAIL (TNF related apoptosis inducing ligand), respectively.

1.2 The CD95 Receptor

The Cluster of Differentiation 95 (CD95) is one death receptor of the TNFR superfamily (also known as CD95, Fas, Apo-1, TNFRSF6). After activation by its cognate ligand CD95L, it can initiate the signaling cascade via the extrinsic pathway (compare previous Chapter 1.1.1). Although initially classified as death receptor, cumulative evidence support that CD95 can also mediate inflammation and cell proliferation, besides its predominant role in cell death [1, 13].

1.2.1 Structure of CD95

CD95 is a type I transmembrane glycoprotein [14] of 319 amino acids and a (monomer) molecular weigh of 38 kDa. Including the precursor sequence that contains the signaling peptide, the sequence comprises 335 amino acids (premature protein). Consequently, there are two different nomenclatures for the amino acid residues of CD95, where the residue 1 of the mature sequence corresponds to the residue 17 of the premature sequence. Protein positions in this thesis will always refer to the premature sequence unless otherwise stated.

The structure of CD95 can be divided in the N-terminal ligand-binding extracellular domain (ECD) and the C-terminal intracellular domain (ICD), connected by a short hydrophobic transmembrane helix (amino acid residues 173-191), the transmembrane domain (TM). Figure 1.2a illustrates the structure of CD95.

The extracellular domain formed by amino acid residues 16-174 is, similar to other TNF Receptors, characterized by three highly conserved cysteine-rich domains (CRDs) that each form three disulfide bridges: CRD1: 44-82, CRD2: 83-127, CRD3: 128-166. The CRD1 was shown to include the PLAD (pre-ligand assambly domain) that contains a motif (amino acids 43–66 [15]) enabling the CD95 ECD to self-interact with other CD95 receptors independent of the ligand [16–18]. Homologous to other TNFRs, CRD2 and CRD3 of CD95 are responsible for ligand binding [8, 16]. A study examining point mutations in CRD2 showed, that two adjacent arginine residues at positions 102 and 103 (corresponding to R86 and R87 in the mature protein), are crucial for ligand binding, while four other residues support the binding but are not critical (K84, L90, E93, H126 in the mature sequence) [19]. As positions equivalent to R103 (mature R87) are implicated in ligand binding for other TNFR family members, only R102 (mature R86) seems to be specific for the CD95-CD95L interaction [19].

The intracellular domain comprises the residues 192-335 and is, as characteristic for TNFRs, mostly constituted by the death domain. The DD (amino acids 226–319) binds the adaptor protein upon ligand addition and by this, transduces the downstream signaling for apoptosis. While the crystal structure of various experimental studies do not superimpose completely, they all confirm a structure of the DD including multiple α-helices. The sequence between the TM and the DD of 36 amino acids length is predicted to be a disordered calcium-inducing domain (CID), whereas the biological role of the last residues of the ICD (320–335) remain largely unknown [20].

1.2.2 The CD95 Ligand

The CD95 Ligand (CD95L, FasL, TNFSF6 or CD178) is a 281 amino acid type II transmembrane protein consisting of an N-terminal cytoplasmic domain, a transmembrane domain and an extracellular domain. The ECD is comprised by a stalk region, a region mediating homotrimerization and a C-terminal receptor-binding domain [21, 22]. Figure 1.2b shows the schematic structure of CD95L.

CD95L shares a high structural homology with other members of the TNF family, which archetypically form trimers [10, 23–26]. Here, each monomer forms a “jelly roll” structure composed of β-sheets that define the TNF homology domain (THD) and self-assembles into noncovalent homotrimers. It is important to note, that literature is often not specific and particularly not consistent in the specification of the THD amino acid residues of CD95L: while most commonly the THD is referred to as residues 137-281 [27] or a length of 150 amino acids [8], others name the residues 183-281 [22]. Despite

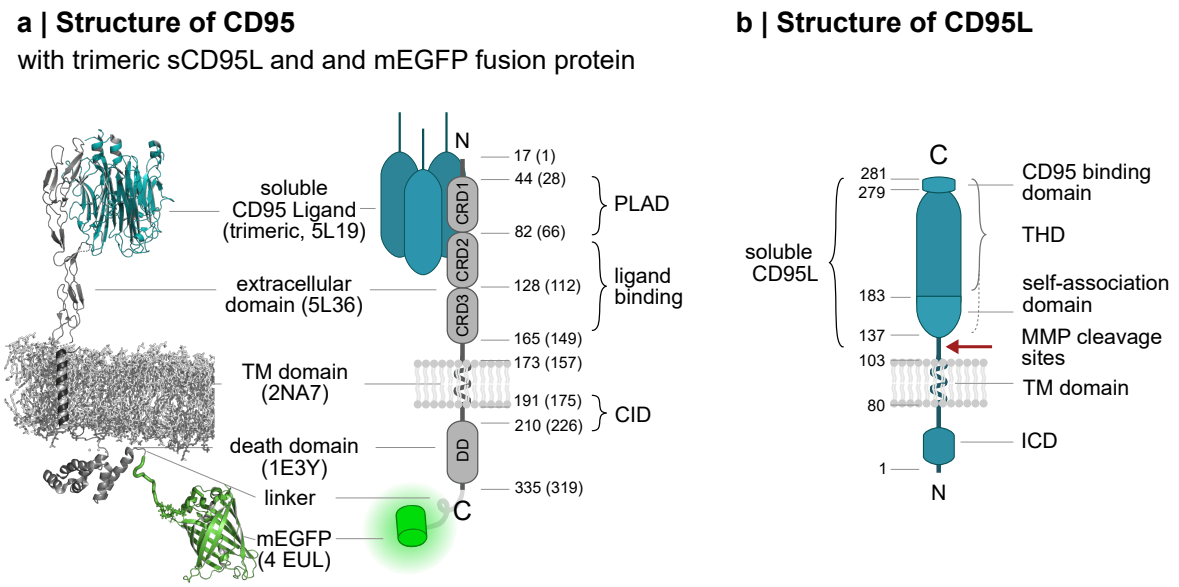

Figure 1.2: Schematic structure of CD95 and CD95L. a | The molecular representation of the CD95 structure (left) alongside its cartoon representation (right). Four letter abbreviations refer to constituent protein database entries. The receptor is bound to CD95L (cartoon simplified) and a C-terminal fusion protein (mEGFP). Labels indicate the main domains of the CD95 protein and numbers refer to the premature (mature) amino acid protein sequence. **b |** Representation of the CD95L structure with its specific domains. Certain matrix metalloproteases can release the soluble sCD95L. Numbers refer to the residues accordingly. More details can be found in the main text.

these discrepancies, the THD clearly encompasses the C-terminal ECD of the CD95 Ligand and exhibits the highest similarity to related proteins of the TNF family, but also mediates highly specific binding to the cysteine-rich domains (CRDs) of the CD95 receptor [8, 21]. Regarding the CD95 interaction, Orlinick at al. showed that as few as the last three amino acid residues of the receptor-binding domain completely disrupts the receptor binding of CD95L [21].

The stalk region of mCD95L (membrane bound CD95L) can be cleaved of by several matrix metalloproteases (MMPs) which leads to the release of the soluble form of the ligand: sCD95L. This soluble form of CD95L was shown to be a homotrimer [28], similar to its membrane-bound counterpart. This is in line with the self-association being independent of the transmembrane or cytoplasmic sequences, as the ability to self-associate was localized to a 47-amino acid region in its extracellular domain. The self-association domain is comprised of the residues 137-183 [21].

1.2.3 CD95 Signaling Pathway

The first step of the apoptosis signal transduction of CD95, is the activation by its ligand. Upon induction, the CD95 signal transmission follows the well-defined steps of the extrinsic pathway (Figure 1.1), that it shares with other death receptors of the TNFR superfamily: The adaptor molecule FADD (Fas-associated-protein with death domain, also called Mort-1) binds via its own death domain homotypically to the death domain of CD95. Besides the DD, FADD is comprised of the so-called Death-effector Domain (DED). Again via homologous interaction, this DED can recruit the DED-carrying procaspase-8 (formerly known as FLICE[1]) as initiator [29]. This formation of the so-called death-inducing signaling complex (DISC) [30] takes place within seconds of receptor engagement [7, 31]. Subsequently, the procaspase-8 is activated at the DISC by autocatalytic self-cleavage, which was shown to crucially depend on proximity-induced dimerization [32–34]. Finally, active caspase-8 is released into the cytoplasm. This active, dimeric species is composed of large and small catalytic subunits [35]. Caspase-8 activates apoptosis directly by cleavage of various proteins in the cell including procaspase-3. This results in caspase-3 activation and further protein cleavage of the "death substrates", ultimately leading to the completion of the cell death program with the characteristic biochemical and morphological changes.

Two Different Pathways - Two Cell Types

In some cells, the described extrinsic pathway is not sufficient to initiate apoptosis directly. While in so-called type I cells [31], the caspase cascade initiated by caspase recruitment at the DISC results in large amounts of active caspases sufficient to induce apoptosis directly, in other (type II) cells, hardly any DISC is formed [31]. Here, the amount of caspase-8 is too small for a direct activation and the intrinsic pathway via mitochondria is used as "amplifier" of the apoptotic signal. The active caspase-8 cleaves the BCL2 family member BID, which can activate the mitochondrial cytochrome c release leading to a caspase cascade and eventually apoptosis (compare Chapter 1.1.1).

The activation of mitochondria can be observed in both cell types but is not strictly necessary for type I cells. In contrast, inhibitors of the mitochondrial pathway like BCL-2 and BCL-X_L (compare next section) fully block the activation of caspases and disable apoptosis in type II cells [31]. This concept has been applied to HeLa cells which have been shown to behave as type II cells since the overexpression of BCL2

[1] short for FADD-like ICE, or FADD-Homologous ICE/CED-3–like Protease, where ICE describes the Interleukin-1β–Converting Enzyme and CED-3 the Caenorhabditis Elegans cell Death gene 3.

prevents CD95-mediated apoptosis [36, 37]. Further, CEM and Jurkart cells (both T-cell lines) were categorized as type II cells, while H9 (T-lymphoma cell line) and SKW6.4 (B-lymphoblastoid cell line) belonged to the type I category [31]. Interestingly, MCF7 cells (breast adenocarcinoma cell line) overexpressing CD95 showed an ambivalent phenotype indicating that the effect depends on signaling protein concentrations. In MCF7 cells, DISC formation and caspase-8 activation occur as in type I cells, while apoptosis is blocked by mitochondrial pathway inhibitors as in type II cells, which can be switched towards full type I behavior by heterologous expression of caspase-3 [31].

Regulation of Apoptosis Signaling

Naturally, a self-destructive process such as apoptosis needs a tight control and regulation machinery. There are various proteins that can regulate the two apoptosis pathways at different levels (compare Figure 1.1).

The regulation on the level of death receptors takes place via FLIPs (FLICE (caspase-8)-like inhibitory proteins) - DED containing proteins that compete with procaspase-8 for the FADD binding. While initially found in a certain class of herpes viruses, two (cellular) homologues called c-FLIP (a long form (c-FLIP$_L$) and a short form (c-FLIP$_S$)) were identified in human cells [38]. The structure of c-FLIP with two DEDs and a caspase-like domain is similar to caspase-8, however it lacks residues that are important for a catalytic activity [38]. Although widely assumed to inhibit the procaspase-8 mediated apoptosis, some studies suggest c-FLIP to be anti- or pro-apoptotic, depending on the cellular context [33, 39, 40].

For the intrinsic pathway, the family of BCL2 proteins execute the regulatory functions at the mitochondrial level, precisely based on their influence of the mitochondrial membrane permeability. There are BCL2 family members with pro-apoptotic and anti-apoptotic functions. For example, while pro-apoptotic BAX and BAK work via insertion into the mitochondrial membrane, oligomerization and the formation of protein-permeable channels, anti-apoptotic BCL2 inhibits the conformational change or the oligomerization of BAX and BAK [41].

Further along the signaling cascade of both pathways, inhibitors of apoptosis proteins (IAPs) can bind to and inhibit effector caspases. In human cells, nine proteins that belong to the IAP family, have been identified [41]. Naturally, these inhibitors can be regulated by further control mechanisms and pro-apoptoticc inhibitors, e.g. SMAC (small mitochondria-derived activator of caspases) to round out the regulatory function.

Proliferation/Survival Pathways

While CD95 was initially identified as pure death receptor, there is cumulative evidence showing that CD95 is not solely inducing cell death, but can also trigger a variety of other cellular responses reaching from the promotion of inflammation over the stimulation of proliferation and differentiation to induction of cell migration [1, 42]. Among many more examples, the triggering of CD95 has been reported to drive cell-cycle progression in glioma cells [43] and CD95-induced migration was observed in cultured renal tubular cells [44]. The apoptosis-independent signaling mechanisms of CD95 were implicated in a diverse array of different signaling pathways:

CD95 activation was shown to be linked to (tumor) cell growth via signaling pathways that trigger the activation of transcription factors of the NF-κB (Nuclear Factor κB) family. Precisely, the activation of the NF-κB pathway was shown to be mediated by FADD both in the CD95L and TRAIL induced signaling [45–47]. Interestingly, it was found that an inflammatory NF-κB-related response is enhanced by a high expression of FLIP-independent apoptosis inhibitors like BLC2 or caspase inhibitors [46].
Further, there is evidence that CD95 can also activate a MAPK (mitogen-activated protein kinases) signal. MAPKs were shown to be involved in a diverse cellular processes including inflammation, cell migration and differentiation as well as cell cycle control and apoptosis [48]. Their activation via CD95 can follow a multitude of ways from apoptosis-associated to apoptosis-independent, from caspase-mediated to caspase activity-independent (reviewed in [42]).
The PI3K (phosphoinositid 3-kinases) pathways are related to a variety of cellular processes - most prominently in cell survial and proliferation - and were also shown to be induced by CD95 activation (reviewed in [49]). Particularly, PI3K was related to pro-tumorigenic CD95-signaling [1, 13]. Kleber et al. [13] showed, that the CD95L activation of CD95 on glioblastoma cells recruits the p85 subunit of PI3K to CD95, which triggers basal invasion of glioblastoma *in vivo*.

Although there is an increased recognition of the biological and pathophysiological relevance, the cell death-independent signaling mechanisms seem to be highly diverse and complex and are not yet fully understood.

1.2.4 Membrane Organization of CD95

So far, much is known about the molecules participating in the CD95 signaling pathways. However, insights about the membrane organization including receptor kinetics, interactions, the formation of supramolecular patterns, as well as the role of molecular

concentrations remain sparse. In few cases models of signal initiation exist for CD95 or TNFRs in general, proposing a receptor organization at molecular or supramolecular scales. As the TNF superfamily members including CD95 show high structural homology [8, 50], the experimental results and proposed models of other TNFRs are relevant and potentially transferable for CD95. Among the proposed membrane organization of TNFR, two models are primarily discussed to explain the mechanism underlying signal initiation, supported by different experimental results. Figure 1.3 illustrates the two models:

The first model (Figure 1.3, left) proposes an immediate, unamplified transduction of the signal from the extracellular to the intracellular side. Here, the trimeric TNF ligand binds up to three receptors, thus forming small oligomer units of trimer-trimer receptor-ligand configurations. In this activated state of the receptor the intracellular death domain opens and allows for recruitment of one adaptor molecule (such as FADD) per receptor via DD-DD interaction [51]. Thereafter, the (extrinsic) signaling pathway relying on the autoproteolytic process after caspase dimerization is started. In this model any stimulus arriving on the extracellular side would be transduced to the intracellular side in a non-amplified, one-to-one manner. Moreover, signal initiation may occur already at low molecular expression levels.

A second model (Figure 1.3, right) proposes the formation of inactive receptor dimers prior to any activation, which in turn assemble into a supramolecular honeycomb structure [10]. After TNF ligand binding to the vertex position of this lattice, the receptor dimer decouples and recruits an adaptor molecule to the opened DDs. FADD may crosslink the DDs to re-establish a hexagonal structure of $\sim 35\,\mathrm{nm}$ diameter [10] on the intracellular membrane side. The model of hexagonal crosslinking is appealing, as it suggests a unique signaling complex as well as signal amplification by a factor of ≈ 2 [52]. Within the noisy environment of the cell, such mechanisms may be beneficial to increase signaling robustness to better distinguish true from random stimuli. On the other hand, formation of such supramolecular structures becomes less and less probable with increasing size and may require high molecular expression levels or heterogeneous molecular distributions inside the cell and the plasma membrane.

To understand the origin of these two models, one needs to scrutinize the various levels of potential CD95 oligomerization. Before ligand induction, the receptors have to interact via their PLAD, TM or intracellular domain, while after ligand binding there are the additional levels of extracellular CD95L- or intracellular FADD-supported oligomerization.

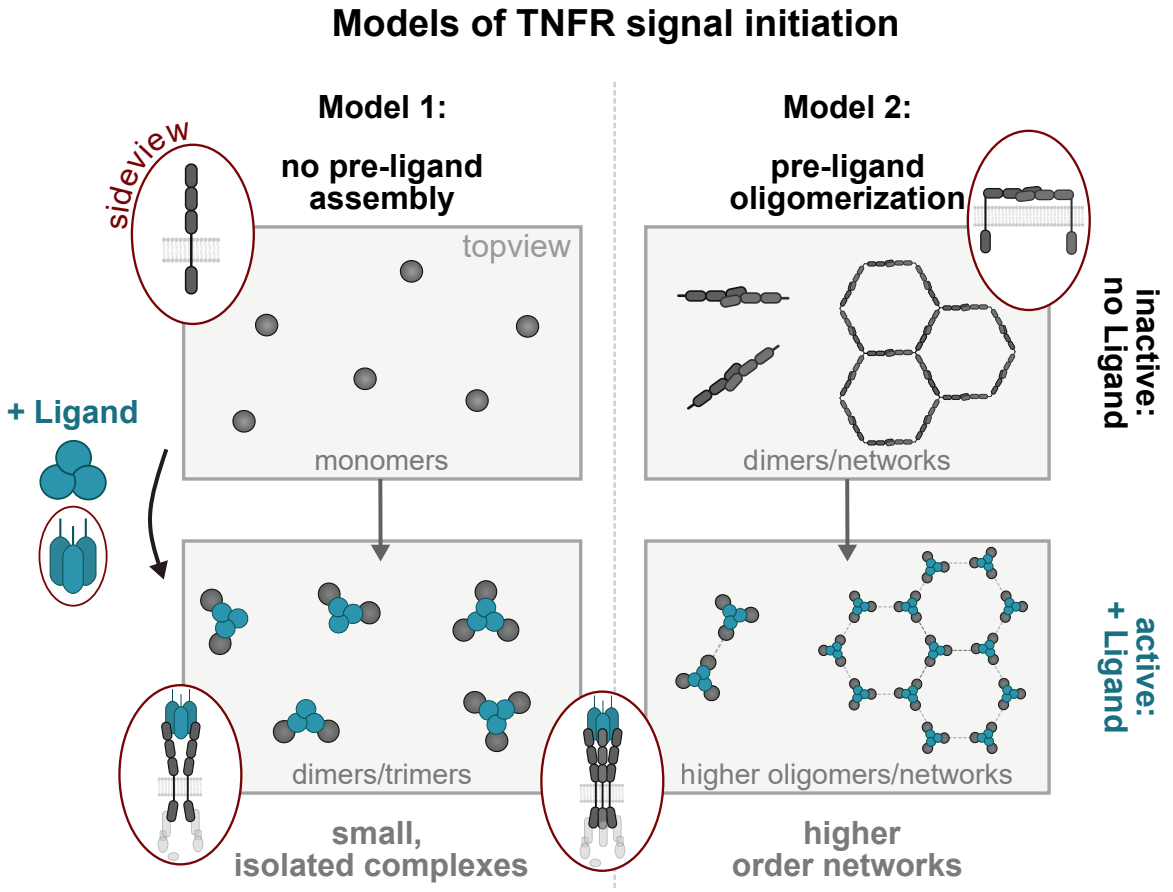

Figure 1.3: Schematic illustrations show two proposed models of TNFR signal initiation by a trimeric ligand. Left: monomeric receptors (no pre-ligand assembly) form small, isolated complexes after ligand recruitment with a maximal possible three-to-three stoichiometry. No crosslinking between the complexes. Right: receptors form pre-ligand complexes/networks via the PLAD and/or intracellular regions, which extend to higher order oligomers/networks after ligand binding.

Pre-Ligand Assembly

Due to the structural homology and the well-studied trimerization of TNF ligands, CD95 and other TNFRs were commonly assumed to be trimeric [53, 54]. The CD95 self-association in absence of the CD95 was found in various biochemical studies using purified proteins or cell lysates. Papoff et al. showed the homo-oligomerization (pre-assosiation) via PLAD using gel filtration and chemical crosslinking experiments of recombinant CD95 [17]. The formation of new discrete bands ranging approximately between 120 and 180 kDa was apparently corresponding to dimeric and trimeric receptors [17]. The pre-association was confirmed by Siegel et al. in Western Blots studies finding an apparent molecular size of CD95 in cell lysates of 140 kDa under non-reducing conditions [18]. They further used Förster Resonance Engery Transfer (FRET) dur-

ing flow cytometry measurements indicating the formation of pre-associated receptor complexes [18]. Edmond et al. specified that the region between amino acids 43 to 66 corresponds to the minimal motif involved in CD95 homotypic interaction as the respective depletion avoided self-interaction as studied by gel filtration and immunoplot analysis of CD95 ECD variants [15]. Further they showed, that a CD95(1-66) fragment fails to form homotrimers, but rather forms dimeric structures, suggesting that the PLAD cannot bind more than one receptor [15].
These findings on CD95 are supported by studies of other TNFRs due to their structural homology. The flow cytometric approach to analyze FRET was also applied to TNFR1, TNFR2, CD40, and DR4 – all members of the TNFR family – confirming the self-interaction of these receptors in living cells but do not show interactions with ECDs from heterologous receptors [16]. The same study found complexes for TNFR2 that exhibited molecular sizes of approximately three times the unit size [16]. In contrast, the unliganded dimerization of the TNFR1 ECD was shown by crystallographic evidence [55]. It was further classified into two distinct dimers of the receptor - one dimer formed by a parallel arrangement of receptors and the other by an antiparallel arrangement of TNFR1 [56, 57]. It has been proposed that the antiparallel dimers may represent the resting or "non-signaling" state.

While there is clear evidence, that the PLAD may only induce the receptors to homodimerize, there is also evidence for the commonly believed pre-ligand trimerization. The combination of the pre-ligand trimer and dimer symmetries results in a model describing the formation of hexagonal networks comprised by receptor trimers with an inter-trimer PLAD-mediated crosslinking as shown in Figure 1.3 (right) [10, 54].

Ligand-induced Oligomerization

Due to the one-to-one interaction of CD95-CD95L, the CD95 trimerization upon binding of trimeric CD95L is a common and straight-forward oligomerization model. It is supported by studies on the crystal structure of multiple TNF-TNFR complexes, which were all resolved into trimer-trimer complexes [58–63]. While there is no study on the crystal structure of CD95-CD95L interaction, the trimeric structure of CD95L and its homology to other ligands (compare Chapter 1.2.2) highly suggest a similar behavior.

Fu et al. support the ligand-induced trimerization model of CD95 by studies on its transmembrane domain [64]. Applying a combination of techniques including SDS-PAGE (sodium dodecyl sulfate polyacrylamide gel electrophoresis), NMR (nuclear magnetic resonance) structure analysis, FRET and super-resolution microscopy, they

demonstrate that the TM domains of the CD95 form stable homotrimers in lipid bilayer but conclude that the principal function of the TM domain is to stabilize the liganded state of the receptor, rather than pre-ligand association [64]. Similar results were found for DR5 in [65].

The ligand-induced oligomerization is part of both models presented in Figure 1.3. While the ligand is the initial stimulus for any oligomerization in the 1st model, it might serve as secondary crosslinking mechanism in the 2nd model where it triggers the restructuring towards a signaling-active receptor organization.

Death Domain and FADD-mediated Clustering

The intracellular association of CD95 with FADD via their death domains was initially found using the yeast two-hybrid system in 1995 [66] and confirmed by biochemical and cell-based evidence [30, 67].

The structure of the CD95 DD in complex with FADD has been resolved by multiple research groups independently, all finding a complexed arrangement of multiple FADD death domains with multiple CD95 death domains [51, 68, 69].
Scott et al. proposed, that a 40 Å opening of the CD95 DD exposes its FADD binding site and simultaneously generates a CD95-CD95 bridge [51]. This self-association of CD95's death domain was already found before using a yeast two-hybrid screening [70] and specified by Esposito et al. in crystal structure studies indicating that the CD95 DD has the potential to self-dimerize via the conformational transition from a closed (inactive) to an open (active) form [69].
The predominant CD95-CD95 bridges observed in the structures gave rise to the model of DD-mediated complexation of individual CD95 trimers, stabilized by FADD [51]. The model proposes each monomer of a ligand-bound CD95 trimer to be linked to one monomer of a neighboring trimer resulting in an hexameric (network) structure [10, 51, 52]. One CD95-CD95 bridge is then stabilized by two FADD proteins via weak CD95-FADD interactions, collectively forming the DISC. Ring-like arrangements of purified CD95-FADD complexes could be visualized using electron microscopy (EM) after long incubation times (> 20 h) of full-length proteins [51] and protein DDs [68].
A similar hexameric model was proposed for DR5 by Reis et al. suggesting an influence of receptor density on the complex formation [71].

The DD/FADD-mediated oligomerization mechanism is included in the 2nd model of Figure 1.3 where dashed lines indicate the intracellular binding between trimeric complexes forming a hexagonal network.

External Factors Mediated Stoichiometry

Aside from interaction partners and structural aspects, there are external factors that were shown to influence the CD95 stoichiometry, the most noted of them being pre-ligand CD95 translocation into membrane domains called membrane or lipid rafts [72–75]. This accumulating evidence introduced the idea that lipid rafts serve as scaffolds for the recruitment and clustering of CD95 death receptor and downstream signaling molecules, leading to the formation of the so-called clusters of apoptotic signalling molecule-enriched rafts (CASMERs) (reviewed in [76]).
For example, Muppidi et al. showed, that the presence of CD95 in lipid rafts increased the sensitivity to CD95L-stimulation and -mediated apoptosis in activated human CD4+ T cells [72]. They further show that the pre-ligand presence of CD95 in lipid rafts is restricted to type I cells, which was confirmed by Eramo et al. [74]. Eramo et al. additionally showed, that in both cell types after stimulation CD95 was recruited to lipid rafts which consistently appeared to be the major site of DISC formation and caspase-8 activation [74].

The findings presented in this Chapter provide insight on potential CD95 stoichiometry and the underlying oligomerization mechanisms. However, these findings are partly contradictory and support two differing models of oligomerization. Clear evidence for the oligomerization state and at physiological conditions measured on the plasma membrane of living cells before and after ligand induction is still lacking.

2 State-of-the-Art Fluorescence Microscopy and Spectroscopy Techniques

The phenomenon of fluorescence is widely applied in various scientific analytical methods, particularly in the biological sciences. Fluorescence describes the ability of a photoactive atom, molecule or crystal to fluoresce - a form of light emission after prior excitation by light absorption. The basic molecular and physical principles of fluorescence were described by Alexander Jablonski in 1935 [77]. Particularly, fluorescence became a powerful tool in microscopy and spectroscopy, as it enables us to create a contrast of designated structures in otherwise transparent samples. Consequently, there has been dramatic growth in the application of fluorescence for cellular and molecular imaging during the past decades. Fluorescence imaging can reveal the localization of intracellular molecules, sometimes at the level of single-molecule detection. In combination with fluorescence spectroscopy and time-resolved fluorescence, it can can provide information on a wide range of molecular processes including distances, conformational changes, binding interactions and (rotational) diffusion of biomolecules. Overall, fluorescence microscopy and spectroscopy techniques contribute towards the understanding of biomolecular structures and their dynamics while being highly sensitive, minimally invasive and highly selective to the examined specimen.

2.1 Techniques to Unravel Membrane Protein Organizations and Oligomeric States

The full knowledge of a biological system such as CD95 induction requires information on its spatial organization but also its temporal dynamics. Albeit the recent advances in fluorescence microscopy, probing the dynamic organization and oligomeric state of membrane proteins in intact, preferably live, cells is not straightforward.

The most prominent approach in the recent year with the potential to study the

oligomeric states of membrane proteins in intact cells is single-molecule localization microscopy (SMLM), which relies on the stochastic nature of fluorescent on/off state transitions. The idea is that only a sparse number of dyes is activated and imaged at a time and thus can be localized with high precision by Gaussian fitting. By repeated measurements of random subsets of fluorophores (either actively switched or passive blinking behavior) a super-resolved image of all fluorophore localizations can ultimately be reconstructed. The numerous SMLM techniques are mostly based on the two prototypes PALM and STORM (photoactivated localization microscopy and stochastic optical reconstruction microscopy). In all cases, special photoswitchable fluorophores and costly image reconstruction are required [78].

Next to SMLM, various other microscopic and spectroscopic methods that are not based on image reconstruction feature similar insights and can even be used with ubiquitous, genetically-encodable fluorescent proteins such as the monomeric enhanced green fluorescent protein (mEGFP) or mCherry. The following sections will elucidate the benefits and challenges of selected techniques that were and can be used to unravel the organization of membrane proteins.

2.1.1 Stimulated Emission Depletion (STED)

Stimulated Emission Depletion (STED) is a super-resolution technique overcoming the diffraction limit of resolution proposed by Ernst Abbe, which is known to be

$$\Delta r \approx \frac{\lambda}{2n\sin(\theta)} = \frac{\lambda}{2NA} \tag{2.1}$$

and has been the limit of microscopic resolution for over a century. It depends on the wavelength λ, the (immersion) medium's refractive index n and the angle θ of the cone of focused light. NA describes the numerical aperture of the objective.

The concept of STED was first introduced by Stefan Hell in 1994 [79] and rewarded with a Nobel Prize in 2014 for the development of super-resolved fluorescence microscopy. His idea was to deplete the fluorophores in the outer region of the diffraction limited spot with a second, ring-shaped laser by stimulated emission, leading to a reduction of the effective confocal volume.

The STED FWHM (full width at half maximum) resolution Δr of the effective fluorescent spot caused by a doughnut-shaped STED focus can be described by:

$$\Delta r \approx \frac{\lambda}{2n\sin(\theta)} \frac{1}{\sqrt{I_{\mathrm{STED}}^{\mathrm{max}}/I_{\mathrm{sat}} + 1}}. \tag{2.2}$$

The amount by which the conventional Abbe limit is reduced is determined by the Saturation Factor ($I^{\max}_{\mathrm{STED}}/I_{\mathrm{sat}}$). This is the ratio between the maximal intensity in the STED depletion beam ($I^{\max}_{\mathrm{STED}}$) and the intensity at which the probability of the dye's fluorescence emission is reduced by half (I_{sat}).

In consequence, the chosen fluorophore will largely determine the maximal obtainable resolution. For this reason, STED often requires additional staining with artificial dyes. While there are genetically encodable, STED-able far-red fluorescent proteins [80], common mEGFP or mCherry proteins cannot be used and require the use of additional staining techniques.
As for most fluorescence staining techniques, it is important to bear in mind that the measured signals do not arise from the target molecules themselves but from attached fluorophores. Choosing the optimal labeling strategy can be particularly challenging for quantitative applications. If there is no option of using certain genetically encoded labels or certain Tag-technologies, an antibody-based labeling of specific proteins (so-called immunostaining) is often the means of choice.
In any case, the fluorophores often are positioned a full label's (linker/tag/antibody) length away from the target. In the case of immunostaining, the label's size can be quite large compared to the resolution of the technique and any assertion of molecule locations cannot be entirely accurate. Thus, it is favorable to utilize much smaller probes than antibody fragments ($\sim 150\,\mathrm{kDa}/15\,\mathrm{nm}$), for example nanobodies ($\sim 15\,\mathrm{kDa}/2\,\mathrm{nm}$) [81]. Additionally, the labeling stoichiometry (also known as degree of labeling (DOL)) of fluorophore to label and label to target, as well as the labeling efficiency have to be considered [78].
Although there are recent advancements towards live-STED applications [80, 82, 83], the slow acquisition speed, the potential phototoxic effect of the STED laser, the dependence on selected depleteable fluorophores and special staining techniques often require cell fixation to achieve the highest possible spatial resolution. A fixation intends to immobilize or "fix" the molecules in place for subsequent imaging. Thus, optimizing spatial resolution is at the expense of temporal resolution. Furthermore, fixation itself is one of the biggest sources of imaging artifacts for biological samples and needs to be mitigated by careful selection and optimization of the fixation strategies to preserve the native (membrane) protein distributions [78].

For successfully designed STED probes, the highest benefit of STED is its improved resolution which in cell biology routinely obtains resolutions in the range of 20-50 nm [81]. Applied to membrane proteins, this enables to uncover their organization on the membrane on a sub-diffraction level.
STED images give rise to classical image analysis such as localization, size, shape and

intensity of the imaged objects. To go a step further and quantify the sub-resolution distribution of the emitting molecule number in space, the simplest approach is usually dividing the measured fluorescence by that of a single emitter, if accessible. However, the brightness of individual emitters can vary strongly in a STED sample due to local environment heterogeneity or fixed fluorophore orientations. Moreover, with increasing (super-) resolution, fewer molecules are found per pixel, making this approach even more unreliable. Overall, observed Poisson statistics of the fluorescence signal do not lend themselves to distinguish the number of the emitters from their brightness.

One novel analysis approaches to overcome the challenges of molecular counting in STED is the careful analysis of the photon arrival statistics which depends on the number of molecules and their brightness [84, 85]. The concept relies on the idea that fluorophores can only emit a single photon at a given time, and thus a simultaneous detection of multiple photons should indicate the presence of multiple molecules. With extensive calibrations and image analysis, it is possible to establish the number and local brightness of up to 20 molecules per confocal recording volume [84, 85].
Aside from this novel technique, the molecular quantification remains mostly elusive for most STED imaging studies unless combined with other techniques. For example, Walther et al. combined STED with FCS (fluorescence correlation spectroscopy) to determine the concentrations and absolute copy numbers as well as the subchromosomal distributions of mitotic chromosome structure proteins [86].

Concluding, STED enables highly valuable sub-diffraction resolved imaging of the organization and structure of (membrane) proteins inside a cell. It is mostly limited to standard image analysis as molecular counting approaches require an intensive calibration and image analysis procedure and are not yet well-established.

2.1.2 Confocal Photobleaching Step Analysis (cPBSA)

Photobleaching Step Analysis (PBSA) is a fluorescence-based molecular counting method enabling to resolve stoichiometries within protein complexes that are too small to be spatially resolved by the sub-diffraction resolution limit of todays super-resolution techniques, such as STED (>20 nm) [81]. It was first introduced by Ulbrich and Isacoff in 2007 [87]. As indicated by its name, PBSA utilizes the observation of photobleaching steps of individual fluorophores to determine the number of dyes within a complex. Figure 9.1 illustrates the principle of PBSA.
While this technique convinces with its simplicity in data acquisition and the (relatively) straightforward analysis and interpretation, so far it was mostly limited to total internal reflection fluorescence (TIRF) microscopy data and fluorophores exhibiting

high quantum efficiencies and little bleaching, as it requires a high signal-to-noise ratio (SNR) [87, 88]. Naturally, this microscopy technique exclusively works well for proteins in the lower plasma membrane of an attached cell but not for proteins in intracellular organelles.

One limit of single-molecule photobleaching in cells is its restriction to low expression levels and fixed cells. The fluorescently labeled proteins need to be immobilized at low density for spatial separation of individual molecule complexes and long measuement times [88]. While being a solid approach for subunit counting, PBSA is a diffraction-limited method and thus lacking a high resolution of the protein localization on the membrane. Thus, it is impossible to distinguish between true oligomerization and density-related protein crowding, underlining the need for a low protein expression level and complementary methods.
As for most other fluorescence microscopy/spectroscopy techniques, it depends on refined sample preparation in terms of labeling and cell fixation (compare Chapter 2.1.1 before). Particularly, it requires a well-defined DOL - only if every subunit carries exactly one functional fluorescent label, the maximum number of bleaching steps directly reveals the oligomerization state of the protein. Additionally, a large fraction of the subunits (ideally $> 75\,\%$ [88]) needs to be fluorescently labeled for an accurate determination of a protein's oligomerization state.
As mentioned before, PBSA relies on a high SNR, which is achieved using bright and photostable dyes. Thus, the method is most reliable with to organic fluorophores. Previous applications were for example the determination of the number of fluorescent labels on DNA origami [89] or the degree of Qdot labeling [90]. Counting photobleaching steps on fluorescent proteins could only be observed from GFP and YFP variants as blue and red FPs suffer from low photostability, and therefore bleaching occurs too fast for distinguishing individual steps.

Overall, PBSA is a robust and computationally inexpensive counting approach with limitations of fixed, photostable samples and diffraction-limited resolution.

2.1.3 Förster Resonance Energy Transfer (FRET)

The Förster Resonance Energy Transfer (FRET) is the transfer of energy of one excited fluorophore to one or more other fluorophores. This effect can occur when the emission spectrum of the excited fluorophore (donor/D) overlaps with the excitation spectrum of the coupled fluorophore(s) (acceptor/A) and the two fluorophores are in close proximity. If these preconditions are met, the energy transfer results from dipole–dipole coupling processes between the fluorophores. After the transfer took place, the donor is quenched

while the acceptor is excited and can emit the newly gained energy in form of its characteristic emission spectrum. Here it is important to mention, that the energy transfer in principle can happen if the acceptor is not capable of fluorescence emission, but usually the term FRET is used for microscopic and spectroscopic applications, where the energy-accepting species is a fluorophore. The phenomena of FRET was theoretically correctly described for the first time by Theodor Förster in 1946 and 1948 [91, 92].

The extent of FRET depends on the spectral overlap of donor and acceptor as well as their distance. As the spectral overlap is a property of a specific donor-acceptor pair, it can be described in terms of the so-called Förster Radius R_0. Typical Förster Radii are in the magnitude of proteins, approximately between 20 to 60 Å. The rate of energy transfer $k_\mathrm{T}(r)$ shows the strong dependence of FRET on the donor-acceptor distance r:

$$k_\mathrm{T}(r) = \frac{1}{\tau_\mathrm{D}} \left(\frac{R_0}{r}\right)^6, \tag{2.3}$$

where τ_D is the lifetime of the donor in absence of energy transfer. As the FRET rate $k_\mathrm{T}(r)$ decays with r^{-6}, FRET can be used as molecular ruler to determine if and how close donor and acceptor are.

The combination of FRET with light microscopy enables to conclude about sub-resolution structures. There are two possible ways to detect a FRET effect: intensity-based FRET or FLIM (fluorescence lifetime imaging)-FRET. The latter is based on the fact, that the donor's lifetime decreases as it is losing its energy more rapidly in proximity of an acceptor.

FRET can be based on genetically encoded fluorescent proteins and thus is ideally suited to report on the oligomerization of (membrane) proteins due to its biocompatibility and the ubiquity of fluorescently tagged proteins [93, 94] avoiding labeling-related issues as described for STED. This is making FRET in principle compatible with live cells and standard cell conditions.

In recent years, several approaches to quantify FRET measurements evolved. Multiparameter Fluorescence Image Spectroscopy (MFIS)- FRET obtains quantitative lifetime- and intensity-based FRET information in addition to anisotropy [95–97]. Quantitative Imaging (QI)- FRET [98, 99] and its successor Fully-quantified Spectral Imaging (FSI)-FRET [100] use intensity-based FRET on a widefield microscope to measure dimer concentrations quantitatively. The latter two methods rely on vesiculation or osmotic swelling to produce flattened membranes, thus disturbing the endogenous state of the cell and are mostly used to detect large changes in FRET efficiency. Most recently,

FRET nanoscopy combines the sub-diffraction resolution of super-resolved fluorescence microscopy with multiparametric FRET spectroscopy [101] or intensity-based FRET [102, 103], but have mostly been applied to DNA origami probes and not yet established in (live) cells.
Although FRET complies with all requirements, none of these methods exploits its full potential for live-cell oligomerization studies and has the sensitivity required to elucidate the subtle spatial-temporal dynamics of molecular interactions in live cells.

2.1.4 The Synergy of Complementary Techniques

In summary, technical challenges and methodological limitations make rigorous studies of membrane protein organization and single-molecule stoichiometry on intact cells remarkably challenging. Super-resolution microscopy and single molecule spectroscopy techniques require highly specific experimental strategies optimizing either temporal or spatial resolution [104]. Namely, high resolution requires stationary fluorophores over long measurement times and to capture a dynamic organization in a fixed state is problematic. In consequence, each technique is limited and does not allow for a unique interpretation of the molecular structures which evolve over time. Thus, the elucidation of combined spatio-temporal information on membrane receptor activation using a single technique remains challenging, even impossible [105, 106]. These limitations trigger the need to acquire information from different angles in order to obtain robust results and the fact that most microscopy and spectroscopy approaches are complementary, promotes research environments with access to multiple techniques. Using a synergy of complementary state-of-the-art fluorescence microscopy and spectroscopy techniques is the key towards achieving the goal of a full spatio-temporal resolution.

One limit that is not to overcome with complementary techniques, is what they all have in common: they do not detect the target molecule itself, but the linked fluorophores. This induces undetectable fractions of target molecules, which in the case of genetically-encoded, directly linked fluorescent proteins are largely attributed to incomplete maturation, misfolding, or premature photobleaching of the fluorescent probe. To get hold of this global challenge, a validation of all methods at anytime with proteins standards/control samples using the same labeling strategy is the key towards a truly robust interpretation.

3 Study Outline

3.1 Aim of This Work

In this work, I have investigated the CD95 spatio-temporal receptor activation and its oligomeric state as a basis for our mechanistic understanding of CD95 apoptosis signal initiation. For this, a synergetic combination of state-of-the-art fluorescence microscopy and spectroscopy techniques of complementary sensitivity (in terms of spatio-temporal resolution and molecular concentration detection) was used.

To elucidate the CD95 activity states and dynamics, a robust methodology of complementary microscopic and spectroscopic techniques is applied to CD95 in its most natural state - integrated in a plasma membrane of human cells. Observing CD95 in its natural environment is achieved by means of transient transfections and stable cell lines and evades the use of artificial expression systems and potentially harsh purification procedures.
In order to answer the biological question and scrutinize the CD95 oligomerization model, I further intended to exploit and, where required, advance the complementary molecular sensitive imaging techniques: confocal Photobleaching Step Analysis, time-resolved FRET, quantitative STED, and FCS in combination with time-lapse imaging. With this, CD95 interactions are probed over the whole dynamic range from µs to hours, molecular to cellular scales and with particular focus on molecular concentrations to elucidate the CD95 activation comprehensively.

Furthermore, I aimed to contribute to projects in the field of clinical research on the development of CAR (Chimeric Antigen Receptor) T-cell therapy approaches with the microscopic visualization and analysis of CAR T-cell killing. As most (pre-)clinical methods are bulk approaches, microscopy can contribute towards a more differentiated understanding of the system as it enables to “see” single-cell interactions combined with their spatio-temporal dynamics.

3.1.1 Thesis Outline

As a first step to unravel CD95 membrane organization, the expression of CD95 and the resulting apoptosis dynamics in live HeLa cells – the expression system of choice – is characterized. Here, confocal microscopy helps to study the expression of localization of CD95 in the cell, quantitative flow cytometry characterizes the number of CD95 receptors in different cell lines and time-lapse microscopy is utilized to observe the dynamics of CD95 Ligand induced apoptosis.
Secondly, the organization and mobility of CD95 on the plasma membrane is scrutinized. A quantitative STED analysis uncovers the organization of the death receptor on fixed cells. To complement the steady-state STED result, FCS is used to explore the mobility of CD95 receptors in the membrane of living cells.
In a last step, the stoichiometry of CD95 is resolved exploiting two parallelized techniques - confocal PBSA and FRET. While both methods are established techniques, they were advanced towards the use case of membrane receptor oligomerization to record and interpret data with single molecule precision in noisy cell data reliably.
In all cases, CD95 data was benchmarked against robust monomer and dimer controls, allowing to distinguish photophysics- or concentration-related effects from CD95 oligomeric states and to quantify these.

The main research result of my study on CD95 activity states is presented in a monographic style following the common representation with an introductory chapter (Part I), the used materials and methods (Part II), experimental results (Part III) followed by a conclusive discussion (Part IV). Here, the technical advancements and specific details of all techniques required to unravel the CD95 receptor activity state down to single molecule level and exceeding the established scope of the respective methods are presented as scientific achievements in the Results Chapter.

My second project of the microscopic visualization and analysis of CAR therapy in head and neck squamous cell carcinoma (HNSCC) cells is presented as cumulative excursion into this clinical research field (Part V). It includes a general introduction into CAR therapy as well as a summary of benefits and challenges of their microscopic visualization. Further, the Results Part comprises the peer-reviewed publications achieved within this collaborative project.
The first manuscript includes the killing dynamic of CD44v6 CAR T-cells against a primary human HNSCC cell line unraveled with two-color time-lapse microscopy. Secondly, the immunological synapses formed between CAR NK cells and their target cancer cells could be visualized with a three-color-channel experiment design. The

third contribution to this project included a microscopic journal cover image of the CD19 CAR T-cell killing accompanying the associated publication of our collaboration partners and enhancing the significance and informative value of the microscopic visualization of cellular processes.

3.1.2 Contributions

In my main research project on the spatio-temporal receptor activation of CD95, I designed, implemented and executed all experiments including the optimization and preparation of measurement samples, as well as data analysis, interpretation and representation. As member of the Collaborative Research Center (CRC) 1208 "Identity and Dynamics of Membrane Systems - From Molecules to Cellular Functions" of the German Research Foundation (DFG), my results arose from close collaborations with other members of the CRC1208, which is why I will refer to the pronoun *we* presenting the accomplishments of this project.

Detailed Contributions:

Prof. Dr. Cornelia Monzel proposed the question on CD95 spatio-temporal activity states, conceived the study and supervised the project,

Prof. Dr. Claus A M Seidel conceived the project and supported with advisory capacity,

Nicolaas T M van der Voort designed and performed the experiments and analyses on FCS, STED cPBSA and FRET with me in close cooperation with his focus on technical aspects,

Arthur Bister and *Dr. Constanze Wiek* organized and performed flow cytometry measurements,

Dr. Annemarie Greife contributed to the design of plasmids and provided substantial advice for FRET measurements, and

Miriam Tappel performed control measurements of Hela $CD95^{KO}$ apoptosis dynamics as part of her Bachelor Thesis under my supervision.

The contributions to the project on CAR therapy are listed separately in the respective Results Chapter 12 and in the associated (and attached) peer-reviewed publications.

3.1.3 Publications

The work on CD95 (Parts I to IV) was summarized and is ready for submission in the following manuscripts [M]:

[M1] *A Minimal Model of CD95 Signal Initiation Revealed by Advanced Super-resolution and Multiparametric Fluorescence Microscopy.*
Nina Bartels, Nicolaas T M van der Voort, Annemarie Greife, Arthur Bister, Constanze Wiek, Claus A M Seidel, Cornelia Monzel

[M2] *Quantifying the Spatio-Temporal Evolution of Protein Interactions in Live Cells using ATR-FRET Microscopy.*
Nicolaas T M van der Voort, Nina Bartels, Cornelia Monzel, Claus A M Seidel

Furthermore, this work has been published in the Form of posters [P] or talks [T] on the following occasions:

[P1] GerBI Spring School: "Trends in Microscopy" | 03/2020 | Münsingen, DE
Nina Bartels and Cornelia Monzel
Interrogating CD95 Membrane Protein Complex Formation and its Signalling for Life or Death

[T1] CRC1208 Retreat | 09/2021 | Krefeld, DE
Nina Bartels and Cornelia Monzel
Interrogating CD95 Membrane Protein Complex Formation and its Signalling for Life or Death

[P2] DGZ International Meeting: "Life In Between" | 09/2021 | virtual meeting
Nina Bartels, Nicolaas van der Voort, C.A.M. Seidel, C. Monzel
Elucidating Cluster Formation in CD95 Signaling using Multiparametric Image Spectroscopy

[P3] Biophysical Society Annual Meeting | 02/2022 | San Francisco, USA
Nina M. Bartels, Nicolaas T. van der Voort, Claus A.M. Seidel, Cornelia Monzel
Elucidating Receptor Oligomerization States in CD95 Signaling with Multiparametric Image Spectroscopy

[T2] CRC1208 Conference | 03/2022 | Düsseldorf, DE
Nina Bartels, Nicolaas van der Voort, Claus A. M. Seidel, Cornelia Monzel
Elucidating CD95 Signal Initiation with DNA-Origami Based Synthetic Signaling Platforms and Multiparametric Image Spectroscopy

[P4] CRC1208 Conference | 03/2022 | Düsseldorf, DE
Nina Bartels, Nicolaas van der Voort, C. Seidel, C. Monzel

Elucidating Receptor Oligomerization States in CD95 Signaling with Multiparametric Image Spectroscopy

[T3] GBM Fall Conference: "Molecular Basis of Life" | 09/2022 | Düsseldorf, DE
Cornelia Monzel, Nina Bartels, Nicolaas van der Voort, Claus A. M. Seidel
Elucidating Receptor Oligomerization States in CD95 Signaling with Super-Resolution Microscopy and Multiparametric Image Spectroscopy

[T4] GBM Fall Conference: "Molecular Basis of Life" | 09/2022 | Düsseldorf, DE
Nicolaas van der Voort, Nina M Bartels, Claus AM Seidel, Cornelia Monzel
To unlock sensitive molecular switches in live cells using high throughput FRET

The work on CAR therapy (Part V) was published in peer-reviewed journal articles [J] as follows:

[J1] *CD44v6-targeted CAR T-cells specifically eliminate CD44 isoform 6 expressing head/neck squamous cell CARcinoma cells.*
Corinna Haist, Elena Schulte, Nina Bartels, Arthur Bister, Zoe Poschinski, Tabea C. Ibach, Katja Geipel, Constanze Wiek, Martin Wagenmann, Cornelia Monzel, Kathrin Scheckenbach and Helmut Hanenberg
Oral Oncology | 05/2021 | Volume 116 | Article 105259

[J2] *Genetic Engineering and Enrichment of Human NK Cells for CAR-Enhanced Immunotherapy of Hematological Malignancies*
Maren Soldierer, Arthur Bister, Corinna Haist, Aniththa Thivakaran, Sevgi Can Cengiz, Stephanie Sendker, Nina Bartels, Antonia Thomitzek, Denise Smorra, Maryam Hejazi, Markus Uhrberg, Kathrin Scheckenbach, Cornelia Monzel , Constanze Wiek , Dirk Reinhardt , Naghmeh Niktoreh and Helmut Hanenberg
Frontiers in Immunology | Volume 13 | 04/2022 | Article 847008

[J3] Journal Cover Image: *A novel CD34-derived hinge for rapid and efficient detection and enrichment of CAR T cells*
Arthur Bister, Tabea Ibach, Corinna Haist, Denise Smorra, Katharina Roellecke, Martin Wagenmann, Kathrin Scheckenbach, Norbert Gattermann, Constanze Wiek, Helmut Hanenberg
Molecular Therapy: Oncolytics | Volume 23 | 12/2021 | Page 1

II

Materials and Methods

4 Molecular Cell Biology

4.1 Cell Lines, Plasmids and Molecular Cloning

4.1.1 Stable Cell Lines

To study CD95 in the cellular environment, various stable clones of the HeLa cell line were used. HeLa is the abbreviation of Henrietta Lacks, the name of a 31-year-old US American woman, whose tissue sample of a cervix carcinoma led to the first established immortal human cell line in 1951. Table 4.1 provides an overview over the used stable HeLa clones in this work:

Name	Description
HeLa WT	Wild type HeLa cell line
HeLa CD95-mEGFP	Stable HeLa cell line overexpressing CD95-mEGFP on top of endogenous CD95
HeLa $CD95^{KO}$	Stable HeLa cell line with knockout of CD95

Table 4.1: Overview of the stable HeLa cell lines.

The HeLa WT cell line was purchased from the American Type Culture Collection (ATCC, Manassas, Virginia, USA). All modified HeLa cell lines were kindly provided from Joël Beaudouin (formerly IBS, Grenoble). The sequences and production of the cell lines HeLa $CD95^{KO}$ and HeLa CD95-mEGFP are described in [107–109].

Receptor Quantification by Flow Cytometry

To quantify CD95 expression levels of the stable cell lines, a kit for quantification of cell surface antigens by flow cytometry based on calibration beads is used: the QIFIKIT (Agilent Technologies, Inc., Santa Clara, California, USA, #K007811-8). Measure-

ments were performed on a MACSQuant Analyzer 10 (Miltenyi Biotec B.V. & Co. KG, Bergisch Gladbach, Germany) following the producer's protocol accurately. For CD95 detection, a monoclonal CD95 antibody, anti-human (Miltenyi Biotec, #130-108-066) was used. A negative control was achieved using an antibody against CD28 (Tonbo™ A Cytek Brand, San Diego, California, USA, #70-0281). As the provided secondary FITC antibody interfered with the mEGFP of the stable cell line, a secondary anti-mouse APC antibody (eBioscience™ , Invitrogen, #17-4010-82) was used for all samples instead. The measurement was repeated two times independently.

The linear calibration curve was fitted to the calibration bead mean fluorescent intensities (MFI) using MATLAB (R2019a, The MathWorks, Inc., Natick, Massachusetts, USA) following the producers protocol.

4.1.2 Protein Sequences and Plasmids

For CD95, four different constructs with different amino acid (aa) sequences were used:

- the full-length protein CD95 (amino acids 1-335),
- a death domain truncated version CD95(ΔDD),
- CD95(R102S), which cannot bind the ligand, as well as
- the pre-ligand assembly domain depleted CD95(ΔPLAD).

For CD95(ΔDD), amino acids 211-335 of the premature protein were truncated. The CD95(ΔPLAD) construct is missing amino acids 26-83, which corresponds to the CRD1 including the PLAD. The signaling peptide (SP) was linked to CD95(84-335) via the amino acid sequence GTALGSLK. All amino acid numbers refer to the premature protein sequence (including signaling peptide). As monomer control plasmid, the full-length sequence of CD86 was used. For the dimer control CTLA4, the last 23 amino acids of the sequence were removed in order to reduce the internalization of the receptor and to concentrate it at the plasma membrane [110]. For a second dimer control, a *pseudo dimer* consisting of CD86 bound to two mEGFPs was developed. The UniProtKBs of CD95, CTLA4 and CD86 are P25445, P16410 and P42081-3, respectively.

Figure 4.1 shows a schematic overview of the used constructs. As the fluorescent proteins (FP) are the measurement target, it is relevant to understand their distance from the protein of interest, which is defined via the connecting linker. Table 4.2 provides the respective amino acid linker sequences between receptor and FPs and the

lengths of flexible sequence parts around the linker ($\#aa_{flex}$).

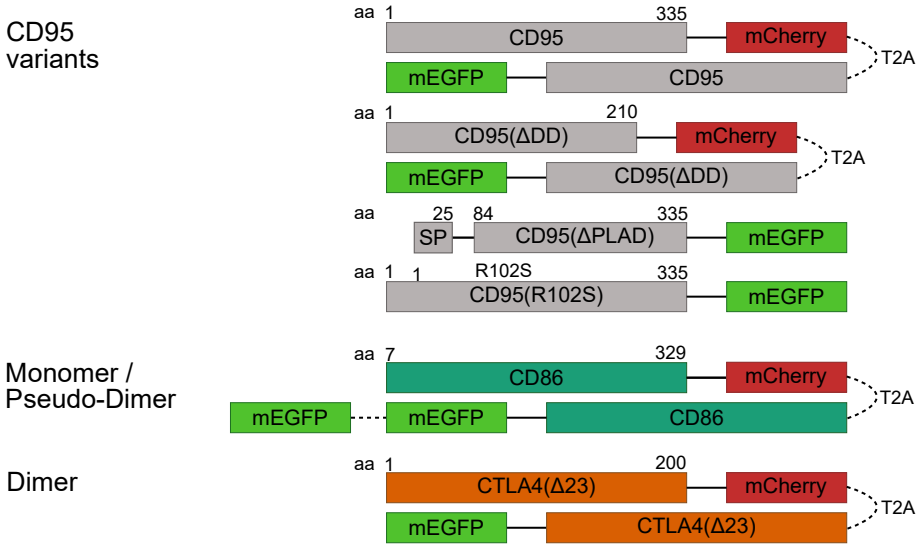

Figure 4.1: Schematic illustration of the used protein sequences from N-terminus to C-terminus, numbers indicate the amino acid (aa) position. Linkers are shown as black lines. Dashed lines indicate two versions of the construct, bicistronic plasmids or additional fluorescent proteins (FP) linked at the respective position.

All plasmids except CD86-mEGFP-mEGFP were kindly provided by Joël Beaudouin. These constructs were designed by fusing the coding sequences of the respective proteins' C-terminus (intracellularly) via a linker to mEGFP or mCherry in the pIRES-puro2 vector (Clontech). The cloning procedures of the plasmids provided by Joël Beaudouin are described in more detail in [108, 111]. The fluorescent fusion proteins mEGFP (EGFP-A206K-L221K) (also called D0 / Donor only) and mCherry are described in [112, 113] and [114], respectively. The protein sequences of all used constructs including linkers and fluorescent proteins are listed in the Supplementary Information (SI) A. For CD95, CD95(ΔDD) and CD86, monocistronic plasmids with both fluorophores (separately) were available. Additionally, for all proteins including CTLA4, we additionally used bicistronic plasmids combining the mCherry and mEGFP versions of a protein into one plasmid for FRET measurements to ensure equal co-expression of donor and acceptor (also called DA / Donor-Acceptor). The bicistronic constructs use the T2A sequence EGRGSLLTCGDVEENPGP surrounded by short linker sequences between the two proteins [108] (more details in SI Chapter A, Table A.1 shows the amino acid letter code used here). Note, that solely $CTLA4_{DA}$ was used instead of $CTLA4_{D0}$, as the latter did not localize to the membrane exclusively.

The CD86-mEGFP-mEGFP pseudo dimer control was synthesized using a cloning

service (BioCat GmbH, Heidelberg, Germany) by fusing two linked mEGFP proteins C-terminally to the CD86 full-length sequence of CD86 in a pcDNA3.1(+) vector (BioCat GmbH). To enable a purification, this plasmid contains a C-terminal Spot- and His-Tag (Supplementary Information A) to provide variable purification options, as suggested by Annemarie Greife.

If necessary, plasmids were amplified using the NucleoBond Xtra Maxi Plus EF Kit (MACHEREY-NAGEL GmbH & Co. KG, Düren, Germany, #740426) following the product instructions closely. Sequencing of the plasmids was achieved using an external service (TubeSeq Service, Eurofins Genomics Germany GmbH, Ebersberg, Germany).

Sequence Name	Linker Sequence	#aa$_{flex}$ pre	#aa$_{flex}$ linker	#aa$_{flex}$ post	#aa$_{flex}$ total
CD95–mEGFP	GG + L1	9[1]	25	12	46
CD95–mCherry	GG + L2	9[1]	23	16	48
CD95(ΔDD)–mEGFP	L1	16	23	12	51
CD95(ΔDD)–mCherry	L2	16	21	16	53
CTLA4–mEGFP	L1	16[2]	23	12	51
CTLA4–mCherry	L2	16[2]	21	16	53
CD86–mEGFP	L1	-[3]	23	12	35
CD86–mCherry	L2	-[3]	21	16	37
CD86–mEGFP–mEGFP	L2 | L3	- | 11	23 | 20	12 | 12	35 | 43

Table 4.2: Sequence overview including linker lengths. Specifications of linker lengths for used constructs including flexible amino acids (aa) before (*pre*) and after (*post*) the artificial linker. The linker sequences L1, L2 and L3, are the following:
Linker L1: GGGPVPQWEGFAALLATPVGGAV,
Linker L2: GGGPVPQWEGFAALLATPVAT,
Linker L3: GSSGSSNAAIINAAGSSGSS.
[1] 9 amino acids are used to model the flexible orientation of the death domain [51].
[2] Linker length based on the residual 16 intracellular amino acids after transmembrane domain.
[3] Flexible part of CD86 could not be estimated because the structure of the CD86 TM domain is not known, hence considered to be zero.

4.2 Cell Culture and Transfections

4.2.1 Cultivation of Cells

The cultivation of all cell lines was maintained in a controlled atmosphere at 37 °C at 5 % CO_2. Cells were cultivated and passaged following the general protocol in Supplement B.1.
Depending on the measurement, the cells were either seeded in 8-well glass bottom slides (ibidi GmbH, Gräfelfing, Germany, #80827) with a density of $\sim 30 \cdot 10^3$ cells per well (all live cell measurements as well as cPBSA measurements). For fixed STED immunostaining, $100 \cdot 10^3$ - $150 \cdot 10^3$ cells were seeded on a sterile coverslip (no. 1.5 H) in wells of a 12-well plate. The cells were seeded on the day prior to transfections or measurements.

4.2.2 Transfections

Transient transfections were obtained using ViaFect™ Transfection Reagent (Promega Corp., Madison, Wisconsin, USA, #E4981,) at a cell density of 60-70 % following the Supplementary Protocol B.2.

For all measurements with transient transfections, the HeLa $CD95^{KO}$ cell line was used as Hela cells naturally express CD95 (compare Chapter 4.1). Note, that HeLa cells naturally do not express CTLA4 or CD86 (nTPM=0.0)[2] as determined before [111, 115]. For Apoptosis Dynamics measurements, FCS, STED and PBSA the cells were transfected with 25 ng of target DNA and 975 ng empty vector (pIRES-puro2 or pcDNA) for all used plasmids. The empty vector helps to downregulate the expression levels by competing for transcription factors as it uses the same promotor (CMV) as the target plasmids. For FRET measurements, the bicistronic plasmids were transfected using varying amounts of target DNA to cover a broad range of expression levels: for a transfection in 2 wells of the imaging slide (ibidi), the combinations 25 ng target DNA + 975 ng empty vector, 100 ng target DNA + 900 ng empty vector, 250 ng target DNA + 750 ng empty vector as well as 1000 ng target DNA (no empty vector) were used. Donor only controls (the monotrinsic mEGFP fusion version of the proteins) were expressed at these varying concentrations as well.
To allow the relocation of the membrane proteins from the endoplasmic reticulum to

[2] nTPM (normalized transcripts per million) of the genes CD86 and CTLA4 available from v21.1.proteinatlas.org:
https://www.proteinatlas.org/ENSG00000114013-CD86/subcellular
https://www.proteinatlas.org/ENSG00000163599-CTLA4/subcellular

the plasma membrane, live experiments or fixations were done 48-72 h after the transfections.

4.3 Sample Preparation

4.3.1 Live Cell Sample Preparation

For all live-cell experiments (time-lapse imaging, FCS and FRET), the cells were washed with DPBS (Gibco, Life Technologies Inc., Carlsbad, California, USA, #14025050) once and incubated in Leibovitz's L-15 Medium (Gibco, #21083027) without phenol red, supplemented with 10 % FBS and 1 % Penicillin-Streptomycin (P/S).

For all apoptosis experiments including the CD95 Ligand, the *FasL, soluble (human) (recombinant) set* (Enzo Life Sciences Inc., Loerrach, Germany, #ALX-850-014-KI02) was used. The ligand was prepared according to the manufacturer's protocol and further diluted to the desired concentration in the respective cell culture or imaging medium. The provided enhancer was used for all experiments except FCS, in order to monitor the unbiased receptor mobility. For experiments using the cross-linking reagent (Enhancer), the enhancer concentration was always chosen to be 100-fold higher than the ligand concentration to ensure effective crosslinking. For all experiments except the apoptosis dynamics time-lapse microscopy, the ligand concentration was 200 $^{ng}/_{ml}$.

4.3.2 Cell Fixation and Immunostaining

For PBSA and STED immunostaining, cells were fixed after transfection within the respective seeding vessel (compare Chapters 4.2.1 and 4.2.2). For experiments including the CD95 Ligand (Enzo Life Sciences Inc.), the ligand was incubated for 2 hours at 37 °C before the fixation was started. Next, the cells were fixed and stained following the Supplementary Protocol B.3.

The **STED** immunostaining technique of intracellular mEGFP, exploits the technology of small, high specific nanobodies - the smallest known antibodies (for product details compare SI B.3). The here used products have a constant degree of labeling for higher reproducibility and reliability [116].

5 Advanced Optical Microscopy and Spectroscopy Techniques

In this thesis, we apply a wide range of multiparametric fluorescence microscopy and spectroscopy techniques. To ensure a comprehensive understanding and enable reproducibility, the technical details of all applications using fluorescence including setup, measurement procedure and analysis details will be provided in this chapter.

5.1 Widefield Microscopy

A widefield microscope represents the oldest and most basic form of light microscopy, featuring a wide range of different contrast techniques. For this study, phase contrast was combined with fluorescence microscopy.

The phase contrast technique was introduced 1932 by the Dutch scientist Frits Zernike [117] being awarded with the Nobel Prize in 1953. The technique is based on phase shifts of the illumination light upon the interaction of objects with different refractive indices. It enables to visualize objects which are almost invisible in brightfield microscopy - for example thin, biological membranes in cells which only absorb a small amount of light. While phase contrast enables to visualize fine subcellular details in an unstained specimen, fluorescence microscopy can capture specifically labeled (otherwise transparent) objects. The first working fluorescence microscopes with widefield illumination were developed in the early 20^{th} century by Oskar Heimstädt and Karl Reichert after initial findings of August Köhler and Henry Siedentopf using ultraviolet light [118–120].

5.1.1 Olympus IX83 Microscope Setup

Widefield images and time-lapse videos were acquired with an IX83 P2ZF inverted epifluorescence microscope system (Olympus Europa SE & CO. KG, Hamburg, Germany). The microscope is equipped with the motorized TANGO Desktop stage (Märzhäuser

Wetzlar GmbH & Co. KG, Wetzlar, Germany) and the Photometrics Prime BSI camera (Teledyne Photometrics, Tucson, Arizona, USA). An internal halogen lamp and the SOLA Light Engine (Lumencor Inc., Beaverton, Oregon, USA) served as light source for transmitted (brightfield (BF) and phase contrast (PH)) and reflected (fluorescence) illumination, respectively. For epi-fluorescence, four different filter sets were available: DAPI HC Filterset (excitation (exc.) 377/50nm, emission (em.) 447/60nm, #F36-500), EGFP ET Filterset (exc. 470/40nm, em. 525/50nm, #F46-002), DsRed ET Filterset (exc. 545/30nm, em. 620/60nm, #F46-005) and Cy5 ET Filterset (exc. 463/30nm, em. 690/50nm, #F46-009) (all AHF analysentechnik AG, Tübingen, Germany).
The available objectives used for this work where a 20x oil-objective (NA 0.85, UPLSAPO20xO), a 60x oil-objective (NA 0.65–1.25, UPLFLN60XOIPH) and a 100x oil-objective (NA 1.49, UAPON100XOTIRF), all from Olympus Europa SE & CO. KG. For live cell measurements an on-stage heating system with Incubator PM 2000 RBT, Heating Insert P Lab-Tek™2000 and TempController 2000-1 (all PeCon GmbH, Ulm, Germany) was used at 37 °C. The microscope was operated using the OLYMPUS cellSens Dimension 2.3 software (Build 18987, Olympus Europa SE & CO. KG).

5.1.2 Time-lapse Imaging for Apoptosis Dynamics

For live-cell video recording of the apoptosis dynamics on the Olympus IX83 microscope, the cells were prepared as described before (Chapter 4.3). The CD95 Ligand was added to the cells to the desired final concentrations of $0.2 - 200\,{}^{\mathrm{ng}}/_{\mathrm{ml}}$. Time-lapse videos of multiple positions in the phase contrast channel were acquired with the CellSense Dimensions Software (Olympus). For transiently transfected cells sequential imaging of the EGFP channel and the phase contrast channel at multiple positions was performed in order to identify positively transfected cells. Frames were acquired every $5 - 15$ minutes during a time of maximum 16 hours. While a cycle time of 5 minutes worked fine for single-channel PH time-lapses, a cycle time of 15 minutes had to be selected for transfected cells to avoid light-induced cell stress and death as a fluorescence channel was recorded additionally.

Image analysis was performed with Fiji [121], using an intensity-based threshold to the fluorescence channel in order to detect successfully transfected cells. Apoptotic cells were identified via the phase contrast channel manually by the detection of cell blebbing and/or shrinkage.

For a mathematical description, the percentage of apoptotic cells was plotted as a function of time $P(t)$, resulting in a sigmoidal apoptosis dynamics curve. This was

fitted using the hill equation to characterize the dynamics and efficiency of the signal transduction:

$$P(t) = P_{\max} - \frac{P_{\max} - P_{\min}}{(1 + (t/t_{\text{half}})^n)} \tag{5.1}$$

$P_{\min}$ and $P_{\max}$ are the minimal and maximal fractions of apoptotic cells and t_{half} is the characteristic time after which half of all apoptotic cells died. The hill coefficient n indicates the steepness of the curve and how immediate the signal was transduced. The fitting was performed using MATLAB (R2019a, The MathWorks, Inc.).

5.2 Confocal Microscopy and Polarization-Resolved TCSPC

While conventional widefield fluorescence microscopy excels in a variety of contrast techniques while maintaining simplicity and a comparatively low technical effort, confocal microscopy reveals a broad spectrum of new applications in fluorescence microscopy thanks to its key feature: an unprecedented signal-to-noise ratio (SNR). The key element of the beam path is a pinhole in the focal plane of the system ensuring that only light emitted from a small sample region (called *confocal* volume) is focused through it and eventually caught by the detector. A 2D image is achieved by scanning a particular slice of the sample in x and y without detecting any signal from the planes above or below, where the size of the pinhole determines the slice thickness. Because of this slice selection a strongly suppressed detection of out-of-focus light and a significantly improved SNR are achieved. Scanning multiple z-planes enables 3D images. The first confocal microscope was introduced by Marvin Minsky in the late 1950s, granted with a patent in 1961 [122].

The confocal microscopes used for CD95 oligomerization studies are additionally equipped with single-photon counting abilities and polarization-sensitive readouts, which means the following:

TCSPC (Time-Correlated Single Photon Counting) is based on the time-resolved registration of single photons of a periodically excited (and emitted) fluorescence signal. Thus, pulsed lasers are required for the periodic excitation. The excitation pulse period is kept very short ensuring that the probability of registering more than one photon per cycle is very low as the detectors can only measure the arrival time of one photon at a time. In this way, it is possible to collect enough photons to reconstruct the fluorescence

decay profile from single-photon events accumulated over many cycles. The principles of this methods were first described in 1984 by Desmond O'Connor and David Phillips [123].

Polarization-resolved Microscopy. The absorption of light depends on the angle between the orientation of the fluorophore dipole axis and the polarization of the excitation light. Including polarization-sensitive readouts into the beam path, it is possible to measure the molecular orientation from the fluorescence anisotropy of the fluorescent sample. In this case, the sample is excited by linearly polarized light and the fluorescence decay is detected in the two directions of polarization, parallel (P) and perpendicular (S) to the excitation.

5.2.1 Abberior Expert Line Microscope Setup

The custom-designed Abberior Expert Line system (Abberior Instruments GmbH, Göttingen, Germany) using an Olympus IX83 microscope body is equipped with excitation laser wavelengths 485 nm, 561 nm and 640 nm (pulse width < 100 ps) and a STED depletion laser (775 nm, pulse width 1.2 ns) (only relevant laser lines are mentioned). Polarization control can be achieved using $\lambda/2$ and $\lambda/4$ waveplates (Abberior Instruments). The device is provided with four APDs (Excelitas Technologies Corp. Waltham, Massachusetts, USA, #SPCM-AQRH-13-TR) which follow dye-specific band pass filters, such that two polarization-resolved colors can be measured simultaneously. The used filters were: ET525/50 nm bandpass filters (Chroma Technology Corp., Below Falls, Vermont, USA) for mEGFP, ET608/45 nm (AHF analysentechnik AG) for mCherry and ET685/70 nm (Abberior Instruments) for Atto647N. Single-photon counting was achieved with the external TCSPC unit Hydra Harp 400 (PicoQuant GmbH, Berlin, Germany). The microscope is operated using the Abberior microscope software Imspector (version 14.0.3060, Abberior Instruments GmbH), adapted for our customized setup.

The instrument beampath is schematically illustrated in Figure 5.1 and further details of the setup are described in [101].

5.2.2 Olympus Fluoview 1000 Microscope Setup

The Olympus Fluoview 1000 microscope setup is as well a custom setup: the FluoView1000 IX81 inverted microscope body (Olympus) was modified with pulsed excitation and polarization-sensitized TCSPC readout (Hydra Harp 400, PicoQuant). For

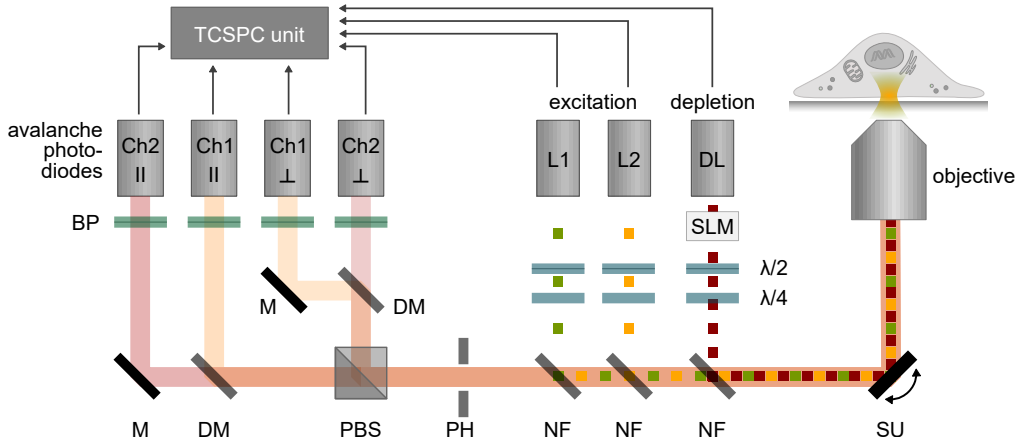

Figure 5.1: Abberior Expert Line custom beampath. Scheme of the Abberior microscope with 2 channel pulsed laser excitation (L1 and L2) and a depletion laser (DL). Available excitation wavelengths: 485 nm, 518 nm, 561 nm and 640 nm, available depletion wavelengths: 595 nm and 775 nm. The depletion laser is modulated by a spatial light modulator (SLM) to generate 2D donut transverse modes. The polarized excitation and depletion laser beams are overlaid by notch filters (NF) and focused on the sample via the scanning unit (SU) and the objective. The emitted light is guided back through a pinhole (PH), split by polarization using a polarizing beam splitter (PBS), split spectrally by dichroic mirrors (DM), directed via reflective mirrors (M) and filtered by band pass filters (BP) in front of the detectors for the two channels. BPs can be adapted to the required laser lines. Lasers and detectors are synchronized via a TCSPC unit.

excitation, a diode laser driver Sepia II (PicoQuant GmbH) driving a LDH-D-C-485 laser head (PicoQuant) is used. To separate emitted light onto multiple detectors, a DM405/488/559/635 quadband mirror (Olympus) was available. The emitted fluorescence split into perpendicular and parallel components using a polarizing beam splitter cube (VISHT11, Gsänger Optoelektronik GmbH, Planegg, Germany) and finally detected. For mEGFP detection (excited with 488 nm) the device is equipped with BS 520/35 nm bandpass filters (Semrock Inc., Rochester, New York, USA) and single photon avalanche detectors (PDM50-CTC, Micro Photon Devices, Bolzano, Italy). For live-cell imaging, there is the heating insert HP-LabTek (Pecon GmbH, Erbach, Germany) available.

5.3 Stimulated Emission Depletion (STED)

The method of Stimulated Emission Depletion (STED) was introduced in Chapter 2.1.1.

5.3.1 Measurement Details

STED measurements were preformed on the Abberior Expert Line setup (Abberior Instruments, details in Chapter 5.2.1). All immunostained samples (Chapter 4.3.2) were imaged with a 640 nm excitation laser (5.3 µW) and a 775 nm STED depletion laser (41 mW) using an 100x oil-immersion objective (NA 1.4, UPLSAPO 100XO, Olympus). Before the measurements, channel alignment was performed manually using TetraSpeck Microspheres (Invitrogen, # T7279). Per sample, 20 ROIs of 5 µm × 5 µm (10 nm pixel size, 4.00 µs dwell time, 5 frames) of the bottom cell membrane of at least 10 cells were recorded.

5.3.2 STED Image Analysis

Deconvolution & Object Analysis

STED image data analysis was employed to images comprising the sum of intensities of the different polarization channels. As a first step of data processing, time-gating of the first 2.2 ns was employed to increase the achievable resolution. For deconvolution and image data analysis, Huygens Professional (HuPro Version 21.10.1p2 64b, Scientific Volume Imaging B.V., Hilversum, Netherlands) was used. The deconvolution was performed using the CMLE (classic maximum likelihood estimation) algorithm with a signal-to-noise ratio (SNR) of 3.0, as estimated by the software. The quality stop criterion was set to 0.010 and the maximum of iterations to 40 runs. The automatic background estimation was used with a search area of 0.7 µm radius. After deconvolution, the Object Analyzer of Huygens Professional was used to quantify the object properties of the membrane protein spots. For the threshold-based object segmentation, the watershed method was used. Figure 8.1 illustrates the principle of STED object analysis. No Gaussian smoothing filter (sigma) was applied before the segmentation. The global, absolute object threshold was 1.2 with a seeding level of 1.3, the garbage volume was 2 voxels. Objects touching the image border were excluded from the analysis and only circular objects with an aspect ratio $0.9 < D_x/D_y < 1.11$ of the object diameter D in x and y were considered, as elongated objects result from crowding.

Spot Anisotropy

The spot intensities of the parallel (P/$\parallel$) and perpendicular (S/$\perp$) channel, $I_\parallel$ and $I_\perp$, were determined with an individual object analysis of both images as described before. The anisotropy r was then calculated with

$$r = \frac{G \cdot I_\parallel - I_\perp}{G \cdot I_\parallel + 2 \cdot I_\perp}, \tag{5.2}$$

where the polarization correction factor $G = \frac{\eta_\parallel}{\eta_\perp}$ accounts for the instrument's polarization dependent transmission where $\eta_\parallel$ and $\eta_\perp$ are the detection efficiencies of the parallel and perpendicular detection channels. The polarization correction factor G was determined to be 0.905.

Pair Correlation Analysis

The pair correlation function is a means for the statistical analysis of a spacial object distribution, with inter-object center distance d_{ij}. The pair correlation function $g(r)$ is defined as [124]:

$$g(r) = \frac{1}{\pi \rho^2 r \gamma(r)} \sum_{i=1}^{n} \sum_{j=i+1}^{n} k(r - |p_i - p_j|), \tag{5.3}$$

where ρ is the object density in the image, and $\left|\mathrm{p}_i - \mathrm{p}_j\right|$ is the distance between two object points p_i and p_j with two-dimensional position (x, y), equal to d_{ij}. The object positions were assumed to be planar as we recorded the flat bottom membrane of the cell. The covariance function γ corrects for edge effects of a rectangular image with height h and width w. In our case, images had a size of 5000×5000 pixels corresponding to $5 \times 5\,\mu\mathrm{m}$. It is defined as [125]:

$$\gamma(r) = hw - \frac{2(h+w)}{\pi} r + \frac{r^2}{\pi}, h \leq w. \tag{5.4}$$

The kernel $k(x)$ is definded as [126]:

$$k(x) = \begin{cases} \frac{3}{4\epsilon}\left(1 - \frac{x^2}{\epsilon^2}\right) & , |x| \leq \epsilon, \\ 0 & , |x| > \epsilon \end{cases} \tag{5.5}$$

with ϵ as bandwidth. The pair correlation of a random distribution is $g(r) = 1$.

The pair correlation of the objects found by the Huygens Object Analyzer (compare Chapter 5.3.2) was calculated using a self-written MATLAB script (R2019a, The MathWorks, Inc.) following the example of Peckys et al. [127]. The correlation histogram $g(r)$ was calculated for binned distances with a bin width of 10 nm and a bandwidth of 5 nm. The data of all STED images per sample were averaged.

Random Spot Distribution Simulations. In order to compare the pair correlation of real STED images with a simulation of randomly distributed objects, we simulated images comparable to the real data. Using MATLAB (R2019a, The MathWorks, Inc.), 5000x5000 pixel images with randomly distributed object centers were created. The number of object points per image was selected randomly between 300 and 600 and the pixel value was adjusted to 4 (photons/pxl) to match the real data average. Next, the spots were filtered using a 2D Gaussian smoothing kernel with standard deviation of $\sigma = 2.5$ pixel. Afterwards, the images were resized to the original size of 500x500 pixel to achieve Gaussians centers to be shifted with respect to the pixel center. Subsequently, 20 simulated images were analyzed for objects similar to the real data (Huygens Object Analyzer, Chapter 5.3.2) and finally the pair correlation $g(r)$ of simulated data was calculated.

5.4 Fluorescence Correlation Spectroscopy (FCS)

The Fluorescence Correlation Spectroscopy (FCS) is a technique used to analyze temporal fluctuations of the fluorescence intensity $F(t)$ using a correlation analysis. It was first introduced by Douglas Magde, Elliot Elson, and W. W. Webb in 1972 [128]. FCS offers insights into the photophysics as well as equilibrium kinetic behavior of fluorophores causing the characteristic intensity fluctuations in the detection volume. The most prominent application for FCS is the measurement of (average) diffusion time/-constant and molecular concentrations of freely diffusion single molecules entering or leaving the excitation volume, which is usually deployed by a stationary laser beam. Hence, a sensitive confocal microscope is a typical setup for FCS experiments.

5.4.1 Measurement Details

FCS measurements were performed at the Olympus Fluoview 1000 setup (compare Chapter 5.2.2) with a 60x water immersion objective (NA 1.2, UPLSAPO, Olympus).

Calibrations

Calibration of the setup was performed according to established procedures in the collaborating research group [129]. Briefly, the optimal objective correction collar position adapting the coverglass thickness was found by tuning the collar position until the maximum count rate was obtained for a Rhodamine 110 (Rh110, Sigma-Aldrich, #83695) solution. For all our experiments the correction collar matched the coverslip thickness (170 µm). The instrument response function (IRF) was determined to enable time correlated single photon counting (TCSPC) analysis by using a mirror. Next, we measured a Rhodamine 110 solution with $1-5$ molecules in the focus to obtain 1) a calibration for the confocal spot shape factor, z_0/ω_0 or κ, 2) the ratio of the parallel and perpendicular detection efficiencies, γ, 3) the number and brightness of Rhodamine 110 molecules in the focus and 4) the confocal detection volume by inserting a Rhodamine 110 diffusion constant of 430 $\mu m^2/s$ at 22.5 °C [130] or 600 $\mu m^2/s$ when recorded at 37 °C considering the temperature dependence of D.

The laser power was measured at the objective using an immersion S170C power meter head (Thorlabs Inc., Newton, New Jersey, USA) attached to a PM400 power meter body (Thorlabs Inc.). As the measured power varied by ∼10 % when translating in x, y and z, we avoided a systematic error by varying the position until maximum power was reached.

Recording Procedure

Cells were imaged using confocal microscopy by focusing on the bottom membrane. The diffraction limited focus was placed in a stationary position away from the edge of the cell and away from the endoplasmic reticulum (ER) and Golgi apparatus. FCS curves were recorded over 5 minutes using a 5 µW pulsed 488 nm excitation beam, a 200 µm or 2.1 AU (airy units) pinhole (see also SI Chapter D.1), the 60x water objective and polarization sensitized readout (compare setup Fluoview 1000 in Chapter 5.2.2). The measurements in solution were performed using identical settings except for placing the focus 50 µm above the glass surface and recording Rh110 and mEGFP for 1 minute and 5 minutes, respectively.

5.4.2 FCS Curve Fitting

All cell measurements were fitted with two diffusion terms, corresponding to a cytoplasmic (cp) and a membrane (mem) component:

$$G(t) = 1 + \frac{\rho_{\mathrm{cp}}}{\left(1 + \frac{t}{t_{\mathrm{diff,cp}}}\right)\left(1 + \frac{t}{\kappa^2 t_{\mathrm{diff,cp}}}\right)} + \frac{\rho_{\mathrm{mem}}}{\left(1 + \frac{t}{t_{\mathrm{diff,mem}}}\right)\left(1 + \frac{t}{\kappa^2 t_{\mathrm{diff,mem}}}\right)} + G_\infty, \quad (5.6)$$

where ρ denotes the species correlation amplitude, t_{diff} the species diffusion time, G_∞ the residual correlation at infinity, κ^2 the aspect ratio of the focus and t the correlation time. As the signal-to-noise was limited, the stability of the fit was improved omitting an additional bunching term to account for triplet as it did not affect the values of the diffusion times. To improve the stability of the fit further, $t_{\mathrm{diff,cp}}$ was fitted globally over a set of 11 points from 7 CD95 transfected cells (see Supplementary Figure D.1), yielding a diffusion time of 0.60 ms to be kept fixed for all subsequent analysis. For more information on obtaining robust results from noisy live cell FCS data see Supplementary Note D.1.

Curve weighting according to the standard deviation (SD) calculated by the statistical evaluation of several auto-correlation functions (σ_{AV}) [131] was preferred because of its ability to provide accurate weights at long correlation times. Our measurements fulfilled the requirement for the recording to be be divided in >10 chunks of 20 seconds each. FCS curves were created and fitted using the SymPhoTime software (PicoQuant GmbH).

5.5 Confocal Photobleaching Step Analysis (cPBSA)

An introduction of the details and applications of Photobleaching Step Analysis (PBSA) have been substance of Chapter 2.1.2. Here, we advance PBSA to a confocal setup (cPBSA) where the spatial flexibility of the confocal setup enables measurements at any position of the cell with minimal background intensity without bleaching large areas of the cell. Moreover, we present strategies to characterize the signal fluctuations due to dark states and polarization effects that enable a robust interpretation of mEGFP bleaching steps despite its lower stability and higher noise level compared to stable organic fluorophores.

5.5.1 Data Acquisition

The confocal approach of PBSA was preformed on the Abberior Expert Line Setup (Abberior Instruments, details in Chapter 5.2.1) using a UPLSAPO 100XO objective (NA 1.4, Olympus) and circular polarized excitation. The Data acquisition using a confocal microscope is generally slower than TIRF-based PBSA because only one molecular assembly can be measured at a time. To gather sufficient statistics, a data acquisition script was written by Nicolaas T M van der Voort, that automates data acquisition after a manual area selection. The program uses the Python Application Programming Interface (API) from the Imspector acquisition software and contains a graphical user interface (GUI). Data acquisition works as follows (Figure 9.1):

1. A suitable area (20x20 μm^2) is selected on the lower membrane by the user.
2. An overview image is recorded using 50 nm pixel size, 10 µs dwell time, 5 % 488 nm excitation and summed over 3 frames. The output corresponding to 5 % laser power fluctuated around 1.3 µW (compare Table 5.1).
3. The overview image is smoothened using a Gaussian filter with a standard deviation (σ) of 1 pixel.
4. Molecular assemblies are identified from local maxima that exceed $3 - 5$ counts on the smoothed image. The threshold level was adjusted per area as needed to select all spots while avoiding crowding by visual inspection.
5. Local maxima that are closer than 450 nm to any other local maxima are not considered for further analysis, considering the confocal resolution limits.
6. A photon trace is recorded for each remaining local maximum by placing the confocal beam there for a duration of 3 seconds.
7. A quick display is rendered for user feedback.

We established an experimental procedure to optimize the quality of our data. Firstly, our sample fixation procedure minimizes autofluorescence (compare Chapter 4.3). Secondly, only molecular assemblies that are close or below the nucleus were recorded to ensure that the lower membrane was not in close proximity to the top membrane, as cells deflate upon fixation (see Figure 7.1). To avoid deflation as far as possible, we forgo upside-down mounting on a cover slip and image cells in well slides instead (compare Chapter 4.2). Thirdly, low excitation power and integration time was used for creating an overview image in order to avoid premature bleaching.

5.5.2 Data Analysis

Trace Fitting

The data analysis was done using the Kalafut-Visscher (KV) algorithm [132] implemented by Hummert et al. in Python [89]. Figure 9.1 shows an example trace. The KV algorithm takes a minimal step size as a sole user input, limiting user bias. As our TCSPC modality records the arrival time of each photon, we can set the time binning of our data ($t_{\text{bin}}(s)$) post-acquisition. The threshold was chosen at 50 counts per t_{bin} of 5 ms, corresponding to 10 kHz, at a laser power of 1.36 µW. To compensate for variations in the laser power, the minimum step size was corrected according to:

$$\text{minimum step size} = 50\frac{P_{485}}{1.36\,\mu\text{W}}, \tag{5.7}$$

where P_{485} is the laser power of the 485 excitation laser for that measurement in µW. Resulting minimum step sizes for all measurements are shown in Table 5.1. Bleaching traces where no steps were found are disregarded from further analysis. No other selection criteria were applied.

Dataset	Date	Laser power [µW]	Minimum step size [counts]
CD95	2021-07-22	1.36	50
CD95 + Ligand	2021-07-23	1.60	58
CD95(ΔDD)	2021-07-22	1.36	50
CD95(ΔDD) + Ligand	2021-07-23	1.60	58
CD86-mEGFP	2021-07-22	1.36	50
CD86-mEGFP	2021-11-24	1.37	50
CTLA4$_D$A	2022-02-02	1.00	36
CD86-mEGFP-mEGFP	2022-02-02	1.00	36

Table 5.1: cPBSA minimum step size determination. Due to laser fluctuations the threshold was adjusted such that the ratio of the power and the threshold remains constant.

Trace Polarization

The intensities of x and y polarization (Figure 9.1) were calculated for traces that showed a single step by integrating fluorescence while the fluorophore was on. As circular polarization was used, fluorescence polarization was calculated using

$$p = \frac{I_\mathrm{x} - g \cdot I_\mathrm{y}}{I_\mathrm{x} + g \cdot I_\mathrm{y}}, \tag{5.8}$$

where I_x is the signal oriented along the x-axis and I_y was the signal along the y-axis and

$$g = \frac{g_\mathrm{ox}}{g_\mathrm{oy}} \tag{5.9}$$

is the relative detection efficiency along the x and y axis under circular polarization.

Trace Cross-Correlation

The I_x and I_y signals of detector x- and y-polarization sensitized detectors were cross-correlated and analyzed using the in-house developed program Kristina [133]. All traces were used without any filtering. The signal-to-noise ratio was very high despite having a low total amount of photons as all photons correlated. Similar to FCS data, the correlation curve was fitted with one diffusion term and 3 bunching terms. This fitting model for the cross-correlation of cPBSA traces was determined by optimization of $\chi^2_\mathrm{red,avg}$ (compare SI Table E.1):

$$\begin{aligned} G(t_\mathrm{c}) = & \frac{1}{N} \frac{1}{1 + \frac{t_\mathrm{c}}{t_\mathrm{bleach}}} \frac{1}{\sqrt{1 + \frac{t_\mathrm{c}}{\kappa^2 t_\mathrm{bleach}}}} \\ & \cdot \left(1 - A_\mathrm{d1} + A_\mathrm{d1} \cdot e^{t_\mathrm{c}/t_\mathrm{d1}} - A_\mathrm{d2} + A_\mathrm{d2} \cdot e^{t_\mathrm{c}/t_\mathrm{d2}} - A_\mathrm{d3} + A_\mathrm{d3} \cdot e^{t_\mathrm{c}/t_\mathrm{d3}}\right), \end{aligned} \tag{5.10}$$

where A denotes the amplitudes, t the correlation times and κ^2 was fixed to 100 such that the expression under the root is ~ 1. Results are summarized in Table 5.2. While the cross-correlation of a bleaching event is different from a diffusion event, no specialized model for this scenario was available. The resulting residuals around the bleaching time are acceptable as we are mainly interested in the bunching terms. Additionally, Variance from cPBSA cross-correlation curves were predicted for comparison, Supplementary Chapter E.2.

Parameter	CD95	CD95 + L	CD95(ΔDD)	CD86
$G(\infty)$	0.95	1.01	0.95	0.98
N	0.78	0.72	0.98	0.77
A_{bleach} [%]**	84	84	84	84
t_{bleach} [ms]*	69.9	68.5	68.5	64.9
κ*	100	100	100	100
A_{d1} [%]	13.3	14.0	11.0	15.6
t_{d1} [ms]*	5.0	5.0	5.0	5.0
A_{d2} [%]	10.0	11.5	13.0	11.7
t_{d2} [ms]*	0.56	0.56	0.56	0.56
A_{d3} [%]	6.8	6.0	7.5	7.8
t_{d3} [ms]*	0.011	0.011	0.011	0.011

Table 5.2: Fit parameters for cross-correlation fits on ensemble cPBSA traces (see Supplementary Figure E.2).
* fitted globally.
** calculated using $A_{\text{bleach}} = 100 - A_{\text{d1}} - A_{\text{d2}} - A_{\text{d3}}$.

5.6 Förster Resonance Energy Transfer (FRET)

The technical details and state-of-the-art applications of FRET have been introduced in Chapter 2.1.3. For the oligomerization studies of CD95, we use and advance the lifetime based FRET method of FRET-induced donor decay analysis.

5.6.1 Recording Procedure

Live cells were mounted on the Abberior Expert Line setup using an 60x water-immersion objective (NA 1.2, UPLSAPO 60XW, Olympus) and kept at 37 °C using an objective heater (see Chapter 5.2.1). A large membrane protein concentration range was sampled by transfecting with 25, 100 or 250 ng per 2 wells and selecting cells to cover the desired concentration level (compare Chapter 4.2). On each measurement day, a donor only sample was recorded to serve as a reference, followed by multiple

donor-acceptor samples. Data acquisition was highly accelerated by first manually selecting locations of interest and subsequently measuring those locations automatically using an in-house program by Nicolaas T M van der Voort that interfaces with the instrument control software. In presence of a ligand, the program was used to visit the same areas repeatedly (compare Figure 9.5 A2), where one round of 10 areas needed 28.5 minutes with our imaging settings. The focus of the microscope was kept stable on the cell bottom membrane over hours using the autofocus function. Statistics were improved by analyzing multiple cells per area. Images were recorded using Alternating Line Excitation (ALEX) (compare Figure 9.5 A1) using 485 nm excitation at 7.8 µW as a prompt and a 561 nm excitation at 7.5 µW as a delay, a 100µm pinhole, 5µs pixel integration time and 21 frames. The image size was 80µm×80µm with a pixel size of 100 nm.

5.6.2 FRET-induced Donor Decay Analysis

Preparation of Live Cell Data

The TCSPC data was transformed into an $(x, y,$ micro time) array where the first two dimensions correspond to the spatial coordinate and the last dimension contains the histogram of photon arrival times using 1024 bins with 32 ps/bin. Multiple frames were recorded and summed over to increase statistics. A lifetime decay was generated by integrating over a (x, y) mask as desired for the experiment. Masks were generated manually for each cell using the freehand selection tool in imageJ [134]. Cell contact sites containing fluorescent signal from multiple cells were excluded. Additional masks containing only the bright or only the dark areas were subsequently generated automatically using home-built code by Nicolaas T M van der Voort. Thereafter, the mask are used to perform the FRET induced donor decay analysis (compare Figure 9.5 A3)

High and Low Brightness Masks

Single cell areas were selected by applying previously hand-drawn masks. Images were smoothed with a Gaussian filter using a sigma of 1 pixel to remove shot noise. To ensure a constant SNR, cells were split in bright and dark areas each containing 50 % of the total image countrate. The split threshold was determined by plotting the cumulative distribution function of photons against the pixel brightness and determining the half-value (illustrated in Figure 9.9b). The split threshold was different for each cell as the expression level and brightness distribution varied for each cell. High and low brightness masks were determined by applying the split threshold to the smoothed

data. The entire process is automated.

FRET-induced Donor Decay Fitting

FRET induced donor decays were fitted similar to the method described previously [95, 97], with the difference that a tailfit was used without Instrument Response Function (IRF) convolution. The data was fitted from 1.92 ns at the IRF maximum up to 22.4 ns. The donor-only (D0) decay was fitted using two lifetimes:

$$f_{\mathrm{D|D}}^{(\mathrm{D0})}(t) = A_0 \left(x_{\mathrm{D},1} \cdot e^{-t \cdot k_{\mathrm{D},1}} + (1 - x_{\mathrm{D},1})\, e^{-t \cdot k_{\mathrm{D},2}} \right) + b \cdot g_1 = A_0 \cdot f_{\mathrm{D|D}}^{\prime(\mathrm{D0})}(t) + b \cdot g_1. \tag{5.11}$$

The total amount of photons is used to constrain the fit and the normalized donor only decay $f_{\mathrm{D|D}}^{\prime(\mathrm{D0})}$ can be accurately determined. The FRET induced (DA) donor decay was subsequently fitted assuming a donor only fraction and a FRET fraction (Figure 9.5 A3),

$$\begin{aligned} f_{\mathrm{D|D}}^{(\mathrm{DA})}(t) &= A_1 \left((1 - x_{\mathrm{FRET}})\, f_{\mathrm{D|D}}^{\prime(\mathrm{D0})}(t) + x_{\mathrm{FRET}} f_{\mathrm{D|D}}^{\prime(\mathrm{D0})}(t) \cdot e^{-t \cdot k_{\mathrm{FRET}}} \right) + b \cdot g_2 \\ \Leftrightarrow f_{\mathrm{D|D}}^{(\mathrm{DA})}(t) &= A_1 \cdot f_{\mathrm{D|D}}^{\prime(\mathrm{D0})}(t) \epsilon_{\mathrm{D}}(t) + b \cdot g_2, \end{aligned} \tag{5.12}$$

where we substituted

$$\epsilon_{\mathrm{D}}(t) = x_{\mathrm{FRET}} \cdot e^{-t \cdot k_{\mathrm{FRET}}} + (1 - x_{\mathrm{FRET}})\,. \tag{5.13}$$

As the normalized donor only decay is already known from the donor only fit and the amplitude is constrained by the total number of photons, only x_{FRET}, k_{FRET} and the background are free fit parameters, lending accuracy and robustness to the fit result. Data was fitted by Nicolaas T M van der Voort using the *optimize.curve_fit* function from the python *scipy* library using the Levenberg-Marquardt method.

5.6.3 Advanced FRET Methods

Determination of Receptor Surface Concentration in FRET Samples

We obtained a calibration for the brightness of a single fluorophore using a titration series for EGFP (Biorbyt Ltd, Cambridge, UK, #orb84840) and mCherry (OriGene Technologies, Inc., Rockville, Mayland, USA, #TP790040) in DPBS (Gibco, #14190144). First, the concentration was measured using an absorption spectrometer (Cary 4000 UV-Vis Spectrophotometer, Agilent Technologies, Inc., Santa Clara,

California, USA) and extinction coefficients of 55 900 $cm^{-1}M^{-1}$ and 72 000 $cm^{-1}M^{-1}$ for EGFP and mCherry, respectively. Molecular weights were 30.6 kDa (EGFP) and 26.5 kDa (mCherry) following the producer specifications. Subsequently, the brightness per confocal volume was measured on the Abberior setup (compare Chapter 5.2.1) at three different excitation powers for each sample. All three values of the power-normalized brightness (detector counts per time and laser power [$^{kHz}/_{\mu W}$]) were plotted against the measured concentration [µM] and fitted using a linear fit $b \cdot x$ (Figure 9.6) resulting in the slopes $b_D = 266.2\,^{kHz}/_{(\mu M \cdot \mu W)}$ or equivalently $^{Hz}/_{(nM \cdot \mu W)}$ and $b_A = 133.3\,^{kHz}/_{(\mu M \cdot \mu W)}$ for the donor D (EGFP) and acceptor A (mCherry), respectively. The fitting was performed using MATLAB (R2019a, The MathWorks, Inc.).

The confocal volume V was obtained from FCS (at identical pinhole settings) using Rhodamine 110 (Rh110, Sigma-Aldrich, #83695) in DPBS (Gibco, #14190144) as a calibration dye for excitation with 485 nm. The confocal volume was determined to be $V_{485} = 0.543 \pm 0.1$ fl by fitting a single diffusion time and triplet state while assuming $D_{Rh110} = 470\,^{\mu m^2}/_{s}$ for the Rh110 diffusion constant at 25.8 °C (summer) lab room temperature [130, 135, 136]. The confocal volume at 561 nm excitation was calculated based on V_{485} and its wavelength dependence in all three dimensions. It results in:

$$V_{561} = 0.543\,\text{fl} \left(\frac{485\,\text{nm}}{561\,\text{nm}}\right)^3 = 0.840\,\text{fl}. \tag{5.14}$$

The size of the 561 nm confocal volume was additionally confirmed by an FCS measurement of Rhodamine 101 (Rh101, also known as Rhodamine 640 perchlorate) solution (Exciton, Luxottica Group S.p.A., Lockbourne, Ohio, USA, #06400). The fit of a single diffusion time with triplet at a given confocal volume of 0.840 fl results in a diffusion constant $D_{Rh101} = 431 \pm 10\,^{\mu m^2}/_{s}$. The slower diffusion matching the slightly larger size of Rh101 compared to Rh110 as well as literature values for other Rhodamine dyes of comparable structural size, for example Rhodamine 6G [130, 136, 137].

The molecular brightness can now be calculated as follows:

$$B = \frac{b}{N_A \cdot V} \tag{5.15}$$

with the Avogadro constant N_A, resulting in the molecular brightnesses of $B_D = 814\,^{Hz}/_{(molecule \cdot \mu W)}$ and $B_A = 264\,^{Hz}/_{(molecule \cdot \mu W)}$. In order to validate these values, we calculated the expected ratio between B_A and B_D depending on the quantum yield of the fluorescent proteins and the setup detection efficiencies (compare next Section). The experimental ratio of $\frac{B_A}{B_D} = 0.324$ is confirmed by the calculated value of 0.34.

The performed FCS studies on CD95, CD86 and CTLA4 membrane receptors (compare

Chapter 8.2) showed that while focusing the confocal volume strictly on the bottom cell membrane, there is still a fast diffusion component to be fitted. This diffusion was attributed to the presence of cytoplasmic mEGFP and mCherry, since their presence was confirmed by 3D confocal images of live cells (compare Figure 7.1). The analysis of 73 cells in the FCS study resulted in a mean cytoplasmic fraction of $p_{\mathrm{cp}} = 38 \pm 6\,\%$ and $p_{\mathrm{mem}} = 62 \pm 6\,\%$ of the signal originating from the membrane. In these studies, it was taken care to not bleach the fraction of proteins in the membrane before and during the FCS measurements as this would falsify the result because slow diffusing membrane proteins bleach faster than fluorophores in the cytoplasmic fraction with shorter diffusion times. This was done by choosing the measurement and power settings carefully to achieve the highest countrate while keeping the bleaching below 10 % over the course of the measurement.

Finally, the number of mEGFP and mCherry molecules per cell surface area A_{cell} – the average label surface concentration - was determined by:

$$\rho_D = \frac{F_{\mathrm{cell,D|D}} \cdot p_{\mathrm{mem}}}{P_{485} \cdot A_{\mathrm{cell}} \cdot B_{\mathrm{D}}}, \tag{5.16}$$

$$\rho_A = \frac{F_{\mathrm{cell,A|A}} \cdot p_{\mathrm{mem}}}{P_{561} \cdot A_{\mathrm{cell}} \cdot B_{\mathrm{A}}}, \tag{5.17}$$

where $F_{\mathrm{cell,D|D}}$ and $F_{\mathrm{cell,A|A}}$ are the fluorescence rates for the donor D and acceptor A in Hertz upon excitation with the respective D and A lasers, and P_{485} and P_{561} are the excitation powers for the donor and acceptor lasers, respectively. The results are then used to determine absolute concentrations of all monomeric/oligomeric species during FRET induced donor decay fitting (Figure 9.5 D).

Brightness Relation of mEGFP and mCherry

To confirm the experimentally determined values for the brightness of one fluorescent molecule of mEGFP and mCherry, we derived the theoretical ratio of the brightnesses using the relative extinction coefficients ϵ, quantum yields Φ and detection efficiencies g:

$$\frac{B_{\mathrm{mCh}}}{B_{\mathrm{EGFP}}} = \frac{g_{561}}{g_{485}} \frac{\epsilon_{\mathrm{mCh}}}{\epsilon_{\mathrm{EGFP}}} \frac{\Phi_{\mathrm{mCh}}}{\Phi_{\mathrm{EGFP}}}, \tag{5.18}$$

where the detection efficiency of the measurement setup was calculated using the in-house developed program *detection efficiencies* and other values obtained from litera-

ture [114, 138]. Yielding

$$\frac{B_{\mathrm{mCh}}}{B_{\mathrm{EGFP}}} = \frac{1}{1.38}\frac{72000\,\mathrm{M^{-1}cm^{-1}}}{55900\,\mathrm{M^{-1}cm^{-1}}}\frac{0.22}{0.60} = 0.34. \tag{5.19}$$

Accessible Volume Simulations

To obtain the oligomer fraction from x_{FRET}, we calculate the maximal FRET signal for pure DA dimers, $x_{\mathrm{FRET,AV}}$, from accessible volume (AV) simulations. This value depends on the distance between the fluorophore anchors as well their probability density which depends on the linker lengths.
AV simulations were performed using the in-house developed program Olga [139]. To model a dimer in a membrane a plane was generated using a Python script with two points 40 Å above the membrane surface and separated by 22 Å, consistent with PDB (Protein Data Bank) structures 2NA7 for CD95 [64, 140] . For CTLA4 no structural model of the transmembrane domain (amino acids 162-182) is available, hence all known information is captured using the CD95 model representing a dual helix across the membrane. The length of the linker was determined by adding up the flexible amino acids from the membrane protein structure of CD95, CD95(ΔDD) and CTLA4), the additional flexible linker and the flexible part of mEGFP. The contributions to the total linker length for each construct are found in Table 4.2. All constructs have similar (total) linker lengths between 46 to 53 amino acids, allowing the use of 51 amino acids to simulate all constructs. This value represents the average and can be used globally as the maximum linker lengths deviation of ±5 amino acids (approx. 1.8 nm) corresponds to a maximal error in $x_{\mathrm{FRET,\,AV}}$ result of $39.8 \pm 1\,\%$. This is lower than the uncertainty in linker flexibility and thus acceptable.
Figure 9.5 C illustrates the AV cloud and the donor-acceptor distance distribution.

FRET Dependency on D:A Ratio

In order to calculate the maximal possible FRET fraction $x_{\mathrm{FRET,max}}$ for a purely dimeric sample, the fraction of FRET capable donors must be determined. The formation of the three possible dimer configurations (DD, DA, AA) follows a binomial probability with number of trials $n = 2$, depending on the initial probability p_{D} of a donor. This dimer probability depends on the expression ratio A:D of acceptor to donor within the sample, e.g. if the ratio of donors to acceptors is 1:4, $p_{\mathrm{D}} = 20\,\%$ and $p_{\mathrm{A}} = 80\,\%$ (exemplary illustrated in Figure 9.5 C (2.)). The probability for a certain dimer configuration $P_{\mathrm{config}}(d|n,p)$ with number of trials n and success probability p can be

calculated with:

$$P_{\text{config}}(d|n,p) = \sum_{i=0}^{d} \binom{2}{i} {p_{\text{D}}}^{i} \left(1-p_{\text{D}}\right)^{n-i}, \tag{5.20}$$

where d is the number of donors in the dimer.

For the FRET sensitized donor analysis, the fraction of donors able to FRET $x_{\text{D,FRET}}$ (in DA dimers) compared to donors that are not able to FRET (in DD dimers) is relevant. This fraction equals the initial probability p_{A} of acceptors in the sample as it resembles the chance of one donor to find an acceptor as interaction partner. Analogous, the fraction of donors in DD dimers that cannot FRET $x_{\text{D,noFRET}}$ is equal to p_{D}:

$$x_{\text{D,FRET}} = p_{\text{A}}, \tag{5.21}$$

$$x_{\text{D,noFRET}} = p_{\text{D}}. \tag{5.22}$$

Figure 9.5 C (2.) illustrates one exemplary A:D distribution in a dimeric sample as well as the resulting $x_{\text{D,FRET}}$.

Combined with the maximal possible FRET fraction $x_{\text{FRET,AV}}$ resulting from AV simulation (compare previous section), the overall maximum FRET fraction results from

$$x_{\text{FRET,max}} = x_{\text{FRET,AV}} \cdot x_{\text{D,FRET}}. \tag{5.23}$$

Proximity FRET Corrections

The model used for proximity FRET $x_{\text{FRET,prox}}$ correction was

$$x_{\text{FRET,prox}}(c_{\text{prox}}|c_{\text{A}}) = 1 - e^{c_{\text{A}}/c_{\text{prox}}}, \tag{5.24}$$

where c_{A} is the concentration of acceptors and c_{prox} is the characteristic acceptor concentration at which 63 % proximity FRET occurs. Note that this model has only a single fitting parameter and can hence be robustly determined. The corrected $x_{\text{FRET,corr}}$ can be straightforwardly determined using

$$x_{\text{FRET,corr}} = x_{\text{FRET,raw}} - x_{\text{FRET,prox}}. \tag{5.25}$$

Note, that the model for proximity FRET was previously applied to efficiency-based FRET analysis by King et al. [141]. As the FRET efficiency E and the FRET fraction

x_{FRET} are directly proportional following

$$E = x_{\mathrm{FRET}} \frac{k_{\mathrm{FRET}}}{k_{\mathrm{FRET}} + k_0}, \tag{5.26}$$

it is clear that the proximity contribution to x_{FRET} follows the same relation as for E. Here, k_{FRET} describes the FRET rate and k_0 is the sum of decay rates in absence of FRET.

CTLA4 K_{D} Homodimerization Model

We derive the fraction of homodimers from first principle for the reaction

$$[A_2] \rightleftharpoons [A] + [A] \tag{5.27}$$

using the mass action law

$$K_{\mathrm{D}} = \frac{[A]^2}{[A_2]} \tag{5.28}$$

and assuming a total amount of proteins

$$c_0 = [A] + 2[A_2]. \tag{5.29}$$

We define the fraction of proteins that are part of a dimer as

$$x_{\mathrm{dimer}}(K_{\mathrm{D}}, c_0) = \frac{2[A_2]}{c_0} \tag{5.30}$$

and solve for $[A]$ and $[A_2]$ for given c_0, K_{D} to obtain

$$x_{\mathrm{dimer}}(K_{\mathrm{D}}, c_0) = \frac{K_{\mathrm{D}}}{4c_0} \left(1 + \frac{4c_0}{K_{\mathrm{D}}} \pm \sqrt{1 + \frac{8c_0}{K_{\mathrm{D}}}} \right), \tag{5.31}$$

which behaves similar to the commonly known Langmuir equation.

III

Results

6 Advancing Mutiparametric Fluorescence Microscopy and Spectroscopy Techniques

In order to elucidate the spatio-temporal activity states of CD95, we have developed a robust methodology based on state-of-the-art fluorescence microscopy and spectroscopy techniques exhibiting complementary resolution capacity. In particular, we advance and synergize the readouts of Stimulated Emission Depletion (STED), polarization and time-resolved Förster Resonance Energy Transfer (FRET), polarization-sensitive confocal Photobleaching Step Analysis (cPBSA), and Fluorescence Correlation Spectroscopy (FCS). In addition, we used time-lapse widefield microscopy to examine the apoptosis dynamics of different CD95 expression levels and ligand concentrations. We apply these methods to a small library of CD95 variants with different signal initiation competency as well as monomer and dimer controls (compare Chapter 4.1). In all cases rigorous image analysis and benchmarking against control samples allowed us to identify concentration and photophysical effects and to quantify CD95 oligomeric states. Figure 6.1 shows an overview of the strategy we followed to map the regulation of CD95 before and during the whole signaling process up to the point of cell death with single molecule to higher oligomer precision using a combination of multiparametric fluorescence microscopy techniques.

To accomplish the central goal of this work - the characterization of CD95 activation states with up to single molecule precision - significant technical and analytical advancements were required to draw reliable biological conclusions from the measurement results. On the one hand, this included the advancement of different microscopy and spectroscopy techniques in terms of sample preparation and recording strategies. On the other hand, new evaluation routines were developed. For instance, in order to quantify the CD95 oligomerization fraction into absolute concentrations, the information derived from FRET, FCS, and AV simulations had to be combined. In the following, the technical advancements and specific details of each technique will be presented together with the respective conclusions on the CD95 activation state.

a | Method overview

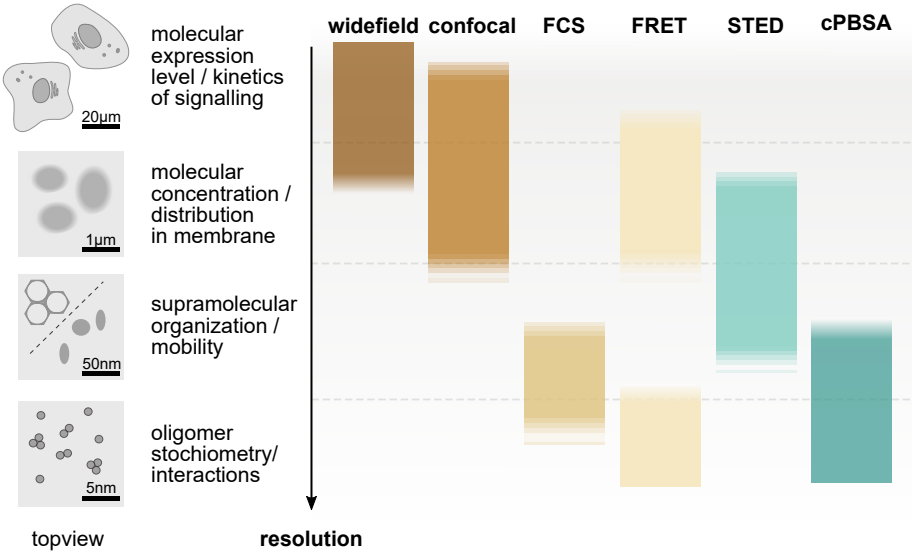

b | Method properties

	fixed/ live cells	specific time / continuous	measured variable	concentration sensitivity
widefield	live	continuous	2D image	no limit
confocal	live	continuous	3D image	no limit
FCS	live	continuous	diffusion times	≤ 2000 oligomers/µm²
FRET	live	continuous	donor fl. lifetime	≤ 2000 oligomers/µm²
STED	fixed	specific time	super-resolution image	≤ 200 oligomers/µm²
cPBSA	fixed	specific time	bleaching steps	≤ 10 oligomers/µm²

Figure 6.1: Overview of methods used in this study to gain a comprehensive understanding of the CD95 signal initiation and its stoichiometry down to the molecular level: a | Method overview: Widefield and confocal time-lapse microscopy are tools to monitor apoptosis dynamics, cell-to-cell variations and membrane homogeneity. STED and FCS provide complementary information about CD95 on the scale of molecular assemblies while cPBSA and the advanced FRET induced donor decay $\epsilon(t)$ analysis elucidate the receptor stoichiometry on a few-molecule level. **b |** Each method features different measurement parameters and properties. The combination of steady-state techniques with fixed cells (STED, PBSA) and live cell methods covering different concentration sensitivities elucidate the full spatio-temporal organization of CD95.

In order to fully exploit the potential of all methods, we have collected a small library of mEGFP and mCherry labeled CD95 variants with different signaling competency to recognize and transduce the signal initiated by CD95L. In addition, we have benchmarked the obtained data against identical recordings of receptors known to occur as monomers and dimers, CD86 and CTLA4, respectively. The plasmids of genetically modified receptors comprise the full-length protein CD95 as well as a death domain truncated version CD95(ΔDD) with either mEGFP or mCherry fused to the intracellular C-terminus. CD95(ΔDD) is not capable to transduce the intracellular signal and is hence ideally suited for long-time observations after ligand incubation as well as to probe oligomerization mediated by the extracellular and transmembrane domain of CD95. Another variant of CD95 exhibiting a mutation at amino acid 102 (premature protein) CD95(R102S) is suitable as control that cannot bind the ligand. A PLAD (pre-ligand assembly domain) depleted variant CD95(ΔPLAD) may be used to detect pre-oligomerization based on transmembrane and intracellular interactions (Figure 4.1). As monomer control, we chose the full-length sequence of CD86 [111] with genetically fused mEGFP. From this construct also a pseudo-dimer control was generated fusing a second mEGFP to the first mEGFP, in order to verify the CTLA4 dimerization state. In case of the CTLA4 dimer control, the last 23 amino acids of the sequence were removed to reduce internalization of the receptor, as previously reported [110]. Besides these monocistronic constructs, bicistronic plasmids were used combining mCherry and mEGFP labeled proteins via a T2A cleavable peptide to ensure homogeneous co-expression of donor and acceptor fluorophores during FRET measurements (Figure 4.1). Due to the lower maturation efficiency of mCherry compared to mEGFP [142, 143], mCherry was placed first in the design of bicistronic plasmids. Correct integration into the plasma membrane was verified using confocal microscopy (see Chapter 7.1). Figure 6.2 schematically illustrates the main samples of this study together with the universal color code used in the results figures.

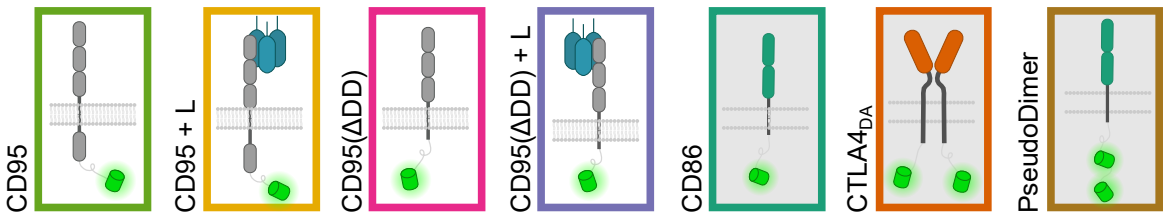

Figure 6.2: Sample color legend and schematic illustration of membrane receptors. The cartoon illustrates the membrane receptor samples mainly used in this study: CD95 variants (with/without death domain and CD95 Ligand), the monomer and dimer controls CD86 and CTLA4, all coupled to mEGFP as well as the PseudoDimer CD86-mEGFP-mEGFP. The color code of the boxes is valid for all figures of this Results Part III (except for Chapter 7.3).

7 Characterization of CD95-expressing Cells and their Apoptosis Dynamics

7.1 CD95 Localization in Living Cells

The goal of this study is to resolve the spatio-temporal activity states of CD95 on the plasma membrane of cells. In order to examine CD95, we mostly use florescence microscopy techniques requiring a fluorescent dye in order to "see" the receptor in the cell. We use the common method of transfecting cells with a recombinant receptor consisting of the natural or genetically modified receptor of interest fused to a fluorescent protein (FP). The transfection enables a transient expression of the gene of interest in a target cell line. While transfections with fluorescent proteins are an important tool in order to examine cells in a natural, live state without harmful staining procedures, it also brings challenges we need to overcome.

Firstly, the target proteins have to be expressed and inserted correctly into the membrane. One challenge here is that the target proteins can not only be found at their final destination, but also along internal production and trafficking pathways including the endoplasmic reticulum (ER), the Golgi apparatus and the cytoskeleton. We try to reduce the intracellular signal by measuring 48 to 72 hours after the transfection in order to provide enough time for the relocation of the membrane proteins to the plasma membrane. Furthermore we account for the remaining intracellular signal, where needed (compare Chapters 8.2 and 9.2.1). Figure 7.1d shows the intracellular signal of CD95 in a $CD95^{KO}$ HeLa cell in a mid-cell cross section. A quantitative comparison of the intensities from the intracellular versus the membrane region of this image region revealed, that the membrane signal is approximately 4-fold higher compared to the cytoplasm.

Another challenge of membrane proteins and their quantification, is the shape of the membrane itself. Although the plasma membrane is a 2D surface, it is a dynamic

structure that can fluctuate and bend. To quantify the receptor distribution reliably, we imaged the lower plasma membrane instead of the top membrane as it lies mostly flat in one layer unlike the ruffled/extended structures at the edge and on top of the cell (compare Figure 7.1b/c). Additionally, on the cell edges, the top and bottom membrane of a flat, adherent cell are close above each other and may both be detected within the same confocal volume (and hence be not distinguishable). Thus, we focus the confocal volume during our measurements in the middle of the bottom membrane (Figure 7.1a), where the displacement in z is small and hence can be neglected [144]. To verify if CD95L can induce CD95 signaling via the bottom cell membrane, we additionally confirmed that the ligand in solution diffuses underneath the attached cell using confocal microscopy (compare Supplementary Figure C.1).

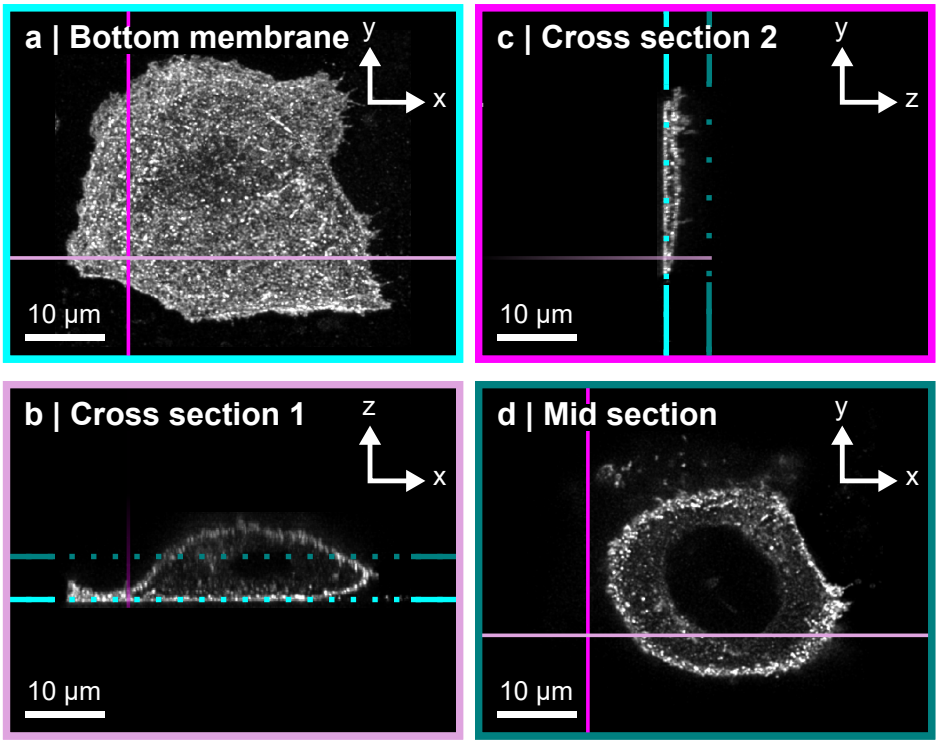

Figure 7.1: Cross sections of a 3D confocal image showing a CD95 transfected fixed cell. a | Fixed HeLa $CD95^{KO}$ cell transfected with CD95-mEGFP, (xy) cross section of the bottom membrane of a 3D stack. **b, c |** (xz) and (yz) cross section as indicated by colored planes in a and d. Both show that top and bottom membrane can be in close proximity when apart from nucleus. (z) Positions of ross sections corresponding to magenta colored, solid lines in a and d. **d |** Mid-segment of same 3D image (xy), intensity gradient same as in a. Signal is brightest in the membrane, but also cytoplasmic intensity is visible. Intensity in the membrane is 4-fold higher than in the cytoplasm. No fluorescent signal is present in the nucleus. **a, d |** Bottom and mid sections corresponding to cyan colored, dashed lines in b and c.

7.2 Quantification of the Surface Receptor Density in Stable Cell Lines

To characterize the stable cell lines relevant for all further measurements, we assessed the quantitative CD95 expression level of the stable cell lines HeLa WT, HeLa CD95^{KO} and HeLa CD95-mEGFP using a kit for quantification of cell surface antigens by flow cytometry based on calibration beads (compare Methods Chapter 4.1). The measurement was repeated two times independently.

The QIFIKIT provides several calibration bead populations with a well-defined number of primary mouse antibodies on the bead surface. By staining and measuring the beads using the identical protocol applied to cell measurements, it enables to translate the arbitrary units of mean fluorescent intensity (MFI) into a quantitative surface antigen number using a calibration curve.
To determine the numbers accurately, it was accounted for unspecific staining and background signals using an irrelevant primary antibody of the same isotype as the unconjugated primary CD95 antibody as well as blank beads, which were stained and measured with the same secondary antibody and measurement procedure as the positive samples. This apparent background antibody binding capacity was subsequently deducted from the calibration curve.

Table 7.1 shows the result of the two measurements of at least 50 000 cells per measurement as well as the weighted mean receptor number $\langle N_{CD95} \rangle$ per cell and standard deviation (SD).

Cell lines	Run 1 N_{CD95}	Run 2 N_{CD95}	Weighted mean $\langle N_{CD95} \rangle \pm SD$
HeLa WT	25 365	21 992	23 079 $\pm$ 1 474
HeLa CD95-mEGFP	533 572	399 220	446 320 $\pm$ 61 176
HeLa CD95^{KO}	0	0	0 $\pm$ 0

Table 7.1: Expression levels of stable cell lines measured by quantitative flow cytometry. The expression of the stable HeLa CD95-mEGFP is approximately 20-fold higher compared to wild type HeLas. The knock out of CD95 successfully prevents the expression of CD95.

The quantification showed that the overexpressing cell line HeLa CD95-mEGFP has a 20-fold higher average number of CD95 receptors compared to the endogenous expression of HeLa WT cells, while the knockout in the HeLa CD95^{KO} cell line successfully eliminated the endogenous CD95 expression completely. As no information is pro-

vided by the producer, Supplementary Chapter C.1 includes a short discussion on the precision of this method, concluding that the QIFIKIT can only assess the order of magnitude of receptor numbers on a cell population but not precise quantities. As our cell lines differ in several orders of magnitude, we believe the result to be sufficiently accurate.

7.3 CD95 Apoptosis Dynamics depends on Ligand and Receptor Concentrations

This chapter aims to examine the CD95 signal initiation and transduction on the molecular level and to quantify effects of ligand and receptor concentrations on the signaling kinetics and outcome. To this end, we recorded HeLa cell lines which exhibited CD95 receptor expression levels from 0 to $4.5 \cdot 10^5$ receptors per cell as quantified with flow cytometry (compare Chapter 7.2). The cells were exposed to various ligand concentrations while kinetics of the cellular fate decision were monitored. Several hours after CD95L incubation, the cells showed typical apoptosis characteristics such as initial blebbing followed by cell shrinkage (see Figure 7.3a). In all cases, the kinetics of apoptosis signaling followed a sigmoidal progression with an initial onset one hour after ligand addition, indicating the minimal time the signaling requires from its initiation until the eventual cell fate decision. The predominant time interval of apoptosis events occurred from 1 to 5 hours after ligand addition, and the slowest signaling outcome was detected after 5 to 7 hours depending on the experimental situation. Thereafter, only few additional apoptosis events were recorded which are likely to arise from naturally occurring apoptosis. We observe a ligand dependent efficiency of apoptosis induction ranging from 3 % to 99 % apoptotic cells, when the ligand concentration was increased from 2 to 200 $^{\mathrm{ng}}/_{\mathrm{ml}}$. Similarly, initiation of apoptosis signaling scaled with the number of receptors expressed on the cell surface. A complete knockout of CD95 (0 receptors, compare Chapter 7.2) led to no initiation of signaling upon ligand addition, $2.5 \cdot 10^4$ CD95 receptor molecules to 60-75 % of apoptotic cells, whereas $4.5 \cdot 10^5$ CD95 led to 99 % of dead cells (Figure 7.3b/c). A curve fitting using the Hill function yielded the half-time after which 50 % of all apoptotic cells had died. Half-times ranging from 1.5 to 8 hours became faster with higher CD95 Ligand or receptor concentrations (Figure 7.3d).

Cells expressing CD95(ΔDD) and CD95(R102S) served as a negative control and showed cell death of less than 15 % within 10 hours caused by stress due to transfection or (fluorescence) imaging (Figure 7.2). For CD95(ΔPLAD) apoptosis dynamics slightly exceeding the negative controls and with up to 25 % apoptotic cells were observed.

All apoptosis kinetics exhibited a strong correlation with ligand and receptor concentration, demonstrating that signal initiation is strongly dependent on the absolute number of activated receptors. Any quantitative study of signal initiation should hence pay particular attention to the number of ligands and receptors in their system. The analysis of apoptosis kinetics not only demonstrated a correlation with increasing ligand and receptor concentration, but also enabled to define characteristic time points of

the signaling process for subsequent measurements with advanced FRET, cPBSA, FCS or STED: (i) time points before signal initiation, (ii) directly after ligand addition, (iii) the time interval when most cells underwent apoptosis, and (iv) the time point, when all signaling events resulted in apoptosis.

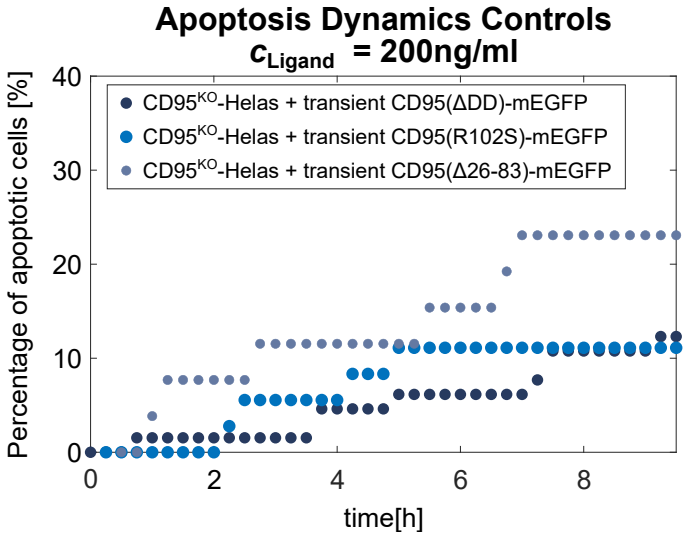

Figure 7.2: Apoptosis dynamics of CD95 controls. Apoptosis Dynamics of transiently transfected Hela $CD95^{KO}$ cells with the CD95 variants CD95(ΔDD), CD95(R102S) and CD95(Δ26-86). While the first two variants show apoptosis caused by natural apoptosis or transfection stress, the PLAD-depleted variant CD95(Δ26-86) shows an increased apoptosis rate up to 25 % of dead cells.

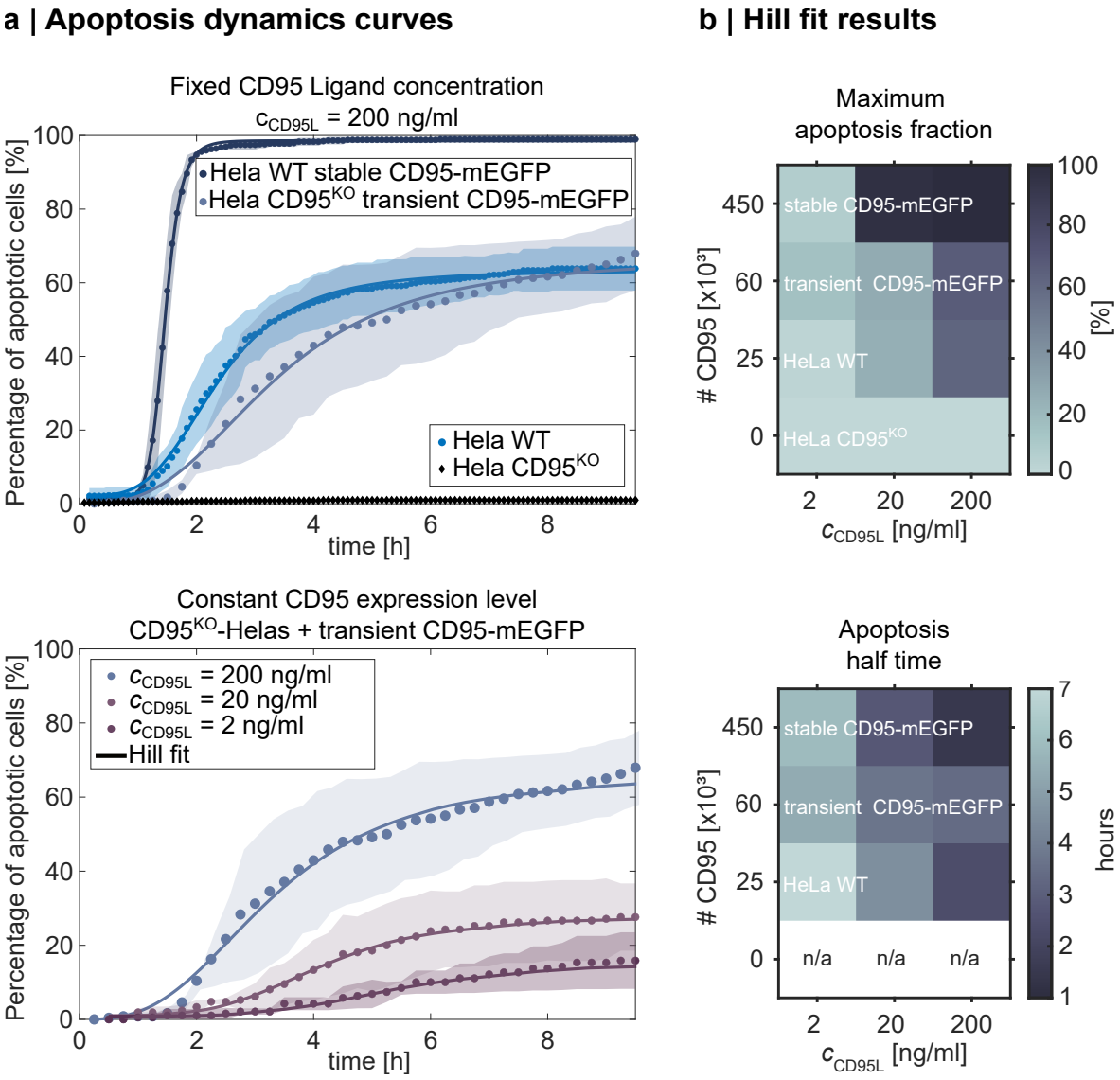

Figure 7.3: Characterization of molecular concentration dependent apoptosis dynamics. a | Percentage of apoptotic cells over time after CD95 Ligand induction. A Hill equation fit (solid line) determines characteristic apoptosis dynamics parameters shown in b). Top: Comparison of cell lines with different CD95 expression level exposed to 200 $^{ng}/_{ml}$ of ligand. Bottom: Comparison of Hela CD95^{KO} transient CD95-mEGFP cell line exposed to various ligand concentrations of $c_{CD95L} = 2, 20, 200\,^{ng}/_{ml}$. Data points show the weighted mean, shaded area the standard deviation of three independent measurements. $N > 180$ cells per sample. **b |** Hill fit parameters: maximum apoptosis fraction (top) and apoptosis half time (bottom) of different cell lines and ligand concentrations c_{CD95L}. *n/a* indicates data where no Hill fit was possible due to a low percentage of apoptotic cells. For further details see Methods Chapter 5.1.2.

8 Organization and Mobility of CD95 on the Plasma Membrane

8.1 STED reveals Resolution Limited Receptor Spots

In order to test the CD95 membrane distribution for local accumulations or supramolecular cluster formation, we scanned the membrane surface with 40 nm FWHM resolution using Stimulated Emission Depletion Microscopy and established a quantitative spot analysis.

8.1.1 STED Quantitative Spot Analysis

To record the data at maximum achievable resolution, we fixed transfected cells 2 hours after ligand addition and used a GFP-nanobody Atto647N as CD95-mEGFP label (compare Methods Chapter 4.3.2). The nanobody-labeling of genetic encoded FPs enables a quantitative analysis because the invariable label-target stoichiometry of 1:1 means that there is no risk of molecules being "overcounted". STED images were gated and deconvolved using Huygens' Classic Maximum Likelihood Estimation (CMLE) based algorithm. Supplementary Figure C.2 shows a comparison between the confocal resolution and a STED image of the same Region of Interest (ROI) including the time-gated raw data and the deconvolved result. After the deconvolution, an intensity threshold-based object detection (Huygens) with watershed segmentation was applied for high-fidelity segmentation of CD95 membrane spots and subsequent analysis of spot characteristics (illustrated in Figure 8.1). This segmentation considers all pixels above a certain threshold T to be part of an object and detects local minima ("watersheds") to separate close objects from each other which else would merge in one object. Further, a seeding (minimum peak height), garbage level (minimum pixel number) and Gaussian (smoothing) filter can be applied to discard dim/tiny objects and noise-related local minima, respectively. We select a low object threshold of avoid a selection bias of

bright objects and to consider all photons for the object brightness (for further details compare Methods Chapter5.3.2).

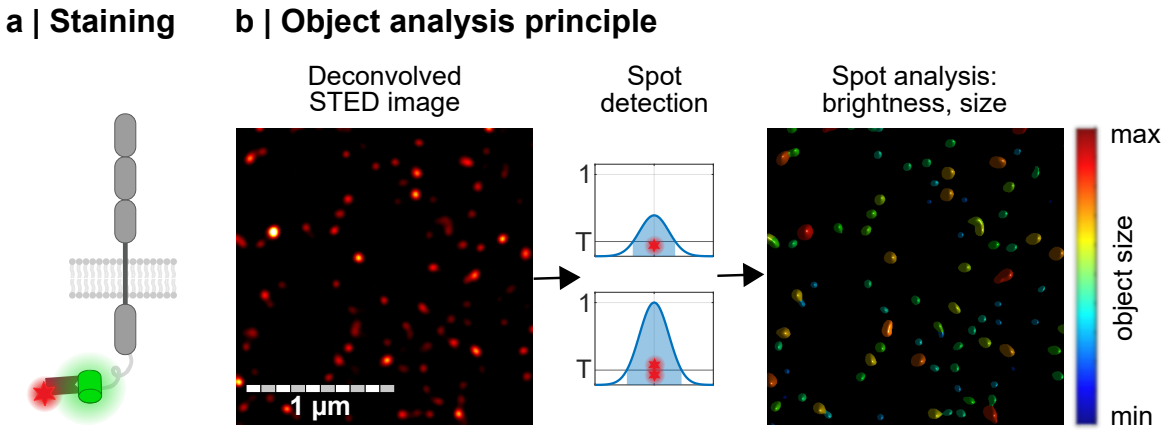

Figure 8.1: STED object analysis principle. **a |** Schematic representation of CD95-mEGFP with GFP-nanobody Atto647N labeling. **b |** Exemplary deconvolved STED image (left) of Hela $CD95^{KO}$ transiently transfected with CD95-mEGFP and threshold-based spot detection and filtering (middle) followed by spot analysis (right) using Huygens Professional (Scientific Volume Imaging B.V.).

Figure 8.2a shows the enlarged deconvolved STED image of CD95 in the outer cell membrane forming small, individual resolution limited spots of receptors. The corresponding detected objects are shown in Figure 8.2b. The comparison of both images shows, that all spots are detected as objects and close objects are successfully separated by the watershed algorithm.

8.1.2 STED Pair Correlation shows Isolated, Randomly Distributed Spots

We first calculated the pair correlation function of the spot centers in order to test for higher order pattern within the receptor spot distribution (Figure 8.2c). Our data confirmed a random distribution of spots for all CD95 receptors in absence and presence of the ligand up to the point where the PSF (point spread function) size caused a decrease in correlation at radii below 130 nm. The same holds for the monomer and dimer controls CD86, CTLA4 and the PseudoDimer CD86-mEGFP-mEGFP. The pair correlation analysis was applied to simulated images of randomly distributed spots with a PSF, which additionally verifies that the decrease in correlation for $r < 130\,\text{nm}$ arises from finite PSF size effects and not a particular distribution (Figure 8.2c, left). Thus, receptors are homogeneously distributed over the membrane surface. From this data we also determined an average concentration of $20\,{}^{\text{spots}}/_{\mu\text{m}^2}$, corresponding to an

average distance of 224 nm between spots and an intermediate expression level of about $4 \cdot 10^4$ to $8 \cdot 10^4$ receptors per cell if few receptors are assumed to be present in one spot.

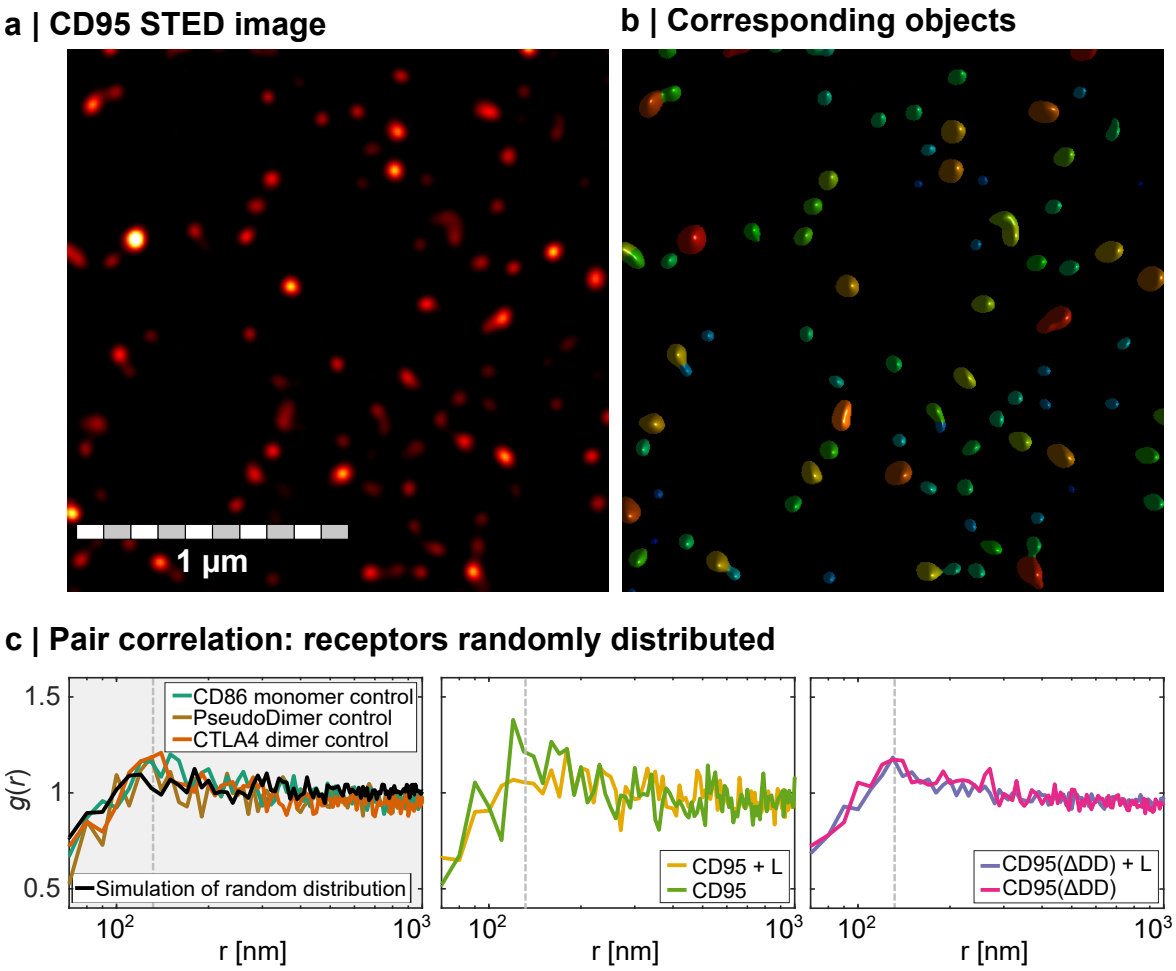

Figure 8.2: STED imaging uncovers randomly distributed CD95 membrane spots. **a |** $2 \times 2\,\mu m^2$ ROI of a deconvolved STED image of CD95-mEGFP in HeLa CD95^{KO} cells stained with GFP-nanobody Atto647N. CD95 forms small, mostly resolution-limited spots in the cell membrane. Supplementary Figure C.2 shows the full ROI and the corresponding confocal image and raw data. **b |** The image from a) analyzed with the Huygens Object Analyzer. Each spot is detected as individual object, a color map is used to distinguish the objects from each other. **c |** Averaged pair correlation histograms of the detected CD95 objects with/without ligand for both CD95 variants and of monomer and dimer controls. For distances of $r > 130\,nm$ (indicated by dashed line), $g(r) \approx 1$ meaning a random distribution for all samples. For $r < 130\,nm$, the comparison with simulated images containing randomly distributed PSF spots, shows that PSF extent caused a decrease in correlation, hence this behavior is not attributed to a higher-order distribution pattern.

8.1.3 STED Spot Analysis Reveals Systematic Changes in Spot Brightness

We analyzed the size of CD95 spots before and after ligand incubation, which are not larger than spots of the CD86 monomer control and/or CTLA4 and PseudoDimer controls (Figure 8.3a). Thus there is no indication for the presence of higher oligomers/networks. Same holds for spots of CD95(ΔDD) with and without ligand. To further quantify spot characteristics, we evaluated the circularity as well as intensities and compared the spot brightness [$^{\text{photons}}/_{\text{pixel}}$] of mostly resolution-limited spots before and after ligand addition (Figure 8.3b). The large spread in spot brightness of CD95 samples may *a priori* be associated with the existence of CD95 monomers and higher oligomers or networks. However, similar distributions also appeared for monomer and dimer controls. In their case, bright and non-resolution limited spots may only arise from local concentration fluctuations, variations in labeling efficiency or photophysical effects. Consequently, in case of CD95 high spot brightness may also arise from these secondary effects instead of true oligomerization. This observation highlights the importance to design high-fidelity monomer or dimer controls to create molecular benchmarks. In addition, our polarization sensitized readout revealed a broad distribution of fluorescence anisotropy values with an average value of 0.4, indicating a preferred and fixed orientation of fluorescent molecular dipoles parallel to the cell membrane. Figure 8.4 illustrates membrane spots with different signal intensities in the P (parallel) and S (perpendicular) channel as well as the anisotropy distribution. Based on this observation, care was taken to sum all intensities of the different polarization channels for spot analysis.

Overall, for rigorous understanding of brightness values we find that a simple intensity-based study may be deficient and that polarization-based analyses and benchmarking against controls are important. Comparing the median values of samples revealed significant differences (Figure 8.3b), where the monomer sample exhibited a median brightness of 1.91 photons per pixel, the dimer samples have a median brightness of 2.04 (CTLA4) and 2.08 (CD86-mEGFP-mEGFP) photons per pixel. Note, CTLA4_{DA} was used instead of CTLA4_{D0}, as the latter did not show correct expression and localization to the membrane, leading a slightly lower average brightness compared to CD86-mEGFP-mEGFP. The lower brightness for CTLA4_{DA} can be understood by (i) the presence of donor-acceptor pairs in addition to donor-donor pairs where the antibody only recognizes GFP variants. (ii) the protein does not build 100 % dimers, rather the dimer fraction depends on the total receptor concentration (as determined with FRET, see Chapter 9.2.5). CD95 samples in the absence of a ligand exhibited a median close to the monomer value, whereas after ligand addition a systematic shift

toward a median value of 2 was obtained. These considerations suggest that no networks larger than 1 hexagon, comprising 18 receptors, may develop. Only few of the sub-diffraction bright spots may arise from higher oligomerization states instead of crowding and polarization effects.

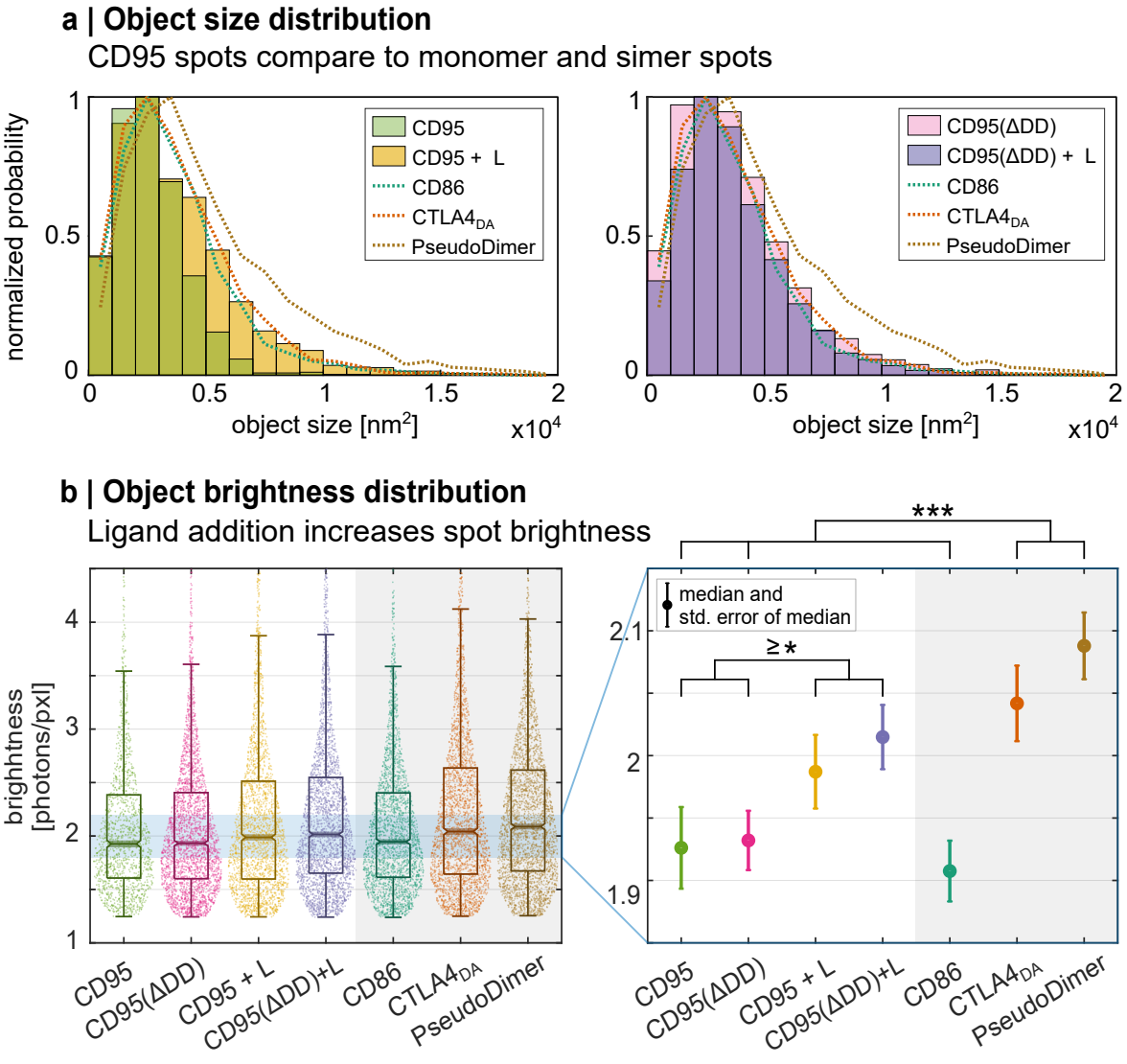

Figure 8.3: STED object analysis reveals systematic changes in object brightness. **a |** Size distribution of detected spots. CD95 and CD95(ΔDD) object sizes in the presence and absence of CD95 Ligand do not exceed the spot sizes adapted by the monomer and dimer controls (dashed lines). **b |** Violin-box plots show the distribution of object brightness up to 4.5 $^{\text{photons}}/_{\text{pxl}}$ for all samples (left). Detail of median brightness (right) reveals a significantly higher value for dimer controls ($> 2\,^{\text{photons}}/_{\text{pxl}}$) compared to CD86 and CD95(ΔDD) in absence of the ligand. Ligand addition shifts the median brightness of CD95 and CD95(ΔDD) towards the dimer controls. Mann-Whitney U-test with ***: $p < 0.001$, *: $p < 0.05$.

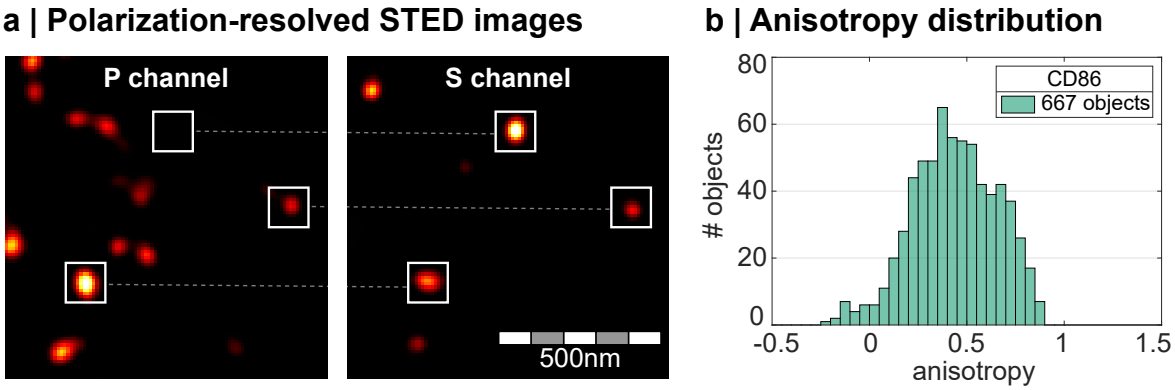

Figure 8.4: Polarization effect of STED samples. a | Deconvolved STED images of Hela CD95^{KO} transfected with CD86-mEGFP and stained with Atto647N α-GFP nanobody in P (parallel) and S (perpendicular) channel. The comparison of both images shows, that the emission of different spots is not equally distributed to both channels. **b |** The histogram shows the measured anisotropy of $n = 667$ spots. The spread in anisotropy confirms a strong polarization effect explaining the large spread in object intensities, even within one image.

8.2 Membrane FCS verifies the Mobility of CD95 Receptors

To verify that CD95 is sufficiently mobile and hence able to form (higher) oligomers, we determined the CD95 diffusion constant D during the whole signaling process using Fluorescence Correlation Spectroscopy (FCS). FCS was performed on live cells for $CD95_{D0}$ and $CD95(\Delta DD)_{D0}$ before and between 100 to 200 minutes after ligand addition as well as for $CD86_{D0}$ and $CTLA4_{DA}$ as single and double transmembrane helix references, respectively (Figure 8.5a) . FCS curves were generated for each cell and fitted with two diffusion terms and no bunching term (see methods, Chapter 5.4). The fast diffusion term was attributed to the presence of cytoplasmic mEGFP, which was confirmed by 3D confocal images of live cells (see Chapter 7.1). FCS is sensitive to this cytoplasmic mEGFP, as the confocal detection volume extends halfway into the cytoplasm.

To confirm that the fast diffusion component was of cytoplasmic origin, we fitted the fast diffusion term globally for all curves from the CD95 sample yielding a value of $t_{\text{cytoplasm}} = 0.60\,\text{ms}$ (corresponding to $D = 20\,\mu\text{m}^2/\text{s}$), reminiscent of soluble protein diffusion, with typical values $24\,\mu\text{m}^2/\text{s}$) for eukaryotic cells [145]. In addition, we measured diffusion of free mEGFP in the cytoplasm and obtained two diffusion times, 0.27 ms and 2.2 ms, with a weighted average time of 0.50 ms (see Supplementary Figure D.1 in SI Figure D.1) close to the cytoplasmic component of CD95. In the following, the fast diffusion term was kept fixed for all samples to improve the sensitivity of the fit for the slow diffusion time (see Figure 8.5a).

The time of the slow diffusion process turned out to be in the range of $30 - 100\,\text{ms}$ and matches literature values for membrane proteins [146, 147]. No difference in the diffusion constant was found between CD95 species within the measurement accuracy (see Figure 8.5c), with absolute D values of $0.21 - 0.24\,\mu\text{m}^2/\text{s}$. Interestingly, $CTLA4_{DA}$ showed similar diffusion times of on average $D = 0.19\,\mu\text{m}^2/\text{s}$, but CD86 was significantly slower with $D = 0.15\,\mu\text{m}^2/\text{s}$ indicating that the number of transmembrane helices is not the only dominant factor of receptor diffusion. This result indicates that CD95 is sufficiently mobile to exhibit dynamic changes in its oligomeric state over time. In addition, comparison of the absolute values suggests that CD95 does not form supramolecular structures as this would result in a highly decreased diffusion constant.

Finally, we tested whether the mobility of CD95 would change after ligand addition. To this end, CD95 and CD95(ΔDD) diffusion was monitored over $100 - 200$ minutes after ligand addition (Figure 8.5d).

Overall, our data confirm sustained CD95 mobility during the whole signaling process. Despite this possibility to accumulate into higher ordered structures, CD95 did not show any systematic change in its diffusion, thus indicating no excessive change in the receptor oligomerization state.

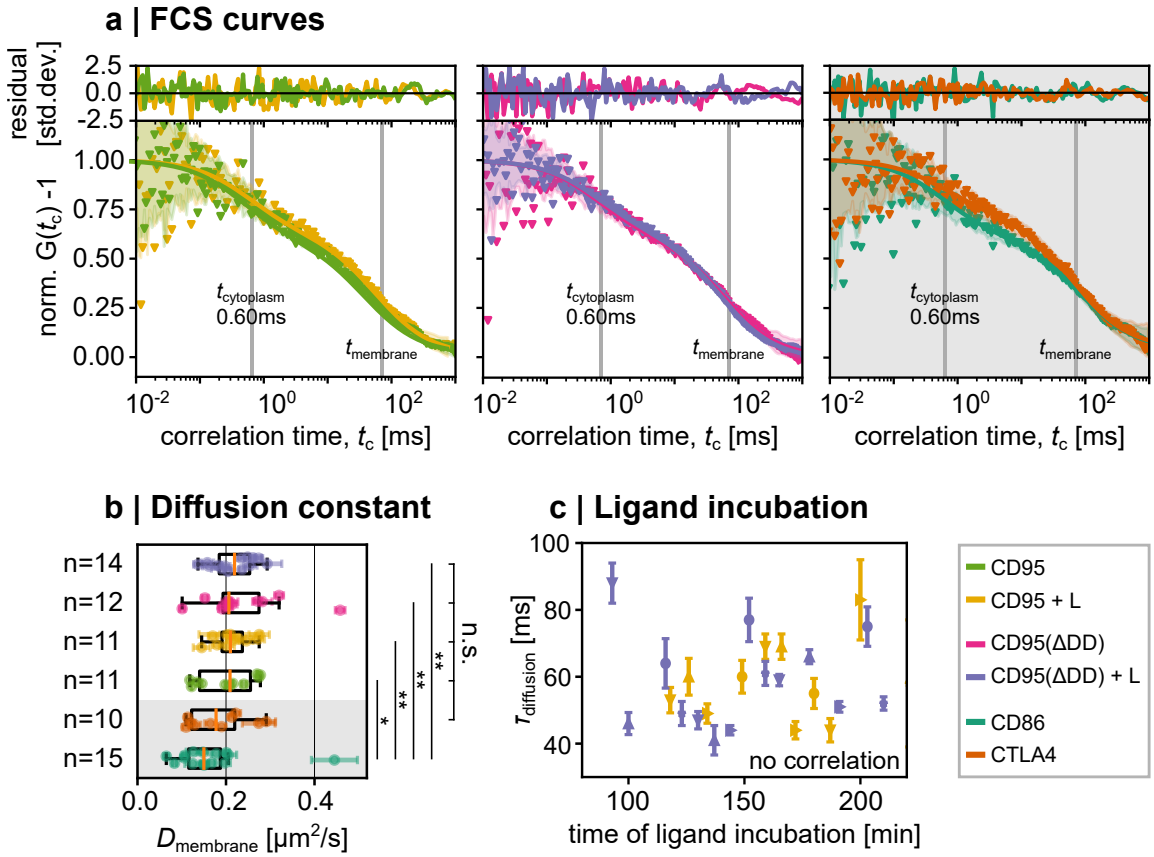

Figure 8.5: Live cell FCS to obtain diffusion times. **a |** Exemplary curves are shown for CD95 before (green) and 159 minutes after ligand addition (yellow) CD95(ΔDD) before (magenta) and 178 minutes after ligand addition (purple). CD86 monomeric control (teal) and CTLA4 dimer control (orange). All curves were fitted with two diffusion terms. The cytoplasmic diffusion term was fitted globally over 11 curves for the CD95 sample and fixed to this value for all other samples (see methods, Chapter 5.4). **b |** Membrane diffusion constants were obtained from the membrane diffusion times. Mann-Whitney U-test was used to test for significance ($^*p < 0.05$, $^{**}p < 0.01$). **c |** Membrane diffusion time plotted against time since ligand addition. No significant change was observed. At least ten different positions from at least 7 different cells were measured per sample (cells were revisited over time) and fitted subsequently.

9 CD95 Stoichiometry

While the previously presented, complementary techniques of fixed quantitative STED spot analysis and live cell FCS both provided evidence that higher oligomerization states do not exist, they do not allow to resolve the CD95 stoichiometry entirely. In order to determine the oligomerization state of CD95 precisely and down to a single-molecule level, we performed confocal PBSA and advanced FRET measurements, as presented in the following.

9.1 cPBSA Reveals the Stoichiometry of CD95 in Fluorescent Spots

Since quantitative STED spot analysis and FCS are insensitive to derive CD95 stoichiometric values in resolution-limited spots, we first used Photobleaching Step Analysis (PBSA). In the past, PBSA was primarily used to measure *in vitro* samples with photostable organic fluorophore labeling, to determine the degree of Qdot labeling [90] or the number of fluorescent labels on DNA origami [89]. Here, we advance PBSA to a confocal setup where the spatial flexibility of the confocal setup enables measurements at any position of the cell with minimal background intensity without bleaching large areas of the cell (Figure 9.1a). Moreover, we present strategies to characterize the signal fluctuations due to dark states and polarization effects that enable a robust interpretation of mEGFP bleaching steps despite its lower stability and higher noise level compared to stable organic fluorophores.

9.1.1 The Confocal Advancement of PBSA

Confocal PBSA (cPBSA) was realized by a fast area scan of the cell bottom membrane to identify receptor locations, followed by placing a diffraction limited spot at the respective position and recording the bleaching trace (time trace of fluorophore bleaching) there (see illustration in Figure 9.1b, compare Methods Chapter 5.5). As

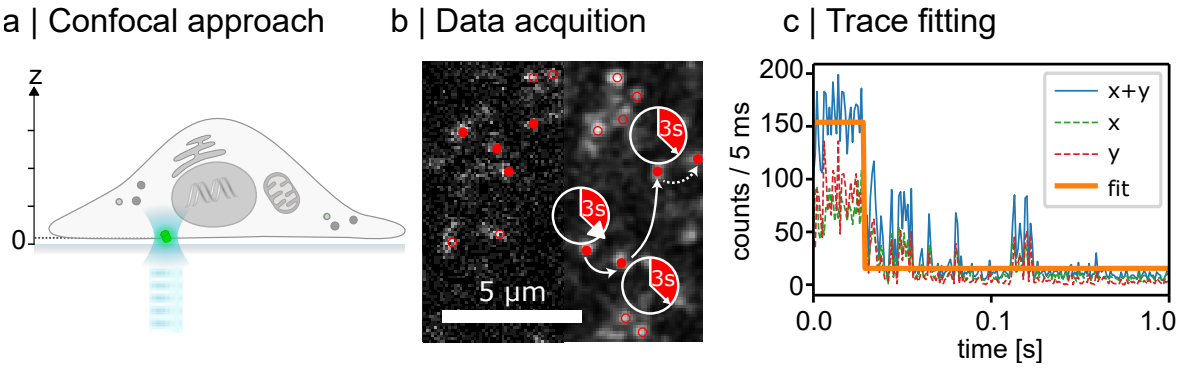

Figure 9.1: Confocal PBSA method overview. **a |** Confocal approach minimizes out-of-focus bleaching and has the potential to enable measuring intracellularly. **b |** cPBSA data acquisition: First a confocal overview image is measured (left) and smoothed using a Gaussian filter with 1 pixel sigma (right). Local maxima higher than 4 photons are selected (red circles) and filtered for having no adjacent neighbors or too large area (red dots). The confocal spot is placed on each red dot for 3 seconds to record a trace. **c |** Exemplary one-step trace fitting. Traces are recorded polarization sensitized. The summed trace $(x + y)$ is fitted using the Kalafut-Visscher (KV) algorithm [132].

the fixation necessary to immobilize the receptors leads to deflation of the cell, we ensured a single membrane layer is in the focus by measuring the area underneath/close to the nucleus. On the cell edges, the top and bottom membrane of a flat, adherent cell are too close to each other (illustrated in Figure 7.1). Additionally, we avoided deflation in the first place as far as possible by forgoing upside-down mounting on a coverslip, as this applies further pressure onto the cells. Thereafter, the trace bleaching steps were identified using the Kalafut-Visscher (KV) algorithm [89, 132] (Figure 9.1c).

A crucial factor on cPBSA analysis is the correct determination of the minimal step size (threshold). Due to the inherent noise level and varying fluorophore brightness a low threshold will count noise as events, overestimating the real number of fluorophores, whereas a high threshold will discard bleaching events, underestimating the real number of fluorophores. Figure 9.2a shows this effect: an increase of the minimal step size leads to a decrease in the detected average number of bleaching steps $\langle N_{\text{steps}} \rangle$ in an exemplary dataset of the monomer control CD86. If the time binning is scaled in the same proportion as the minimal step size, the effect disappears (Figure 9.2b). The minimal step size was chosen carefully to balance the effects of over- and underestimation by manual verification of the fitting. For the example data (Figure 9.2a/b), the optimal fitting was found for a minimal step size 50 cnts, resulting in $\langle N_{\text{steps}} \rangle \approx 1.3$. Further, we found the optimal minimal step size to scale with the absolute laser power and to be afflicted by the inherent noisiness of the mEGFP-in-cell traces. To render this step

size determination robust, we introduced a scaling factor for the laser power and used a temporal binning of 5 ms (Methods Table 5.1), resulting in a minimal step size per 5 ms time bin of 36 $^{\text{cnts}}/_{\mu\text{W}}$.

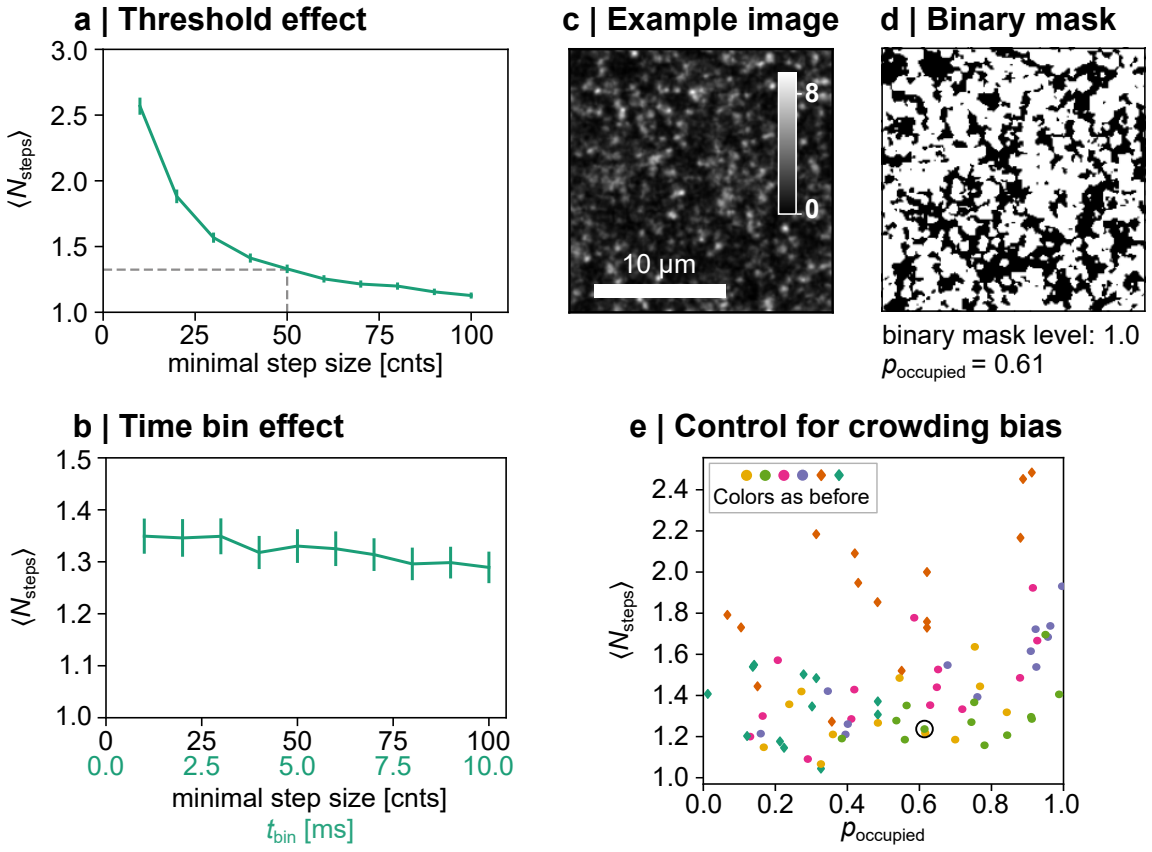

Figure 9.2: Controls for confocal Photo-Bleaching Step Analysis. a | Effect of the threshold (minimal step size) criterion from cPBSA analysis on the average number of fluorophores for a CD86 dataset (recorded at 1.36 µW laser power, time binning: 5 ms). The dashed line indicates the optimized minimal step size, determined by manual verification of the fitting. **b |** The effect disappears when increasing the time bins in the same proportion as the threshold, measured on same dataset. **c |** Exemplary overview image smoothed with a 1 pixel sigma Gaussian filter of the CD95 sample. **d |** Corresponding binary image using a mask level of 1 count per pixel is used to estimate the surface fraction occupied by mEGFP molecules (p_{occupied}), as an indicator of multi-molecule events due to crowding. **e |** Average numbers of fluorophores according to cPBSA of one ROI is plotted against its p_{occupied} value. Colors indicate samples matching the global legend (Figure 6.2). Black circle indicates the ROI shown in c-d.

After minimal step size optimization, the Kalafut-Visscher algorithm [132] was used to derive the number of fluorophores per measurement spot. Multi-step events corresponding to multiple fluorophores in a single confocal detection volume were found in all datasets, including the monomer control dataset. As in case of quantitative STED image analysis, such events may either indicate true oligomers or molecular accumula-

tion due to local concentration fluctuations (Figure 9.3b).

To control for multi-step traces originating from multiple monomers or oligomers proximal in the confocal volume, we calculated an indicator for the occupancy probability, p_{occupied}, from the fraction of surface exceeding the background level for each area (see Figure 9.2c/d). A weak correlation was found between p_{occupied} and $\langle N_{\text{steps}} \rangle$, as expected due to an inherently increased proximity of molecules in more occupied ROIs. As the spread of the occupancy probability was similar for all samples, this created no systematic shift in the data, wherefore no additional correction had to be introduced (see Figure 9.2e).

9.1.2 CD95 Stoichiometry revealed by cPBSA

cPBSA was applied to HeLa CD95$^{\text{KO}}$ cells expressing CD95-mEGFP, CD95(ΔDD)-mEGFP and the controls CD86-mEGFP (monomer), CTLA4$_{\text{DA}}$ (dimer) and CD86-mEGFP-mEGFP (PseudoDimer). In case of all confocal PBSA measurements mostly single, double or triple bleaching steps were detected. Only dimer controls exhibited bleaching traces with a higher number of fluorophores per spot. In case of CD95 and CD95(ΔDD) more than 70 % of traces exhibited a single step, 23 % two steps and about 2 % three or more bleaching steps. Upon ligand addition, the fraction of monomers decreased to about 60 %, whereas traces of two, three or more bleaching steps rose to 25 % and 5 %, respectively (Figure 9.3b). In the absence of the ligand, CD95 with or without death domain exhibits a highly similar distribution of detected fluorophore numbers compared to CD86 as well as an identical average fluorophore number $\langle N_{\text{fluorophores}} \rangle$ of 1.33. Thus, CD95 is monomeric in its inactive state. Upon ligand incubation, a slight shift to higher oligomerization states is observed for CD95 (+7 %) and CD95(ΔDD) (+6 %, see Figure 9.3b/c) with an average fluorophore number rising to 1.42. To interpret this change accounting for local concentration fluctuations or photophysical effects, we rated it against the dimer controls CTLA4$_{\text{DA}}$ and CD86-mEGFP-mEGFP. The two-step controls were significantly higher than all other measurements (Mann-Whitney U-test $p < 0.001$) with CD86-mEGFP-mEGFP and CTLA4$_{\text{DA}}$ exhibiting $\langle N_{\text{fluorophores}} \rangle$ of 1.92 and 1.78, respectively. As in the case of quantitative STED analysis (Chapter 8.1), the value for CTLA4$_{\text{DA}}$ is slightly lower than for CD86-mEGFP-mEGFP. Both values are slightly less than the average fluorophore number of 2 due to maturation and folding efficiencies of mEGFP below 100 % [142]. The probabilities to detect fluorescence from a fluorescent protein (apparent fluorescence probability) were reported to be 80 % for mEGFP in *Xenopus laevis* oocytes [87] and 53 % for a superfolder GFP variant in human embryonic kidney cells (HEK293T) [148] in studies performing subunit counting. For CTLA4$_{\text{DA}}$, the presence of donor-acceptor pairs in

addition to donor-donor pairs as well as the overall dimeric fraction below 100 % for low expression levels (compare Chapter 9.2.5) lower the expected value additionally.

Overall, cPBSA measurements show that only few percent of CD95 receptors accumulate within spots after ligand addition and still trigger apoptosis efficiently. Before ligand addition, CD95 spots show the same bleaching step distribution as the monomer control sample.

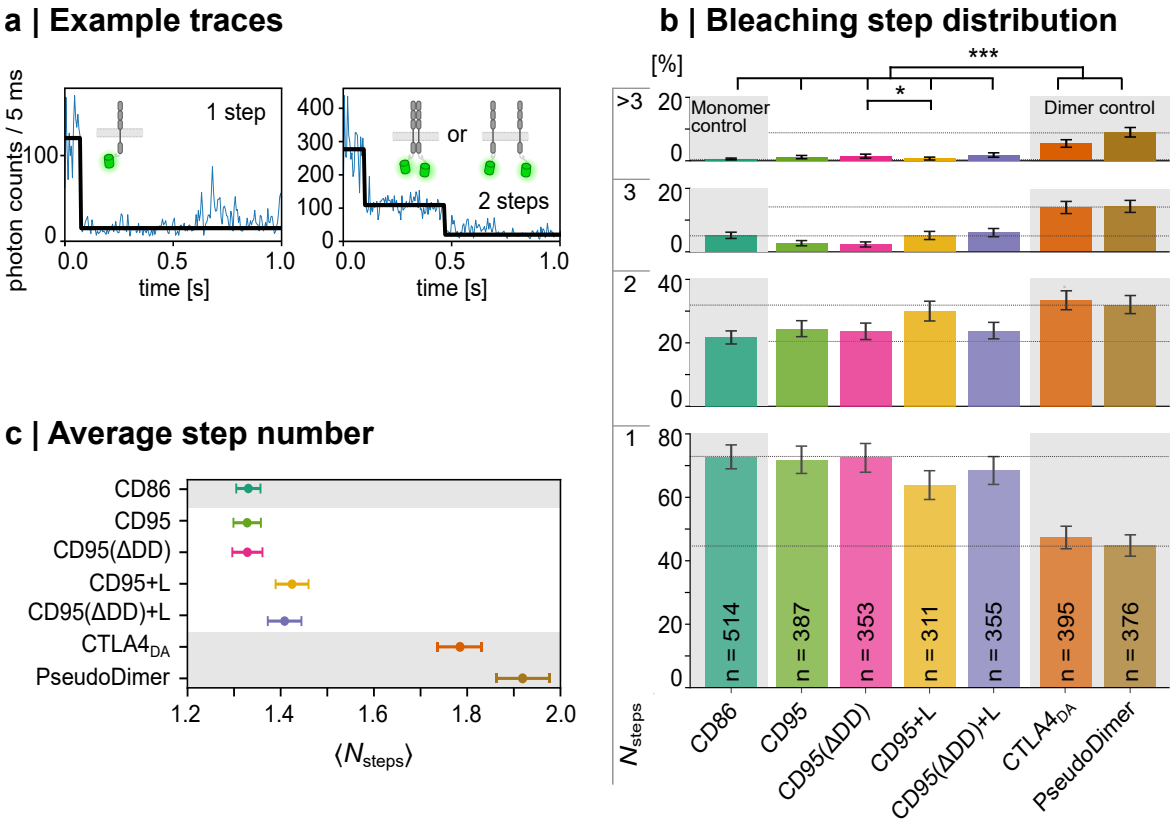

Figure 9.3: Confocal PBSA reveals the stoichiometry of CD95 in fluorescent spots. **a |** Left: exemplary trace of a monomer. Right: exemplary trace for either a dimer or two monomers in one confocal spot (crowding). **b |** Bar diagram of step occurrence. Primarily 1,2 and 3 photobleaching steps were detected. The monomer and dimer controls are used to characterize the fraction of multimer events attributed to crowding. Errors bars are calculated from Poisson statistics. **c |** Mean number of fluorophores and standard error of the mean for data shown in c). A small increase in fluorophore number is detected for CD95 (* with $p = 0.026$) and CD95(ΔDD) (n.s. with $p = 0.169$, Mann-Whitney U-test with ***: $p < 0.001$, *: $p < 0.05$) in presence of the ligand. The average fluorophore number is significantly smaller compared to those of dimer controls.

9.1.3 Increase in cPBSA Robustness with Hybrid Fluorescence Spectroscopy

Interestingly, besides the spatial localization due to the confocal configuration (Methods Figure 9.1a) our time-tagged measurements give us full access to spectroscopic tools, such as efficiency-based FRET, lifetime-based FRET, anisotropy and correlation analyses. These readouts are advantageous to identify contributions from dark states, blinking events and molecular orientation in the bleaching trace which is used to predict the expected variance of our traces (Figure 9.4a/b and Methods Chapter 5.5.2). Firstly, we characterize the sources of noise in our traces being either of photophysical origin or sample related, which was useful to optimize the sample preparation process and to interpret our data (see Supplementary Figure E.1). To characterize fluorophore blinking, we calculate the cross-correlation function of the intensity trace polarization channels globally for the CD95, CD95(ΔDD), CD86 and CTLA4 samples, identifying three dark states with characteristic times of 0.011 ms, 0.56 ms and 5.0 ms in addition to the characteristic bleaching time of 84 ms (see Figure 9.4b, Supplementary Figure E.2 and Tables 5.1 and E.1). The cross-correlation, in addition, enables to predict the variance of a trace segment, allowing us to interpret whether the KV algorithm over- or underestimates the number of bleaching steps. The increase in trace segment residual variance due to the fluorophore being in a dark state increases with the duration of the dark state, hence we consider only the longest dark state that has a t_{on} of 5 ms and t_{off} of 30 ms (see Methods Chapter 9.1) to obtain a theoretical expression and to perform Monte Carlo simulations of the expected variance (see Supplementary Note E.2). As t_{off} is comparable to the average bleaching time (84 ms), the number of blinks in a trace varies stochastically around an average value of ~ 2.5 resulting in some traces showing no blinks and others many. We average out the spread in variance by considering the variance of the residuals of many traces (Supplementary Figure E.3b). Comparison of the measured and theoretical residual trace variance show good agreement indicating that the KV trace analysis with the chosen threshold is capable of correctly extracting the number of fluorophores from the noisy traces. We note an excess of residual variance at low brightness and a shortage at high brightness, which is explained in part due to the presence of additional noise sources as characterized in this manuscript, but also points to a slight overestimation of the number of fluorophores at high brightness values.

Furthermore, we study the polarization of single-bleaching step emitters (see Methods Chapter 5.5.2) and found a freely rotating population centered around 0 polarization and a static population whose dipole orientation can be inferred from the amplitude of the polarization signals (Figure 9.4c/d). Similar to the STED experiment, the presence

of static dipoles causes a spread in the single fluorophore brightness due to different alignment with the incident excitation field.

In conclusion, we've introduced a robust approach to apply PBSA on noisy mEGFP data, that provides an unbiased assessment for the minimum step size and identifies that polarization effects are the cause of varying single fluorophore brightness. Our results highlight the need for a Bayesian trace fitting algorithm as published before [149, 150].

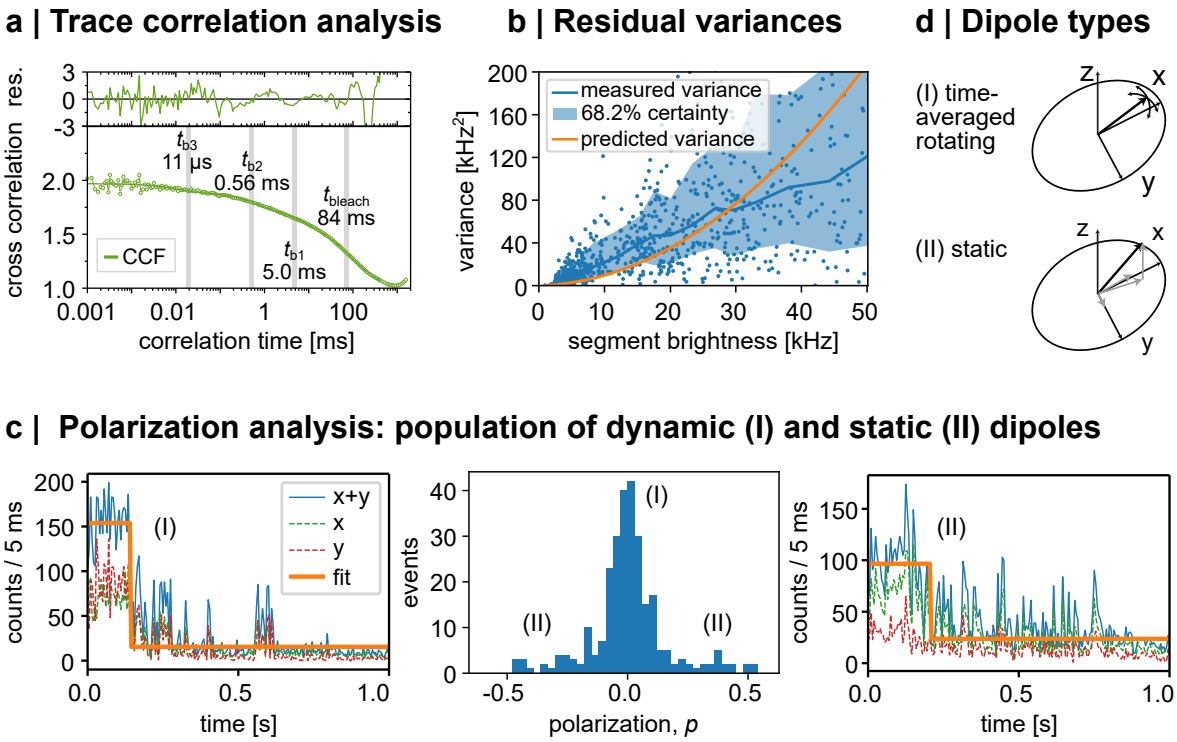

Figure 9.4: Confocal PBSA technical advancements. **a |** Cross-correlation of CD95 bleaching traces yield characteristic correlation times of mEGFP blinking and bleaching events in cells. Characteristic time scales are derived from a 3-4 parameter global fit (see Supplementary Figure E.2). **b |** Obtained blinking times are used to predict residual variances and confirm that our approach neither over- nor underestimates the number of fluorophores (see Supplementary Note E.2). **c |** Polarization resolved fluorescence traces reveal dynamic mEGFP dipoles (left) and fixed dipoles (right) from which the polarization angle can be calculated. (Middle) Distribution of mEGFP dipole polarization in CD95 single-step traces. Static dipoles have non-uniform brightness, whereas dynamic dipoles do not exhibit a net polarization. **d |** Graphical illustrations of time-averaged dynamic (I) and static (II) dipoles.

9.2 FRET uncovers Molecular Interactions of CD95

Finally, since the above techniques are not capable to distinguish molecular proximity from intermolecular interactions within diffraction- or depletion-limited spots and have limited capacity to probe a variability in biological phenotype, we used and advanced FRET (Förster resonance energy transfer) microscopy to probe cells exhibiting highly different receptor expression levels. With its properties as a molecular ruler, FRET is ideally suited to report on molecular binding effects. Here, a FRET signal only occurs if a CD95 receptor labeled with mEGFP donor and a second receptor with an mCherry acceptor molecule are in close proximity ($< 10\,\mathrm{nm}$) [91, 92].

9.2.1 FRET Advancements

While intensity-based FRET is a well-known tool in order to attest prominent molecular bindings, there are no established advancements towards a FRET study uncovering elusive interactions of the cell quantitatively in its natural state. In this work, we developed a new methodology of quantitative, lifetime-based FRET. It relies on a confocal lifetime-based FRET method, also known as FRET-sensitized fluorescence donor decays. Here, molecular proximity gives rise to changes in the donor fluorophore lifetime, which we quantify in form of the FRET-sensitized donor decay ($\epsilon(t)$) (see Chapter 5.6). Figure 9.5a gives a comprehensive overview on our new, in-depth FRET approach: the fluorescence is measured in the FRET sample (DA) as well as control sample, expressing the donor in absence of the acceptor (D0). Normalization of the DA fluorescence decay with respect to the average D0 decay shows the fraction of donors that was quenched due to FRET in the presence of acceptor(s). While FRET-sensitized fluorescence donor decays alone can be used to identify the fraction of FRETing molecules x_{FRET} in a sample, we advance the methodology to an extend where it is possible to identify switching between bound and unbound states as well as absolute donor and acceptor, monomer and oligomer surface concentrations. It is compatible with live-cells under endogenous expression levels and normal cell conditions.

Our advanced FRET method requires of a confocal microscope with two excitation lines compatible with the excitation spectrum of the FRET pair and pulsed excitation combined with TCSPC readout to enable (donor) lifetime measurements (compare Figure 9.5 A1). To measure the acceptor concentration, Alternating Line Excitation (ALEX) is required to distinguish the donor-induced acceptor emission from the acceptor emission upon acceptor excitation. The donor-induced emission of the acceptor

can be caused by FRET and donor crosstalk.

When measuring small effects as well as sampling large cell variations, for example in concentration, in addition to the natural cell-to-cell variability, a high number of single-cell data is required. For this purpose, we used an automated data acquisition program that interfaces with the microscope control software *Imspector* requiring ~ 10 minutes to set up for recording time series dataset of up to 50 cells, as this kind of automation was not available for our setup. The program written by Nicolaas T M van der Voort enables to pre-select multiple regions of interest with multiple cells manually, to select the image acquisition settings and finally to image all positions in the stage loop once or repeatedly in a time loop, if required (compare Figure 9.5 A2). After the acquisition, the recorded images have to be segmented according the scientific question – from multiple cells to specific subcellular domains (Figure 9.5 A3 (1.)). We used single cell segmentations to examine whole cells (compare Chapter 9.2.2) as well the effect of local CD95 concentration fluctuations (high and low brightness) on the oligomerization state (compare Chapter 9.2.3).

The analysis of the FRET-sensitized fluorescence donor decays was done following a decay fitting method previously established (compare Methods Chapter 5.6.2). It measures changes in the donor decay due to FRET by measuring changes with respect to a donor only control (compare Figure 9.5 A3). As the donor only control was recorded under identical circumstances as the FRET sample, this provides an internal calibration against temperature or pH induced lifetime changes. In contrast to intensity-based methods that measure the weighted average of FRET species, the FRET-sensitized donor decay is more informative by distinguishing the fraction of FRET-capable donors x_{FRET} and their average FRET rate k_{FRET} in addition to the fraction of non-FRET-capable donors (x_{noFRET}). Here, we used a python-based analysis toolkit requiring only minimal input settings to batch analyze data, reducing the manual time required to analyze a dataset to ~ 10 minutes in addition to computer runtime. The toolkit was coded by Nicolaas T M van der Voort.

Absolute Donor and Acceptor Concentrations

To transform the fluorescent brightness of an image to a number of fluorophores, we obtain calibrations for the brightness of single fluorescent proteins using a brightness calibration curve for the FRET fluophores EGFP and mCherry. For a titration series of each fluorescent protein, the concentration was measured using absorption spectrometry. Supplementary Figure F.1 shows the absorption measurement results. Subsequently, the brightness per confocal volume wa measured on the FRET measurement

setup (compare Methods Chapter 5.6.3). The brightness-per-concentration curve (normalized for the laser power) can then be fitted linearly resulting in a slope coefficient b (brightness per concentration, $[^{kHz}/_{(\mu M \cdot \mu W)}]$). Our calibration measurements (Figure 9.6) yielded in $b_D = 266.2\,^{kHz}/_{(\mu M \cdot \mu W)}$ for EGFP and $b_A = 133.3\,^{kHz}/_{(\mu M \cdot \mu W)}$ for mCherry. Accounting for the size of the confocal volume obtained with FCS calibration, the

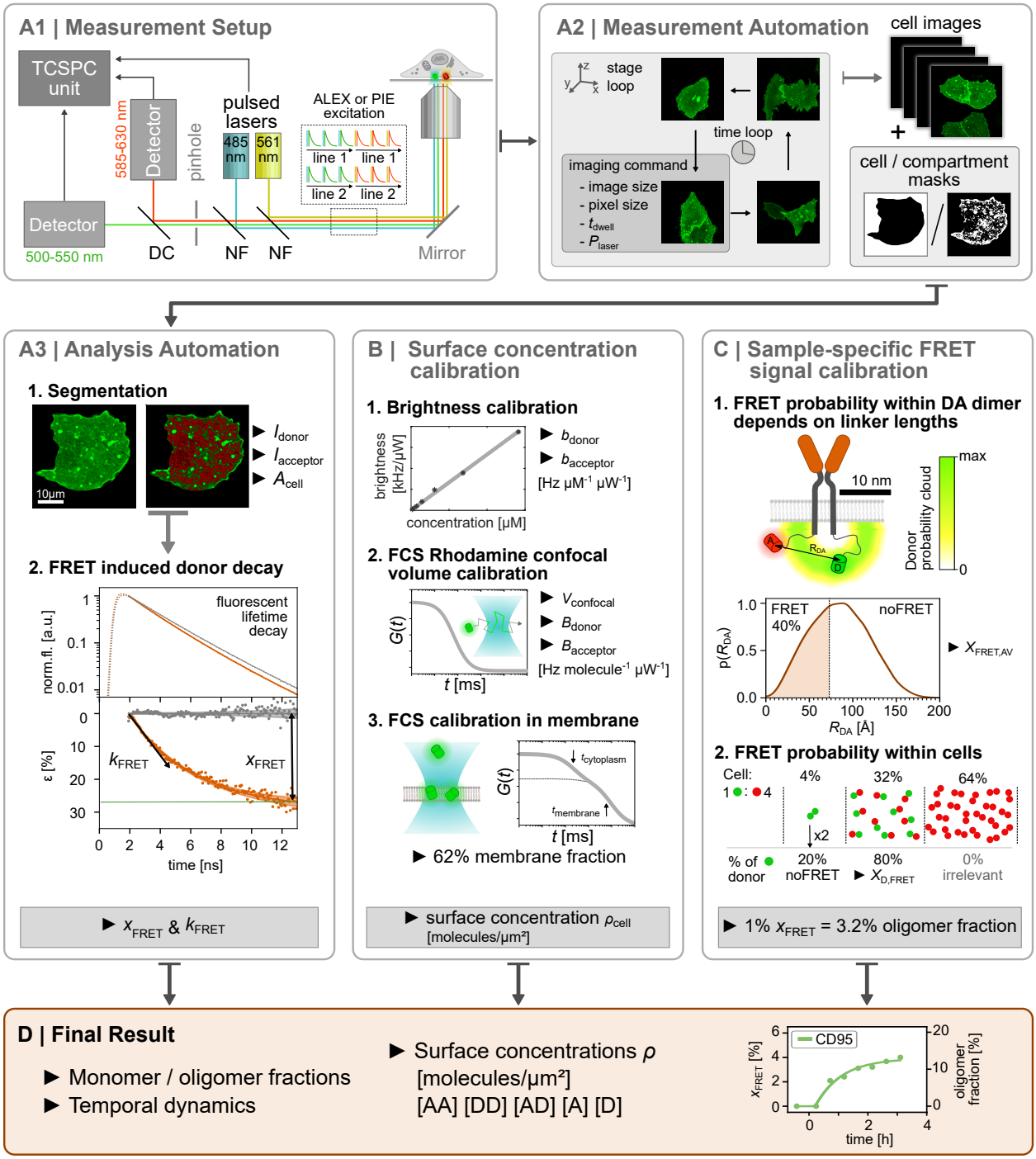

Figure 9.5: Schematic overview of all pillars of our in-depth FRET approach. (Caption continues on next page.)

A1 | The method requires a confocal setup with single photon counting ability (TCSPC) and pulsed interleaved- or alternating line excitation (PIE/ALEX). DC = Dichroic Mirror, NF = Notch Filter. **A2 |** Multi-cell images are recorded in an automated manner using stage- and time-loops. The images can be segmented using whole cell or cell compartment masks to select the regions of interest for analysis. **A3 |** The automated analysis calibrates and fits the FRET induced donor lifetime, yielding the FRET fraction and rate, x_{FRET} and k_{FRET}, and derives image information like the channel intensities $I_{\mathrm{D}}/I_{\mathrm{A}}$ and the segmented areas, in our case A_{cell}. **B |** Precise calibration of the receptor surface is achieved with 1. brightness vs. concentration calibrations using the confocal setup and absorption spectroscopy, 2. confocal volume calibrations (FCS) with well-defined reference dyes (here: Rhodamines) and for membrane proteins, and 3. sample-specific FCS calibrations to distinguish between membrane and intracellular signal. **C |** To derive the sample-specific maximum FRET fraction $x_{\mathrm{FRET,max}}$ two steps are required: 1. AV simulation of the constructs can determine the FRET probability die to linker lengths and distances. 2. The ratio of donor to acceptor concentration can be used to determine the fraction of FRET-capable oligomers (here: dimers). **D |** All three pillars (**A,B,C**) converge to the highly accurate determination of absolute concentrations and precise oligomer fractions, that can be tracked in time and space.

brightness can finally be transformed into a brightness per molecule $\left[{}^{\mathrm{kHz}}/_{(\mathrm{molecule}\cdot\mu\mathrm{W})}\right]$.

In order to transfer this value to the FRET image data, the following points are to consider: 1) the cell membrane can be wrinkled under certain circumstances, leading to an overestimation of the receptor surface density, 2) there is also intracellular fluorescent signal originating from the cell's production and transport machinery, as visible in Figure 7.1. Here, we avoid membrane roughness altogether by measuring the bottom of the cell membrane, which is flat to a high degree [144]. Further, we account for the intracellular fraction of the fluorescent signal as determined by the fast diffusion component of our FCS measurements on membrane receptors (Chapter 8.2) which was found to be composed of a mean cytoplasmic fraction of $p_{\mathrm{cp}} = 38\,\%$ and $p_{\mathrm{mem}} = 62\,\%$ of the signal originating from the membrane, based on the FCS analysis of 60 cells with strict focus on the bottom cell membrane.

Altogether, the brightness per molecule and the FRET image brightness corrected for the laser power and cytoplasmic component can be transferred into a receptor surface density (compare Methods Chapter 5.6.3). This step is a crucial advancement of the analysis for a quantification of the absolute receptor and oligomer numbers. Note, that for large FRET fractions the donor brightness is reduced in the presence of the acceptor, which should be accounted for. In the case of CD95 we measured small FRET fractions (below 6 %, compare Chapter 9.2.2), wherefore we can neglect this effect.

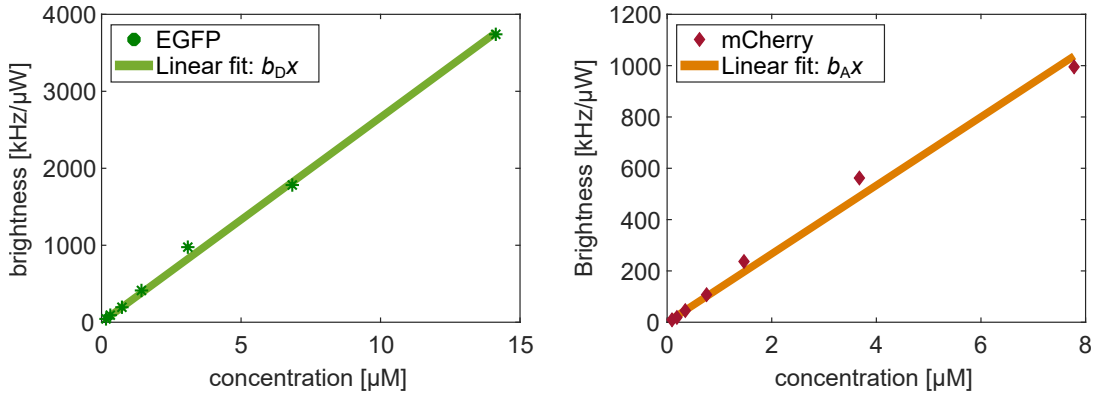

Figure 9.6: Brightness vs. concentration calibration curves of fluorescent proteins EGFP (left) and mCherry (right) in solution. The concentration of the dilution series was measured with absorption spectroscopy (Supplementary Figure F.1) while the brightness was obtained from confocal microscopy under conditions of FRET measurements. The brightness of each dilution step was obtained at three different laser powers. All data points were used for the linear fit $b \cdot x$, graphs show the mean of the three data points per sample. The fit results can be found in the main text.

Maximum FRET Fraction

The FRET-sensitized donor only decay analysis results in the fraction of FRET-ing donor molecules x_{FRET}. To translate this fraction into an oligomer fraction, it is important to understand and correct for oligomers not able to FRET due to 1) flexible or long linkers of the fluorescent proteins that diffuse in and out of their FRET range although the target molecules do bind/interact within the range. And 2), in particular for homotypical interactions, homo-oligomers with similar fluorophores (for dimers constituted of donor-donor (DD) and acceptor-acceptor (AA) pairs).

In order to correct for 1), we calculate the maximal FRET signal for pure DA dimers with the specific linker lengths, $x_{\mathrm{FRET,AV}}$, from accessible volume (AV) simulations. This value depends on the distance between the fluorophore anchors as well their probability density which depends on the flexible linkers. The fluorescent protein as well as the labelled protein have flexible domains at the end of their peptide chains in addition to a flexible linker added during plasmid design, leading to a 46 to 53 amino acid linker for our constructs (Table 4.2). Truncation of the linker and/or flexible domain is often not feasible as they are required for correct protein folding. As the fluorescent proteins diffuse on a tether, previous work from our collaborators calculated the extension distribution for a given peptide length illustrated as the colored area in Figure 9.5 C (1.) with an average displacement from the anchor point of 7 nm, which is much shorter than the elongated linker. As both donor and acceptor diffuse, we

perform AV simulations to obtain the distribution of donor and acceptor distances R_{DA} (Figure 9.5 C (1.)) using anchor points separated by 22 Å, consistent with PDB structure ID 2NA7 [64, 140] for CD95 (compare Methods Chapter 5.6.3). The FRET range was set to 75 Å, corresponding to 10 % FRET for our Förster radius of 52 Å, yielding that a FRET pair is FRET-ing 39.8 % of the time.

To correct for homo-oligomers (2), the ratio of donor to acceptor in the cell is relevant. As cPBSA revealed a number of bleaching steps for CD95 in the regime of monomer and dimers (see Chapter 9.1), we assume dimeric oligomers here. The fraction of FRET-capable donors is determined by the abundance of donor-donor homo-dimers in addition to donor-acceptor hetero-dimers and can be calculated following a binomial distribution (compare Methods 5.6.3). Note, that acceptor-acceptor dimers also form, but do not affect the donor lifetime measurement. Figure 9.5 C (2.) illustrates one exemplary A:D distribution in a dimeric sample as well as the resulting fraction of FRET-capable donors in the sample $x_{D,FRET}$ for different D:A ratios. For CTLA4 the average ratio between donor to acceptor was 1:3.5 yielding 78 % heterodimers and for CD95 and CD86 variants it was 1:2.5 yielding 71 % heterodimers. The absolute ratio of mEGFP to mCherry can be calculated by transformation of the image intensities into absolute receptor surface concentration, as explained in the previous section of this chapter.

Finally, the maximum FRET fraction for a homotypical interaction $x_{FRET,max}$ is obtained by multiplying the probability that the dyes are in the FRET range $x_{FRET,AV}$ and the fraction of heterodimers $x_{D,FRET}$, yielding an $x_{FRET,max}$ of 31 % for CTLA4 and 28 % for CD95 and CD86. The absolute number of dimers is straightforwardly obtained by multiplying the total receptor concentration with the fraction of dimers and dividing by two.

9.2.2 Advanced FRET identifies a Sensitive Transition after Signal Initiation

Finally, the advanced FRET methodology was used to examine the molecular interactions during CD95 signal initiation. As before, we measured CD95, CD95(ΔDD) as well as the monomer CD86 as negative non-FRET control and CTLA4 as dimeric positive control. In all cases, bicistronic plasmids were used to ensure similar donor and acceptor expression levels (Figure 9.7). In order to obtain further insights about local molecular concentration fluctuations suggested by the above techniques, we systematically tuned the range of receptor concentrations by titrating the amount of receptor DNA used for transfection against an empty vector, while keeping the total amount

of DNA constant. To then derive the average oligomerization state with great accuracy, we evaluated FRET data of the CD95 receptor on the lower cell membrane and summed all photons over the cell bottom surface.

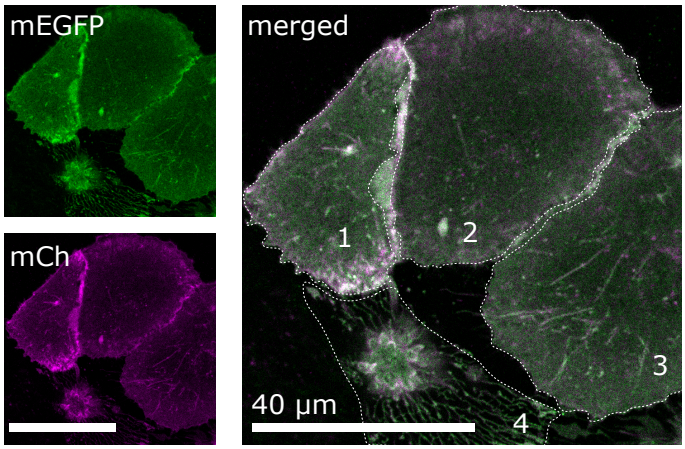

Figure 9.7: Hela CD95^{KO} cells expressing CD95 with donor (mEGFP) and acceptor (mCherry) for FRET measurements (bicistronic plasmid). Confocal fluorescence image indicating correct incorporation and colocalization of mEGFP and mCherry labeled CD95 in the membrane. The image was recorded 113 minutes after addition of CD95L. Cells 1, 2 and 3 are alive at the time point of measurement, whereas cell 4 already underwent apoptosis.

Figure 9.7 shows the localization of the CD95 receptor in live cells by confocal images on the lower cell membrane. The increased intensity at cell edges and cell-to-cell contacts confirm the primary integration of the receptor proteins into the cell plasma membrane. Similar images of CD95(ΔDD), CD86 and CTLA4 are found in Supplementary Figure C.3. To evaluate FRET data of the CD95 receptor quantitatively, we benchmarked it against signals obtained from the CD86 and CTLA4 controls. As expected, no FRET signal was measured for CD86 up to a concentration of 2000 $^{\text{receptors}}/_{\mu\text{m}^2}$. At this point a systematic increase in FRET indicates the onset of proximity-induced FRET and a similar rise was observed for CD95 and CD95(ΔDD) in the absence of the ligand (compare Chapter 9.2.5). For this reason and since proximity FRET has been reported before in this concentration range [151], we evaluated FRET data only up to the threshold of 2000 $^{\text{receptors}}/_{\mu\text{m}^2}$. FRET measurements of CD95 and CD95(ΔDD) in the absence of the ligand show that both receptors are monomeric. Upon ligand addition the portion of x_{FRET} increases immediately by a few percent, which in relation to the CTLA4 signal suggests dimer to trimer formation (Figure 9.8a). The oligomer fraction is obtained from x_{FRET} following sophisticated calibrations described above (Chapter 9.2.1).

In order to probe how the oligomerization states change over time until the point of

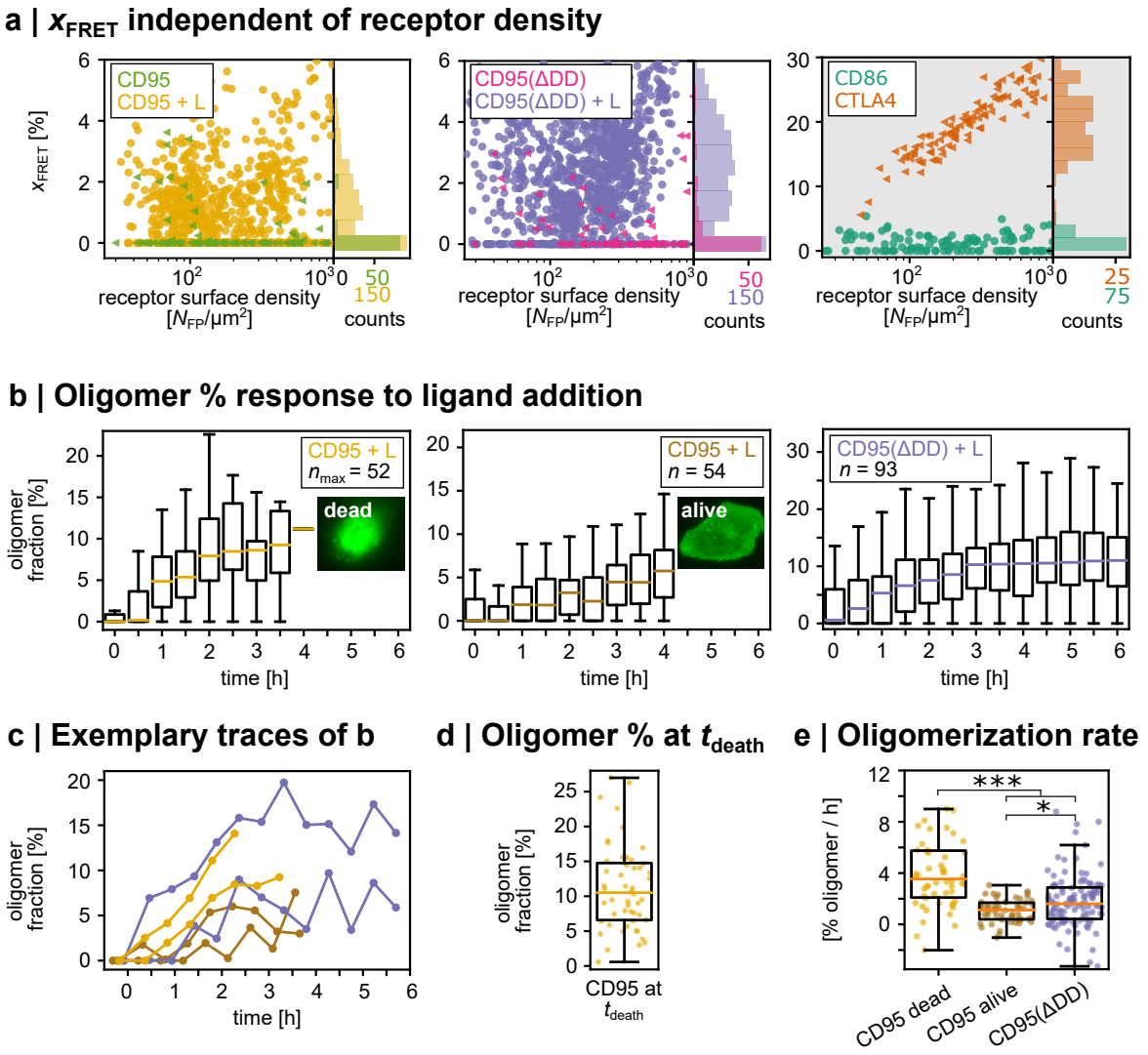

Figure 9.8: FRET quantifies the CD95 oligomerization state over a large concentration range. **a |** x_{FRET} histogram and scatter plot as a function of receptor surface density. CD95, CD95(ΔDD) and the monomer control CD86 are monomeric over the whole concentration range. After CD95 Ligand incubation a small fraction of CD95 and CD95(ΔDD) oligomerizes to dimers or trimers. Intriguingly, CTLA4 switches from a monomer to a dimer with increasing receptor concentration. $N = 324$ cells from at least 4 independent experiments were analyzed per condition. **b |** Dynamics of oligomer formation after CD95 Ligand addition. The oligomer fraction was calculated from repeated measurement of the same cells and averaging over many traces. Boxplots show colored medians. **c |** Exemplary evolution of the oligomer fraction in single cells over time. Oligomer fractions saturate after 3 - 4 hours. Color legend same as in b). **d |** Boxplot of the oligomer fraction of cells that died during the measurement, at the last time point before visible apoptosis (blebbing, shrinkage). **e |** Oligomerization rate over maximal the first 3 hours (or less if timepoint of cell death was before). Legend same as in d). Confidence intervals, *: $p < 0.05$, ***: $p < 0.001$, Mann-Whitney U-test.

cell death, we recorded FRET data over 0 - 6 hours after ligand addition by repeated measurements of the same cells. Three classes of experimental observations of CD95 oligomerization were identified and statistics (Figure 9.8b) and exemplary traces (Figure 9.8c) are shown. Here, cell responses after ligand addition could be classified into three categories exhibiting common characteristics in terms of the absolute amount of x_{FRET}, the speed of oligomer formation, the resting time before oligomerization started and whether x_{FRET} diminishes: 1) The first class comprises cells expressing full-length CD95 which underwent apoptosis within 4 hours of observation. Here, an oligomer fraction starting at close-to-zero and increasing quickly up to 8 % median was observed. Note, that the number of cells per time bin decreased as cells progressively died. 2) The second class comprises cells expressing full-length CD95 that did not die over a period of 4 hours after ligand addition. Here, the increase in oligomer formation was slowed reaching a ~ 5 % median after 4 hours. 3) In the third class, cells expressing CD95(ΔDD) did naturally not exhibit any apoptosis and a slightly higher initial oligomer fraction and increase up to 11 % median as well as steady-state after ~ 3 hours was obtained. In the individual cell traces (Figure 9.8c) in some cases a slight rise and fall of the oligomer fraction was detected over time, which may stem from transient CD95 dimerization or recruitment of CD95 around CD95L followed by CD95L release without signaling activation. To further quantify CD95 oligomerization as prerequisite to initiate apoptosis, we derived the oligomer fraction. The oligomerization state for cells just prior to cell apoptotic blebbing and shrinkage was plotted, amounting to an interquartile range between 6 - 15 % with a median value of 10 % (Figure 9.8d). Additionally, we determined the oligomerization rate from the change in oligomer fraction per time interval, which was faster in case of CD95 transfected cells that died (with 3.5 % $^{\mathrm{oligomers}}/_{\mathrm{h}}$) compared to CD95 or CD95(ΔDD) transfected cells which stayed alive (with 1.1 % and 1.6 % $^{\mathrm{oligomers}}/_{\mathrm{h}}$ respectively, Figure 9.8e).

Overall, our results demonstrate that oligomerization requires ligand addition, oligomers form within 2 - 3 hours over the whole membrane, they can occur in absence of a death domain, and only about 6-15 % oligomers in the form of dimers and potentially few trimers are necessary for efficient signal initiation. Moreover, the absence of oligomerization prior to any ligand addition indicates that the CD95 oligomerization may be mediated via ligand binding or by the transmembrane domain only in the receptor activated state, as previously suggested [64].

9.2.3 Mapping the Oligomerization States over the Single-Cell Membrane

Our fluorescent images of membrane proteins consistently show bright membrane domains of $0.5-3\,\mu m^2$ size on the cell membrane indicating a local concentration of CD95 receptors. These membrane structures could also be found for CTLA4 and CD86 (see Supplementary Figure C.3). As shown by our previous data (Chapters 8.1 and 9.1), the domains do not contain higher order networks, but rather consist of a high concentration of monomers before ligand addition and a monomer/oligomer mixture after ligand addition.

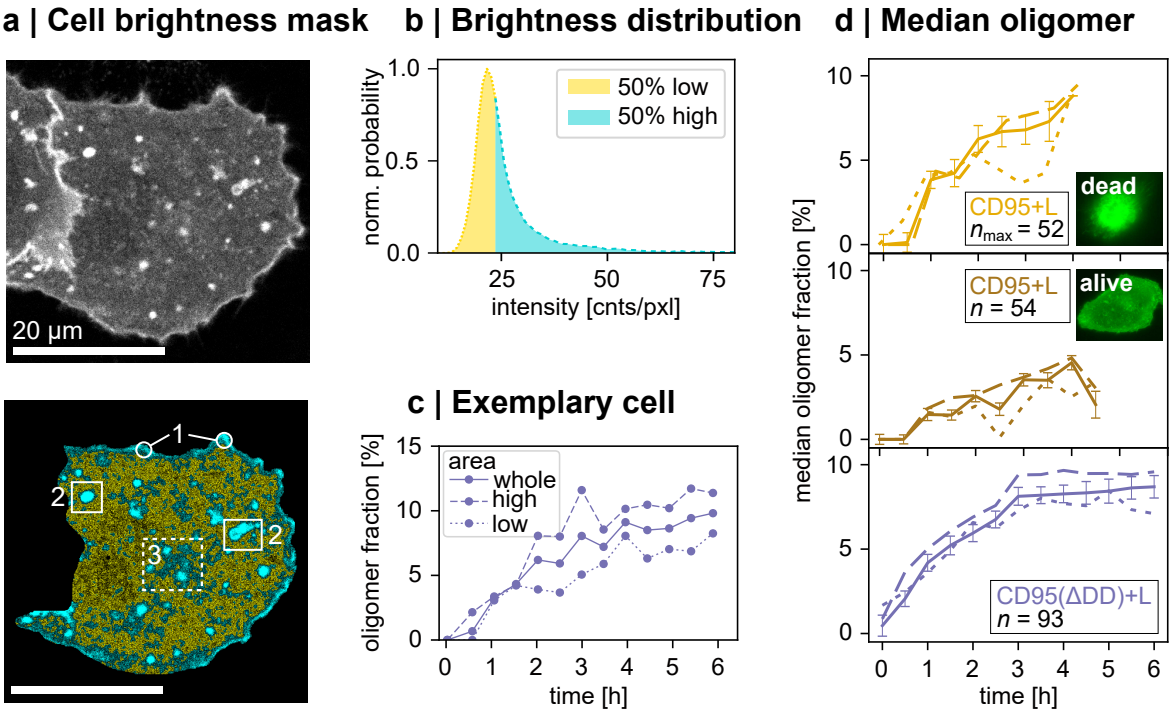

Figure 9.9: FRET probes oligomerization state in protein agglomerations. **a |** Hela $CD95^{KO}$ transiently transfected with CD95(ΔDD) linked to mEGFP and mCherry (top) shows areas of high CD95 concentration identified as (1) vertical orientation of the cell membrane, (2) high concentration areas on the bottom cell membrane and (3) compartments of the (fluorescent) protein biosynthesis machinery in membrane proximity (bottom). **b |** Brightness segmentation: The area is divided by half to obtain low- and high- brightness areas with each 50 % of the cell's total photon counts. The area where two cells overlap is excluded. **c |** Time-evolution of the oligomer fraction for the cell in a/b. **d |** Median oligomer fractions for full-length CD95 transfected cells that die (top), that remained alive (middle) and CD95(ΔDD) (bottom). Error bars are obtained from standard error of the mean.

To investigate the possibility of higher oligomeric states further and to explore whether the $\sim 6-15\,\%$ oligomer formation is predominantly localized in particular membrane

areas, we probe the oligomeric state of the bright and dim areas by modifying our analysis to separately high- and low brightness membrane areas. The high brightness area contains signal from the cell edges, compartments of the (fluorescent) protein biosynthesis machinery in close membrane proximity and, interestingly, bright circular areas of unknown origin. In contrast, the low brightness area contains the mostly flat horizontal membrane (Figure 9.9a). In order to avoid bias from unequal fit quality, the areas were chosen such that the high and low areas contain an equal number of photons (Figure 9.9b). Exemplary data of one cell shows that oligomerization occurs in both, high and low brightness areas, although overall slightly more and faster oligomerization occurs in high brightness areas (Figure 9.9c). Analysis of the dataset from Figure 9.8b-e shows that this trend is representative of the population and occurs for all CD95 variants (Figure 9.9 d), albeit the oligomerization trend of the low brightness areas follows the high brightness areas closely. Over the course of the ligand incubation time, the oligomer fraction within high and low brightness areas only deviates about 2-3 % on average.

9.2.4 Single-Cell Time Evolution reveal $x_{\mathbf{FRET}}$ Dynamics with High Precision

With our new FRET methodology presented in Chapter 9.2.1, we are able to map the oligomer time evolution of a single cell or even of cellular sub-compartments. While mainly focusing on ensemble cell data in the Chapters before (9.2.2 and 9.2.3), we can monitor the evolution of the oligomer fraction of a single cell in time, as already shown in Figures 9.8 c and 9.9 c, where ligand addition changes the equilibrium state of CD95 from purely monomeric to a mixture of monomers and oligomers.

Within the time evolution of multiple single cells, we find different patterns for the characterization of the time traces after ligand perturbation. We identified three categories for the time evolution of the oligomeric fraction (Figure 9.10). In the first category, selected cells ($n = 76$, 34 %) showed an asymptotic approach to a new steady-state corresponding to a purely kinetics driven response. In a second category ($n = 139$, 63 %), various modulations of the oligomer fraction in time were observed. In a third category ($n = 6$, 3 %) were traces that were too short to clearly identify characteristics.

Cells of the first category showing a saturation trend in the FRET fraction could be well described using a model where a perturbed system approaches a new steady-state for

the FRET fraction. x_{FRET} dynamics were fitted according to the following relation

$$x_{\mathrm{FRET}}(t) = \begin{cases} 0 & \text{if } t < t_{\mathrm{offset}}, \\ A\left(1 - e^{-\frac{t - t_{\mathrm{offset}}}{t_{\mathrm{rise}}}}\right) & \text{if } t \geq t_{\mathrm{offset}}. \end{cases} \tag{9.1}$$

Here, A describes the amplitude of the response and t_{rise} the characteristic time the response increased to 63 %. t_{offset} accounts for an additional time offset, precisely the time delay before any response is registered. Fitting this model to the cell traces allowed us to disentangle the measurement error from fluctuations due to cellular self-control processes.

By this, we obtain a conservative estimate of the measurement precision by considering the residuals of six selected CD95 and six selected CD95(ΔDD) cells corrected for the number of fit parameters, yielding 0.25 % x_{FRET} corresponding to 0.9 % oligomer fraction. Supplementary Figure F.2 shows an selection of steady-state time evolution traces together with their precision. We further characterize the error in the internal reference posed by the donor only control to be 0.36 % x_{FRET} or 1.2 % oligomer fraction caused by temperature changes (Supplementary Figure F.4). This error represents an absolute offset to all x_{FRET} values recorded on that day, affecting accuracy but not precision.

The modulations observed in the second category of oligomer evolution in time can be highly diverse, for example a temporal delay of increasing oligomer fraction > 1 hour (the fastest time after which the signaling response is observed), oscillations of various timescales or a decrease in the oligomer fraction. Supplementary Figure F.3 shows exemplary traces for the various modulations of dynamic responses. In order to investigate these responses, we confirmed the absence of visible artifacts, such as cell movement and focus drift by visual inspection of selected cells. As the fluctuations clearly exceed our error, we suggest that these fluctuations indicate a rich multitude of underlying cellular processes that control the oligomerization state in a complex manner. Potential reasons for fluctuations of x_{FRET} might be transient oligomerization states due to a weak binding affinity between CD95 and CD95L, which was found to be in the low nM to pM range for CD95 and other TNFRs [71, 73]. Further, CD95 internalization was shown to be a late event in CD95L stimulated type II cells [74] and could cause a decrease of CD95 oligomers on the membrane.

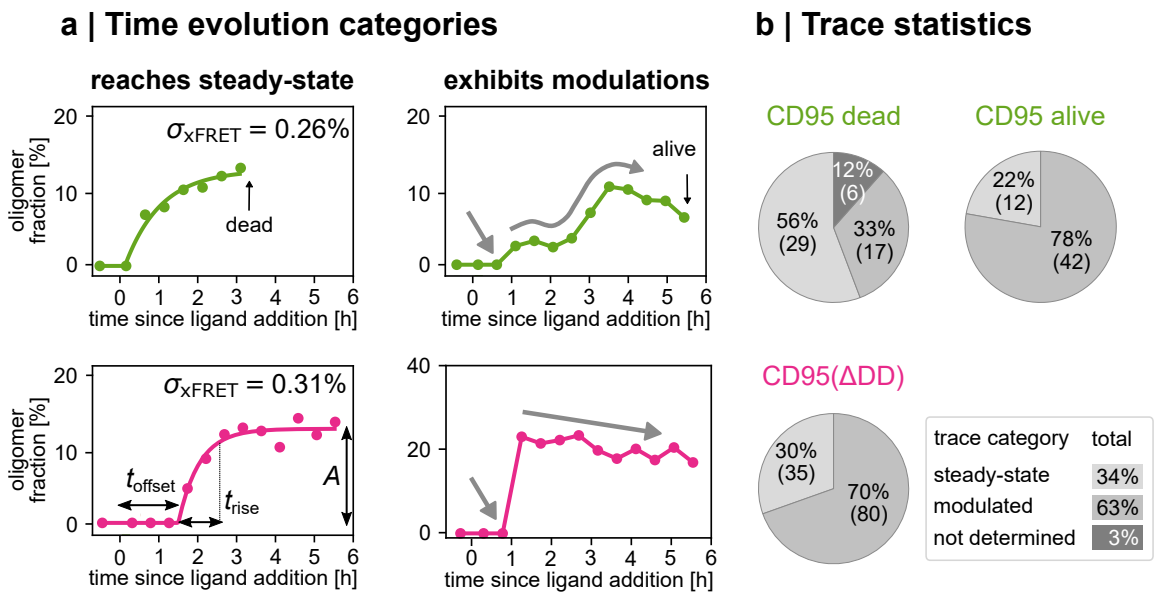

Figure 9.10: The time evolution of single cells can be categorized. Single-cell oligomerization responses to ligand addition are categorized. **a |** Exemplary traces for the steady-state and dynamic response type. Steady-state responses can be described following a model (compare main text) and determine the precision of x_{FRET}. Fitting parameters are illustrated. Dynamic responses show for example jumps, fluctuations/oscillations and decrease of oligomer fractions. More exemplary traces of both categories can be found in the SI Section F. **b |** Statistical analysis of trace characteristics. Apoptosis competent CD95 expressing cells that undergo apoptosis cells show more steady-state traces compared to CD95 cells that stay alive and CD95(ΔDD).

9.2.5 | Proximity FRET and the Dimerization of CTLA4

Our study of CTLA4 as a control (Figure 9.8a) shows a clear increase of x_{FRET} as a function of receptor surface concentration, indicating for the first time that the protein undergoes a concentration dependent monomer to dimer transition. Comparison to the monomeric samples CD95, CD95(ΔDD) and CD86 (compare Chapter 9.2.2) clearly illustrates that in addition to FRET due to dimerization, the x_{FRET} signal is affected by unspecific interactions due to crowding at high concentrations, also known as proximity or bystander FRET.

Our results show that proximity-induced FRET arises already at the common transfection conditions used here and hence accentuates the importance to test and correct for it. Figure 9.11 shows the proximity effect of CD95, CD95(ΔDD) and CD86, dominating from an acceptor surface density of 10^3 $^{\mathrm{acceptors}}/_{\mu\mathrm{m}^2}$ upwards for all samples consistently and dashed lines illustrate the proximity fits. The x_{FRET} dependency on concentration can be reliably modeled (compare Methods Chapter 5.6.3), depending on a single concentration parameter c_{prox}, describing the receptor concentration at which proximity FRET is responsible for 63 % FRET fraction. The fitting of our data yields c_{prox} to be $(1.87 \pm 0.08) \cdot 10^4$, $(1.87 \pm 0.05) \cdot 10^4$ and $(2.51 \pm 0.12) \cdot 10^4$ $^{\mathrm{receptors}}/_{\mu\mathrm{m}^2}$ for CD86, CD95(ΔDD)and CD95, respectively, errors obtained from least-squared fit. Advantageously, this method works like an internal control which is robust and does not rely on any calibration factors.

Finally, we use the correction based on the CD95 monomer for its robustness and good fit quality, to correct the CTLA4 data. The corrected data is eventually fitted following a model for homo-dimerization (compare Methods Chapter 5.6.3) yielding a final $\log_{10} K_{\mathrm{D}}$ of 2.30 $^{\log_{10}\mathrm{receptors}}/_{\mu\mathrm{m}^2}$. The CTLA4 fit residuals have a standard deviation of 2.55 % x_{FRET}. To ascertain the quality of our model, we visually inspect the fit residuals for systematic errors (Figure 9.11b) and quantify this using the Durbin-Watson test, yielding a good value of 1.48 close to the ideal value for random residuals of 2.0. Note that the χ^2_{red} parameter was not used as no reliable method was available to estimate the weights.

Taking advantage of the precision of our FRET approach (see previous Chapter 9.2.4), we note that the residuals of the CTLA4 fit (equals 8.0 % dimer fraction), represent biologically-relevant variability in the single-cell dimerization fraction. Further, the fitting model includes $x_{\mathrm{FRET,max}}$ as a fitting parameter (see Methods Chapter 5.6.3), which was obtained to be an experimental value of 32.6 %. Figure 9.11b shows the raw and uncorrected data of CTLA4 dimerization.

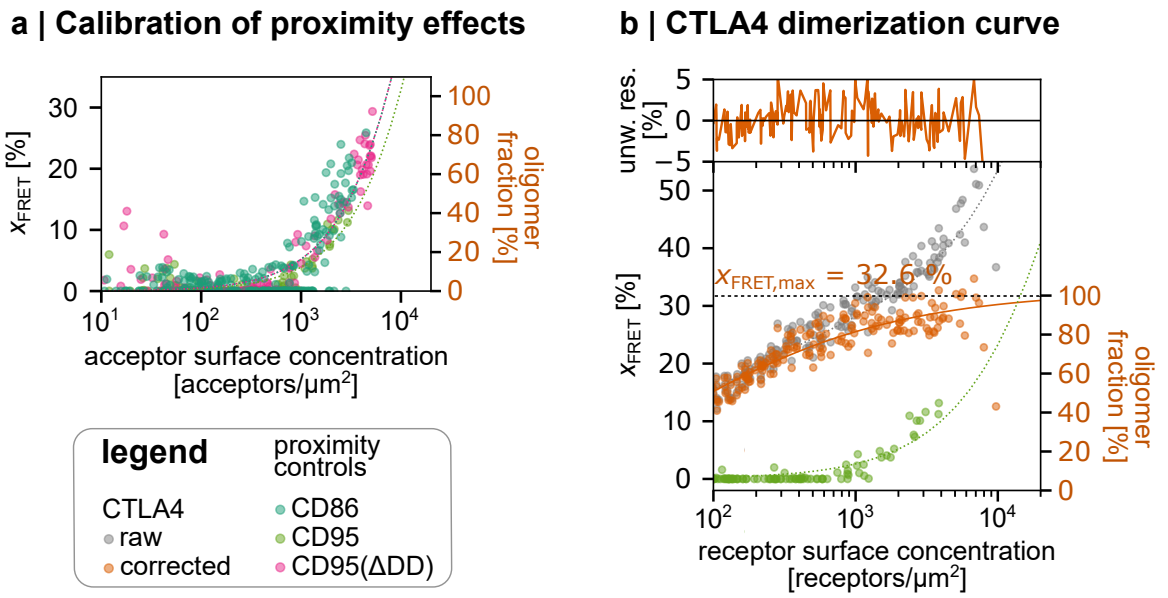

Figure 9.11: Proximity FRET correction and CTLA4 dimerization. a | Proximity calibration of the three different monomer controls: CD86, CD95, CD95(ΔDD) (compare Methods Chapter 5.6.3). Dashed lines illustrate the proximity fits. The proximity effect gets dominant with acceptor surface concentrations $> 10^3$ receptors/µm². **b |** CTLA4 dimerization: x_{FRET} increases with a cell's receptor surface concentration. The raw data (grey) can be corrected (orange) for proximity FRET using a monomer control (green) and fitted with a K_{D}. The FRET fraction can be translated into an oligomer fraction (32.6 %x_{FRET} = 100 % oligomers).

IV

Discussion & Conclusion

10 Advanced Molecular-Sensitive Imaging Unravels CD95 Receptor Activation

10.1 A Minimal Model of CD95 Signal Initiation

Here, we quantify CD95 oligomerization in live cells and prior to ligand induction find receptors to be monomeric and homogeneously distributed on the cell plasma membrane. In previous studies TNFRs (including CD95) were reported to appear as monomers, dimers or trimers in the absence of a stimulus [55, 152]. Interestingly, several works using receptors expressed from E.coli or mammalian cells, purified and reconcentrated (e.g. $\sim 0.5\,{}^{\mathrm{mg}}/_{\mathrm{ml}}$ [56]) and analyzed by gel filtration, western blot or crystallography, report receptor pre-ligand dimer- and mostly trimerization [17, 18, 55]. In three further studies based on crystallography and NMR spectroscopy, CD95 was suggested to form higher oligomeric structures of penta- or hexagonal shape (Figure 1.3). In contrast to these biochemical approaches, molecular sensitive imaging of receptors directly in the cell's plasma membrane revealed only monomer and dimer formation [108, 152]. Our data confirms the latter results and indicates that the situation in the native membrane environment with small or no oligomers developing is significantly different from the purified receptor case (compare Figure 10.1a).

After ligand addition, we find dimers and trimers forming within the first $2-3\,$hours with a final fraction of 6-15 % of receptors exhibiting oligomerization. Interestingly, the majority of previous studies report CD95 and other TNFRs to be trimeric after ligand addition with few additional works suggesting larger receptor accumulations. Among these, molecular sensitive techniques, such as crystallography, single molecule localization microscopy, and biochemical receptor cross-linking studies favor the trimeric state [8, 16, 58, 152, 153]. Molecular clustering was reported using widefield fluorescence microscopy, albeit without specifying molecular numbers of their localization or interaction [1, 152, 154]. Since in this context rigorous quantification of molecular numbers is important but was hitherto difficult, we here provide a generic strategy to address

the associated challenges. Hence, it would be interesting to reconsider cases where molecular clustering was observed in the native membrane environment and to test for the appearance of molecular interactions and complex formation beyond trimers versus their mere accumulation.

From a structural point of view, three different intermolecular interactions are currently discussed to give rise to TNFR signaling-active oligomerization and to explain the reported observations: (i) the direct coupling of up to three receptors to the ligand, without the need of intermolecular interactions between receptors, (ii) interactions between CD95 transmembrane domains after ligand activation [64], and (iii) intracellular crosslinking of two CD95 DDs via FADD [51] (compare Chapter 1.2.4). Cases (i) and (ii) would result in close packing of CD95 receptors with few nm intermolecular spacing around the ligand up to a trimer-trimer configuration [20]. Case (iii) suggests that recruitment of FADD and interaction with the DD results in crosslinking of two DDs. When crosslinking occurs between different trimer-trimer units, a higher oligomeric hexagonal structure develops, placing the receptors $\sim 12\,\mathrm{nm}$ apart (with exact values differing between TNFRs) [10, 51, 52, 68]. However, DD-FADD interaction was shown to be weak and may not occur at low CD95 and FADD concentrations [51]. This may explain the appearance of higher oligomeric structures only for purified and typically reconcentrated CD95 and FADD [68]. Moreover, as shown in our study, full length CD95 exhibited near identical oligomerization behavior compared to DD truncated receptors, demonstrating that oligomerization and potentially efficient signaling is possible in the absence of DD-DD crosslinking. CD95 dimer/trimer formation is hence realized via direct ligand (i) or ligand-induced transmembrane (ii) interactions.

As pointed out, the difference in oligomeric states found in case of purified receptors relative to cell membrane samples underscore the importance of the physical and molecular environment in which CD95 is measured. This is not surprising, as already molecular mobility and consequently any interaction probability is highly different in purified samples compared to CD95 embedded in the cellular plasma membrane (e.g. protein membrane diffusion of $D \sim 0.2\,\mu\mathrm{m}^2/\mathrm{s}$ versus protein diffusion in solution $D \sim 50\,\mu\mathrm{m}^2/\mathrm{s}$ [145]). More importantly, molecular concentration will influence the oligomerization state, which in case of the purified samples was reported to be rather high with $\sim 100\,\mu\mathrm{M}$ [51]. In cell lines, we determined molecular expressions to $10 - 2000\,\mathrm{receptors}/\mu\mathrm{m}^2$, the lower limit marking the typical physiological expression level. Despite this broad range of concentration covered in live cells, our data did not show any signature of higher oligomer formation, suggesting that concentrations are still too low to observe hexagonal network formation. Indeed, previous *in vitro* studies of purified TRAIL coupling to Death Receptors 4 and 5 showed that molecular

stoichiometries in the formed complex would only change upon increasing molecular concentrations by $3-4$ orders of magnitude from nM to $1-10\,\mu M$ [71]. Thus, higher oligomerization states may only develop at elevated CD95 receptor concentrations or may require a different cell membrane environment [71]. The type of oligomerization may also depend on the TNFR and ligand chosen.

While no significant changes in receptor oligomer stoichiometries are detected, there is a remarkable change in signaling dynamics and the percentage of apoptosis events depending on the absolute ligand and receptor number. Here, as well as in previous studies [1, 155], using different cell types and CD95 expression levels between 5000 and $450\,000\,{}^{\text{receptors}}/_{\text{cell}}$, a significant acceleration of downstream signaling and systematic increase of apoptosis events with increasing receptor or ligand concentration was shown. Hence, tuning the absolute number of activated receptors turns out to be a crucial aspect of apoptosis signal initiation.

Overall, our data provides evidence for a minimal model of CD95 as introduced in Chapter 1.2.4 (compare Figure 1.3) with an immediate, unamplified transduction of the signal on membrane level. The model is valid independent of the surface receptor concentration for the here probed concentration range from physiological expression levels up to $2000\,{}^{\text{receptors}}/_{\mu\text{m}^2}$. Figure 10.1b illustrates our findings. While there is no amplification of the signal on the plasma membrane, the absolute number of activated receptors is still crucial for the signaling outcome. This effect might be promoted by an intracellular signal amplification independent of CD95 oligomerization, as chain-like DED/DED interactions have been shown to recruit over-stoichiometric amounts of caspases in the DISC [156–159].

Our investigations mapping the CD95 oligomerization in sub-cellular membrane compartments showed that ligand-induced CD95 oligomerization occurs over the entire membrane, indicating that signaling can presumably be induced from all membrane areas. Only a slightly higher oligomer fraction was found in the areas of high brightness compared to lower brightness regions (about 2-3 %). While the cellular mechanism to create high brightness membrane areas remains elusive as they were not part of this study, we conclude that the bright areas are not higher oligomeric states, but simply locally elevated concentrations, ubiquitous to all membrane receptors including CD86 and CTLA4. The detected slightly enhanced oligomer fractions in high brightness areas may be explained by concentration-induced enhanced binding kinetics. This result points against a necessary translocation of stimulated CD95 into lipid rafts to trigger signal initiation, which consistently appeared to be the major site of DISC formation, as proposed by Eramo et al. [74]. One possible explanation for our result is, that HeLa were categorized as type II cells [36, 37], which overall exhibit less DISC formation [31]

compared to type I cells. Further, it has been proposed, that membrane-bound CD95L is superior to soluble CD95L, as used here, in triggering CD95 lipid raft translocation [73].

To provide the above insights, six techniques including super-resolution and multiparametric fluorescence imaging were used and advanced to record data with single molecule precision. Parallelized measurements using techniques of complementary sensitivity (in terms of spatio-temporal resolution and molecular concentration detection) allowed monitoring a high dynamic range (µs to hours, nm - 100 µm scales, $1 - 10^4$ $^{\text{molecules}}/_{\mu\text{m}^2}$) and to increase data reliability using high statistics to probe the biological variability. In particular, we established quantitative spot analysis of STED data, verified receptor mobility with FCS, and determined CD95 stoichiometries in fluorescent spots from PBSA. In case of the latter, mEGFP fluorescence labeling as well as confocal instead of TIRF imaging was established, making PBSA measurements applicable to common biological samples and more flexible in space, respectively. In case of time-resolved FRET, we apply a new method demonstrating its sensitivity to very small oligomer fractions and enable monitoring of oligomerization kinetics during signal initiation and transduction (more details in Chapter 10.2). Finally, benchmarking CD95 data against robust monomer and dimer controls revealed, that intense regions on the membrane initially associated with higher oligomerization states simply arise from concentration fluctuations and higher local monomers, dimers and trimer concentration across the membrane.

To our knowledge, this study is the first to report a minimal model of CD95 signal initiation identifying 6-15 % CD95 monomers oligomerizing to dimers and trimers as efficient apoptosis signal inducers in live cells (Figure 10.1b). Our results do not exclude the existence of proposed higher order oligomeric states, but confirm that they are not necessary. In this context, our study highlights the importance of molecular concentration level determination as well as the use of high-fidelity monomer and dimer controls for quantitative molecular imaging.

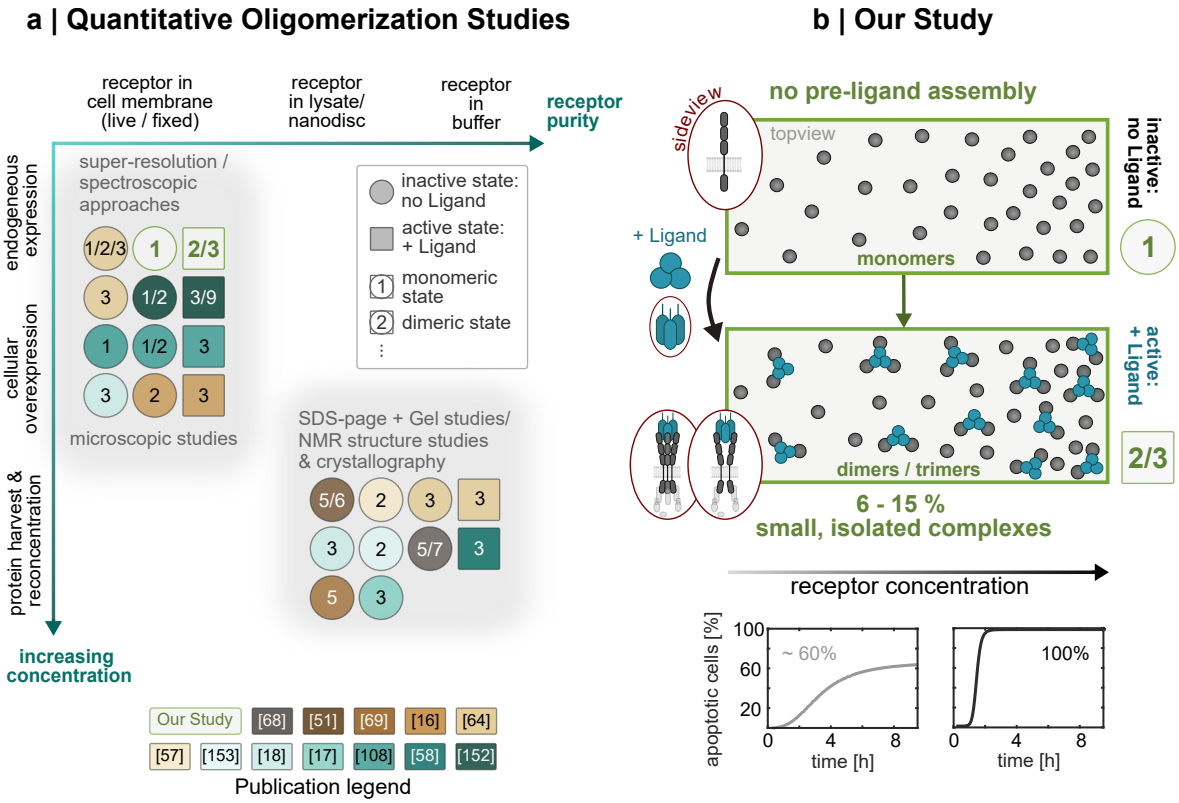

Figure 10.1: Unraveled CD95 oligomerization states. a | Summary of studies on quantitative TNFR oligomerization in context of the measurement parameters receptor concentration and receptor environment for the respective applied measurement technique. Boxed numbers show the measured oligomerization grade. Publication legend numbers correspond to references in the Bibliography of this thesis. No claim to completeness. **b |** Schematic illustration of the here verified model of CD95 signal initiation: 6-15 % of monomeric receptors (no pre-ligand CD95 assembly) form small, isolated complexes after ligand binding. Increasing receptor concentrations (surface expression level) do not lead to a higher fraction of oligomers. As an increased receptor concentration does cause a higher fraction of apoptotic cells, the absolute number of active, oligomerized CD95 receptors must be the decisive parameter.

10.2 A New FRET Methodology to Unlock Sensitive Molecular Switches in Cells

In the process of elucidating the CD95 signal initiation, we advanced the technique of FRET-sensitized fluorescence donor decay to a degree that accomplishes the resolution of highly sensitive changes of molecular interactions inside living cells. In conclusion, it paves the way for advanced oligomerization studies by

1. providing the architecture to obtain large datasets of single-cell data over time,
2. presenting a reliable approach to translate image intensities into absolute membrane protein surface concentrations,
3. providing proximity FRET correction at high concentration levels,
4. determining the sample-specific maximal FRET signal, $x_{\mathrm{FRET,max}}$, and
5. measuring oligomer concentrations down to 1 % precision in live cells at endogenous expression levels.

Using our FRET methodology with the feature to record large datasets and scan a broad range of conditions, such as the cell surface expression level, we are able to uncover and quantify effects a conventional FRET approach would be blind for: crowding-related (proximity) FRET signals as well as the dimerization constant of CTLA4.
For the calibration of proximity FRET effects, our experimental data shows excellent consistency and highlights that our CD86, CD95(ΔDD) and CD95 constructs are well suited to correct for proximity effects at high molecular densities in membranes.
Further, our FRET method is the first to measure the concentration dependent dimerization of CTLA4. Early biochemical studies relied on Western Blot analysis of purified protein constructs, reporting a dimeric state at high concentrations ($\sim 2\,{}^{\mathrm{mg}}/_{\mathrm{ml}}$) [160, 161] or predominantly dimeric state ($89 \pm 13\,\%$) at an unknown concentration [162]. An earlier FRET study [163] increases the total CTLA4 concentration by additional acceptor expression. Within the accuracy of their results, the resulting increase in FRET is attributed completely to an increase of acceptor-donor ratio, although comparison to our results show that it is also consistent with concentration-dependent dimerization. A recent STORM (Stochastic Optical Reconstruction Microscopy) based approach [111] yielded the average fluorophore number in a cluster of 1.93, or 93 % dimers and 7 % monomers, although they only measured at a single concentration. Note that our cells do not express CTLA4 or any of its interaction partners (CD28, CD80) natively[2] [115]. Summarizing our CTLA4 results, we conclude that we observe a transition because we can measure at a wide range of concentrations for the first time,

whereas most previous studies [160–162] found dimers as measurements were performed at high concentrations. Our results shed new light on the interaction mechanisms of CTLA4 and underlines the importance of measuring the oligomeric state at different concentration levels.

The proximity correction brings us in the advantageous position of verifying our result from AV simulation against the CTLA4 protein. From the concentration dependency of CTLA4 and after including proximity FRET corrections, we are able to obtain the steady-state FRET fraction at high receptor concentrations corresponding to a pure dimer sample, yielding 32.5 % x_{FRET}. This is corresponding closely to the 31 % predicted by AV simulations in consideration of the donor-acceptor ratio.

Notable synergies for future improvements lie in the inclusion of the FRET rate, k_{FRET}. Although our analysis obtains k_{FRET} from the lifetime decay, it is used conservatively as the count-rate dependent shift in our detectors block accurate interpretation of k_{FRET}, but not of x_{FRET}. Hence, a change in detectors or a strategy to overcome this effect has the potential to resolve the oligomeric states of protein complexes. Furthermore, the cells could be studied even closer to endogenous conditions by the use of stable cell lines instead of transient transfections, which encode the fluorescently labeled target proteins directly in their DNA. Lastly, the analysis complexity could be reduced for homotypical interaction by measuring the reduction in fluorescence anisotropy due to homo-FRET [97, 164].

Overall, we believe our newly developed FRET methodology is highly relevant for other research fields as it can be applied with commonly available prerequisites: fluorescent protein labeled biomolecules are a cornerstone of biomolecular research and thus are ubiquitously available. Two-color confocal instruments with photon arrival time read-out (TCSPC) are commercially available and commonly found in imaging facilities. Due to its measurement precision, biocompatibility, ease of implementation and particularly its relevance for a large class of problems, we expect that the method can have a large impact on the study of the molecular interactions and oligomerizations.

V

Excursion: Microscopic Visualization and Quantification of CAR-Killing

11 Introduction

11.1 The Immune System and Cancer

The immune system is a complex network of processes with the purpose to defend the body against infections and diseases, maintained by a variety of different cells and proteins. One large class of cells in the immune system are the lymphocytes, which can be categorized into T-cells, B-cells and NK (natural killer) cells. Other cell classes involved in the immune defense are for example granulocytes and macrophages.

Together with B-cells, T-cells determine the specificity of immune response to antigens. T-cells are characterized by the presence of a T-cell receptor (TCR) on their cell surface, which can detect and bind foreign antigens. One requirement for the recognition of these antigens, is their presentation by molecules of the major histocompatibility complex (MHC), which "hold" the antigen peptide on the antigen-presenting cell (ApC) [165]. For humans, the MHC is also called human leukocyte antigen complex (HLA). The binding between TCR and antigen-MHC, is the first step of T-cell activation. Next, the cytoplasmic domains of the TCR-affiliated CD3-complex transduces the signal via phosphorylation of immunoreceptor tyrosine-based activation motifs (ITAMs) and initiates further signaling cascades for T-cell proliferation and differentiation.
In addition to the TCR activation, T-cells need two additional signals to be fully activated. One being the co-stimulation from receptors such as CD28 that similarly bind to B7-molecules on the ApC [166]. Via TCR and co-stimulary connections, the T-cell can form an immunological synapse allowing it to stay in contact with the antigen presenting cell. The third activation signal is provided by cytokines, which stimulate the final T-cell differentiation towards an effector T-cell which is finally able to induce the apoptosis of the target cell, for example via perforin and granzyme B release. This complex activation process ensures the specific response to harmful pathogens and not to self-antigens.

Cancer, as one of the most severe diseases of the world, has the ability to hide from cells of the immune system, and by this can manifest in the body if the autologous immune system fails. One of the mechanisms, tumor cells use to escape the hosts

immune response, is the downregulation of MHC class I molecules on their cell surface [167]. Other mechanisms are for example the recruitment of immunosuppressive cells or the misuse of so-called "immune checkpoints" whose original task is to maintain self-tolerance [168, 169]. One prominent checkpoint example inhibiting the T-cell activation is CTLA4, which competes with CD28 for the same binding partners on the ApC. Additionally, tumor cells originate from the hosts healthy cells and therefore share a majority of "self-antigens" with these healthy cells. Nevertheless, the mutations during tumor development can lead to the overexpression of certain antigens or the expression of novel tumor specific antigens.

To address and overcome the survival strategies of tumor cells in cancer therapy, there are various approaches aiming to manipulate the host immune system in order to enhance its natural ability to fight malignancies and treat cancer successfully. One approach of cancer immunotherapy that targets the specific tumor antigens is the so-called Chimeric Antigen Receptors (CARs).

11.2 Chimeric Antigen Receptors (CARs)

CAR T-cell therapy is the result of several decades of T-cell engineering. Here, the ability of a monoclonal antibody to detect a specific antigen and the activation pathway of the T-cells are combined within one molecule. The specific antigen-recognition enables to recognize the target antigen of the maligned cell without the presence of the MHC and to kill the tumor cell in an MHC-independent manner.

11.2.1 Structure and Function of CAR T-cells

The structure of an artificially designed CAR construct is generally composed of a extracellular antigen-binding domain, a hinge (or spacer) region, a transmembrane (TM) domain and an intracellular signaling domain.
The antigen-binding domain is designed with a single-chain variable fragment (scFv), comprised of a flexibly linked heavy and light chain and derived from a monoclonal antibody. Ideally, it is chosen to detect the epitope of a specific tumor-associated antigen with a suitable affinity [170].
The main task of hinge and TM-domain is the connection of the extra- and intracellular domain. For the hinge, the selection criteria are length and flexibility in order to avoid steric hindrance when the binding domain connects to its cognate antigen [171]. The transmembrane section has to provide stability to anchor the molecule in the T-cell membrane. A common TM-domain used in CARs is the TM-domain of the CD28

receptor [171, 172].

The intracellular signaling domain was adapted over four generations of CARs. Initially used was the cytoplasmic CD3ζ domain of the original T-cell receptor complex that carries three ITAMs. Since the second, and more successful, generation CARs, this section was extended with a co-stimulatory domain like CD28 or CD134 (also known as 4-1BB) for stronger activation [171].

Figure 11.1 illustrates the structure and function of a 2nd generation CAR.

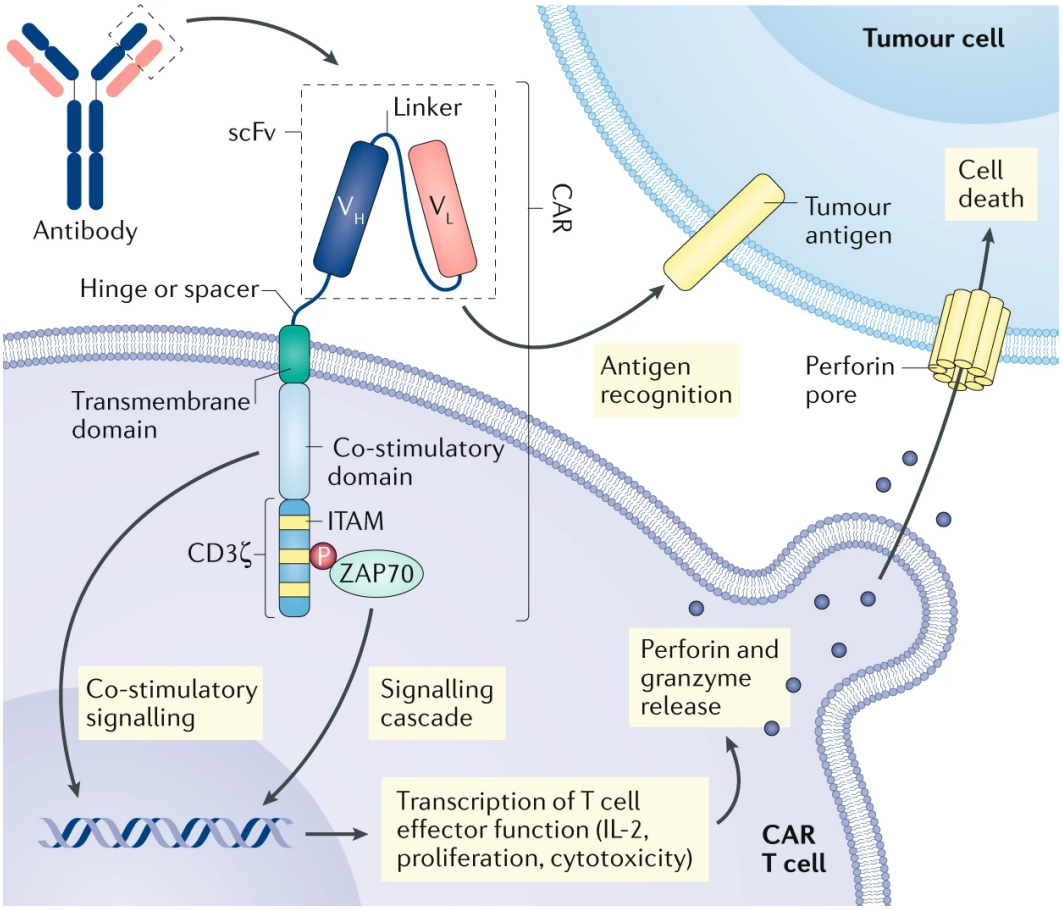

Figure 11.1: Schematic structure and function of a 2nd generation CAR T-cell. The extracellular portion of the chimeric antigen receptor (CAR) is typically generated from a monoclonal antibody against the target. The hinge (or spacer) region anchors the scFv to the transmembrane region that traverses the cell membrane. Intracellularly, the co-stimulatory domain and CD3ζ chain signal once the scFv domain recognizes and binds a tumour antigen. Downstream signaling initiates T-cell effector functions including release of perforin and granzyme, leading to cell death of the target tumor cell. More details in main text. IL-2 = Interleukin 2. (Illustration from Larson et al., 2021 [171].)

The 3rd and 4th generation of CARs are characterized by further developments towards even more effective therapy. Due to their more recent development, they have not yet been tested extensively in research and clinical trials [173, 174].

The 3rd generation is equipped with a second co-stimulatory domain, in addition to the CD28 intracellular part [175]. The 4th generation CARs (also referred to as TRUCKs for T-cells redirected for universal cytokine killing) feature the enhancement of additional cytokine production in order to improve T-cell persistence solid tumors [176].

The functionality of CAR T-cells is similar to the natural T-cell activation via the TCR (Figure 11.1): scFv recognition of the antigen causes clustering and immobilization of the CAR molecules (immunological synapse). Once the tumor antigen is bound, the CD3ζ and the co-stimulatory domain signal and activate the respective signaling pathways. Eventually, a T-cell effector response including proliferation and release of cytokines is unleashed. The cytotoxic function of CAR T-cells is mainly obtained by the secretion of perforin that penetrates the tumor cell surface enabling the entrance of apoptosis inducing granzyme B into the malign cell. There are studies suggesting, that also death receptor-induced pathways including the CD95-CD95L interaction, are utilized to mediate tumor killing after CAR activation [177–179].

11.2.2 Manufacturing and Clinical Use of Adoptive T-cell Therapy

For clinical applications, the CAR T-cells are derived from the patient's autologous T-cells via blood sampling and *in vitro* introduction of the CARs. This avoids issues like rejection of allogenic cells and Graft-versus-host disease[3] (GvHD) but requires expensive individual manufacturing. Prior to adoptive T-cell therapy but after the blood sampling, preparative chemotherapy is used to facilitate a receptive environment for the CAR T-cells by so-called lymphodepletion.
After their extraction, the T-cells are expanded *in vitro* to therapeutic numbers using TCR triggering or cytokine stimulation. Subsequent to the expansion, the T-cells are equipped with the CAR, typically via lentiviral or retroviral gene transfer of the CAR genome into the T-cell DNA. Ultimately, the engineered CAR T-cells are reinfused into the patient's blood circulation via the peripheral veins where they can engage in the elimination of target-antigen expressing cells. The typical dosing of CAR T-cells is a single to only few doses.

The major clinical breakthroughs using CAR therapy in recent years have been achieved for refractory or relapsed acute lymphoblastic leukemia (ALL) and diffuse large B-cell lymphoma targeting CD19, CD20 or CD22 [171]. As those are specific B-cell antigens, this results in the elimination of malignant and also normal B-cells.

[3] A condition that can occur after allogeneic transplant. If donor T-cells (the graft) recognize the host as foreign, a donor cell attack of the host body can be initiated.

The success of adoptive T-cell therapy for solid tumors is more challenging as it already depends on a multitude of different parameters which are even more diverse for the large phenotypic heterogeneity of solid tumors. Hence, development and study of CARs with novel and specific target antigens and structures are of great interest.
Besides being successfully established for the respective tumor cells, CAR T-cell therapy can induce side-effects, such as off-target and off-tumor toxicities or even might face resistance, either in an antigen-dependent or antigen-independent manner.

Apart from the great clinical successes that were achieved with CAR T-cell therapy over the past year, there are ongoing challenges and various approaches like novel engineering and pharmaceutical interventions to overcome these. One engineering approach that goes beyond conventional CAR T-cells is the use of natural killer (NK) cells. As NK cells can be transplanted across HLA (MHC) barriers without causing GvHD, they would present a great asset in CAR therapy. With allogenic CAR NK cells, one could achieve significantly shorter manufacturing periods and thus reduced costs with cells obtained from healthy donors . This would allow *off-the-shelf* usage of pre-manufactured products [180]. However, the CAR NK cell therapy development is clearly lagging behind and entails other problems like the comparably low transduction rates and the challenges in the large-scale genetic engineering of primary human NK cells [181]. Solving these issues is subject of current research.

11.2.3 Benefits and Challenges of CAR T-cell Activity Microscopy and Image Analysis

Microscopy is a powerful tool in science with a wide range of applications. Especially in cell biology and medicine, it can contribute to uncover the secrets of our cells, from studying their basic mechanisms to understanding the processes underlying diseases, as well as testing their reaction to potential therapies. Compared to other biological techniques and assays, it enables to see the process within or among cells by eye rather than determine them by other parameters. By this, microscopy provides spatial information and in combination with a time-lapse option, it gives access to the full spectrum of spatio-temporal information of the studied mechanisms. This benefit of microscopy is extremely useful as it enables to identify time points of important events and dynamics of functional processes – for example CAR T-cell activities - precisely. In the context of clinical therapies, this is particularly useful for an assessment of when to expect first reactions in the *in vivo* situation or when the best time point for transfer of transduced cells would be. Further, microscopy studies facilitate direct comparisons and competition assays of different experimental parameters. For example using spa-

tially separated co-cultures of different cancer cells would enable a direct comparison of T-cell interaction preferences. This is a rare feature not many techniques provide.
Besides the spatio-temporal resolution of microscopy, it also features the ability to resolve single-cell effects. Most (pre-)clinical research studies are bulk approaches, which average out subpopulations which may be interesting to look at. Microscopy can uncover such effects while still providing relatively high statistics thanks to modern acquisition automation.
To exploit the mentioned benefits of microscopic imaging requires a careful experimental design as well as a matching microscope setup.

The studies on CD95 illustrated how complex and versatile the different microscopic applications can be (compare Chapter 5). Multiparametric image microscopic and spectroscopic techniques enable to investigate small molecules like proteins that are actually too small to be seen (resolved), even with super-resolution techniques. In spite of the great features of these advanced techniques, sometimes they do not provide the specifics to investigate a particular biological system of interest.

For the microscopic observation of the characteristics of CAR T-cell induced killing of tumor cells, the technique of choice is widefield microscopy. As introduced in Chapter 5.1, widefield microscopes enable the combination of brightfield and fluorescence contrast techniques. In addition, video recording of multiple positions within a sample is faster and causes less light-induced cell toxicity compared to confocal systems with laser scanning.

These advantages are of great interest for the live cell imaging of CAR T-cell activity. T-cells are with approximately 10 µm diameter rather small compared to most adherent cell lines. To show their tumor killing ability, they have to be co-cultured with the tumor cell line during the microscopic recoding. The tumor cell line of interest can be either adherent or in suspension, while the nature of T-cells is a suspension. For these small and agile suspension cells, camera imaging is favored over area scanning. If both entities are suspension cell lines, it can be challenging to distinguish the two cell types from each other in brightfield mode. This requires the fluorescent staining of at least one of them. Depending on the specific research question, additional fluorescent markers are needed in order to visualize certain proteins or processes. For example, CARs can be stained with antibodies against the hinge region and apoptosis markers can help to detect successful killing if the cells do not distinctly show the common apoptosis morphology (shrinking and blebbing). Consequently, these experiments can require multiple cell staining and multi-channel imaging.
Another challenging aspect of CAR T-cell activity imaging is the time factor. Different events of interest can occur at different time points and, due to the cell agility, at

different positions. For example, the presence of an immunological synapse between T-cell and tumor cell and the resulting apoptosis (marker) signal of the tumor cell, can be minutes to hours apart. Considering the cell movement of suspension cells, even on a coated surface, the necessity of a high time sampling and multiple-position imaging to achieve conclusive image series, is evident. As a result, the cells are exposed to the light radiation frequently over a large time span. As we experienced some cell lines of interest to react quite sensitive towards light radiation, lamp-based one-shot widefield microscopy is our method of choice to overcome these challenges and accomplish high-quality CAR T-cell activity visualization.

12 Results of CAR Microscopy

The following results part includes two peer-reviewed publications and one cover image belonging to a third publication, which emerged from a close collaboration with the Department of Otorhinolaryngology, Head & Neck Surgery of the Heinrich Heine University, Düsseldorf and the Department of Pediatrics III of the University Children's Hospital Essen (University Duisburg-Essen).
The following projects belong to the main research field of our two collaboration partners. Hence, the conceptual ideas and project supervision as well as conceiving and planning of the main experiments were on their side, while it was our input to contribute with expertise in microscopy. My own contribution is assessed for each part towards experimental design, performing of measurements, data analysis and writing the manuscript of the microscopic research.

12.1 CD44v6-targeted CAR T-cells specifically eliminate CD44 isoform 6 expressing head/neck squamous cell CARcinoma cells

Journal: Oral Oncology | May 2021 | Volume 116 | Article 105259 | [182]

Authors: Corinna Haist, Elena Schulte, Nina Bartels, Arthur Bister, Zoe Poschinski, Tabea C. Ibach, Katja Geipel, Constanze Wiek, Martin Wagenmann, Cornelia Monzel, Kathrin Scheckenbach and Helmut Hanenberg

Contribution: My contribution to this study is the careful planning and execution of the time-lapse microscopy experiments including sample preparation as well as the detailed analysis and interpretation of the data, the design and writing of the respective manuscript figure and method section, and, together with the co-authors, the revision of the manuscript.

Oral Oncology 116 (2021) 105259

Contents lists available at ScienceDirect

Oral Oncology

journal homepage: www.elsevier.com/locate/oraloncology

CD44v6-targeted CAR T-cells specifically eliminate CD44 isoform 6 expressing head/neck squamous cell carcinoma cells

Corinna Haist [a,b], Elena Schulte [a], Nina Bartels [c], Arthur Bister [a,b], Zoe Poschinski [a], Tabea C. Ibach [a], Katja Geipel [a], Constanze Wiek [a], Martin Wagenmann [a], Cornelia Monzel [c], Kathrin Scheckenbach [a,1,*], Helmut Hanenberg [a,b,1,*]

[a] Department of Otorhinolaryngology, Head & Neck Surgery, Heinrich Heine University, Düsseldorf, Germany
[b] Department of Pediatrics III, University Children's Hospital, University of Duisburg-Essen, Essen, Germany
[c] Department of Experimental Medical Physics, Heinrich Heine University, Düsseldorf, Germany

ARTICLE INFO

Keywords:
Immunotherapy
Solid tumor
Chimeric antigen receptor
T-cell
CD44v6
HNSCC

ABSTRACT

Immune checkpoint blockade can cause regression of recurrent and/or refractory head and neck squamous cell carcinoma (HNSCC). As a second type of immunotherapy, adoptive cellular therapy with genetically modified patient's T-cells redirected against the autologous malignant cells by expressing chimeric antigen receptors (CARs) recognizing tumor-associated antigens has been established as highly efficient personalized treatment for hematological malignancies. In solid cancers however, the application of these genetically modified immune effector cells still lacks equal response rates. CD44v6 is an isoform of the hyaluronic receptor CD44 that is almost exclusively expressed at high levels on solid cancers and has been associated with tumorigenesis, tumor cell invasion and metastasis. Here, we established a highly specific CAR against CD44v6 on HNSCC cells that can be expressed on normal T-cells with lentiviral vectors. Using primary human HNSCC cells in combination with CRISPR/Cas9 and overexpression approaches allowed us to confirm the high specificity of our CAR construct for the tumor-associated CD44v6 as target antigen and to demonstrate a direct correlation between CD44v6 expression levels and cytotoxicity of the CAR T-cells. Importantly, the design of our clinically applicable lentiviral vector facilitates to co-express a second transgene for *in vivo* control of CAR T-cells, if undesired side-effects or toxicities occur.

Introduction

More than 600,000 patients are annually diagnosed with head and neck squamous cell carcinoma (HNSCC), making HNSCC the 6th most frequent cancer worldwide [1,2]. Multimodal treatment approaches for HNSCC include surgery, platinum-based chemotherapy and radiation [3], however only result in five-year survival rates of approximately 50%, due to high metastasis and recurrence rates [4]. In 2006, the EGF receptor antibody Cetuximab was approved as the first targeted immunotherapy for HNSCC, either as single agent after cisplatin-based therapy or in combination with radiation [5]. While no other specific targeting reagent proved to be clinically effective for HNSCC patients, the antibodies Nivolumab [6,7] and Pembrolizumab [8] as general immune checkpoint inhibitors directed against PD-1 were recently introduced for the treatment of HNSCC for 1st and 2nd line treatment in metastatic and/or recurrent disease.

Chimeric antigen receptors (CARs) are another option to direct autologous immune effector cells against antigens expressed on the surface of malignant cells. CARs are synthetic molecules that combine a single chain variable fragment (scFv), derived from a monoclonal antibody, with cytoplasmatic T-cell activation motifs from the zeta-chain of CD3 and co-stimulatory domains in a single molecule [9]. Expression of CARs on immune cells results in highly efficient recognition and killing of any antigen positive cell in an HLA independent manner [10]. While major clinical breakthroughs have been achieved in recent years for refractory or relapsed acute lymphoblastic leukemia (ALL) and diffuse

* Corresponding authors at: Department of Pediatrics III, University Children's Hospital Essen, University of Duisburg-Essen, Hufelandstraße 55, 45122 Essen, Germany (H. Hanenberg). Department of Otorhinolaryngology, Head and Neck Surgery, UKD, Heinrich Heine University, Moorenstr. 5, 40225 Düsseldorf, Germany (K. Scheckenbach).
E-mail addresses: scheckenbach@med.uni-duesseldorf.de (K. Scheckenbach), Helmut.Hanenberg@uk-essen.de (H. Hanenberg).
[1] contributed equally

https://doi.org/10.1016/j.oraloncology.2021.105259
Received 5 December 2020; Received in revised form 4 February 2021; Accepted 28 February 2021
Available online 22 April 2021
1368-8375/

large B-cell lymphoma using the patient's autologous T-cells equipped with CARs against CD19 or CD20 [11,12], the establishment of CAR T-cell therapy for solid tumors is more challenging [13]. For HNSCCs, only a handful of target antigens have been described as potential CAR candidates, including EGFR, HER2neu/ERBB2 and a specific variant of CD44 [11,12,14].

CD44 is a cell surface glycoprotein, that serves as hyaluronic acid receptor and is involved in tumor growth, differentiation and metastasis [15]. Alternative splicing of the *CD44* gene leads to nineteen CD44 isoforms with different variant exons between the constant upstream (exons 1–5) and down-stream (exons 16–20) regions [16]. The smallest isoform is CD44s, which lacks all variant exons. CD44v6 additionally translates exon 11 [15] and is abundantly expressed on various malignancies including squamous cell carcinomas of the head and neck, lung, skin, cervix and esophagus as well as breast, gastrointestinal, hepatocellular and colorectal cancers and some subtypes of acute myeloid leukemias (AML) [11,15,16]. In normal tissues, CD44v6 is expressed on keratinocytes in the skin and oral mucosa and on cells of the monocytic lineage [17,18]. Experimental studies revealed that expression of CD44v6 on tumors cells is directly associated with tumor progression and metastatic potential [19] and that administration of CD44v6 monoclonal antibodies inhibits the formation of metastases [20]. Clinically, patients with CD44v6 positive tumors experienced more aggressive tumors with reduced overall survival [21,22].

To immunologically target CD44v6 in humans, murine monoclonal antibodies were used that bind to overlapping epitopes encoded by exon 11 of CD44 [16,17]. In clinical phase I/II studies, administration of these antibodies labeled with radionucleotides demonstrated highly tumor-specific uptake of the antibodies but only limited tumor responses were achieved [23,24]. As the murine antibodies led to allergic reactions in patients, humanized derivatives were developed, among them BIWA4 (bivatuzumab) with medium affinity and BIWA8 with high affinity for CD44v6 [25]. To date, numerous studies have been conducted with bivatuzumab conjugated to radionuclides [26] or to mertansine, an anti-microtubule agent [27,28]. While the combination with radionuclides showed no severe side effects and at best stable disease, the administration of bivatuzumab-mertansine led to specific fatal toxicity and the closure of all bivatuzumab studies [28]. Recently however, the use of a CD44v6 CAR became the subject of clinical phase I/II studies for treatment of AML and multiple myeloma as well as solid malignancies such as breast cancer and HNSCCs.[2]

In this study, we investigated the specificity and efficiency of a BIWA8-derived high affinity CD44v6 second generation CAR against HNSCC cell lines *in vitro* as proof-of-principle for *in vivo* mouse models and ultimately for human clinical studies.

Material and methods

Cell culture

HEK293T cells were obtained from DSMZ (Braunschweig, Germany), human oral keratinocytes (HOK) from ScienCell Research Laboratories (Carlsbad, USA), dysplastic oral keratinocytes (DOK) from Merck KGaA (Darmstadt, Germany) and primary human HNSCC cell lines (UM-10B, UM-11B, UM-14C, UM-17A, UT-24A) from the University of Michigan (UM), USA, or the University of Turku (UT), Norway, respectively. All adherent cells were cultured in DMEM GlutaMAX with 10% fetal bovine serum and 1% penicillin/streptomycin (all from Thermo Fisher Scientific, Schwerte, Germany).

Lentiviral constructs and transduction

Standard lentiviral vectors were used for overexpression of CD44s and CD44v6 cDNAs [29]. The latter one was synthesized by BioCat GmbH (Heidelberg, Germany) and the CD44s spliceform generated by removing exon 11 via overlap PCR. The CD44v6 single-chain fragment variable (scFv) sequences were derived from the BIWA8 sequence [25], synthesized after optimization for human codon usage by GeneArt (Regensburg, Germany) and cloned into our CD19 CAR lentiviral vector [29]. For the CD44s and CD44v6 knockout constructs, DNA oligonucleotides for six different gRNAs were designed, synthesized by Eurofins Genomics GmbH (Ebersberg, Germany) and cloned into the lentiviral CRISPR/Cas9 vector LentiCRISPRv2 [30].

VSV-G-pseudotyped replication-deficient infectious lentiviral particles were produced in HEK293T cells [31]. Primary human T-cells were obtained from healthy volunteers, as approved by the local institutional review board/ethics committee (study #4687). After density purification, human primary T-cells were prestimulated on CD3/CD28-coated plates (OKT3, Ortho Biotech, Neuss, Germany/CD28, BD Biosciences, Heidelberg, Germany) for two days and then transduced on the fibronectin fragment CH296 (Retronectin®, Takara Bio Inc., Japan) in the presence of 100 IU/ml IL-2 [29,31]. 72–96 h after transduction, CAR T-cells were enriched by the CD34 MACS system (Miltenyi Biotec, Bergisch-Gladbach, Germany) according to the manufacturer's protocol. For overexpression of CD44s or CD44v6, $1x10^6$ cells were transduced with limiting dilutions of supernatants with lentiviral CD44s or CD44v6 expression plasmids and selected with 1 µg/ml puromycin 48 h post transduction. Lentiviral CRISPR/Cas9 vectors were used in limiting dilutions followed by puromycin selection.

Flow cytometry analysis

CD44v6 and CD44 expression was assessed on a MACSQuantX after staining $1x10^6$ HNSCC cells with the monoclonal antibodies CD44v6-PE-Vio770 antibody or CD44-APC-Vio770 (Miltenyi Biotec). To analyze the expression of the CARs on T-cells, staining was performed with a CD34-PE monoclonal antibody (QBEND/10, Thermo Fisher Scientific) and analyzed on a FACSCalibur (BD Biosciences).

Cytotoxicity assay

The cytotoxicity of CD44v6 CAR T-cells against HNSCC cells was determined by the CellTiter96® AQueous One Solution Cell Proliferation Assay (Promega, Walldorf, Germany). To this end, $2x10^4$ cells were seeded in 96-well plates and cultured overnight at 37 °C. The next day, MACS-selected CAR T-cells were added at different effector to target cell ratios. After 16 h at 37 °C, plates were washed three times to remove non-adherent T-cells and dead tumor cells, incubated with the CellTiter96® substrate according to manufacturer specifications and the number of viable cells was determined with a TECAN sunrise analyzer (Tecan Group AG, Männedorf, Switzerland). The percent lysis was calculated as

100% - (absorption of target cells incubated with T-cells/ absorption of target cellsx100).

Time lapse live video microscopy

For visualization of the interactions between CD44v6 CAR T-cells and HNSCC cells, 10^5 UM-17A cells were seeded per well of an 8-well glass bottom chamber slide (ibidi, Gräfelfing, Germany). The next day, the cells were cultured with 0.5 µl CellEvent Caspase-3/7 Green Detection Reagent in 200 µl of Leibovitz's L-15 imaging medium (both Thermo Fisher Scientific) and incubated with CD19 or CD44v6 CAR T-cells in 100 µl Leibovitz's L-15 medium supplemented with 100 IU/ml IL-2 on a temperature-controlled stage at 37 °C. Time-lapse videos were acquired with a 60x (NA 0.65–1.25) oil objective and the CellSense Dimensions Software (Olympus, Hamburg, Germany) by sequential imaging of the CellEvent marker (excitation 470/40 nm), the T-cells' mCherry red fluorescence (excitation 545/30 nm) and phase-contrast

[2] https://clinicaltrials.gov/ct2/show/NCT04097301

Table 1
Main characteristics of the cell lines used in this study.

Cell line	Sex	Type of lesion	HPV	P53	Literature
UD-01	M	Primary	–	c.96+1G>A, splice	[58–60]
UD-02	M	Primary	+	WT	[58–60]
UD-03	M	Metastasis	–	p.Q224X	[58–60]
UD-04	M	Primary	–	NT 664 del13	[58–60]
UD-05	M	Primary	–	p.H179Y	[59,60]
UD-06	M	Primary	–	p.Y220C	[59,60]
UT-02	M	Primary	–	p.C275F	[60,61]
UT-04	F	Metastasis	–	p.R248-P250del	[60–62]
UT-05	M	Primary	–	p.P151H	[60,63]
UT-06B	F	Metastasis	–	WT	[60,63,64]
UT-07	M	Metastasis	–	p.G266E	[60–62,65]
UT-09	M	Metastasis	–	deletion exon 2-9	[60,62,63]
UT-14	M	Primary	–	c.919+1G>T, splice	[60,63,65]
UT-15	M		–	c.560-1G>T, splice	[60,65–67]
UT-24A	M	Primary	–	c.673-2A>T, splice	[60,63,65–67]
UT-24B	M	Metastasis	–	c.673-2A>T, splice	[60,63,65–67]
UT-33	F		–	p.R282W	[60,65,68]
UT-34	M		–	no transcript	[60,65,68]
UT-50	M		–	c.919+59del46bp	[60,65]
UM-10A	M	Primary	–	p.G245C	[59,65,67,69,70]
UM-10B	M	Metastasis	–	p.G245C	[59,60,65,67,69,71]
UM-11B	M	Primary	–	p.C242S	[59,60,65,67,69,71]
UM-14A	F	Recurrent	–	p.R280S	[59,60,65,67,69,71]
UM-14B	F	Recurrent	–	p.R280S	[59,60,65,67,69,71]
UM-14C	F	Recurrent	–	p.R280S	[59,60,65,67,69,71]
UM-17A	F	Primary	–	WT	[59,60,65,67,69,71]
UM-17B	F	Metastasis	–	WT	[59,60,65,67,69,71]
UM-22B	F	Metastasis	–	p.Y220C	[59,60,67,69,71]
UM-74A	M	Primary	–	WT	[60,65,69]
UM-74B	M	Primary	–	WT	[60,65,69]
UM-104	/	Recurrent	+	WT	[72]

mode on an IX83 microscope system (Olympus). Frames were acquired every 5 min over 16 h at multiple positions. Image analysis was performed with the ImageJ open source software, using an intensity-based threshold to the green channel in order to detect the time of the emerging CellEvent apoptosis signals in the nuclei.

Results

CD44s and CD44v6 expression profiles of primary HNSCC cell lines

We initially employed flow cytometry to analyze the expression profiles of CD44 and its splice variant CD44v6 in 31 primary HNSCC cell lines, which were established from primary tumor lesions or from metastatic sites of human patients (Table 1). All cell lines and dysplastic human oral keratinocytes (DOK) expressed CD44 and CD44v6, while normal human oral keratinocytes (HOK) and HeLa.P3 were only positive for CD44 (Figure 1) [32]. 26 out of the 31 HNSCC lines expressed CD44 on more than 80% of cells, while only 12 cell lines showed equally high CD44v6 expression. We were unable to detect any correlation between these expression patterns and the tumor and patient characteristics (Table 1), similarly to others [33,34].

A CD44v6 CAR for efficient targeting of HNSCC cells

Our CD44v6 CAR construct with the BIWA8 scFv sequences [25], the CD28 transmembrane and cytoplasmic regions and the CD3 zeta (ς) -chain was cloned behind the T2A site into our standard lentiviral vector [29] shown in Fig. 2A. We also included a 99 amino acid stretch from the human CD34 antigen in the CAR as a hinge region (Bister *et al.* in preparation, patent EP3293199[3]). This region of CD34 is recognized by the QBEND10 monoclonal antibody and therefore can be used to detect the expression of the CAR with directly conjugated QBEND10 by flow cytometry or to enrich CAR expressing T-cells by the MACS technology (Miltenyi Biotech). As a control, we also generated a second lentiviral vector, where the CD44v6 CAR was expressed as the sole transgene off the MPSV promoter (Fig. 2A). For the bi-cistronic CD44v6 and CD19 CAR vectors, the TagBFP fluorescent protein was included as a marker gene for the detection of transduced cells in front of the T2A site [29].

Lentiviral particles were produced for the three vectors (BFP-T2A-CD19, BFP-T2A-CD44v6 and CD44v6) and used to transduce peripheral blood-derived T-cells [29,35]. Three days after transduction, 63.7 ± 0.8%, 47.7 ± 4.8% and 65.4 ± 2.4% of the T-cells expressed the three CARs, respectively (condition: pre MACS, Fig. 2B). After enriching the transduced T-cells once on standard MS columns with CD34 magnetic microbeads, the purity of strongly CAR positive T-cells in the eluates post MACS consistently reached ≥ 98%, while only 14.5 ± 1.2%, 17.8 ± 2.8% and 32.1 ± 4.2% CAR T-cells were present in the flow-through for the three lentiviral constructs BFP-T2A-CD19, BFP-T2A-CD44v6 and CD44v6, respectively (Fig. 2B).

To analyze whether the cytotoxicity of the CD44v6 CAR constructs is affected, if a second transgene is expressed via a T2A site, we incubated cells of the strongly CD44v6 expressing cell lines UM-14C and UM-10B

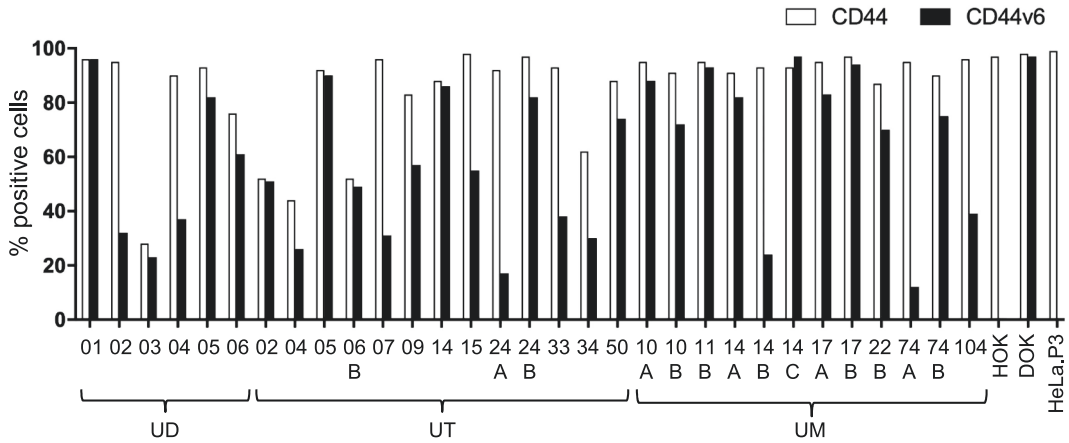

Fig. 1. Screening of CD44 and CD44v6 gene expression in primary HNSCC cell lines. Cells were stained with CD44-APC Vio 770 or CD44v6-PE Vio 770 antibodies according to manufacturer's specifications and analysed by flow cytometry. Percent positive cells (y-axis) are indicated for HNSCC cell lines and reference cells (HOK, DOK, HeLa.P3).

[3] https://data.epo.org/publication-server/rest/v1.0/publication-dates/20180314/patents/EP3293199NWA1/document.pdf

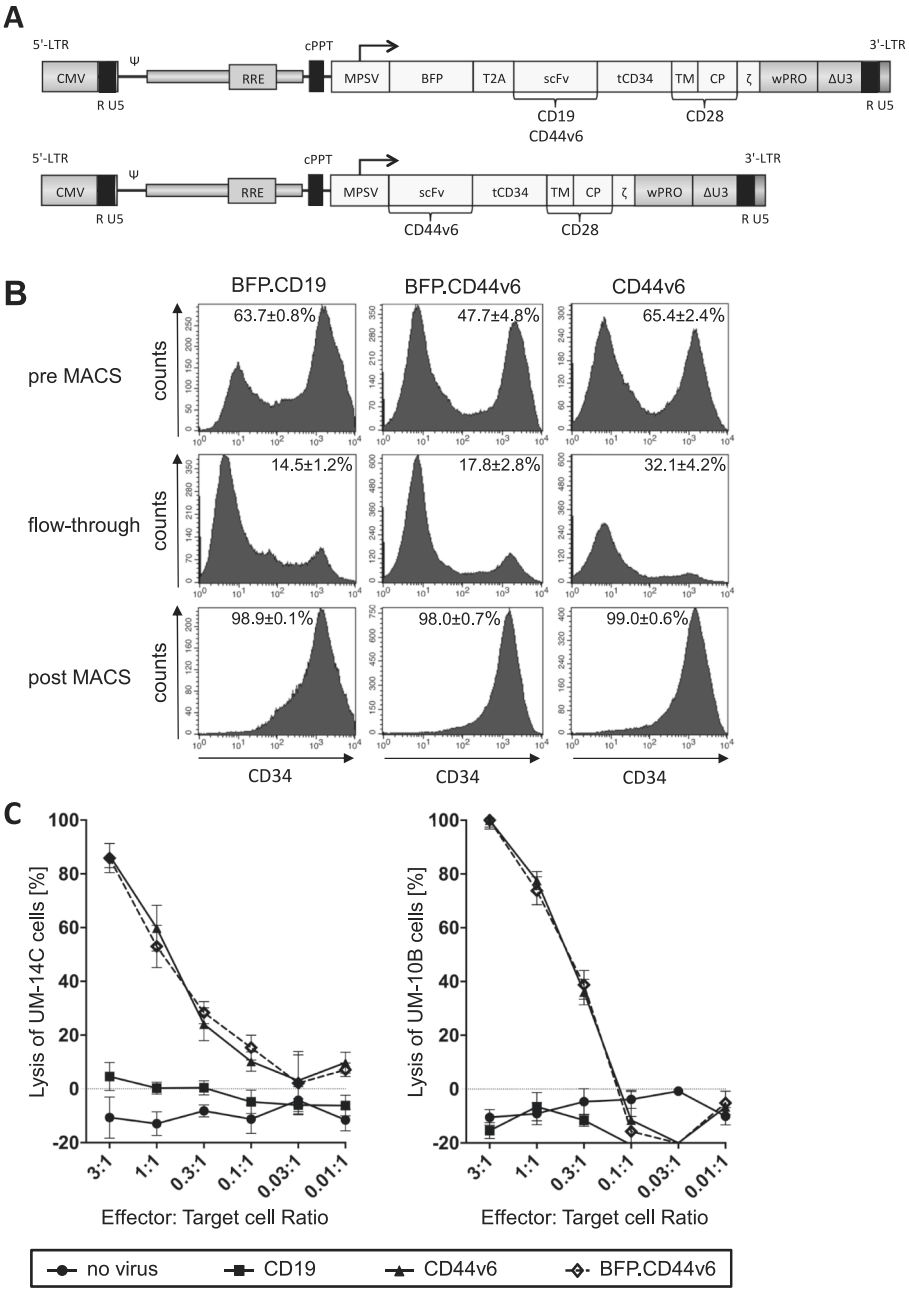

Fig. 2. Design and enrichment of CAR positive T-cells. A) Lentiviral vectors for expression of CARs. The constructs contained CD19 or CD44v6 scFvs, the CD34 hinge domain, the CD28 transmembrane and intracellular domains, and the CD3ζ cytosolic domain. BFP and T2A site were used optionally. B) Flow cytometry analyses of purification and enrichment steps via MACS system. Transduced primary T-cells were sampled for flow cytometry analysis prior to MACS separation and after MACS from the eluate as well as from the flow-through fractions. All constructs were separated with CD34 microbeads. CAR expression (x-axis) was plotted against the relative cell count (y-axis). The histograms also showed the percentage of positive cells as mean ± SEM for three different experiments. C) Identical killing of CD44v6 positive cell lines UM-14C and UM-10B by CD44v6 CAR with or without second transgene. Primary human T-cells were transduced with a CD44v6 and CD19 CAR. After three days, the genetically modified primary human T-cells were selected by MACS, cocultred with target cells for 16 h and finally lysis of target cells was determined via CellTiter96® AQ_{ueous} One Solution Cell Proliferation Assay. Data were depicted as mean ± SEM of three independent experiments.

with MACS-enriched CD44v6 CAR T-cells with or without BFP as second transgene. Untransduced or MACS-enriched CD19-CAR transduced T-cells served as negative controls. As shown in Fig. 2C, the specific killing of HNSCC cells after 16 h of co-incubation was identical for the two CD44v6 constructs at all target to effector cell ratios, while both the CD19 CAR and the untransduced T-cells showed no lysis of the HNSCC cells. These experiments confirmed that the CD44v6 CAR facilitated efficient recognition and killing of cells from both cell lines and that the cytotoxicity of our CD44v6 CAR was not affected by the presence of a second transgene in the lentiviral vector.

Killing of HNSCC cells largely depends on the CD44v6 expression level

To determine the correlation between the CD44v6 expression and the cytotoxicity of CD44v6 CAR T-cells, three HNSCC cell lines with distinct CD44 and CD44v6 expression patterns were chosen (Fig. 3A-C): UT-24A cells had low (MFI: 6.5 ± 0.3), UM-11B cells intermediate (MFI: 11.2 ± 1.2) and UM-14C high (MFI: 14.2 ± 3.2) CD44v6 expression. Analyzing the cytotoxicity of CD44v6 CAR T-cells revealed a clear correlation between the CD44v6 expression levels and the killing of the target cells (Fig. 3A-C): Less than 40% of UT-24A cells, 60–80% of the UM-11B and almost 100% of UM-14C cells were killed at effector to target cell ratios of 3:1 and 1:1, respectively. In contrast, the killing efficiencies did not correlate with the CD44 expression levels detected on the surface of the target cells with an antibody binding to CD44.

In order to assess the specificity of the CAR, we overexpressed CD44v6 on the low expressing UT-24A cells with a lentiviral vector [36]. Compared to the UT-24A cells that were transduced with the control vector and selected in parallel with puromycin (MFI for CD44v6: 4.7 ± 0.6, Fig. 3D), the strongly overexpressing UT-24A + CD44v6 cells (MFI

648.2 ± 28.7) were killed much more efficiently (Fig. 3E).

CD44v6 CAR T-cells specifically eliminate CD44v6 expressing cells

The variable exon 11 in the *CD44* gene is only 204 base pairs long and encodes, when included as variant 6 in the CD44v6 transcript, as little as 68 amino acids. We therefore wanted to prove that the CD44v6 CAR solely and specifically recognized these amino acids.

For targeting of all CD44 transcripts, we generated three 20-nucleotide guide RNAs (gRNAs) against a common region in *CD44* exon 2 using the *chopchop.cbu.uib.no* website [37] and then cloned the gRNAs into the LentiCRISPR V2 vector. To accurately knockout CD44v6, we designed three different gRNAs that specifically target the variable exon 11. We used the empty LentiCRISPRv2 (empty vector) and additionally cloned a gRNA targeting the chicken actin promoter as an off-target control (gNC) [38]. Lentiviral vector particles were used to transduce the robustly CD44v6 expressing cells of the HNSCC cell lines UM-11B and UM-14C at MOIs of less than 0.1. Flow cytometry analysis of the CD44 isoform expression patterns of the CRISPR/Cas9 expressing cells revealed that, depending on the lentiviral construct used, >80% (~89 to 96%) of cells had clearly diminished CD44 and CD44v6 expression levels (data not shown).

We subsequently generated single cell clones with either complete CD44 or CD44v6 knockout and then re-introduced either CD44s or CD44v6 cDNAs with lentiviral expression vectors [36]. Importantly, the CD44 and CD44v6 expression levels were largely unaffected after transduction of the UM-11B and UM-14C cells with the two CRISPR/Cas9 control vectors. Alsothe cytotoxicity of the CD44v6 CAR T-cells remained the same (Fig. 4A/B, left/right panels). Transduction with the CD44 exon 2 CRISPR/Cas9 vector eliminated all CD44 expression; however, it was specifically restored by re-introducing the CD44s isoform (Fig. 4C/D left panels, red curves). Neither the cells without CD44

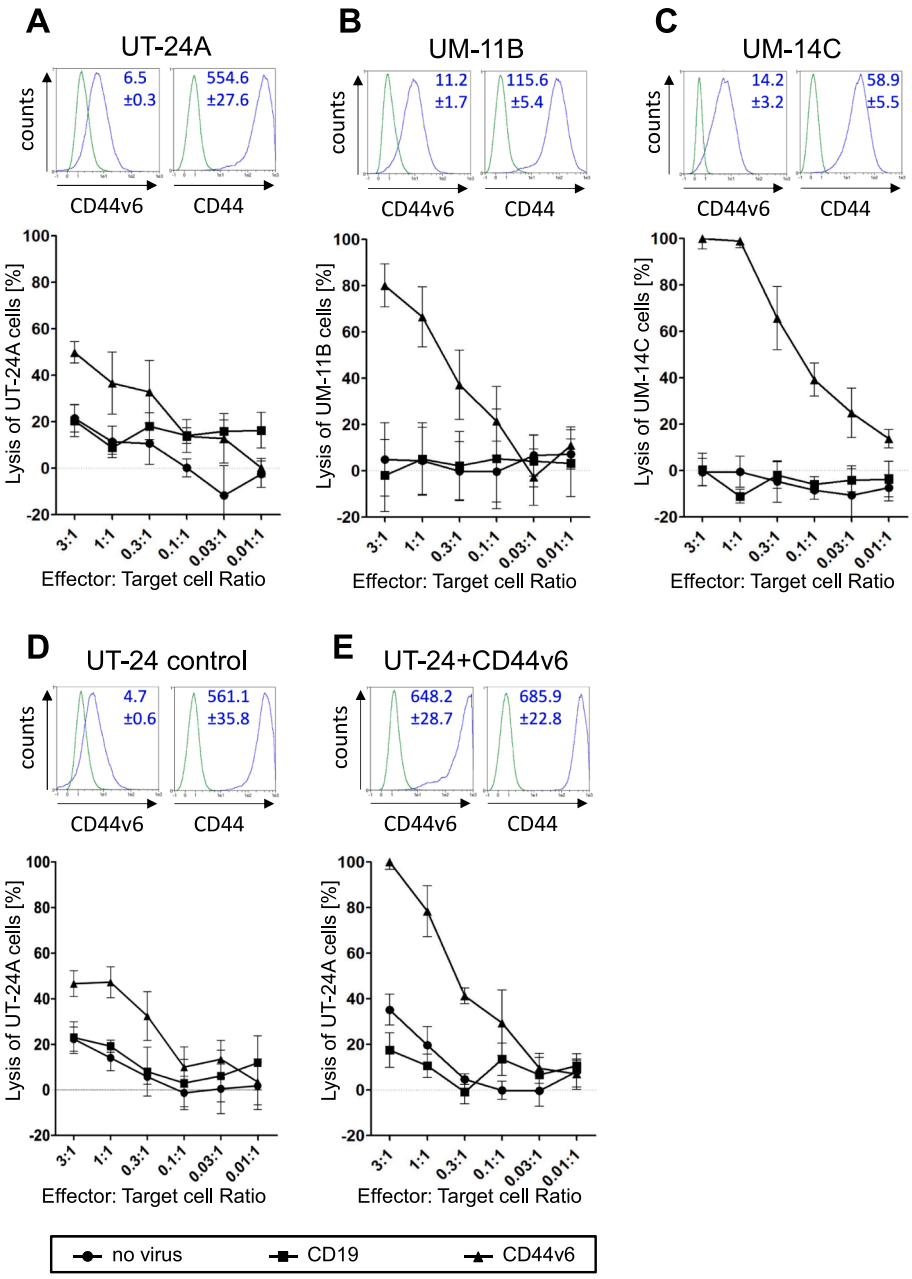

Fig. 3. Correlation between antigen density and killing efficiency. CD44 and CD44v6 expression on the cell surface of primary HNSCC cell lines UT-24A (A), UM-11B (B), UM-14C (C), UT-24A transduced with an empty control vector (D) and UT-24A transduced with an CD44v6 overexpression plasmid (E) were determined by binding of CD44-APC-Vio770 or CD44v6-PE-Vio770 antibodies. Antigen expression in flow cytometry (x-axis) was plotted against the absolute cell count (y-axis) for unstained control cells (green) and stained cells (blue). The mean fluorescence intensities (MFIs) of stained cells were shown from three experiments as mean ± SEM. Primary human T-cells were transduced with a CD44v6 or CD19 CAR. After three days, CAR-positive T-cells were enriched by MACS and co-cultured with target cells. After 16 h, lysis of the target cells was determined via CellTiter96® AQ_{ueous} One Solution Cell Proliferation Assay (Promega). Data were depicted as mean ± SEM for three different experiments.

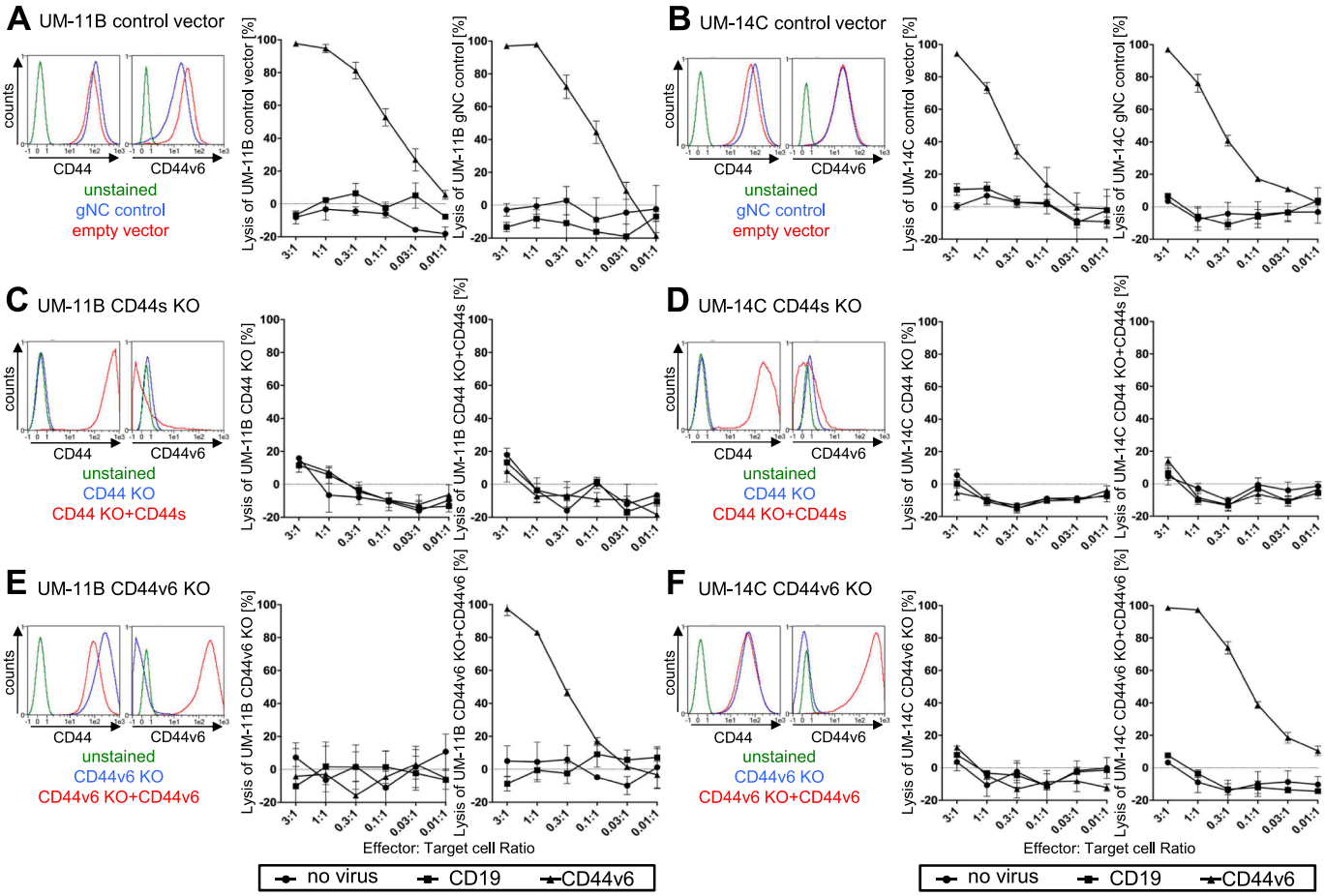

Fig. 4. CD44v6 CAR T-cells specifically recognized CD44v6 on UM-11B and UM-14C cells. Both cell lines were transduced with the CRISPR/Cas9 control vectors (A, B) or contain either CD44s (C,D) or CD44v6 guides (E,F). CD44 and CD44v6 expression on the cell surface of HNSCC cell lines was determined by flo cytometry after staining with CD44-APCVio770 or CD44v6-PE-Vio770 antibodies. Antigen expression (x-axis) was plotted against the absolute cell count (y-axis) for each sample. Primary human T-cells were transduced with a CD44v6 or CD19 CAR. After three days, CAR-positive T-cells were enriched by MACS and co-cultured with target cells. After 16 h, lysis of the target cells was determined via CellTiter96® AQ_{ueous} One Solution Cell Proliferation Assay (Promega). Data were depicted as mean ± SEM for three different experiments.

expression (KO) nor the knockout cells with CD44s overexpression were killed by the CD44v6 CAR T-cells (Fig. 4C/D right panels). Only when CD44v6 was re-introduced into CD44v6 KO cells, both the expression of CD44v6 (Fig. 4E/F left panels, red curves) and the killing of the HNSCC cells by the CD44v6 CAR T-cells were restored (Fig. 4E/F right panels), thus proving the high specificity of our CD44v6 CAR construct.

Killing dynamics of CD44v6 CAR T-cells against HNSCC cells

Finally, in order to understand the killing dynamics of the CD44v6 CAR T-cells, we co-incubated UM-17A cells, characterized by high CD44v6 and CD44 expression (Figure 1), at ratios of 3:1 (red) and 1:1 (yellow) with CD44v6 CAR T-cells and at a 1:1 (blue) ratio with CD19 CAR T-cells for 16 h. The CAR T-cells additionally expressed the red fluorescent protein mCherry (Fig. 5A/B). The HNSCC cells actively undergoing apoptosis showed a green fluorescence by using the CellEvent™ Caspase-3/7 Green Detection Reagent (Fig. 5B). Interestingly, although CAR T-cells were quickly in contact with the HNSCC cells, apoptosis of HNSCC cells was not detected in the first two hours of co-culture (Fig. 5B/C). At an effector:target cell ratio of 3:1, the apoptosis became clearly visible after 3–5 h of co-culture; within 8 h, the T-cells had induced apoptosis in ≥ 80% of HNSCC cells (Fig. 5C). Using an effector:target cell ratio of 1:1 did not delay the induction of apoptosis, but slowed down the killing. These different apoptosis kinetics for the two 3:1 and 1:1 cultures were also visualized in Fig. 5D, demonstrating that the killing of HNSCC cells extends over longer time periods (ratio 3:1 Ø7.6 h, ratio 1:1 Ø12.6 h), if less effector cells are present. Importantly, CD19 CAR T-cells did not exert relevant killing activity during co-cultivation with the UM-17A cells, demonstrating that activated T-cells did not express any receptors that recognized the malignant HNSCC cells.

Discussion

The key for selective targeting of HNSCCs with immune effector cells requires immunologically recognisable differences between the malignant cells and their normal counterparts [39]. Among the different classes of target antigens that have been considered for immunotherapy of HNSCCs are tumor neoantigens, which are derived from somatic mutations in the malignant cells. However, the two most frequently mutated gene in HNSCCs, *TP53* and *RAS*, are both not expressed on the cell surface and can therefore not be targeted by either antibodies or CARs [39]. Although engineering T-cells to express mutation-specific T-cell receptors for altered peptides expressed on HLA class I molecules of the malignant cells is possible [40], this approach is not widely applicable. Another class of target antigens in HNSCCs are cancer testis antigens, that are only present during embryogenesis and in normal germ cells in the testis of adults [41,42]. Peptides of these intracellular antigens are presented on the surface of certain HLA class I molecules and are currently targeted by several immunotherapeutic approaches [39],

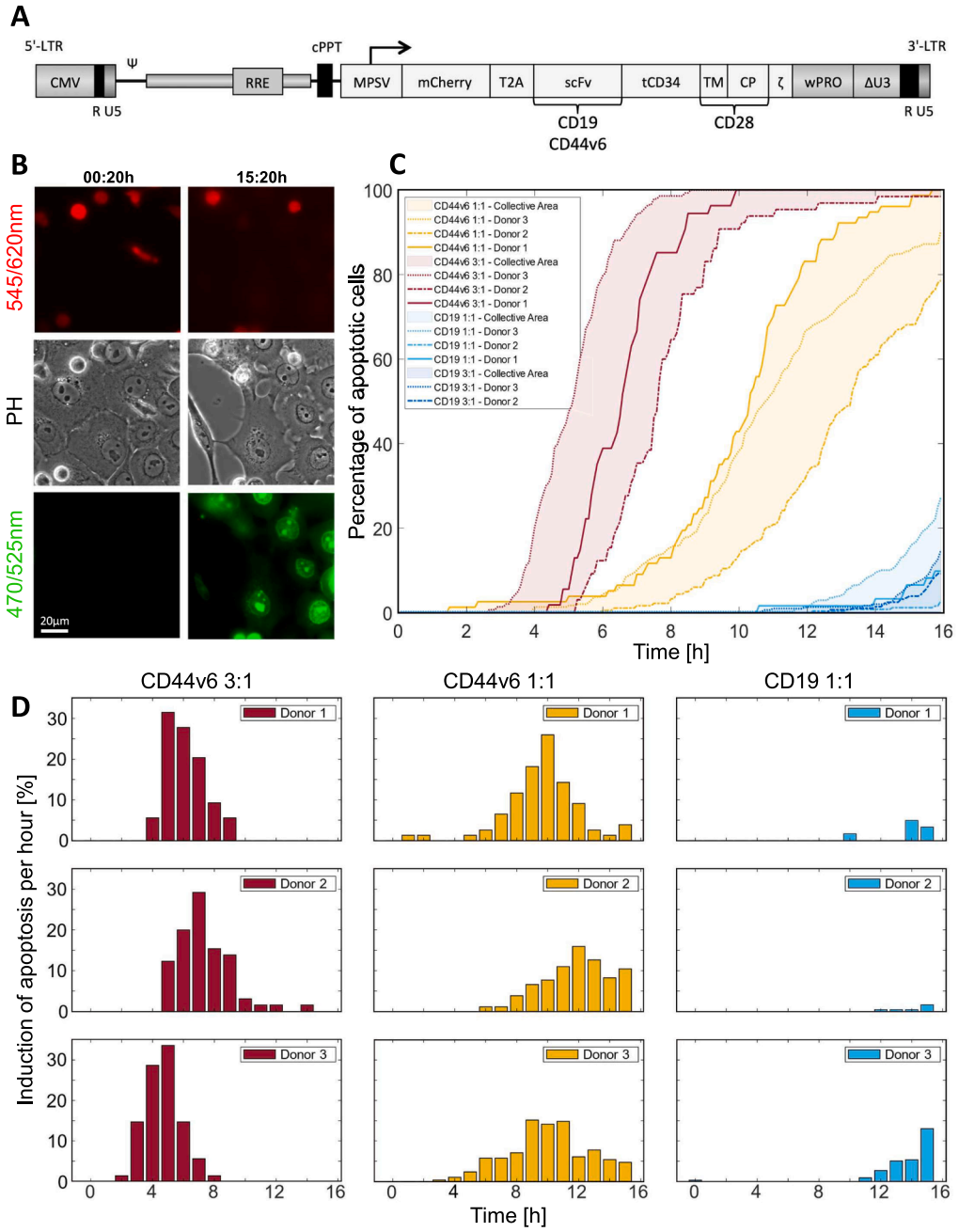

Fig. 5. Killing dynamic of CD44v6 CAR T-cells against CD19^{neg} CD44v6^{pos} UM17-A cells. Primary human T-cells from three healthy 3 donors) were transduced with lentiviral CD44v6 or CD19 CAR vectors. After three days, CAR-positive T-cells were enriched by MACS and co-cultured with UM-17A cells in two effector:target cell ratios (3:1, 1:1) for 16 h while performing live cell imaging to detect apoptotic cells (CellEvent™ Caspase-3/7 Green Detection Reagent (Invitrogen™, 470/525 nm channel). (A) Lentiviral vector with mCherry as a second transgene for detection of the transduced T-cells (B) Co-culture of UM-17A (apoptotic cells shown in green) with CD44v6-CAR-T-cells (red) in the beginning (t = 0:20 h) and at the end (15:20 h) of the measurement. (C) Apoptosis of UM-17A cells lysed by CD44v6 or CD19 CAR T-cells. (D) Apoptosis of UM-17A cells per hour.

including TCR mimics [42,43]. However, data on the clinical outcome in larger patient cohorts are still missing [42–44]. A number of antigens, generally not mutated, are overexpressed on HNSSCs. Among those are EGFR, which is the target for Cetuximab that is not well suited for CAR therapies, and the human epidermal growth factor receptor 2 (ErbB2), which has been frequently used in preclinical and clinical trials albeit not really successful yet [45–47]. Finally, tumor–associated antigens, e.g. the alternatively spliced surface protein EGFRvIII, or abnormal glycoforms, e.g. αvβ6 or MUC1TN, are currently evaluated as targets for CAR T–cell therapy [48–51].

We decided to focus here on CD44v6, an alternatively spliced surface protein that is strongly overexpressed on HNSCCs [24], and where autologous CAR T-cells can be tested in preclinical studies in monkeys [14]. For early human trials, two different types of therapeutic reagents were coupled to CD44v6 antibodies, radionuclides and the highly toxic antimicrotubuli agent mertansine [14]. Phase I clinical studies with radioimmunotherapeutic CD44v6 antibodies were associated with stable disease at higher radioactivity dose levels and also with myelotoxicity and mild oral mucositis [52]. However, the combination of BIWA4/bivatuzumab with mertansine in a phase I dose escalation study in seven patients with advanced untreatable HNSCCs led to fatal grade 4 toxicity in the 7th patient, who experienced loss of the epidermis and defoliation of the whole skin and died three days after the second infusion [28]. Although similarly severe toxicities were not observed with bivatuzumab in animal studies or in the clinical trial, skin toxicities such as depigmentation and desquamation were still present in other patients and in the monkey studies; therefore further clinical testing of CD44v6 antibodies in humans was stopped [52].

For CD44v6 as targeting moiety for autologous CAR T-cells, we chose the single chain variable fragment (scFv) sequences of the humanized high-affinity BIWA8 antibody for our construct [29]. To confirm the specificity of the CAR for HNSCC cells, we assessed the CD44 and CD44v6 expression profiles for 31 HNSCC lines and then chose four cell lines with low to high CD44v6 expression levels as targets in our

cytotoxicity assays. The cytotoxicity of our CAR was comparable when lentivirally expressed either as the single transgene or as the second transgene off the MPSV promoter and the killing efficiency directly correlated with the CD44v6 expression levels on the target cells. Using the CRISPR/Cas9-generated HNSCC knock-out cells with overexpression of CD44s or CD44v6 and a CD19 CAR as control proved the high specificity of our CD44v6 CAR constructs for the amino acid sequence encoded by exon 11 of the *CD44* gene. Finally, the time course studies revealed that the apoptosis in the target cells started approximately 2–3 h after contact with the immune effector cells and was clearly influenced by the target to effector cell ratio.

Based on these results, we expect that expression of our CD44v6 CAR on T-cells will effectively kill CD44v6 positive HNSCC cells in patients. However, as T-cells can readily leave the blood stream and recognize antigens present on cells in tissues, the expression of CD44v6 on normal cells can be a problem. According to the literature, CD44v6 is robustly expressed on keratinocytes in the skin as well as on epithelium in the cervix, in the cornea and in tonsils [53], however the expression levels were lower compared to those on malignant cells [18]. It will be very interesting to see if the expression of CD44v6 on normal tissues will be a major problem in the clinical phase I/II CD44v6 CAR T-cell study that has been opened for AML and multiple myeloma by scientists from Milano and Rome in 2019[2]. To stop any unwanted T-cell activation in off-target organs, they also included a modified thymidine kinase (TK) cDNA as suicide gene in their retroviral vector [54]. A second phase I trial for CD44v6 positive cancers treated with autologous CAR T-cells transduced with a lentiviral vector opened in 2020 in China[4]. The information, whether a suicide gene is also included in the lentiviral vector, has not been disclosed[4].

An attractive possibility to avoid cytotoxicity for normal tissues is to inject multiple doses of CAR T-cells directly into the tumor, similarly as it was already performed in the T4 clinical trial for HNSCC targeting the ErbB receptor family[5]. Although the final results from this phase I trial have not been published, preliminary results demonstrated that the injected T-cells hardly ever left the tumor tissues and never caused off-target effects, even when injecting escalating T-cell doses [55]. Using CARs with lower affinities for the target antigen is another attractive possibility that has been explored for EGFR and ErbB2 overexpressing tumors [46,56]. The Italian CD44v6 study also used the BIWA8-derived scFv for their CAR T-cell trials. Therefore, in case of severe toxicity, we can readily engineer a reduced-affinity CD44v6 CAR by changing two amino acids in the light chain of BIWA8 to residues present in the middle-affinity CD44v6 scFv of BIWA4 at the corresponding positions [25] and then test the two constructs in comparison. Other possibilities to change the activation level of our construct are to include a different co-stimulatory domain (e.g. 4-1BB or 2H4) or to pursue additional strategies for reducing off-target effects of CAR T-cells in solid tumors [57]. While we will proceed with *in vivo* xenograft studies in immunodeficient mice for testing the efficacy of intratumor versus intravenous application of the CD44v6 CAR T-cells, the clinical results including the toxicity from the two open CD44v6 CAR T-cell phase I/II studies in humans will finally guide us which strategy is most likely be successful for our HNSCC patients.

Declaration of Competing Interest

The authors declare that they have no competing financial interests or personal relationships that have influenced the work reported in this paper.

Acknowledgements

We gratefully acknowledge the healthy donors that provided peripheral blood for the cytotoxicity studies. We would like to thank Jörg Schipper, MD, director of ENT clinic, for his support of this research project. We are also in debt to Wolfgang Schulz, PhD, and Michèle Hoffmann, PhD, both in the department of Urology, Heinrich Heine University, for the use of the MACSQuant-10.

Funding

This work was supported, in part, by funding from the Medical Research School Düsseldorf, DSO, Heinrich Heine University, Düsseldorf, and within the framework of the iCAN33 project, funded by the European Regional 470 Development Fund NRW (ERDF, German EFRE) 2014-2020. CM acknowledges the support from VolkswagenFoundation (Freigeist fellowship, project ID 94195). NB and CM acknowledge the support within the DFG Collaborative Research Center 1208 'Identity and dynamics of biological membranes' (project ID 267205415).

[4] https://clinicaltrials.gov/ct2/show/NCT04427449
[5] https://clinicaltrials.gov/ct2/show/NCT01818323

References

[1] Morris LGT, Chandramohan R, West L, Zehir A, Chakravarty D, Pfister DG, et al. The molecular landscape of recurrent and metastatic head and neck cancers. JAMA Oncol 2016;3:244. https://doi.org/10.1001/jamaoncol.2016.1790.
[2] Marur S, D'Souza G, Westra WH, Forastiere AA. HPV-associated head and neck cancer: a virus-related cancer epidemic. Lancet Oncol 2010;11:781–9. https://doi.org/10.1016/S1470-2045(10)70017-6.
[3] Mehra R, Ang KK, Burtness B. Management of human papillomavirus-positive and human papillomavirus-negative head and neck cancer. Semin Radiat Oncol 2012; 22:194–7. https://doi.org/10.1016/J.SEMRADONC.2012.03.003.
[4] Hartmann J, Schüßler-Lenz M, Bondanza A, Buchholz CJ. Clinical development of CAR T cells-challenges and opportunities in translating innovative treatment concepts. EMBO Mol Med 2017;9:1183–97. https://doi.org/10.15252/emmm.201607485.
[5] Bonner JA, Harari PM, Giralt J, Azarnia N, Shin DM, Cohen RB, et al. Radiotherapy plus cetuximab for squamous-cell carcinoma of the head and neck. N Engl J Med 2006;354:567–78. https://doi.org/10.1056/NEJMoa053422.
[6] Ferris RL, Blumenschein G, Fayette J, Guigay J, Colevas AD, Licitra L, et al. Nivolumab for recurrent squamous-cell carcinoma of the head and neck. N Engl J Med 2016;375:1856–67. https://doi.org/10.1056/nejmoa1602252.
[7] Harrington KJ, Ferris RL, Blumenschein G, Colevas AD, Fayette J, Licitra L, et al. Nivolumab versus standard, single-agent therapy of investigator's choice in recurrent or metastatic squamous cell carcinoma of the head and neck (CheckMate 141): health-related quality-of-life results from a randomised, phase 3 trial. Lancet Oncol 2017;18:1104–15. https://doi.org/10.1016/S1470-2045(17)30421-7.
[8] Rischin D, Harrington KJ, Greil R, Soulieres D, Tahara M, de Castro G, et al. Protocol-specified final analysis of the phase 3 KEYNOTE-048 trial of pembrolizumab (pembro) as first-line therapy for recurrent/metastatic head and neck squamous cell carcinoma (R/M HNSCC). J Clin Oncol 2019;37:6000-6000. https://doi.org/10.1200/jco.2019.37.15_suppl.6000.
[9] Stoiber S, Cadilha BL, Benmebarek M-R, Lesch S, Endres S, Kobold S. Limitations in the design of chimeric antigen receptors for cancer therapy. Cells 2019;8:472. https://doi.org/10.3390/cells8050472.
[10] Chmielewski M, Hombach AA, Abken H. Antigen-specific T-cell activation independently of the MHC: Chimeric antigen receptor-redirected T cells. Front Immunol 2013;4.. https://doi.org/10.3389/fimmu.2013.00371.
[11] Ling DC, Bakkenist CJ, Ferris RL, Clump DA. Role of immunotherapy in head and neck cancer. Semin Radiat Oncol 2018;28:12–6. https://doi.org/10.1016/j.semradonc.2017.08.009.
[12] Davies DM, Foster J, Van Der Stegen SJC, Parente-Pereira AC, Chiapero-Stanke L, Delinassios GJ, et al. Flexible targeting of ErbB dimers that drive tumorigenesis by using genetically engineered T cells. Mol Med 2012;18:565–76. https://doi.org/10.2119/molmed.2011.00493.
[13] Mirzaei HR, Rodriguez A, Shepphird J, Brown CE, Badie B. Chimeric antigen receptors T cell therapy in solid tumor: Challenges and clinical applications. Front Immunol 2017;8.. https://doi.org/10.3389/fimmu.2017.01850.
[14] Spiegelberg D, Nilvebrant J. CD44v6-targeted imaging of head and neck squamous cell carcinoma: antibody-based approaches. Contrast Media Mol Imaging 2017; 2017:2709547. https://doi.org/10.1155/2017/2709547.
[15] Martegani MP, Del Prete F, Gasbarri A, Natali PG, Bartolazzi A. Structural variability of CD44v molecules and reliability of immunodetection of CD44 isoforms using mAbs specific for CD44 variant exon products. Am J Pathol 1999; 154:291–300. https://doi.org/10.1016/S0002-9440(10)65275-3.
[16] Cortes-Dericks L, Schmid RA. CD44 and its ligand hyaluronan as potential biomarkers in malignant pleural mesothelioma: Evidence and perspectives. Respir Res 2017;18:1–12. https://doi.org/10.1186/s12931-017-0546-5.
[17] Casucci M, Di Robilant BN, Falcone L, Camisa B, Norelli M, Genovese P, et al. CD44v6-targeted T cells mediate potent antitumor effects against acute myeloid leukemia and multiple myeloma. Blood 2013;122:3461–72. https://doi.org/10.1182/blood-2013-04-493361.
[18] Xu YY, Guo M, Yang LQ, Zhou F, Yu C, Wang A, et al. Regulation of CD44v6 expression in gastric carcinoma by the IL-6/STAT3 signaling pathway and its clinical significance. Oncotarget 2017;8:45848–61. https://doi.org/10.18632/oncotarget.17435.

[19] Wang Z, Zhao K, Hackert T, Zöller M. CD44/CD44v6 a reliable companion in cancer-initiating cell maintenance and tumor progression. Front Cell Dev Biol 2018;6:97. https://doi.org/10.3389/fcell.2018.00097.

[20] Seiter S, Arch R, Reber S, Komitowski D, Hofmann M, Ponta H, et al. Prevention of tumor metastasis formation by anti-variant CD44. J Exp Med 1993;177:443–55. https://doi.org/10.1084/jem.177.2.443.

[21] Mulder JWR, Sewnath M, Offerhaus G, Pals S, Oosting J, Kruyt P, et al. Colorectal cancer prognosis and expression of exon-v6-containing CD44 proteins. Lancet 1994;344:1470–2. https://doi.org/10.1016/S0140-6736(94)90290-9.

[22] Kaufmann M, von Minckwitz G, Heider KH, Ponta H, Herrlich P, Sinn HP. CD44 variant exon epitopes in primary breast cancer and length of survival. Lancet 1995; 345:615–9. https://doi.org/10.1016/S0140-6736(95)90521-9.

[23] Stroomer J, Roos J, Sproll M, Quak J, Heider KH, Wilhelm BJ, et al. Safety and biodistribution of 99mTechnetium-labeled anti-CD44v6 monoclonal antibody BIWA 1 in head and neck cancer patients. Clin Cancer Res 2000;6:3046–55. https://pubmed.ncbi.nlm.nih.gov/10955783/.

[24] de Bree R, Roos JC, Quak JJ, den Hollander W, Snow GB, van Dongen GA. Radioimmunoscintigraphy and biodistribution of technetium-99m-labeled monoclonal antibody U36 in patients with head and neck cancer. Clin Cancer Res 1995;1. https://pubmed.ncbi.nlm.nih.gov/9816020/.

[25] Verel I, Heider K-H, Siegmund M, Ostermann E, Patzelt E, Sproll M, et al. Tumor targeting properties of monoclonal antibodies with different affinity for target antigen CD44V6 in nude mice bearing head-and-neck cancer xenografts. Int J Cancer 2002;99:396–402. https://doi.org/10.1002/ijc.10369.

[26] Börjesson PK, Postema EJ, Roos JC, Colnot DR, Marres HA, van Schie MH, et al. Phase I therapy study with 186Re-labeled humanized monoclonal antibody BIWA 4 (Bivatuzumab) in patients with head and neck squamous cell carcinoma. Clin Cancer Res 2003;9:3961–72. https://pubmed.ncbi.nlm.nih.gov/14506195/.

[27] Sauter A, Kloft C, Gronau S, Bogeschdorfer F, Erhardt T, Golze W, et al. Pharmacokinetics, immunogenicity and safety of bivatuzumab mertansine, a novel CD44v6-targeting immunoconjugate, in patients with squamous cell carcinoma of the head and neck. Int J Oncol 2007;30:927–35. https://doi.org/10.3892/ijo.30.4.927.

[28] Tijink BM, Buter J, De Bree R, Giaccone G, Lang MS, Staab A, et al. A phase I dose escalation study with anti-CD44v6 bivatuzumab mertansine in patients with incurable squamous cell carcinoma of the head and neck or esophagus. Clin Cancer Res 2006;12:6064–72. https://doi.org/10.1158/1078-0432.CCR-06-0910.

[29] Roellecke K, Virts EL, Einholz R, Edson KZ, Altvater B, Rossig C, et al. Optimized human CYP4B1 in combination with the alkylator prodrug 4-ipomeanol serves as a novel suicide gene system for adoptive T-cell therapies. Gene Ther 2016;23: 615–26. https://doi.org/10.1038/gt.2016.38.

[30] Virts EL, Jankowska A, Mackay C, Glaas MF, Wiek C, Kelich SL, et al. AluY-mediated germline deletion, duplication and somatic stem cell reversion in UBE2T defines a new subtype of Fanconi anemia. Hum Mol Genet 2015;24:5093–108. https://doi.org/10.1093/hmg/ddv227.

[31] Hanenberg H, Xiao XL, Dilloo D, Hashino K, Kato I, Williams DA. Colocalization of retrovirus and target cells on specific fibronectin fragments increases genetic transduction of mammalian cells. Nat Med 1996;2:876–82. https://doi.org/10.1038/nm0896-876.

[32] Mulhall HJ, Labeed FH, Kazmi B, Costea DE, Hughes MP, Lewis MP. Cancer, pre-cancer and normal oral cells distinguished by dielectrophoresis. Anal Bioanal Chem 2011;401:2455–63. https://doi.org/10.1007/s00216-011-5337-0.

[33] van Hal NL, van Dongen GA, Stigter-van Walsum M, Snow GB, Brakenhoff RH. Characterization of CD44v6 isoforms in head-and-neck squamous-cell carcinoma. Int J Cancer 1999;82:837–45. https://doi.org/10.1002/(SICI)1097-0215(19990909)82:6<837::AID-IJC12>3.0.CO;2-H.

[34] Soukka T, Salmi M, Joensuu H, Häkkinen L, Sointu P, Koulu L, et al. Regulation of CD44v6-containing isoforms during proliferation of normal and malignant epithelial cells. Cancer Res 1997;57:2281–9. https://pubmed.ncbi.nlm.nih.gov/9187133/.

[35] Pollok KE, Hanenberg H, Noblitt TW, Schroeder WL, Kato I, Emanuel D, et al. High-efficiency gene transfer into normal and adenosine deaminase-deficient T lymphocytes is mediated by transduction on recombinant fibronectin fragments. J Virol 1998;72:4882–92. https://doi.org/10.1128/jvi.72.6.4882-4892.1998.

[36] Wiek C, Schmidt EM, Roellecke K, Freund M, Nakano M, Kelly EJ, et al. Identification of amino acid determinants in CYP4B1 for optimal catalytic processing of 4-ipomeanol. Biochem J 2015;465:103–14. https://doi.org/10.1042/BJ20140813.

[37] Labun K, Montague TG, Krause M, Torres Cleuren YN, Tjeldnes H, Valen E. CHOPCHOP v3: Expanding the CRISPR web toolbox beyond genome editing. Nucleic Acids Res 2019;47:W171–4. https://doi.org/10.1093/nar/gkz365.

[38] Kearns NA, Genga RMJ, Enuameh MS, Garber M, Wolfe SA, Maehr R. Cas9 effector-mediated regulation of transcription and differentiation in human pluripotent stem cells. Development 2014;141:219–23. https://doi.org/10.1242/dev.103341.

[39] Von Witzleben A, Wang C, Laban S, Savelyeva N, Ottensmeier CH. cells HNSCC: tumour antigens and their targeting by immunotherapy. Cells 2020;9.. https://doi.org/10.3390/cells9092103.

[40] Theoret MR, Cohen CJ, Nahvi AV, Ngo LT, Suri KB, Powell DJ, et al. Relationship of p53 overexpression on cancers and recognition by anti-p53 T cell receptor-transduced T cells. Hum Gene Ther 2008;19:1219–31. https://doi.org/10.1089/hum.2008.083.

[41] Figueiredo DLA, Mamede RCM, Proto-Siqueira R, Neder L, Silva WA, Zago MA. Expression of cancer testis antigens in head and neck squamous cell carcinomas. Head Neck 2006;28:614–9. https://doi.org/10.1002/hed.20380.

[42] Jakobsen MK, Gjerstorff MF. CAR T-cell cancer therapy targeting surface cancer/testis antigens. Front Immunol 2020;11:1568. https://doi.org/10.3389/fimmu.2020.01568.

[43] Al-Khadairi G, Decock J. Cancer testis antigens and immunotherapy: Where do we stand in the targeting of PRAME? Cancers (Basel) 2019;11. https://doi.org/10.3390/cancers11070984.

[44] von Witzleben A, Wang C, Laban S, Savelyeva N, Ottensmeier CH. HNSCC: tumour antigens and their targeting by immunotherapy. Cells 2020;9:2103. https://doi.org/10.3390/cells9092103.

[45] Ferris RL. Immunology and immunotherapy of head and neck cancer. J Clin Oncol 2015;33:3293–304. https://doi.org/10.1200/JCO.2015.61.1509.

[46] Caruso HG, Hurton LV, Najjar A, Rushworth D, Ang S, Olivares S, et al. Tuning sensitivity of CAR to EGFR density limits recognition of normal tissue while maintaining potent antitumor activity. Cancer Res 2015;75:3505–18. https://doi.org/10.1158/0008-5472.CAN-15-0139.

[47] Van Schalkwyk MCI, Papa SE, Jeannon JP, Urbano TG, Spicer JF, Maher J. Design of a phase i clinical trial to evaluate intratumoral delivery of ErbB-targeted chimeric antigen receptor T-cells in locally advanced or recurrent head and neck cancer. Hum Gene Ther Clin Dev 2013;24:134–42. https://doi.org/10.1089/humc.2013.144.

[48] Jiang H, Gao H, Kong J, Song B, Wang P, Shi B, et al. Selective targeting of glioblastoma with EGFRvIII/EGFR bitargeted chimeric antigen receptor T cell. Cancer Immunol Res 2018;6:1314–26. https://doi.org/10.1158/2326-6066.CIR-18-0044.

[49] Whilding LM, Parente-Pereira AC, Zabinski T, Davies DM, Petrovic RMG, Kao YV, et al. Targeting of aberrant αvβ6 integrin expression in solid tumors using chimeric antigen receptor-engineered T cells. Mol Ther 2017;25:259–73. https://doi.org/10.1016/j.ymthe.2016.10.012.

[50] Maher J, Wilkie S, Davies DM, Arif S, Picco G, Julien S, et al. Targeting of tumor-associated glycoforms of MUC1 with CAR T cells. Immunity 2016;45:945–6. https://doi.org/10.1016/j.immuni.2016.10.014.

[51] Wang Z, Cao YJ. Adoptive cell therapy targeting neoantigens: a frontier for cancer research. Front Immunol 2020;11:176. https://doi.org/10.3389/fimmu.2020.00176.

[52] Börjesson PKE, Postema EJ, De Bree R, Roos JC, Leemans CR, Kairemo KJA, et al. Radioimmunodetection and radioimmunotherapy of head and neck cancer. Oral Oncol 2004;40:761–72. https://doi.org/10.1016/j.oraloncology.2003.11.009.

[53] Mack B, Gires O. CD44s and CD44v6 expression in head and neck epithelia. PLoS ONE 2008;3:e3360. https://doi.org/10.1371/journal.pone.0003360.

[54] Porcellini S, Asperti C, Corna S, Cicoria E, Valtolina V, Stornaiuolo A, et al. CAR T cells redirected to CD44v6 control tumor growth in lung and ovary adenocarcinoma bearing mice. Front Immunol 2020;11:99. https://doi.org/10.3389/fimmu.2020.00099.

[55] Larcombe-Young D, Papa S, Maher J. PanErbB-targeted CAR T-cell immunotherapy of head and neck cancer. Expert Opin Biol Ther 2020;20:965–70. https://doi.org/10.1080/14712598.2020.1786531.

[56] Liu X, Jiang S, Fang C, Yang S, Olalere D, Pequignot EC, et al. Affinity-tuned ErbB2 or EGFR chimeric antigen receptor T cells exhibit an increased therapeutic index against tumors in mice. Cancer Res 2015;75:3596–607. https://doi.org/10.1158/0008-5472.CAN-15-0159.

[57] Newick K, O'Brien S, Moon E, Albelda SM. CAR T cell therapy for solid tumors. Annu Rev Med 2017;68:139–52. https://doi.org/10.1146/annurev-med-062315-120245.

[58] Balló H, Koldovsky P, Hoffmann T, Balz V, Hildebrandt B, Gerharz CD, et al. Establishment and characterization of four cell lines derived from human head and neck squamous cell carcinomas for an autologous tumor-fibroblast in vitro model. Anticancer Res 1999;19:3827–36. https://pubmed.ncbi.nlm.nih.gov/10628319/.

[59] Hauser U, Balz V, Carey TE, Grénman R, van Lierop A, Scheckenbach K, et al. Reliable detection of p53 aberrations in squamous cell carcinomas of the head and neck requires transcript analysis of the entire coding region. Head Neck 2002;24: 868–73. https://doi.org/10.1002/hed.10128.

[60] Lansford CD, Grenman R, Bier H, Somers KD, Kim SY, Whiteside TL, et al. Head and Neck Cancers. In: Masters JRW, Palssons B, editors. Human Cell Culture, Vol. 2. Kluwer Academic Publishers: Dordrecht; 1999. p. 185–255. https://doi.org/10.1007/0-306-46861-1_12.

[61] Soukka T, Salmi M, Joensuu H, Häkkinen L, Sointu P, Koulu L, et al. Regulation of CD44v6-containing isoforms during proliferation of normal and malignant epithelial cells. Cancer Res 1997;57:2281–9. https://pubmed.ncbi.nlm.nih.gov/9187133/.

[62] Pekkola-Heino K, Kulmala J, Grenman R. Sublethal damage repair in squamous cell carcinoma cell lines. Head Neck 1992;14:196–9. https://doi.org/10.1002/hed.2880140306.

[63] Johansson N, Airola K, Grenman R, Kariniemi A-L, Saarialho-Kere U, Kahari V-M. Expression of collagenase-3 (matrix metalloproteinase-13) in squamous cell carcinomas of the head and neck. Am J Pathol 1997;151:499–508. https://pubmed.ncbi.nlm.nih.gov/9250162/.

[64] Servomaa K, Kiuru A, Grénman R, Pekkola-Heino K, Pulkkinen JO, Rytömaa T. p53 mutations associated with increased sensitivity to ionizing radiation in human head and neck cancer cell lines. Cell Prolif 1996;29:219–30. https://doi.org/10.1046/j.1365-2184.1996.01009.x.

[65] Lin CJ, Grandis JR, Carey TE, Gollin SM, Whiteside TL, Koch WM, et al. Head and neck squamous cell carcinoma cell lines: established models and rationale for selection. Head Neck 2007;29:163–88. https://doi.org/10.1002/hed.20478.

[66] Pekkola-Heino K, Servomaa K, Kiuru A, Grenman R. Increased radiosensitivity is associated with p53 mutations in cell lines derived from oral cavity carcinoma.

Acta Otolaryngol 1996;116:341–4. https://doi.org/10.3109/00016489609137854.
[67] Grénman R, Carey TE, McClatchey KD, Wagner JG, Pekkola-Heino K, Schwartz DR, et al. In vitro radiation resistance among cell lines established from patients with squamous cell carcinoma of the head and neck. Cancer 1991;67:2741–7. https://doi.org/10.1002/1097-0142(19910601)67:11<2741::aid-cncr2820671105>3.0.co;2-s.
[68] Kiuru A, Servomaa K, Grénman R, Pulkkinen J, Rytömaa T. p53 mutations in human head and neck cancer cell lines. Acta Oto-Laryngologica, Suppl., Taylor and Francis A.S. 1997:237–40. https://doi.org/10.3109/00016489709124132.
[69] Bradford CR, Zacks SE, Androphy EJ, Gregoire L, Lancaster WD, Carey TE, et al. Human papillomavirus DNA sequences in cell lines derived 'from head and neck squamous cell carcinomas. Otolaryngol Head Neck Surg 1991;104(3):303–10. https://doi.org/10.1177/019459989110400304.
[70] Krause CJ, Carey TE, Ott RW, Hurbis C, Mcclatchey KD, Regezi JA. Human squamous cell carcinoma: establishment and characterization of new permanent cell lines. Arch Otolaryngol 1981;107:703–10. https://doi.org/10.1001/archotol.1981.00790470051012.
[71] Carey TE, Kimmel KA, Schwartz DR, Richter DE, Baker SR, Krause CJ. Antibodies to human squamous cell carcinoma. Otolaryngol Head Neck Surg 1983;91:482–91. https://doi.org/10.1177/019459988309100503.
[72] Tang AL, Hauff SJ, Owen JH, Graham MP, Czerwinski MJ, Park JJ, et al. UM-SCC-104: a new human papillomavirus-16-positive cancer stem cell-containing head and neck squamous cell carcinoma cell line. Head Neck 2012;34:1480–91. https://doi.org/10.1002/hed.21962.

12.2 Genetic Engineering and Enrichment of Human NK Cells for CAR-Enhanced Immunotherapy of Hematological Malignancies

Journal: Frontiers in Immunology | Volume 13 | April 2022 | Article 847008 | [183]

Authors: Maren Soldierer, Arthur Bister, Corinna Haist, Aniththa Thivakaran, Sevgi Can Cengiz, Stephanie Sendker, Nina Bartels, Antonia Thomitzek, Denise Smorra, Maryam Hejazi, Markus Uhrberg, Kathrin Scheckenbach, Cornelia Monzel, Constanze Wiek, Dirk Reinhardt, Naghmeh Niktoreh and Helmut Hanenberg

Contribution: For this work my contribution includes the design and conduction of the microscopic measurements, the inspection and analysis of image results, their representation in the respective figure as well as the revision of the manuscript, in collaboration with all co-authors.

frontiers | Frontiers in Immunology

ORIGINAL RESEARCH
published: 07 April 2022
doi: 10.3389/fimmu.2022.847008

Genetic Engineering and Enrichment of Human NK Cells for CAR-Enhanced Immunotherapy of Hematological Malignancies

Maren Soldierer[1†], Arthur Bister[1,2†], Corinna Haist[1,2], Aniththa Thivakaran[1], Sevgi Can Cengiz[1], Stephanie Sendker[1], Nina Bartels[3], Antonia Thomitzek[2], Denise Smorra[1], Maryam Hejazi[4], Markus Uhrberg[4], Kathrin Scheckenbach[2], Cornelia Monzel[3], Constanze Wiek[2], Dirk Reinhardt[1], Naghmeh Niktoreh[1] and Helmut Hanenberg[1,2]*

[1] Department of Pediatrics III, University Children's Hospital Essen, University Duisburg-Essen, Essen, Germany, [2] Department of Otorhinolaryngology, Head & Neck Surgery, University Hospital Düsseldorf, Heinrich Heine University, Düsseldorf, Germany, [3] Department of Experimental Medical Physics, Heinrich Heine University, Düsseldorf, Germany, [4] Institute for Transplantation Diagnostics and Cell Therapeutics, Heinrich-Heine University, Düsseldorf, Germany

OPEN ACCESS

Edited by:
Wing Leung, Miltenyi Biotec, United States

Reviewed by:
Maya Caroline Andre, University Children's Hospital Tübingen, Germany
Mitchell S. Cairo, Westchester Medical Center, United States

***Correspondence:**
Helmut Hanenberg
Helmut.Hanenberg@uk-essen.de

[†]These authors have contributed equally to this work

Specialty section:
This article was submitted to NK and Innate Lymphoid Cell Biology, a section of the journal Frontiers in Immunology

Received: *31 December 2021*
Accepted: *28 February 2022*
Published: *07 April 2022*

Citation:
Soldierer M, Bister A, Haist C, Thivakaran A, Cengiz SC, Sendker S, Bartels N, Thomitzek A, Smorra D, Hejazi M, Uhrberg M, Scheckenbach K, Monzel C, Wiek C, Reinhardt D, Niktoreh N and Hanenberg H (2022) Genetic Engineering and Enrichment of Human NK Cells for CAR-Enhanced Immunotherapy of Hematological Malignancies. Front. Immunol. 13:847008. doi: 10.3389/fimmu.2022.847008

The great clinical success of chimeric antigen receptor (CAR) T cells has unlocked new levels of immunotherapy for hematological malignancies. Genetically modifying natural killer (NK) cells as alternative CAR immune effector cells is also highly promising, as NK cells can be transplanted across HLA barriers without causing graft-versus-host disease. Therefore, *off-the-shelf* usage of CAR NK cell products might allow to widely expand the clinical indications and to limit the costs of treatment per patient. However, in contrast to T cells, manufacturing suitable CAR NK cell products is challenging, as standard techniques for genetically engineering NK cells are still being defined. In this study, we have established optimal lentiviral transduction of primary human NK cells by systematically testing different internal promoters for lentiviral CAR vectors and comparing lentiviral pseudotypes and viral entry enhancers. We have additionally modified CAR constructs recognizing standard target antigens for acute lymphoblastic leukemia (ALL) and acute myeloid leukemia (AML) therapy—CD19, CD33, and CD123—to harbor a CD34-derived hinge region that allows efficient detection of transduced NK cells *in vitro* and *in vivo* and also facilitates CD34 microbead-assisted selection of CAR NK cell products to >95% purity for potential clinical usage. Importantly, as most leukemic blasts are *a priori* immunogenic for activated primary human NK cells, we developed an *in vitro* system that blocks the activating receptors NKG2D, DNAM-1, NKp30, NKp44, NKp46, and NKp80 on these cells and therefore allows systematic testing of the specific killing of CAR NK cells against ALL and AML cell lines and primary AML blasts. Finally, we evaluated in an ALL xenotransplantation model in NOD/SCID-gamma (NSG) mice whether human

CD19 CAR NK cells directed against the CD19+ blasts are relying on soluble or membrane-bound IL15 production for NK cell persistence and also *in vivo* leukemia control. Hence, our study provides important insights into the generation of pure and highly active allogeneic CAR NK cells, thereby advancing adoptive cellular immunotherapy with CAR NK cells for human malignancies further.

Keywords: human NK cells, chimeric antigen receptor, genetic engineering, lentiviral vectors (LVS), adoptive cellular immunotherapy, transduction

INTRODUCTION

Cancer immunotherapy, entitled by *Science* as the breakthrough of the year 2013 (1), continues to grow exponentially, and harnessing the power of cellular therapies has contributed significantly to this progress. Although adoptive cellular therapies had been used in the past as rather experimental treatments for patients after stem cell transplantation, with late-stage disease and/or metastatic solid tumors (2–4), the immense potential of cellular immunotherapies became obvious since 2010 through the introduction of second-generation chimeric antigen receptor (CAR) T cells in clinical phase I/II studies (5, 6). Since then, CAR T cells have overcome many limitations of autologous adoptive immunotherapies, which previously were using tumor-infiltrating lymphocytes (TILs) isolated from malignant tissues, expanded *in vitro*, and reinfused into the patients (7). In contrast, CAR T cells do not require extended sampling of tumor tissues, as the patients' autologous circulating T cells are engineered *ex vivo* to recognize tumor-associated antigens, thus making CAR T cell therapy principally applicable for both solid tumors and hematological malignancies (8).

The great clinical success of CAR T cells in early trials for relapsed or refractory hematological malignancies of the B cell lineage has already resulted in the approval of five CAR T cell products, targeting CD19-positive leukemia and lymphoma (Kymriah®, Yescarta®, Tecartus®, and Breyanzi®) or B cell maturation antigen (BCMA)-positive multiple myelomas (Abecma®) (6, 8–10). These second-generation CAR constructs typically consist of extracellular antibody-derived sequences that determine the specificity and two intracellular T cell signaling units, usually the zeta chain of the CD3 complex and either CD28 or 4-1BB/CD137 as co-stimulatory domains. Thus, CARs on competent immune effector cells can recognize surface target antigens independent of any human leukocyte antigen (HLA) constellation and then kill the target cells (6). However, to avoid allogeneic graft-versus-host disease (GvHD), the CAR T cell products need to be generated in autologous settings, which results in very expensive and long manufacturing pipelines. In addition, a high number of clinical trials have reported severe adverse events following autologous CAR T cell treatment, such as life-threatening cytokine release syndrome (CRS) or neurotoxicity (6).

Natural killer (NK) cells are professional immune effector cells of the innate immune system that can recognize and lyse their target cells in a non-antigen-specific manner, thereby enabling them to effectively detect and eliminate malignant cells that have escaped the T cell immune surveillance (11, 12). Most importantly, as NK cells are not HLA-restricted and when transplanted do not cause acute or chronic GvHD, they can readily be administered to HLA-mismatched patients and have, when obtained from healthy donors, significantly shorter manufacturing periods (13). In addition, since large numbers of immune effector cells are required for successful therapeutic transplantation, and leukemia patients often have limited numbers of leukocytes due to their heavy pretreatment regimens, the potential to use allogeneic CAR NK cells of healthy donors for therapeutic infusions would be a major advantage over autologous CAR T cells and allows *off-the-shelf* usage of pre-manufactured products (11). Notably, NK cells can readily be genetically modified with lentiviral vectors (14) and the classical second-generation CARs with either CD28 or 4-1BB signaling domains function well in NK cells and confer additional antitumor effects (11). In preclinical xenograft murine models, the activity of CAR NK cells against malignant cells was similar to that of CAR T cells, albeit with less cytokine release and better overall survival rates, at least for ovarian cancer (15) and acute lymphoblastic leukemia (ALL) (16). Importantly, the first clinical phase I/II trial with CD19 CAR NK cells for the treatment of relapsed or refractory CD19-positive leukemias (NCT03056339) reported high response rates and no treatment-associated occurrence of CRS, neurotoxicity, or GvHD (17). Hence, CAR NK cells for specific target antigens appear to be safe and could potentially be used as *off-the-shelf products*, thus drastically shortening the production time and lowering the costs of CAR-based cellular cancer therapeutics (18).

Compared to a large number of clinical studies with CAR T cells, CAR NK cell therapy development is clearly lagging behind (9). Most of the delay can be attributed to two major problems, the comparably low transduction rates and the challenges in the large-scale genetic engineering of primary human NK cells from healthy donors (19). In contrast to human T cells, which can readily be transduced with lentiviral vectors using the VSV-G glycoprotein as envelope pseudotype (20, 21), NK cells do not express sufficient amounts of the cellular surface molecules of the LDL receptor family that serve as entry receptors for VSV-G (21). Therefore, different envelope pseudotypes are necessary for the efficient entry of the lentiviral particles (22). In their seminal publications, Girard-Gagnepain et al. demonstrated that two constructs derived from the envelope protein of the baboon endogenous virus, BaEV-Rless, and BaEV-TR, are optimally suited for genetically modifying resting hematopoietic cells (14) and also human primary NK cells with lentiviral vectors (21, 23).

The most efficient and reliable large-scale expansion of primary human NK cells up to date can be performed by using genetically engineered cells of the AML cell line K562 as irradiated feeder cells that express the 4-1BB ligand, membrane-bound IL15, and/or IL21 (17, 19, 24, 25). However, using leukemic K562 cells for stimulation of cellular products that will be injected into patients is not ideal.

In this study, we intended to establish the transduction of primary human NK cells derived from peripheral blood in a feeder-cell-free and CliniMACS Prodigy™-compatible system (26) using the NK MACS medium from Miltenyi Biotec and also addressed several issues in genetic engineering of NK cells, including optimized transgene expression, alternative lentiviral pseudotypes, and transduction enhancers. We also established a methodology for the enrichment of human CAR NK cells and developed an assay system to functionally test the CAR-specific cytotoxic activity against leukemic cell lines and primary AML blasts *in vitro*. Finally, we addressed conditions for the prolonged survival of CAR NK cells *in vivo* in immunodeficient NOD/SCID-gamma (NSG) mice with B-cell precursor ALL.

MATERIAL AND METHODS

Cell Culture

The AML cell lines MOLM-14, NOMO-1, CMK, and THP-1 and the ALL cell lines REH and BV-173 were obtained from the DSMZ (Braunschweig, Germany) and cultured in RPMI-1640 GlutaMAX™ medium supplemented with 10% fetal bovine serum (FBS) and 1% penicillin and streptomycin (P/S; all from Thermo Fisher Scientific, Waltham, MA, USA), referred to as complete RPMI-1640. Human embryonic kidney cells (HEK293T, DSMZ) were cultured in Dulbecco's Modified Eagle Medium (DMEM) GlutaMAX™ supplemented with 10% FBS and 1% P/S, referred to as complete DMEM.

Isolation and Culture of Human NK Cells

Primary human NK cells were isolated from peripheral blood of healthy donors, for which they gave written informed consent according to the protocol (#2019-623) approved by the local ethics committee (Heinrich Heine University, Düsseldorf, Germany). Ficoll density gradient centrifugation (Ficoll-Paque Plus; Cytiva Europe, Freiburg, Germany) was performed to collect peripheral blood mononuclear cells (PBMCs). NK cells were then enriched by immunomagnetic negative selection using MojoSort™ Human NK Cell Isolation Kit (BioLegend, San Diego, CA, USA) according to the manufacturer's instructions. NK cell purity and phenotype were determined by flow cytometry (MACSQuant® Analyzer 10, Miltenyi Biotec, Bergisch Gladbach, Germany) on days 0, 7, and 14, using fluorochrome-conjugated antibodies against CD3, CD33, CD56, and CD94 (all REAfinity™ clones from Miltenyi Biotec). NK cells were activated and expanded in NK MACS® Medium (Miltenyi Biotec) supplemented with 5% heat-inactivated human AB serum (Sigma-Aldrich, Darmstadt, Germany), 1% P/S, 500 IU/ml of IL2 (Proleukin, Novartis, Basel, Switzerland), and 10 ng/ml of IL15 (Miltenyi Biotec) at a concentration of 1–2 million cells/ml.

Lentiviral Expression Constructs

All CAR constructs were optimized for human codon usage and synthesized by GeneArt (Thermo Fisher Scientific) or BioCat (Heidelberg, Germany). The CARs were co-expressed *via* a T2A site with the monomeric tag blue fluorescent protein (BFP from Evrogen, Moscow, Russia) under the control of the myeloproliferative sarcoma virus (MPSV) promoter (27) and equipped with our CD34-derived hinge C6 (28), CD28 transmembrane, and co-stimulatory domains as well as the CD3 zeta-chain unit (27). The CD19, CD33, CD123, and epidermal growth factor receptor (EGFR) (clone cetuximab/C225, from now on referred to as Cetux) CARs were previously described (20, 27–29). In the ALL xenograft model, CD19 CARs were co-expressed with codon-optimized soluble human IL15 or human IL15 tethered to the IL15 receptor α-chain (IL15-IL15R). Both IL15 cDNAs used a codon-optimized CD8 leader peptide. The codon-optimized firefly luciferase/enhanced green fluorescent protein (EGFP) fusion (LucEG) (20) and the EGFP/neomycin resistance fusion (EGN) (27) lentiviral expression vectors were previously published. The MPSV, hPGK (human phosphoglycerate kinase 1), modified spleen focus-forming virus (SFFV), and short EF1α (elongation factor 1-α) promoter constructs were also previously published (27). The wild-type SFFV was newly introduced in the pCL6EGNwo vector (27). The optimized EF1α promoter was generated from the long EF1α construct with the wild-type SD and acceptor sites (27) by deleting ~600 bp of the natural intron and mutating an open reading frame (sequences are available upon request).

Production of Lentiviral Particles

The production of lentiviral particles in HEK293T cells was performed on 10-cm dishes as previously described (20, 30). For pseudotyping, the following envelopes were used: the vesicular stomatitis virus glycoprotein (VSV-G, 6 µg per transfection), the codon-optimized baboon endogenous virus lacking the R-peptide (BaEV-Rless, 1 µg per transfection), the codon-optimized BaEV surface and transmembrane units fused to the cytoplasmic units of the amphotropic murine leukemia virus (aMLV; BaEV-TR, 1 µg per transfection), the codon-optimized gibbon ape leukemia virus (GALV) surface unit fused to the transmembrane and cytoplasmic units of aMLV (GALV-TM, 1 µg per transfection), or the previously published (31) feline endogenous virus envelope fused to the cytoplasmic units of aMLV (RD114-TR, 6 µg per transfection). Twenty-four hours after transfection, the culture medium was replaced with 10 ml of IMDM (Sigma-Aldrich) supplemented with 10% FBS, 1% P/S, and 1% L-glutamine (Thermo Fisher Scientific). Cell supernatants containing viral particles were harvested 48 h after transfection, filtered through a 0.45-µm filter, and either used directly or after concentration (5-fold) at 10,000 × *g* for 2 h at 4°C. Lentiviral supernatants were used fresh or stored at −80°C until usage.

Transduction of Human NK Cells

After 7 to 10 days of expansion in a complete NK MACS medium, primary human NK cells were transduced with lentiviral particle-containing supernatants. For the envelope, promoter, and entry enhancer testing, 1 to 1.5 × 10^5 NK cells per well were transduced in flat-bottom 96-well plates in working volumes of 100 µl with serially diluted lentiviral particles encoding EGN. When RetroNectin™ (TaKaRa Bio Inc., Otsu, Japan; from now on referred to as Retronectin) was used as transduction enhancer, non-treated 96-well plates were coated either overnight at 4°C or for 2 h at 37°C prior to use (32, 33). In contrast, Vectofusin®-1 (Miltenyi Biotec, from now on referred to as Vectofusin) was added at a final concentration of 10 µg/ml to tissue culture-treated 96-well plates. For transductions of higher numbers of NK cells, 1 to 1.5 × 10^6 NK cells were transduced on Retronectin-coated 12-well plates (1 ml final volume) or 3.5 to 4 × 10^6 NK cells on Retronectin-coated 6-well plates (2.5 ml final volume) with 500 or 1,250 µl concentrated lentiviral particles, respectively, encoding CD19, CD33, CD123, or Cetux CARs. After 24 h, cells were supplemented with 2 ml (12-well) or 5 ml (6-well) fresh complete NK cell medium. Transduction efficiency was determined 3 to 4 days after transduction by flow cytometry, measuring BFP and/or CD34 (CAR) expression with phycoerythrin (PE)-conjugated QBend-10 CD34 antibody (Thermo Fisher Scientific).

CAR NK Cell Enrichment

Three to four days after transduction, CAR NK cells were enriched on an OctoMACS™ Separator using MS columns or on a QuadroMACS™ Separator using LS columns after staining with CD34 microbeads (clone QBend-10) according to the manufacturer's instructions (Miltenyi Biotec) and similarly as described previously for CAR T cells (28). In order to investigate the MACS enrichment efficiency, the CAR NK cell purity and yield, and the expression of the different CAR constructs on the transduced NK cells, the three cell fractions—before MACS, flowthrough, and after MACS—were collected and analyzed by flow cytometry for BFP expression and/or CD34 positivity. Before any functional analyses were performed, the MACS-enriched CAR NK cells were further cultured for at least an additional 2 days in a complete NK MACS medium.

Blocking and Cytotoxicity Assay

To block the activating receptors, non-transduced and CAR NK cells were incubated with monoclonal REAfinity™ antibodies against NKG2D, DNAM-1, NKp30, NKp44, NKp46, and NKp80 (Miltenyi Biotec) at concentrations of 10 µg/ml in complete RPMI-1640 at 4°C. These REAfinity™ antibodies harbor mutations in their Fc receptors, which prevents their binding to human Fc receptors. Control cells were incubated in parallel with REAfinity™ isotype controls (Miltenyi Biotec). After the 2 h of incubation, the NK cells were added at 3:1, 1:1, and 0.3:1 ratios (without washing) to MOLM-14, NOMO-1, CMK, THP-1, REH and BV-173 cells seeded at 2 × 10^4 cells/well in a 96-well U-bottom plate in complete RPMI-1640 medium. After 16 h, the cultures were harvested, and leukemic cell lysis was analyzed by flow cytometry, using propidium iodide (Sigma-Aldrich) for live/dead cell discrimination. The leukemic cells in the culture were specifically recognized by either EGFP expression (REH, MOLM-14) or after staining with CD15-FITC or CD33-FITC REAfinity™ antibodies. The samples were analyzed on a MACSQuant® Analyzer 10 (Miltenyi Biotec). The specific lysis in % was calculated as [1 – number of viable target cells (sample)/number of viable target cells (control)] × 100%.

NSG Xenotransplantation Mouse Model

All animal experiments were approved by the state animal research committee (LANUV, NRW, Germany). The use of leftover primary blasts from the initial AML diagnosis of children or adolescents treated within the AML-BFM study group was authorized by the ethics committee of the medical faculty at the University of Duisburg-Essen (application number 16-7069-BIO). Each AML-BFM trial was previously approved by their local institutional ethics committees: the Hannover Medical School for AML-BFM 2012 trial and registry (application number 13.03.12/La) and the University of Duisburg-Essen's medical faculty for AML-BFM 2017 registry (application number 17-7462-BO). The primary blasts were injected into 8- to 16-week-old NOD.Cg-Prkdc^{SCID}Il2rg^{tm1Wjl}/SzJ (NSG) mice (Charles River Laboratories, Sulzfeld, Germany) and then sacrificed upon the clinical manifestation of the AML (Füchtjohann, Hanenberg, *in preparation*, 2022).

For analyzing the *in vivo* persistence of NK cells, 8- to 10-week-old NSG mice were treated by i.p. injection of 25 mg/kg of busulfan (Busilvex®, Busulfan, Medac, Darmstadt, Germany) and the next day intravenously transplanted with 10 × 10^6 NK cells containing 50% transduced and 50% untransduced NK cells. Transduced NK cells co-expressed either soluble human IL15 and EGFP or human IL15 bound/tethered to the IL15 receptor α-chain (IL15-IL15R) and EGFP. Control mice were transplanted with 10 × 10^6 untransduced NK cells. Each group consisted of 3 animals. Peripheral blood was analyzed at days 5, 10, 20, and 27 after lysis of erythrocytes with BD Pharm Lyse (BD Biosciences, San Jose, CA, USA) on a MACSQuant™ Analyzer 10 for murine CD18, human CD45, CD56, and EGFP-expressing cells (all antibodies were REA clones from Miltenyi Biotec) as described previously (28).

For the engraftment of REH cells expressing a firefly luciferase/EGFP fusion protein (REH^{LucEG}) (28), 7- to 10-week-old NSG mice were treated by i.p. injection of 25 mg/kg of busulfan and the next day intravenously transplanted with 3.5 × 10^6 REH^{LucEG} cells *via* tail vein injections. Two days later, the animals were randomized into different treatment groups and injected with 3.5 × 10^6 NK cells containing 50% positive CD19 CAR NK cells co-expressing BFP, IL15, or IL15-IL15R and 50% untransduced NK cells (6 mice per group, 7 mice as untreated control). Luminescence analysis was performed on days 7, 15, 22, and 27 as previously described (20) to assess the progression/proliferation of the ALL blasts. Peripheral blood was obtained at days 8, 15, and 22 *via* the tail vein and, after lysis of erythrocytes with BD Pharm Lyse, analyzed on a MACSQuant™ Analyzer 10 for EGFP positive REH^{LucEG} cells and BFP, CD34, CD56, and CD94 NK cells (CD34-PE from Thermo Fisher Scientific, all other antibodies from Miltenyi Biotec).

Fluorescence Microscopy

MACS-enriched CAR NK cells co-expressing BFP were stained with the QBend-10 CD34-PE antibody (as described above) and then co-cultured with EGFP-expressing REH cells in complete DMEM at an NK cell to target cell ratio of approximately 0.3:1. For these experiments, gelatin-treated 8-well slides with glass bottom (ibidi GmbH, Gräfelfing, Germany) were used. Bright-field and epifluorescence images were acquired at 37°C for 1–4 h after the seeding using an IX83 Inverted Microscope (Olympus, Hamburg, Germany), a 100× oil objective (NA 1.49, UAPON100XOTIRF, Olympus, Hamburg, Germany), and the cellSens Dimension software (Olympus, Hamburg, Germany). Images were processed using the open-source Fiji software (https://imagej.net/software/fiji/).

Statistical Analysis

Statistical analyses were performed using GraphPad PRISM 9.0 using the log-rank test, one-way ANOVA with Tukey adjustment for multiple comparisons, and unpaired Student's t-test for single comparison. p-Values ≤ 0.05 were considered significant and indicated with an asterisk.

RESULTS

To define optimal conditions required for the generation of CAR-expressing primary human NK cells and their expansion under Good Manufacturing Practice (GMP)-compliant conditions recently published in cooperation with Miltenyi Biotec (26), we systematically tested a number of variables that are known to influence the cytotoxicity of genetically modified NK cells.

Lentiviral Pseudotypes for Efficient Transduction of Human NK Cells

Recently, two constructs derived from the envelope protein of the baboon endogenous virus, BaEV-Rless and BaEV-TR (14) have been published that are optimally suited for genetically modifying NK cells (21, 23). We additionally wanted to assess the transduction efficiency achieved in human NK cells with an alternative envelope pseudotype, GALV-TM, a chimera generated from the gibbon ape leukemia virus and the aMLV envelope proteins (34), that we previously used for the transduction of human CD34+ stem cells (35). For efficient virus production, our lentiviral vector plasmid pCL6EGNwo, expressing a fusion protein of EGFP and the neomycin resistance gene under the control of a modified SFFV promoter (27), was pseudotyped with the three envelopes. As additional controls, we also pseudotyped the lentiviral vector with the feline endogenous virus chimeric construct RD114-TR (31) and VSV-G (20).

Primary human NK cells were isolated and expanded as previously described (26) and then transduced with serially diluted (1:10 to 1:10,000) non-concentrated supernatants of freshly produced lentiviral vector particles on Retronectin-coated 96-well plates. Three to four days after transduction, NK cells were analyzed by flow cytometry for EGFP expression. As shown in **Figure 1A**, BaEV-Rless was the most efficient pseudotype, as 28% of NK cells were EGFP positive using 1:10-diluted viral supernatant; even a 1:1,000 dilution of this pseudotype was associated with a higher transduction efficiency than VSV-G at a 1:10 dilution. The lentiviral vectors pseudotyped with BaEV-TR or GALV-TM transduced approximately 9% (at 1:10) to 0.3% (at 1:1,000) of the NK cells. While being more efficient than VSV-G, the RD114-TR pseudotype was still rather inefficient with gene transfer rates ranging from 2.2% to 0.1%.

Retronectin *vs.* Vectofusin for Enhancing the Transduction of Human NK Cells

To promote the binding of lentiviral particles on the surface of target cells and thereby increase the likelihood of viral entry, cationic culture additives such as polybrene or protamine sulfate have been used during the transduction procedure and neutralize the electrostatic repulsion between the opposing negatively charged membrane bilayers (36, 37). Vectofusin is such a histidine-rich cationic amphipathic peptide that was developed to promote efficient lentiviral transduction of primary human cells (38), including T and NK cells (39). Alternatively, a recombinant chimeric fragment derived from human fibronectin, CH-296 or Retronectin, is used since 1996 in research settings and in clinical trials to promote colocalization of viral particles and mammalian target cells, thereby increasing the efficiency of the genetic modification for both adherent and non-adherent cells (32, 33). Although the effects of Vectofusin and Retronectin on the transduction of different non-adherent cell types including human CD34+ hematopoietic stem cells (38) and also primary human NK cells (23, 39) have been reported, this type of comparison has not been performed for the lentiviral BaEV pseudotype that mediates the most efficient gene transfer into primary human NK cells (**Figure 1A**).

Therefore, we transduced primary human NK cells with the pCL6EGNwo vector (27) pseudotyped with BaEV-Rless, BaEV-TR, or GALV-TM using serial dilutions, ranging from 1:2 to 1:1,000. Transduction was performed in flat-bottom 96-well plates, either coated with Retronectin or after supplementing Vectofusin to the culture medium. Control NK cells were transduced in 96-well cell culture plates without any additional transduction enhancer. The gene transfer efficiencies into the human NK cells were analyzed 3 to 4 days later by flow cytometry, and the values were normalized by assigning 100% to the highest transduction efficiency achieved within the cell series of each donor. Remarkably, the BaEV-Rless pseudotype on Retronectin mediated the highest gene transfer in each of the four donors and was therefore set at 100%, while the other two pseudotypes BaEV-TR and GALV-TM did not even achieve 50% of the BaEV-Rless transduction efficiency (**Figure 1B**). Using Vectofusin with the BaEV-Rless-pseudotyped lentiviral particles resulted in roughly 80% of the Retronectin-assisted gene delivery and was clearly better than the gene transfer efficiencies observed with the other two pseudotypes BaEV-TR and GALV-TM. The gene transfer without any transduction enhancer was very low regardless of the glycoprotein used. Therefore, for the remaining experiments in this study, we chose to perform the lentiviral transductions of primary human NK cells with the BaEV-Rless pseudotype on Retronectin-coated plates.

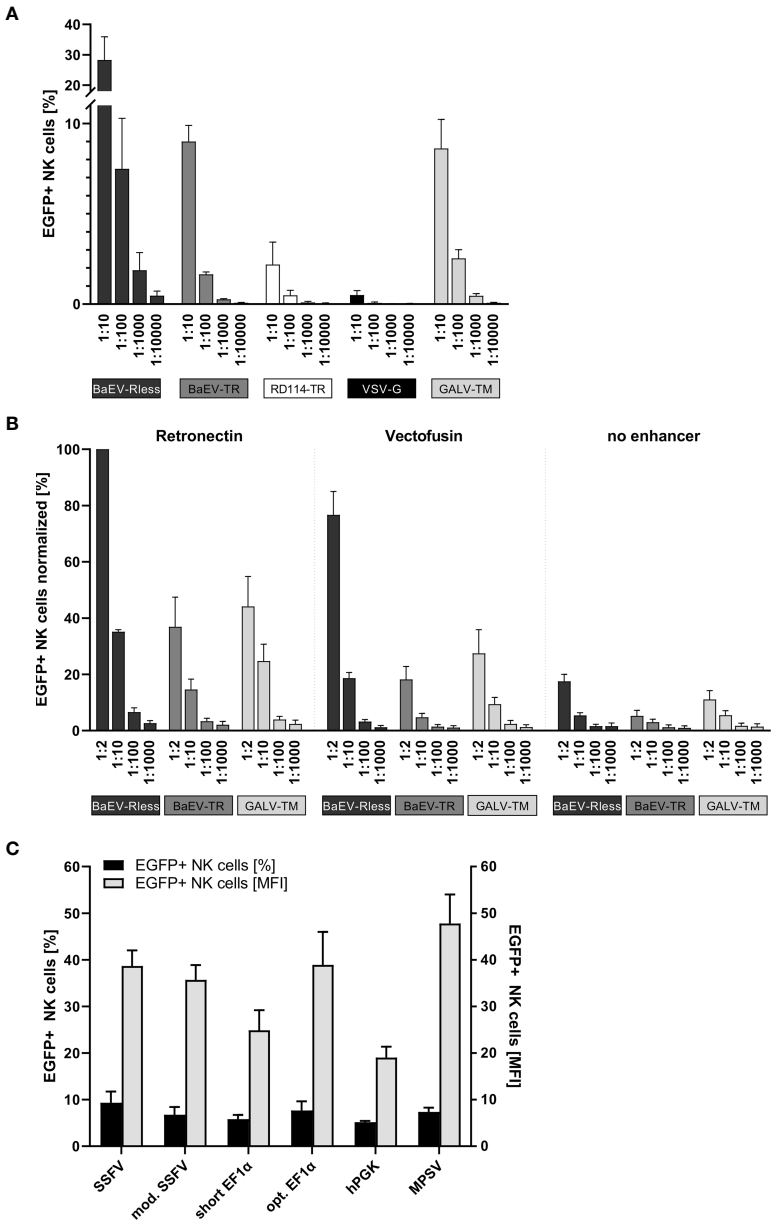

FIGURE 1 | Systematic improvement of primary human NK cell transduction. Primary human NK cells were isolated and cultured as described in the body of the manuscript. **(A)** After 7 to 10 days of expansion, NK cells were transduced with serial dilutions of EGFP-expressing lentiviral particles pseudotyped with BaEV-Rless, BaEV-TR, RD114-TR, VSV-G, or GALV-TM. Three to four days after transduction, EGFP expression was analyzed by flow cytometry. Data are represented as mean ± SEM of four biological replicates. **(B)** Primary human NK cells were transduced with serial dilutions of EGFP-expressing lentiviral particles pseudotyped with BaEV-Rless, BaEV-TR, or GALV-TM, using Retronectin, Vectofusin, or no transduction enhancer, respectively. Three to four days after transduction, EGFP expression was analyzed by flow cytometry. Data are represented as mean ± SEM of five biological replicates. **(C)** Primary human NK cells were transduced with serial dilutions of lentiviral particles pseudotyped with BaEV-Rless, expressing EGFP under the control of the wild-type or modified SFFV, the wild-type or optimized EF1α, the hPGK, or the MPSV promoter. Three to four days after transduction, the expression of EGFP was analyzed. From the serial dilutions, samples with gene transfer rates of between 5% and 10% were analyzed for their EGFP expression intensity [mean fluorescence intensities (MFIs)]. Data are represented as mean ± SEM of four biological replicates.

A Promoter for High-Level Transgene Expression in Human NK Cells

We have previously shown that the U3 region of the MPSV as an internal promoter in our self-inactivating (SIN) lentiviral vectors is the best choice for achieving high-level gene expression in primary human T cells (27). Here, in order to identify an optimal internal promoter for stable high-level CAR expression in primary human NK cells, we tested the MPSV and two

additional viral promoters as internal promoters in our lentiviral pCL6EGNwo vector (27): the U3 regions from SFFV (40) with one (mod. SFFV) or with two enhancer regions (SFFV). We also included two promoters of human cellular housekeeping genes, namely, the human phosphoglycerate kinase-1 (hPGK) (27) and the human elongation factor 1α (EF1α) promoter with (opt. EF1α) or without (short EF1α) an optimized splicing unit as internal promoters.

Primary human NK cells were transduced with serially diluted BaEV-Rless-pseudotyped lentiviral vectors expressing the EGFP-neomycin fusion as marker gene under the control of the different promoters. Three to four days after transduction, NK cells were analyzed for EGFP expression by flow cytometry. We compared the mean fluorescence intensity (MFI) of the different promoters in samples with a gene transfer of approximately 5%–10%, as cells with this gene transfer rate most likely carry only one copy of the vector integrated into their genome (27), thereby eliminating the bias of multiple integrations on the transgene expression levels. As shown in **Figure 1C**, the hPGK and short EF1α promoters with MFIs of 19.0 and 24.9, respectively, were associated with the lowest transgene expression levels. Optimizing the splice unit of EF1α by shortening the intron and correcting an open reading frame in the intron improved the transgene expression levels of the optimized EF1α promoter to those of the SFFV promoters with MFIs ranging from 35.7 to 38.9. However, the MPSV U3 promoter with an MFI of 47.8 still provided the highest level of transgene expression, and thus it was chosen for the expression of CAR constructs in primary human NK cells for our subsequent experiments.

Transduction and Enrichment of Human CAR NK Cells

After the establishment of an optimized transduction protocol, primary human NK cells with low CD33 expression were transduced with 5-fold concentrated BaEV-Rless-pseudotyped lentiviral particles encoding BFP *in cis* with CD19, CD33, CD123, or EGFR CARs, harboring our CD34-derived hinge (20, 29), on Retronectin (**Figures 2A, B**). Three to four days after transduction, the expression of the CARs was analyzed after staining of the C6 hinge region with the QBend-10 antibody and detecting BFP expression by flow cytometry. As shown in **Figure 2C**, CD34/CAR expression strongly correlated with BFP expression for all four CAR constructs. To purify the CAR NK cells, we then performed MACS enrichment on an OctoMACS™ separator using MS columns and CD34 microbeads binding to the C6 hinge. As an indicator of the content of transduced NK cells, BFP expression was analyzed in three fractions: before MACS, the flowthrough, and after MACS (representative samples in **Figure 2D**). Before MACS enrichment, we obtained on average of between 38.8% ± 3.4% (Cetux) and 47.0% ± 3.7% (CD123) CAR-positive NK cells. Enrichment of CAR NK cells on MACS columns led to purification rates of between 96.2% ± 1.2% (CD123) and 97.7% ± 0.8% (CD19). However, the flowthrough contained relatively high percentages of CAR NK cells (between 24.4% ± 2.2% for CD123 and 29.0% ± 4.2% for Cetux), albeit with much lower MFIs than the CAR NK cells before or after MACS (**Figure 2E**).

Reduction of Background Killing of Leukemic Cell Lines by Activated Human NK Cells

For more than 40 years, it is well established that after stimulation, primary human NK cells can exhibit high cytotoxic activities against human leukemic cells (41). This cytotoxicity is often mediated by the expression of antigens on the leukemic blasts that are ligands for activating receptors on NK cells (42). As *in vitro* expanded NK cells are highly activated (26), they often recognize and thus kill leukemia cells independently of CAR antigen binding (42). In order to eliminate this "background" killing for follow-up assays, we planned to systematically block activating receptors of the NK cells in cytotoxic experimental settings. To this end, we co-cultured cells of four AML cell lines and two B-cell precursor ALL cell lines overnight with three ratios of PB-derived 7- to 14-day-old NK cells with the effector-to-target cell ratios of 3:1, 1:1, and 0.3:1. In parallel, overnight co-cultures were set up with the same NK cells, albeit preincubated with monoclonal antibodies that recognized and block either three (NKG2D, NKp30, and NKp46) or six (NKG2D, DNAM-1, NKp30, NKp44, NKp46, and NKp80) activating receptors on NK cells (11, 43). Although these recombinant antibodies were all mutated in their Fc domains and therefore should not bind to human Fc receptors, we still included a co-culture condition with NK cells that were preincubated with the appropriate isotype controls.

As demonstrated in **Figure 3**, the degree of target cell lysis by activated NK cells seemed to be cell line-specific. On the other hand, three AML cell lines [MOLM-14 (AML-M5), THP-1 (AML-M4), and CMK (AML-M7)] and two B-cell precursor leukemic lines [REH and BV-173] were killed efficaciously by the activated NK cells in the absence of blocking antibodies and also in the presence of isotype controls; NOMO-1 (AML-M5) cells were resistant to NK cell killing. Importantly, preincubation with all six antibodies ameliorated the cytotoxicity of the NK cells against the five susceptible cell lines quite efficiently; however, using the three antibodies against NKG2D, NKp30, and NKp46 only partially reduced the NK cell-mediated killing for two AML cell lines, MOLM-14 and CMK (**Figure 3**).

CAR NK Cells Effectively Kill AML and ALL Cell Lines as Well as Primary AML Blasts *In Vitro*

After successfully establishing a blocking protocol, we specifically tested the functionality of CAR NK cells against one ALL and two AML cell lines. To this end, MACS-enriched CAR NK cells of at least five healthy donors with low CD33 expression (data not shown) were blocked with all six monoclonal antibodies described above and then co-cultured overnight with NOMO-1, MOLM-14 (both CD19− CD33+ CD123+), and REH (CD19+ CD33− CD123-) cells at various effector-to-target cell ratios. Flow cytometric analysis revealed the expression patterns of

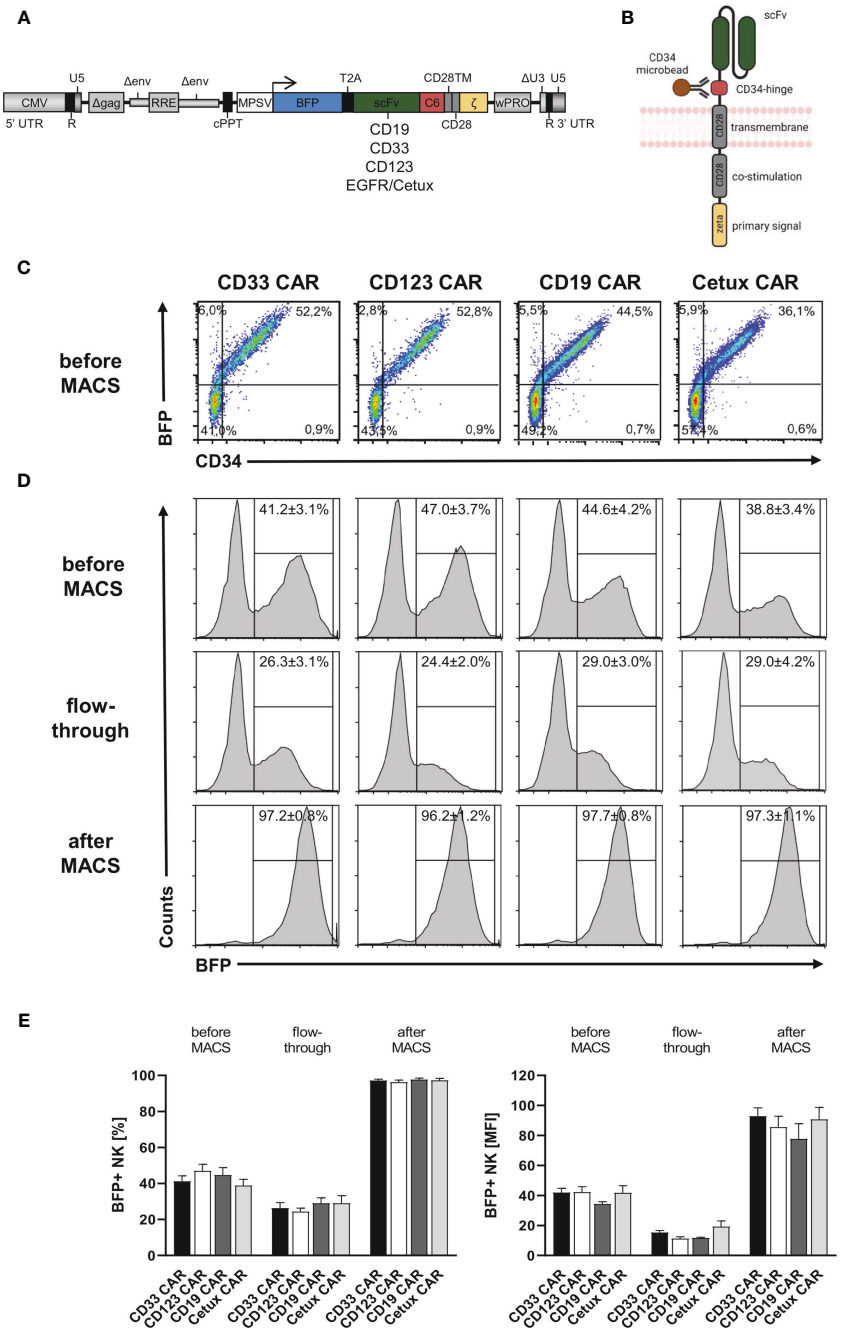

FIGURE 2 | CD34-hinged CAR expression and enrichment in primary human NK cells. Primary human NK cells were transduced with the lentiviral vectors delineated in panels **(A, B)** encoding BFP *in cis* with CD34-hinged CD33, CD123, CD19, or Cetux CARs. **(B)** Schematic representation of CAR construct including CD34-derived C6 hinge for microbead interactions. **(C)** Three to four days after lentiviral CAR transduction, NK cells were analyzed for BFP and CAR (via CD34-PE staining) expression by flow cytometry. Representative dot plots are shown. **(D, E)** CD34-hinged CAR NK cells were enriched *via* magnetic cell sorting using CD34 microbeads and three fractions (before MACS, flowthrough, and after MACS) were analyzed for the content of NK cells expressing BFP by flow cytometry. The histogram blots show representative data. Data are represented as mean ± SEM of at least four biological replicates.

CD19, CD33, and CD123 for each of the target cell lines (**Figure 4A**). After 16 h of co-culture, CD33 and CD123 CAR NK cells efficaciously killed NOMO-1 and MOLM-14 cells with approximately 90% specific lysis at an effector-to-target cell ratio of 1:1 (**Figure 4B**). Interestingly, although CD123 is expressed much lower on NOMO-1 cells than CD33 (**Figure 4A**), CD123 CAR NK cells performed as well as CD33 CAR NK cells in the NOMO-1 co-cultures. REH cells were highly efficaciously (>95%

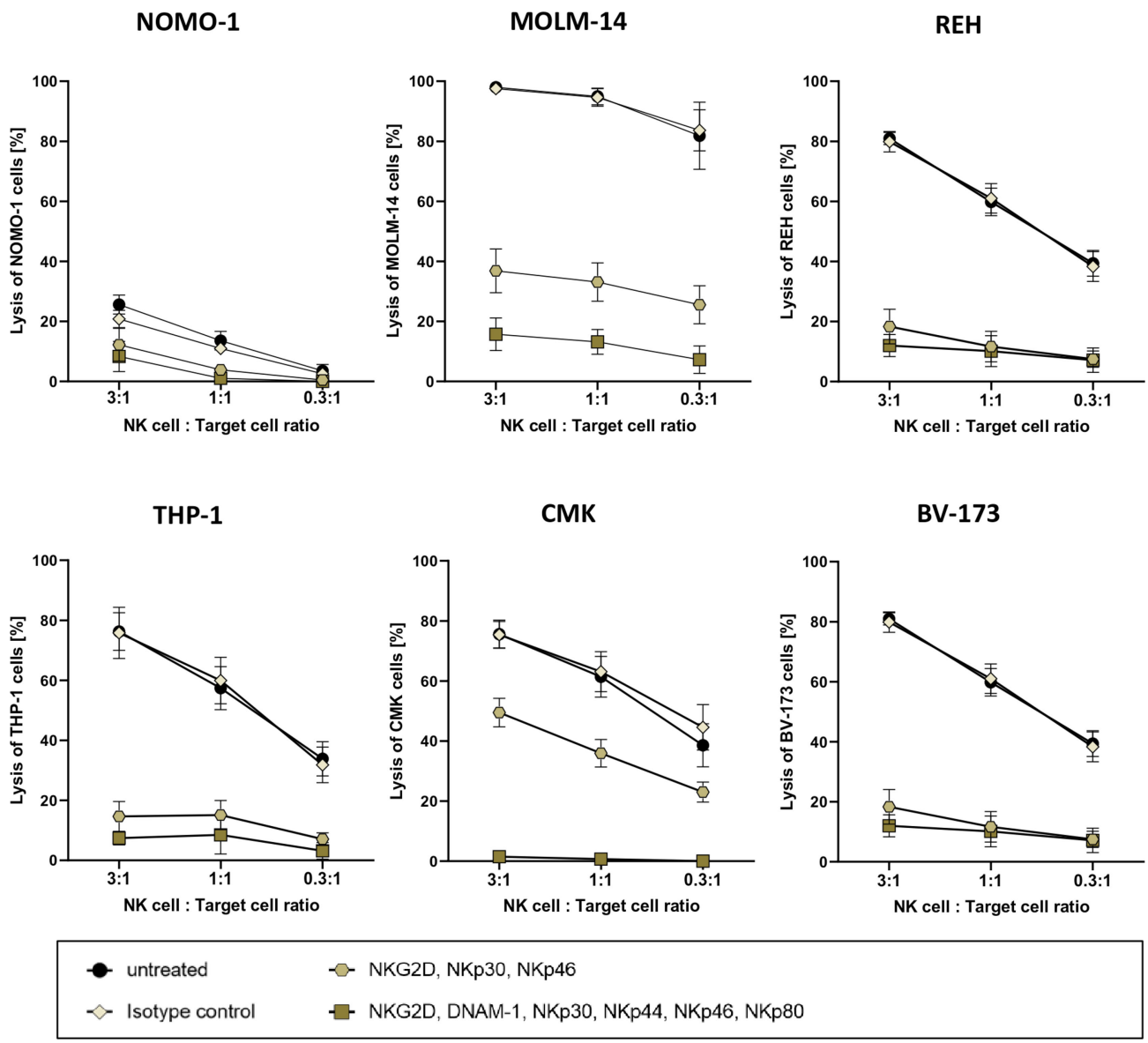

FIGURE 3 | Cytotoxic potency of activated primary human NK cells against acute leukemia. Killing of various leukemic cell lines by activated primary human NK cells was analyzed by co-culture of NK cells and target cells at several ratios. Activated primary human NK cells were incubated with blocking antibodies against activation receptors (as stated) and co-cultured with NOMO-1, MOLM-14, REH, THP-1, CMK, and BV-173 cells at various ratios to determine cytotoxic activity of NK cells. After 16 h of co-incubation at 37°C, the cytotoxicity of the treated and untreated NK cells was analyzed *via* flow cytometry, and the degree of the cell lysis was analyzed as described in the *Material and Methods*. The graphs represent mean ± SEM of four biological replicates.

at 1:1) eradicated by CD19 CAR NK cells, but not by the other CAR constructs (**Figure 4B**). Importantly, the lysis was strongly dependent on the specific antigen expression, and we did not observe off-target toxicities in these experiments.

Next, we hypothesized that the CAR NK cells would also specifically kill primary AML blasts obtained at diagnosis and expanded in NSG mice (Füchtjohann, Hanenberg, *manuscript in preparation 2022*). As AML blasts can express low levels of CD19, we used the EGFR-recognizing Cetux CAR NK cells as negative controls. Flow cytometric analysis revealed the expression patterns of EGFR, CD33, and CD123 for the primary AML blasts used (**Figure 4C**). The results in **Figure 4D** demonstrated that the CD33+ CD123+ primary AML-M4 blasts were specifically killed (up to 90% at 1:1), while only 60% of CD33+ CD123+ primary AML-M5 blasts were eliminated by both CD33 and CD123 CAR NK cells at 3:1 and 1:1 ratios, respectively.

Finally, we took advantage of the fact that our CARs contained the CD34-derived C6 hinge to visualize the specific interaction of CD19 CAR NK cells with the CD19-positive REH

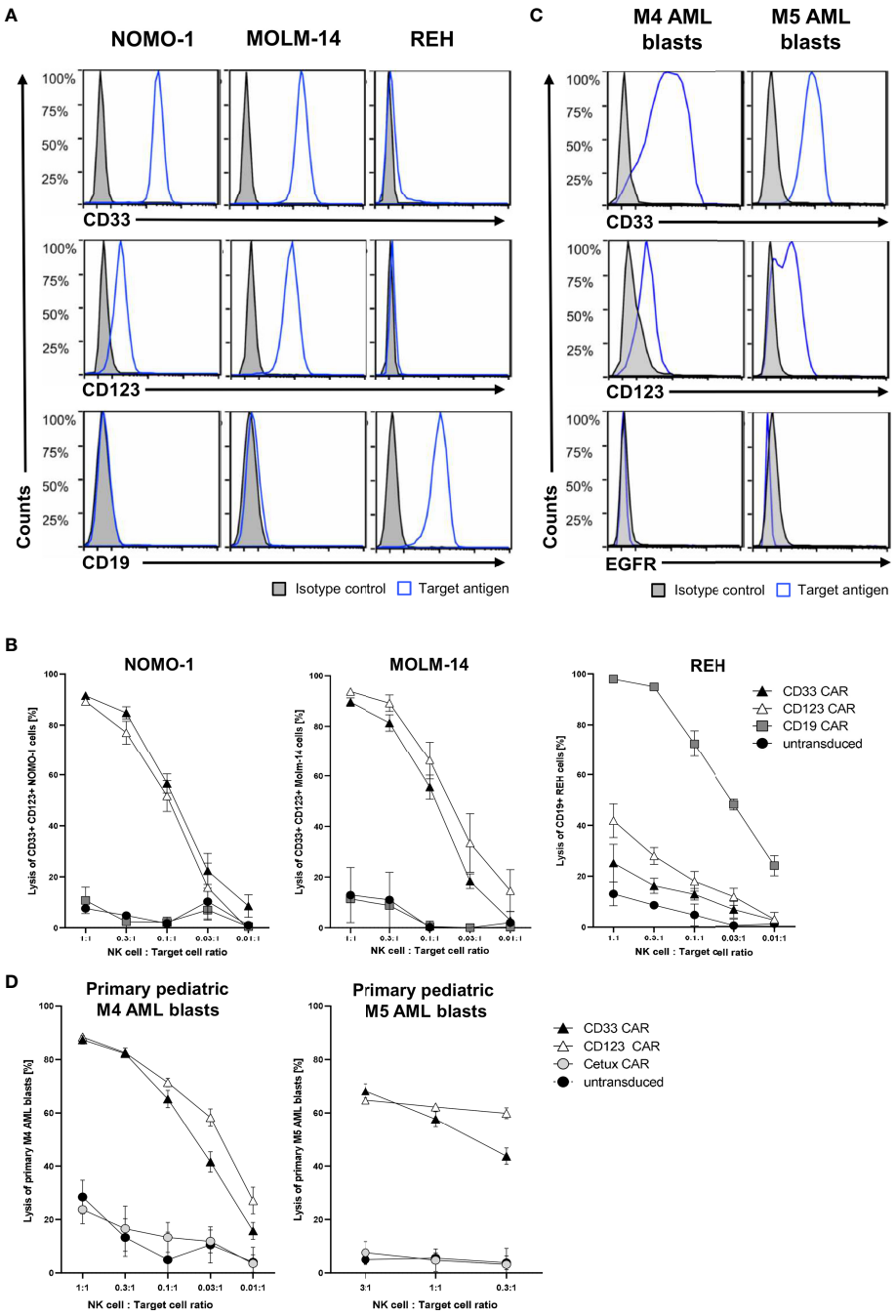

FIGURE 4 | Cytotoxic activity of CAR NK cells against leukemic cells. **(A)** AML cells NOMO-1 and MOLM-14, and ALL cells REH were analyzed for their surface expression of CD19, CD33, and CD123. **(C)** Primary pediatric M4 and M5 AML blasts were analyzed for their surface expression of CD33, CD123, and EGFR using conjugated antibodies by flow cytometry. CAR-transduced and microbead-enriched primary human NK cells were blocked as described previously and co-cultured with NOMO-1, MOLM-14, and REH cells **(B)** or primary pediatric M4 and M5 AML blasts **(D)** at various effector-to-target cell ratios to determine the specific cytotoxic activity of CAR NK cells. The graphs represent mean ± SEM of at least five (cell lines) or three (AML blasts) biological replicates.

cells in the presence of blocking antibodies. For the fluorescence microscopy analysis, the PE-conjugated QBend-10 antibody was employed to label the hinge region of CD19 or CD33 CAR NK cells, which both co-expressed BFP, while the target REH cells expressed EGFP. As indicated by the white arrow in **Figure 5A**, the CD19 CAR constructs on the transduced NK cells accumulated in immunological synapses formed between 1 and 4 h between NK and REH cells. In contrast, the CD33 CAR

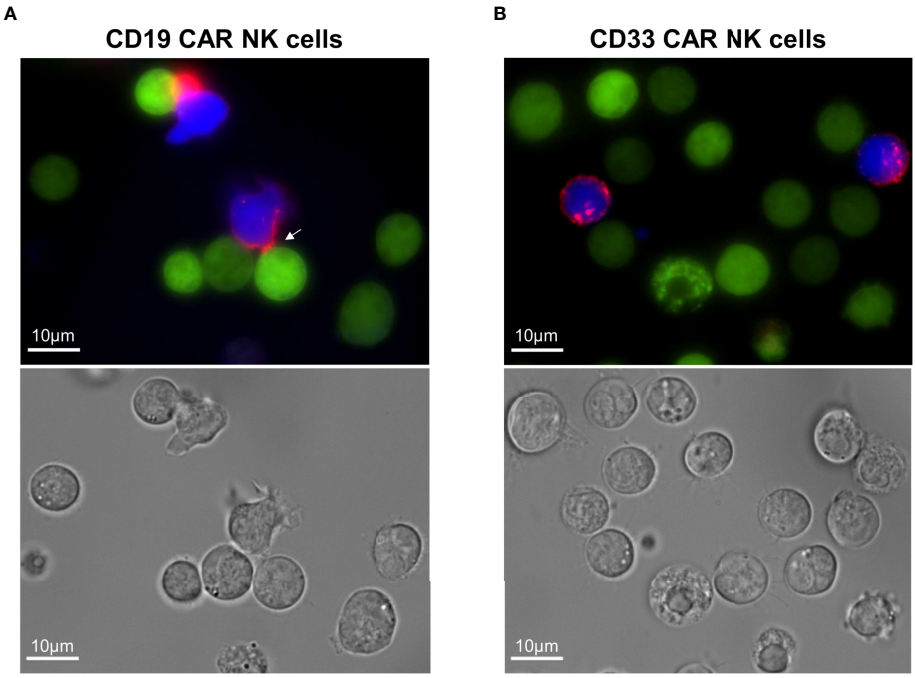

FIGURE 5 | Visualization of the immunological synapses formed between CD19 CAR NK cells and CD19+ REH cells. **(A)** The immunological synapse between CD19 CAR NK cells and CD19+ REH cells was analyzed by fluorescence microscopy, visualizing the CAR expression (CD34-PE-conjugated antibody, red) on MACS-enriched CAR NK cells (BFP expression, blue) in relation to REH cells (EGFP expression, green). **(B)** MACS-enriched CD33 CAR NK cells served as negative controls. Contrast settings are uniform for both images for the channels: brightfield, 377/447 and 470/525 nm. The contrast in channel 545/620 nm was adjusted to maximize the visibility of the cell-to-cell contacts.

constructs were equally dispersed on the cell surfaces of CD33 CAR NK cells (**Figure 5B**), suggesting that no specific interaction with the CD33-negative REH cells occurred.

CD19 CAR NK Cells Effectively Kill CD19+ ALL Cells *In Vivo*

For *in vivo* application of activated NK cells in humans, it is paramount that NK cells do not possess autocrine stimulation loops that would ensure their survival beyond a few days in patients (44, 45). Therefore, allogeneic NK cell therapies are usually accompanied by the subcutaneous application of IL2 or intravenous infusions of lentiviral IL15; both treatments are actually associated with severe side effects in patients (44, 45). In order to evaluate the impact of IL15 signaling on the persistence of NK cells *in vivo*, we generated two lentiviral IL15 vectors (**Figure 6A**): the first expressed soluble human IL15 and EGFP, and the second human IL15 tethered to the IL15 receptor α-chain (IL15-IL15R) and EGFP. Importantly, both IL15 constructs were able to mediate the expansion of primary NK cells in *in vitro* experiments in the absence of any other growth factors (data not shown). Next, NSG mice were injected with 5×10^6 EGFP+ NK cells expressing either soluble IL15 or IL15-IL15R and 5×10^6 untransduced NK cells. We used this 1:1 ratio *in vivo* to investigate potential survival advantages of IL15 expressing NK cells over untransduced NK cells in each mouse and also to understand the impact of IL15-tethering for both populations. The persistence of human NK cells was assessed for 27 days (**Figure 6B**), using the gating strategy shown in **Figure 6C** for the peripheral blood analysis on day 10. **Figure 6D** reveals that the NK cell survival was highly dependent on IL15 signaling, as the percentages of NK cells in the blood of the mice transplanted with untransduced NK cells progressively decreased over time. In contrast, both strategies to express IL15 *in vivo* drastically improved the initial NK cell engraftment and also the persistence of NK cells at all sampling time points. Remarkably, the ratio of EGFP positive to negative cells stayed rather constant at 1:1 for the soluble IL15, while the IL15-IL15R expressing NK cells appeared to slowly outgrow the untransduced cells over time: after 27 days, approximately 70% of all NK cells in the blood of the animals were EGFP positive.

Finally, we used an ALL xenograft model in NSG mice to evaluate the impact of IL15 signaling for the survival and leukemia control of CAR NK cells *in vivo*. For this experiment, three CD19 CAR vectors were generated (**Figure 7A**) co-expressing *via* a T2A site either BFP, soluble human IL15 (17), or human IL15 tethered to the IL15 receptor α-chain (IL15-IL15R) (46). For the *in vivo* experiments, NSG mice were transplanted intravenously with 3.5×10^6 REH cells expressing a firefly luciferase/EGFP fusion protein (REH^{LucEG}). Two days later, 3.5×10^6 total primary human NK cells with 50% non-transduced and 50% transduced cells were injected *via* the tail

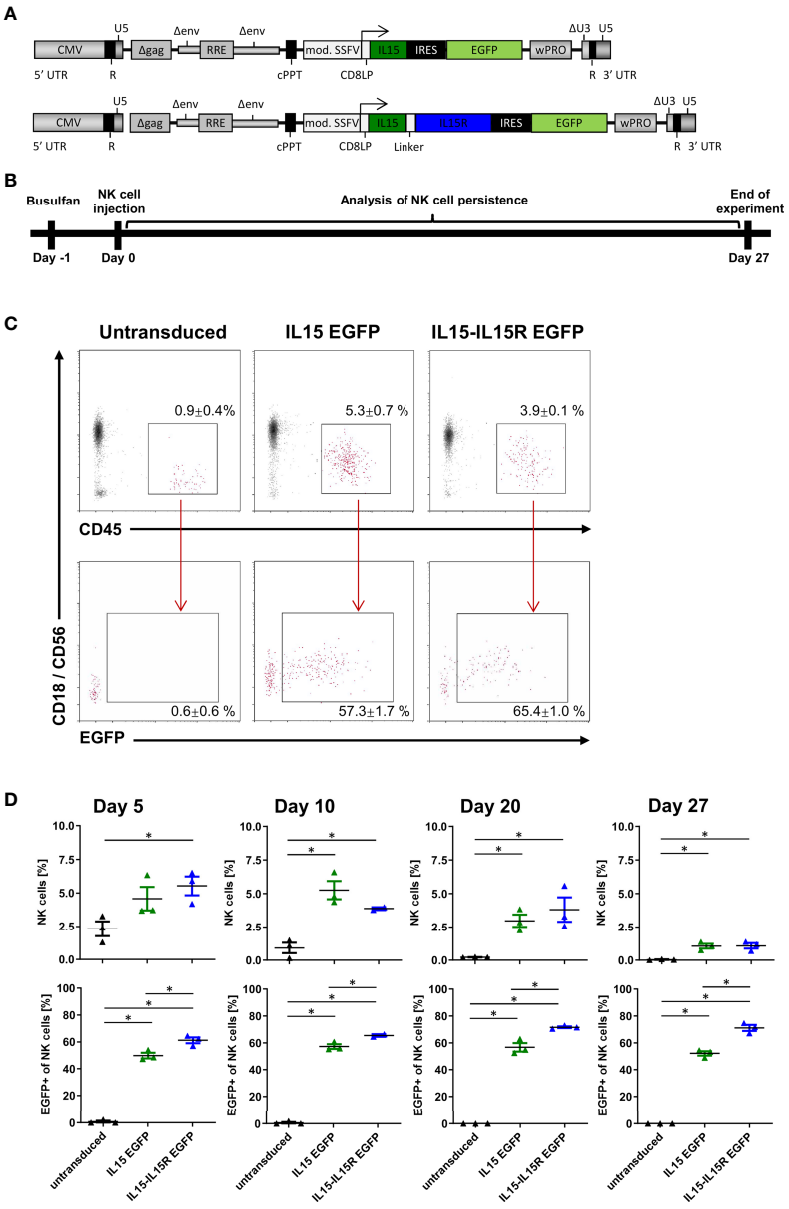

FIGURE 6 | NK cells rely on endogenous IL15 production for *in vivo* persistence in NSG mice. **(A)** Schematic representation of the vector maps of the IL15 constructs used for NK cell transduction. **(B)** Primary human NK cell preparations consisting of 50% EGFP/IL15 or EGFP/IL15-IL15R and 50% untransduced NK cells (or 100% untransduced cells as control group) were injected into busulfan-preconditioned mice (3 animals per group). On days 5, 10, 20, and 27, NK cell persistence in the bloodstream was analyzed by mouse CD18, human CD45, and CD56 staining as well as EGFP expression. **(C)** Example of gating strategy showing representative data from day 10. Values indicate mean ± SEM of all three animals. **(D)** NK cell persistence in the blood including ratios of transduced to untransduced NK cells. Data are represented as mean ± SEM. Significances of $p<0.05$ are indicated by an asterisk (*).

vein (**Figure 7B**). Untreated NSG mice showed rapid leukemia progression and had to be sacrificed between days 17 and 19 (**Figures 7C, D**). Surprisingly, treatment of the mice by infusion of BFP/CD19 CAR NK cells did not improve the survival at all (**Figures 7C, D**). For these two groups, the REH cells made up between 0.3% and 0.4% of peripheral blood cells on day 7 and between 3.3% and 7% on day 15 (**Figure 7E**). Interestingly, the BFP/CD19 CAR NK cells were still detectable at day 8 (2.3% of peripheral blood cells) but did not persist in the blood beyond this time point (**Figure 7F**). When the CD19 CAR NK cells additionally expressed IL15 or IL15-IL15R instead of BFP, the leukemia progression was markedly reduced as seen by luminescence imaging (**Figure 7C**) and peripheral blood analysis (**Figure 7E**). We attributed the improved survival of the animals to the robust increase in the persistence of CAR NK cells, as these immune effector cells were detected at high levels

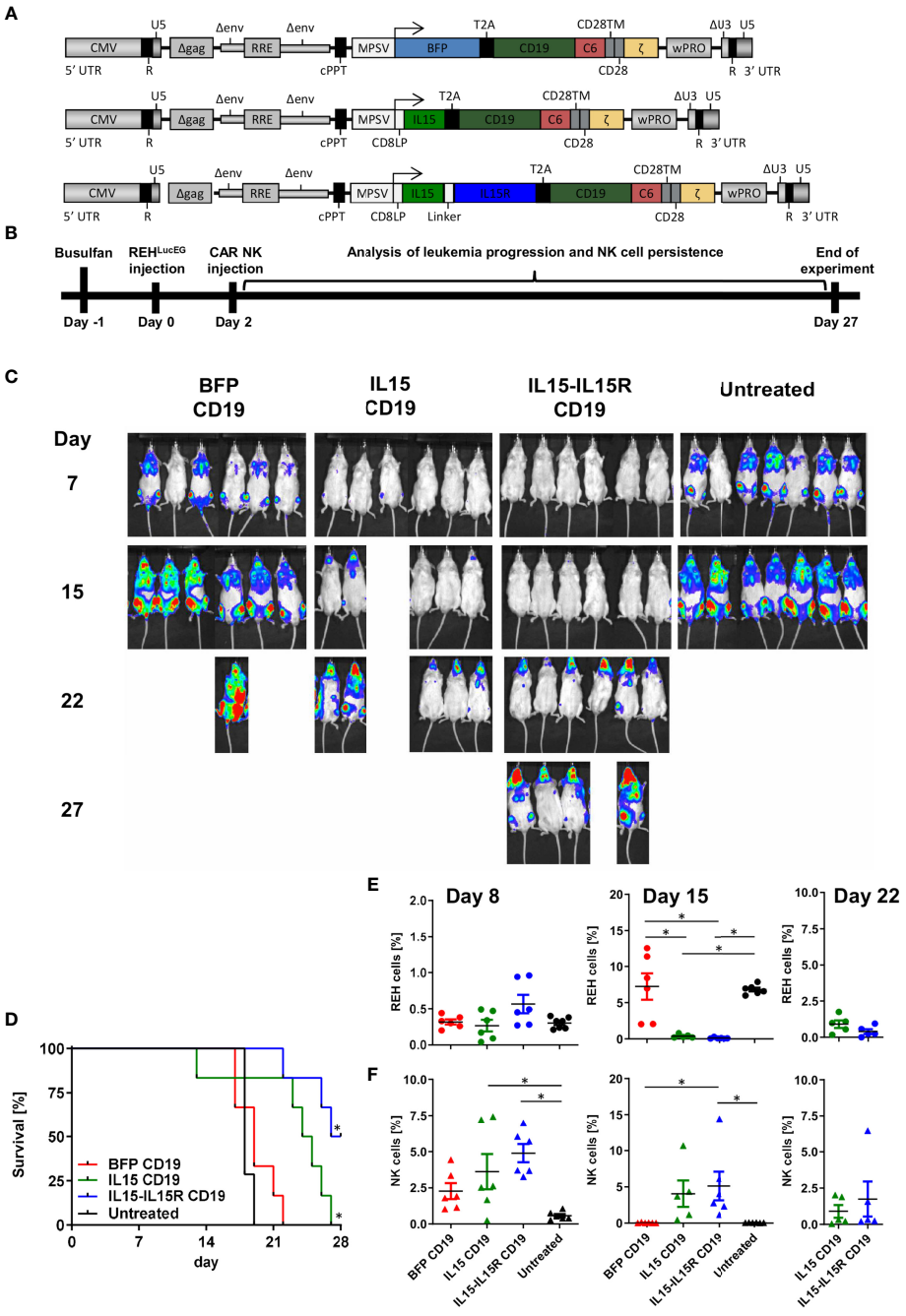

FIGURE 7 | CAR NK cells rely on endogenous IL15 production for leukemia control in an ALL xenograft model. **(A)** Schematic representation of vector maps of CAR constructs used for NK cell transduction. **(B)** Primary human NK cell preparations consisting of 50% BFP/CD19 CAR, IL15/CD19 CAR, or IL15-IL15R/CD19 CAR and 50% non-transduced NK cells were injected 2 days after xenotransplantation of REH^{LucEG} into busulfan-preconditioned NSG mice (6 animals per group, 7 animals as untreated control). **(C)** On days 7, 15, 22, and 27, leukemia progression was analyzed by luminescence imaging in a Caliper device. **(D)** Kaplan–Meier survival curves for the three treatment groups and the untreated control animals. **(E)** REH^{LucEG} and **(F)** NK cell persistence in the bloodstream was analyzed by CD19, CD34, CD45, and CD56 staining as well as EGFP expression by flow cytometry. Data are represented as mean ± SEM. Significances of $p<0.05$ are indicated by an asterisk (*).

on day 15 (4% for IL15/CD19 and 5.1% for IL15-IL15R/CD19 CAR NK cells) and were even present at lower levels on day 22 in the peripheral blood of the animals (**Figure 7F**). Importantly, however, the animals in the IL15 and IL15-IL15R groups all showed ALL persistence in central nervous system (CNS) lesions (**Figure 7C**). These lesions partly led to neurological deficits/abnormalities, and the majority of these animals had to be sacrificed between days 22 and 27. At the termination of the

experiment, three NSG mice of the IL15-IL15R/CD19 CAR NK cell group were still alive, albeit all affected by CNS leukemia.

DISCUSSION

The application of risk-adapted treatment protocols has greatly improved the survival of children and adolescents with ALL and acute myeloid leukemia (AML) during the past four decades (47). However, a significant number of patients, at least 10% of pediatric ALL and 25% of pediatric AML, still suffer from relapse and/or refractory disease and despite all efforts ultimately succumb to their leukemia (48–51). For these patients, phase I/II clinical trials with adoptive cellular therapies generally were only beneficial in post-transplantation settings, where lymphocyte infusions of the stem cell donors are often sufficient to treat minimal residual disease and even full-blown relapses (52). Infusions of allogeneic NK cells have also been tested in clinical trials and were tolerated well without any GvHD; however, the therapeutic benefits were rather limited, and the concomitant treatment with IL2 or IL15 was associated with profound acute toxicities (11). Recently, antibody-based immunotherapies with bispecific T cell engagers or CAR T cells have achieved remarkable initial success, predominantly for B cell-associated malignancies (53, 54). However, for patients with relapsed/refractory leukemias, the generation of autologous CAR T cells often takes too much time, is technically quite difficult in small children or heavily pretreated patients, and rather impossible for AML patients due to the lack of suitable target antigens for the long-term persistent CAR T cells (53, 54). Here, generating allogeneic CAR NK cells for *off-the-shelf* usage and with limited persistence *in vivo* in patients might be ideal for inclusion in salvage treatment protocols for relapsed/refractory patients, e.g., as a blast-reductive treatment/bridge to allogeneic stem cell transplantation. Taking advantage of the new possibilities to generate allogeneic CAR NK cells on the CliniMACS Prodigy® platform (Miltenyi Biotec) with chemically defined media, we systematically tested variables affecting the transduction and cytotoxic efficacy of allogeneic NK cells with these tools.

The efficacy of CAR immune effector cells to eliminate their target cells is influenced by several factors, including the affinity of the scFv present in the CAR construct, the expression levels of the CAR itself on the effector cells, and availability of the targeted antigen/epitope on the target cell (8, 29). Thus, for CARs with a low affinity or when the target antigen is expressed at low levels, high and stable CAR expression is crucial to ensure excellent antitumor cytotoxicity. To this end, the internal promoter in the SIN lentiviral vector and the CAR/transgene sequence(s), e.g., after the codon optimization, are the main tools to improve CAR expression levels. As we already employed cDNAs optimized for human codon usage, the systematic testing of various promoters was our final step to optimize CAR expression in primary human NK cells. To our knowledge, only Allan et al. tested multiple internal promoters in lentiviral vectors for the transduction of human primary NK cells and finally favored the short human EF1α promoter as the best out of eight candidates for their bicistronic CAR expression cassette (55). In our study, we observed the same relationships when comparing the transgene expression levels of the short EF1α, the EF1α with optimized splicing cassette, and the hPGK promoters, but all eight promoters from Allan et al. still appear to be much weaker than the MPSV promoter that we originally established for robust lentiviral CAR expression in human T cells (27). The original EF1α (56), the human CMV (14), or the SFFV promoter (23, 39) was also used in other studies to express CAR constructs in primary human NK cells. However, since NK cell culture and transduction protocols differ greatly between groups, we analyzed the activity of these commonly used promoters in NK cells expanded in the NK MACS medium from Miltenyi and realized that the MPSV promoter outperformed the hPGK, both SSFV and both EF1α promoters, which is in line with our CAR T cell study (27).

A major advantage of HIV-1-derived lentiviral vectors is their promiscuity in accepting multiple heterologous viral envelopes as pseudotypes, thus allowing a wide tropism of target cells (57). While T cells can readily be genetically modified with the VSV-G pseudotype, neither quiescent nor activated NK cells express sufficient levels of the low-density lipoprotein receptors that are employed by VSV-G pseudotypes to enter target cells (23, 56). Changing the lentiviral pseudotype to BaEV-TR (23, 56) or RD114-TR (39) has resulted in better transduction efficiencies, as the cellular glycoproteins that serve as viral receptors, ASCT-1 and/or ASCT-2, are higher expressed on activated but not on naïve/resting NK cells (23, 56). Noteworthy here is that IL2 priming of human NK cells especially leads to upregulation of the glutamine transporter ASCT2 (14, 58). We also showed that GALV-TM-pseudotyped lentiviral vectors facilitate robust transduction of primary human NK cells, probably as the viral receptor PIT1 is sufficiently expressed on activated human NK cells (59, 60). The three envelopes BaEV-TR (14), RD114-TR (31), and GALV-TM (34) are actually chimeric/fusion proteins between the surface units of the three viral envelopes and the cytoplasmic domains of the aMLV; this is necessary as the lentiviral protease from HIV-1 cannot cleave the R-peptide of the three wild-type glycoproteins but can process the one of aMLV during the extracellular maturation process of the budding lentiviral particles (14, 31, 34). In the BaEV-Rless glycoprotein, the R-peptide is already removed from the wild-type envelope, which resulted in a drastically enhanced fusogenic capacity of this pseudotype already during virus production in the HEK293T cells, as described by Girard-Gagnepain et al. and others (14, 61). Nevertheless, despite the huge syncytia formation, the release of physical particles seems to be almost similar for both pseudotypes, BaEV-Rless and BaEV-TR (14). In agreement with this work, our human codon-optimized BaEV-Rless version also here outperformed all other envelopes and provided by far the most efficient gene transfer into primary human NK cells.

In our studies, the use of the transduction enhancer Retronectin was associated with an 8-fold increase in gene transfer efficiency over the control wells without any enhancer

and thus superior to Vectofusin, which mediated a 7-fold increase. For research purposes, these values are quite comparable; however, for clinical applications, Miltenyi has adapted the use of their Vectofusin reagent for the automated processes in the closed tube system on the CliniMACS Prodigy® (26). Thus, using Vectofusin will thus be the easiest way to achieve high transduction efficiencies for clinical CAR NK cell products.

We previously established a novel element for CARs, the CD34-derived C6 hinge, that facilitates detection and enrichment of CAR T cells in clinical processes and does not negatively influence the functional characteristics of genetically transduced and enriched T cells *in vitro* and *in vivo* in mice (28). In the present study, we demonstrated that C6 as a hinge in CAR constructs expressed on human NK cells also allows to easily detect transduced NK cells *in vitro* or the peripheral blood of mice using the QBend-10 antibody by flow cytometry. Additionally, the C6 hinge also facilitates rapid enrichment of genetically modified CAR NK cells to purities of >95% using CD34 microbeads on MACS columns. However, compared to CAR T cells (28), enriching CAR NK cells with the same CD19 CAR construct with the C6 hinge resulted in a higher loss of CAR NK cells in the flowthrough, 29.0% for CAR NK cells (**Figure 2**) compared to only 11.7% for CAR T cells (28). We believe that these differences in the MACS enrichment efficiency are due to the lower expression levels (MFIs) of the CAR constructs on NK cells (data not shown). Even when the CAR T and NK cells originate from the same donors and both cell types showed similar gene transfer rates, more CAR NK cells are lost in the flowthrough (data not shown). One possible explanation is that the MPSV promoter, although still the best promoter tested for NK cells, might not express transgenes in NK cells as strongly as it does in T cells. However, in clinical settings, the loss of transduced NK cells in the flowthrough might not be as relevant as for autologous CAR T cell therapy, as the NK cell numbers can easily be adapted in allogeneic settings and one CAR NK cell product from apheresis might still be sufficient for several recipients (26). The key point here is that allogeneic NK cells with high CAR expression levels can readily be purified on a system that is compatible with GMP conditions and where the CD34 microbeads might not need to be removed (62, 63).

In order to verify the specific functionality and cytotoxic activity of our enriched CAR NK cells, we overcame the impediment of profound NK cell killing of leukemic cells by introducing blocking antibodies against six activating NK cell receptors in the co-cultures. Previously, a decrease in the NK cell cytotoxicity was reported when singularly blocking DNAM-1 (64) or NKG2D (65) on NK cells prior to incubation with AML cells. Additionally, Boermann and colleagues tested the effects of blocking NKG2D, DNAM-1, NKp30, NKp44, and NKp46 on primary human NK cells prior to co-culture with rhabdomyosarcoma cell lines (66). Others just overexpressed the target antigen for their CAR NK cells on cells that were not attacked per se by activated NK cells (26). Currently, we are in the process of systematically analyzing the effect(s) of each ligand on leukemic blasts for NKG2D, DNAM-1, NKp30, NKp44, NKp46, and/or NKp80 on *in vitro* activated and expanded NK cells (data not shown). So far, the success of blocking individual receptors seems to be target cell line-dependent. Paramount is that despite the blocking of their activating receptors, the MACS-enriched NK cells expressing CD19, CD33, or CD123 CARs still exhibit highly specific cytotoxic activity against ALL and AML cells *in vitro*. Fluorescence microscopy of CD19 CAR NK cells attacking CD19-positive REH target cells revealed that the C6 hinge is also an ideal tool to visualize the immunological synapses where the direct interaction between the CAR NK cells and the target cell occurs. We additionally demonstrated that primary AML blasts from pediatric patients expanded in NSG mice can be used as important target cells to determine the specific cytotoxicity of allogeneic CAR NK cells against these primary blasts.

Although CD19 CAR NK cells efficaciously killed the two CD19-positive B-cell precursor ALL cell lines REH and BV-173 in overnight cultures *in vitro*, our *in vivo* experiments clearly demonstrated that support of the CD19 CAR NK cells by IL15 co-expression is an absolute prerequisite for the control of the ALL blasts *in vivo*. While the co-expression of soluble IL15 was required to increase survival of the animals, as also reported by others (17, 67), the group of animals that received CAR NK cells, where IL15 is tethered to the IL15 receptor α-chain, lived slightly longer. These results seemed to confirm previous observations by Imamura et al. (68), where the tethered IL15 sustained NK cell survival and expansion in an autocrine stimulation and might mediate survival and growth advantages over NK cells co-expressing non-membrane-bound IL15. However, the initial accumulation of REH cells in the CNS already at day 15 and then strongly at day 22 suggested that migration and/or defect for NK cells with soluble IL15 expression might exist for the CNS, while human CAR NK cells with IL15 tethered to the IL15R might be better suited to survive and function in the CNS of mice. Thus, the survival of the REH leukemic blasts in the CNS of the animals might simply reflect the reduced capabilities of NK cells to cross the blood–brain barrier of the animals. Noteworthy here is that we used the same REH ALL mouse model in our previous publication (28) where we showed that the C6 hinge in a CD19 CAR is as efficacious as a commonly used CD8-derived hinge to control B-cell leukemia *in vivo* by CAR T cells. In this work, all mice in the CD19 CAR T cell groups survived, and no REH leukemia cells were detected in the CNS of the animals at any time point (28). Whether human CAR NK cells have defects in the homing to the CNS only in NSG mice or whether diminished migration of human CAR NK cells might also be a problem in humans needs to be addressed in future studies.

In summary, we established an efficient protocol for expansion and transduction of primary human NK cells with BaEV-pseudotyped CAR lentiviral vectors, which allow enrichment of the CAR NK cells to high purities. We also developed a simple method for blocking activation receptor-dependent killing of target cells by NK cells, thereby paving the way for successful evaluation of CAR NK cells targeting a variety of antigens on leukemic blasts and also on other malignant cells

in future studies. Since the MACS enrichment protocol can easily be established under GMP conditions, our study seems to be highly informative for the *off-the-shelf* manufacturing of CAR NK cells for clinical use in cellular immunotherapy.

DATA AVAILABILITY STATEMENT

The original contributions presented in the study are included in the article/supplementary material. Further inquiries can be directed to the corresponding author.

ETHICS STATEMENT

The use of peripheral blood from healthy donors was approved by the local ethics committee (Heinrich Heine University, Düsseldorf, protocol #2019-623).

AUTHOR CONTRIBUTIONS

MS, AB, CH, NB, MU, CW, DR, NN, and HH planned the experiments. MS, AB, CH, AThi, SCC, NB, SS, ATho, DS, MH, and NN conducted the experiments. MS, AB, CH, AThi, SCC, SS, NB, ATho, DS, MH, MU, KS, CM, CW, DR, NN, and HH critically analyzed data. MS, AB, CH, NN, and HH wrote the manuscript with the help of the other authors. All authors approved the final manuscript.

FUNDING

This work was supported, in part, by funding from the Medical Research School Düsseldorf, DSO, Heinrich Heine University, Düsseldorf; the Essener Elterninitiative zur Unterstützung krebskranker Kinder e.V.; and the UMEA Clinician Scientist Program of the Medical Faculty of the University of Duisburg-Essen funded by the Deutsche Forschungsgemeinschaft (DFG) and within the framework of the iCAN33 project, funded by the European Regional 470 Development Fund NRW (ERDF, German EFRE) 2014-2020. NB and CM acknowledge financial support from the DFG through the SFB1208 program "Identity and Dynamics of Membrane Systems" (A12). CM acknowledges financial support *via* the "Freigeist fellowship" of the Volkswagen Foundation.

ACKNOWLEDGMENTS

We would like to gratefully acknowledge all healthy donors who provided peripheral blood for the *in vitro* and *in vivo* studies. We would like to thank the children and adolescents with AML and their parents for providing primary AML samples and for supporting our research. **Figure 2B** was created with BioRender.com.

REFERENCES

1. Couzin-Frankel J. Breakthrough of the Year 2013. *Cancer Immunother Sci* (2013) 342(6165):1432–3. doi: 10.1126/science.342.6165.1432
2. Dudley ME, Wunderlich JR, Robbins PF, Yang JC, Hwu P, Schwartzentruber DJ, et al. Cancer Regression and Autoimmunity in Patients After Clonal Repopulation With Antitumor Lymphocytes. *Science* (2002) 298(5594):850–4. doi: 10.1126/science.1076514
3. Dudley ME, Wunderlich JR, Yang JC, Hwu P, Schwartzentruber DJ, Topalian SL, et al. A Phase I Study of Nonmyeloablative Chemotherapy and Adoptive Transfer of Autologous Tumor Antigen-Specific T Lymphocytes in Patients With Metastatic Melanoma. *J Immunother* (2002) 25(3):243–51. doi: 10.1097/00002371-200205000-00007
4. Dudley ME, Wunderlich JR, Shelton TE, Even J, Rosenberg SA. Generation of Tumor-Infiltrating Lymphocyte Cultures for Use in Adoptive Transfer Therapy for Melanoma Patients. *J Immunother* (2003) 26(4):332–42. doi: 10.1097/00002371-200307000-00005
5. Kochenderfer JN, Wilson WH, Janik JE, Dudley ME, Stetler-Stevenson M, Feldman SA, et al. Eradication of B-Lineage Cells and Regression of Lymphoma in a Patient Treated With Autologous T Cells Genetically Engineered to Recognize CD19. *Blood* (2010) 116(20):4099–102. doi: 10.1182/blood-2010-04-281931
6. June CH, Sadelain M. Chimeric Antigen Receptor Therapy. *N Engl J Med* (2018) 379(1):64–73. doi: 10.1056/NEJMra1706169
7. Hinrichs CS, Rosenberg SA. Exploiting the Curative Potential of Adoptive T-Cell Therapy for Cancer. *Immunol Rev* (2014) 257(1):56–71. doi: 10.1111/imr.12132
8. Larson RC, Maus MV. Recent Advances and Discoveries in the Mechanisms and Functions of CAR T Cells. *Nat Rev Cancer* (2021) 21(3):145–61. doi: 10.1038/s41568-020-00323-z
9. Albinger N, Hartmann J, Ullrich E. Current Status and Perspective of CAR-T and CAR-NK Cell Therapy Trials in Germany. *Gene Ther* (2021) 28(9):513–27. doi: 10.1038/s41434-021-00246-w
10. Alexander M, Culos K, Roddy J, Shaw JR, Bachmeier C, Shigle TL, et al. Chimeric Antigen Receptor T Cell Therapy: A Comprehensive Review of Clinical Efficacy, Toxicity, and Best Practices for Outpatient Administration. *Transplant Cell Ther* (2021) 27(7):558–70. doi: 10.1016/j.jtct.2021.01.014
11. Morvan MG, Lanier LL. NK Cells and Cancer: You Can Teach Innate Cells New Tricks. *Nat Rev Cancer* (2016) 16(1):7–19. doi: 10.1038/nrc.2015.5
12. Abel AM, Yang C, Thakar MS, Malarkannan S. Natural Killer Cells: Development, Maturation, and Clinical Utilization. *Front Immunol* (2018) 9:1869. doi: 10.3389/fimmu.2018.01869
13. Miller JS, Soignier Y, Panoskaltsis-Mortari A, McNearney SA, Yun GH, Fautsch SK, et al. Successful Adoptive Transfer and *In Vivo* Expansion of Human Haploidentical NK Cells in Patients With Cancer. *Blood* (2005) 105(8):3051–7. doi: 10.1182/blood-2004-07-2974
14. Girard-Gagnepain A, Amirache F, Costa C, Levy C, Frecha C, Fusil F, et al. Baboon Envelope Pseudotyped Lvs Outperform VSV-G-Lvs for Gene Transfer Into Early-Cytokine-Stimulated and Resting Hscs. *Blood* (2014) 124(8):1221–31. doi: 10.1182/blood-2014-02-558163
15. Li Y, Hermanson DL, Moriarity BS, Kaufman DS. Human Ipsc-Derived Natural Killer Cells Engineered With Chimeric Antigen Receptors Enhance Anti-Tumor Activity. *Cell Stem Cell* (2018) 23(2):181–92 e5. doi: 10.1016/j.stem.2018.06.002
16. Quintarelli C, Sivori S, Caruso S, Carlomagno S, Falco M, Boffa I, et al. Efficacy of Third-Party Chimeric Antigen Receptor Modified Peripheral Blood Natural Killer Cells for Adoptive Cell Therapy of B-Cell Precursor Acute Lymphoblastic Leukemia. *Leukemia* (2020) 34(4):1102–15. doi: 10.1038/s41375-019-0613-7
17. Liu E, Marin D, Banerjee P, Macapinlac HA, Thompson P, Basar R, et al. Use of CAR-Transduced Natural Killer Cells in CD19-Positive Lymphoid Tumors. *N Engl J Med* (2020) 382(6):545–53. doi: 10.1056/NEJMoa1910607
18. Depil S, Duchateau P, Grupp SA, Mufti G, Poirot L. 'Off-the-Shelf' Allogeneic CAR T Cells: Development and Challenges. *Nat Rev Drug Discov* (2020) 19(3):185–99. doi: 10.1038/s41573-019-0051-2
19. Gong Y, Klein Wolterink RGJ, Wang J, Bos GMJ, Germeraad WTV. Chimeric Antigen Receptor Natural Killer (CAR-NK) Cell Design and Engineering for

Cancer Therapy. *J Hematol Oncol* (2021) 14(1):73. doi: 10.1186/s13045-021-01083-5
20. Haist C, Schulte E, Bartels N, Bister A, Poschinski Z, Ibach TC, et al. CD44v6-Targeted CAR T-Cells Specifically Eliminate CD44 Isoform 6 Expressing Head/Neck Squamous Cell Carcinoma Cells. *Oral Oncol* (2021) 116:105259. doi: 10.1016/j.oraloncology.2021.105259
21. Bari R, Granzin M, Tsang KS, Roy A, Krueger W, Orentas R, et al. Corrigendum: A Distinct Subset of Highly Proliferative and Lentiviral Vector (LV)-Transducible NK Cells Define a Readily Engineered Subset for Adoptive Cellular Therapy. *Front Immunol* (2019) 10:2784. doi: 10.3389/fimmu.2019.02784
22. Reindl LM, Albinger N, Bexte T, Muller S, Hartmann J, Ullrich E. Immunotherapy With NK Cells: Recent Developments in Gene Modification Open Up New Avenues. *Oncoimmunology* (2020) 9 (1):1777651. doi: 10.1080/2162402X.2020.1777651
23. Colamartino ABL, Lemieux W, Bifsha P, Nicoletti S, Chakravarti N, Sanz J, et al. Efficient and Robust NK-Cell Transduction With Baboon Envelope Pseudotyped Lentivector. *Front Immunol* (2019) 10:2873. doi: 10.3389/fimmu.2019.02873
24. Imai C, Iwamoto S, Campana D. Genetic Modification of Primary Natural Killer Cells Overcomes Inhibitory Signals and Induces Specific Killing of Leukemic Cells. *Blood* (2005) 106(1):376–83. doi: 10.1182/blood-2004-12-4797
25. Somanchi SS, Lee DA. *Ex Vivo* Expansion of Human NK Cells Using K562 Engineered to Express Membrane Bound IL21. *Methods Mol Biol* (2016) 1441:175–93. doi: 10.1007/978-1-4939-3684-7_15
26. Hejazi M, Zhang C, Bennstein SB, Balz V, Reusing SB, Quadflieg M, et al. CD33 Delineates Two Functionally Distinct NK Cell Populations Divergent in Cytokine Production and Antibody-Mediated Cellular Cytotoxicity. *Front Immunol* (2021) 12. doi: 10.3389/fimmu.2021.798087
27. Roellecke K, Virts EL, Einholz R, Edson KZ, Altvater B, Rossig C, et al. Optimized Human CYP4B1 in Combination With the Alkylator Prodrug 4-Ipomeanol Serves as a Novel Suicide Gene System for Adoptive T-Cell Therapies. *Gene Ther* (2016) 23(7):615–26. doi: 10.1038/gt.2016.38
28. Bister A, Ibach T, Haist C, Smorra D, Roellecke K, Wagenmann M, et al. A Novel CD34-Derived Hinge for Rapid and Efficient Detection and Enrichment of CAR T Cells. *Mol Ther Oncolytics* (2021) 23:534–46. doi: 10.1016/j.omto.2021.11.003
29. Grunewald CM, Haist C, Konig C, Petzsch P, Bister A, Nossner E, et al. Epigenetic Priming of Bladder Cancer Cells With Decitabine Increases Cytotoxicity of Human EGFR and CD44v6 CAR Engineered T-Cells. *Front Immunol* (2021) 12:782448. doi: 10.3389/fimmu.2021.782448
30. Wiek C, Schmidt EM, Roellecke K, Freund M, Nakano M, Kelly EJ, et al. Identification of Amino Acid Determinants in CYP4B1 for Optimal Catalytic Processing of 4-Ipomeanol. *Biochem J* (2015) 465(1):103–14. doi: 10.1042/BJ20140813
31. Sandrin V, Boson B, Salmon P, Gay W, Negre D, Le Grand R, et al. Lentiviral Vectors Pseudotyped With a Modified RD114 Envelope Glycoprotein Show Increased Stability in Sera and Augmented Transduction of Primary Lymphocytes and CD34+ Cells Derived From Human and Nonhuman Primates. *Blood* (2002) 100(3):823–32. doi: 10.1182/blood-2001-11-0042
32. Hanenberg H, Xiao XL, Dilloo D, Hashino K, Kato I, Williams DA. Colocalization of Retrovirus and Target Cells on Specific Fibronectin Fragments Increases Genetic Transduction of Mammalian Cells. *Nat Med* (1996) 2(8):876–82. doi: 10.1038/nm0896-876
33. Hanenberg H, Hashino K, Konishi H, Hock RA, Kato I, Williams DA. Optimization of Fibronectin-Assisted Retroviral Gene Transfer Into Human CD34+ Hematopoietic Cells. *Hum Gene Ther* (1997) 8(18):2193–206. doi: 10.1089/hum.1997.8.18-2193
34. Stitz J, Buchholz CJ, Engelstadter M, Uckert W, Bloemer U, Schmitt I, et al. Lentiviral Vectors Pseudotyped With Envelope Glycoproteins Derived From Gibbon Ape Leukemia Virus and Murine Leukemia Virus 10A1. *Virology* (2000) 273(1):16–20. doi: 10.1006/viro.2000.0394
35. Leurs C, Jansen M, Pollok KE, Heinkelein M, Schmidt M, Wissler M, et al. Comparison of Three Retroviral Vector Systems for Transduction of Nonobese Diabetic/Severe Combined Immunodeficiency Mice Repopulating Human CD34+ Cord Blood Cells. *Hum Gene Ther* (2003) 14(6):509–19. doi: 10.1089/104303403764539305
36. Andreadis S, Palsson BO. Coupled Effects of Polybrene and Calf Serum on the Efficiency of Retroviral Transduction and the Stability of Retroviral Vectors. *Hum Gene Ther* (1997) 8(3):285–91. doi: 10.1089/hum.1997.8.3-285
37. Davis HE, Rosinski M, Morgan JR, Yarmush ML. Charged Polymers Modulate Retrovirus Transduction *via* Membrane Charge Neutralization and Virus Aggregation. *Biophys J* (2004) 86(2):1234–42. doi: 10.1016/S0006-3495(04)74197-1
38. Fenard D, Ingrao D, Seye A, Buisset J, Genries S, Martin S, et al. Vectofusin-1, a New Viral Entry Enhancer, Strongly Promotes Lentiviral Transduction of Human Hematopoietic Stem Cells. *Mol Ther Nucleic Acids* (2013) 2:e90. doi: 10.1038/mtna.2013.17
39. Muller S, Bexte T, Gebel V, Kalensee F, Stolzenberg E, Hartmann J, et al. High Cytotoxic Efficiency of Lentivirally and Alpharetrovirally Engineered CD19-Specific Chimeric Antigen Receptor Natural Killer Cells Against Acute Lymphoblastic Leukemia. *Front Immunol* (2019) 10:3123. doi: 10.3389/fimmu.2019.03123
40. Hoerster K, Uhrberg M, Wiek C, Horn PA, Hanenberg H, Heinrichs S. HLA Class I Knockout Converts Allogeneic Primary NK Cells Into Suitable Effectors for "Off-the-Shelf" Immunotherapy. *Front Immunol* (2020) 11:586168. doi: 10.3389/fimmu.2020.586168
41. Pattengale PK, Sundstrom C, Yu AL, Levine A. Lysis of Fresh Leukemic Blasts by Interferon-Activated Human Natural Killer Cells. *Nat Immun Cell Growth Regul* (1983) 3(4):165–80. doi: 10.1002/ijc.2910290102
42. Paczulla AM, Rothfelder K, Raffel S, Konantz M, Steinbacher J, Wang H, et al. Absence of NKG2D Ligands Defines Leukaemia Stem Cells and Mediates Their Immune Evasion. *Nature* (2019) 572(7768):254–9. doi: 10.1038/s41586-019-1410-1
43. Parham P, Moffett A. Variable NK Cell Receptors and Their MHC Class I Ligands in Immunity, Reproduction and Human Evolution. *Nat Rev Immunol* (2013) 13(2):133–44. doi: 10.1038/nri3370
44. Cooley S, He F, Bachanova V, Vercellotti GM, DeFor TE, Curtsinger JM, et al. First-in-Human Trial of Rhil-15 and Haploidentical Natural Killer Cell Therapy for Advanced Acute Myeloid Leukemia. *Blood Adv* (2019) 3 (13):1970–80. doi: 10.1182/bloodadvances.2018028332
45. Romee R, Cooley S, Berrien-Elliott MM, Westervelt P, Verneris MR, Wagner JE, et al. First-in-Human Phase 1 Clinical Study of the IL-15 Superagonist Complex ALT-803 to Treat Relapse After Transplantation. *Blood* (2018) 131 (23):2515–27. doi: 10.1182/blood-2017-12-823757
46. Hurton LV, Singh H, Najjar AM, Switzer KC, Mi T, Maiti S, et al. Tethered IL-15 Augments Antitumor Activity and Promotes a Stem-Cell Memory Subset in Tumor-Specific T Cells. *Proc Natl Acad Sci USA* (2016) 113(48):E7788–E97. doi: 10.1073/pnas.1610544113
47. Rossig C, Juergens H, Schrappe M, Moericke A, Henze G, von Stackelberg A, et al. Effective Childhood Cancer Treatment: The Impact of Large Scale Clinical Trials in Germany and Austria. *Pediatr Blood Cancer* (2013) 60 (10):1574–81. doi: 10.1002/pbc.24598
48. Schrappe M. Detection and Management of Minimal Residual Disease in Acute Lymphoblastic Leukemia. *Hematol Am Soc Hematol Educ Program* (2014) 2014(1):244–9. doi: 10.1182/asheducation-2014.1.244
49. Pui CH, Yang JJ, Hunger SP, Pieters R, Schrappe M, Biondi A, et al. Childhood Acute Lymphoblastic Leukemia: Progress Through Collaboration. *J Clin Oncol* (2015) 33(27):2938–48. doi: 10.1200/JCO.2014.59.1636
50. Rasche M, Zimmermann M, Steidel E, Alonzo T, Aplenc R, Bourquin JP, et al. Survival Following Relapse in Children With Acute Myeloid Leukemia: A Report From AML-BFM and COG. *Cancers (Basel)* (2021) 13(10):2336. doi: 10.3390/cancers13102336
51. Rasche M, Zimmermann M, Borschel L, Bourquin JP, Dworzak M, Klingebiel T, et al. Successes and Challenges in the Treatment of Pediatric Acute Myeloid Leukemia: A Retrospective Analysis of the AML-BFM Trials From 1987 to 2012. *Leukemia* (2018) 32(10):2167–77. doi: 10.1038/s41375-018-0071-7
52. Dickinson AM, Norden J, Li S, Hromadnikova I, Schmid C, Schmetzer H, et al. Graft-Versus-Leukemia Effect Following Hematopoietic Stem Cell Transplantation for Leukemia. *Front Immunol* (2017) 8:496. doi: 10.3389/fimmu.2017.00496
53. Boissel N, Rabian F. Immunotherapies in Acute Leukemia. *Therapie* (2021). doi: 10.1016/j.therap.2021.12.003
54. Herrera L, Santos S, Vesga MA, Carrascosa T, Garcia-Ruiz JC, Perez-Martinez A, et al. The Race of CAR Therapies: CAR-NK Cells for Fighting B-Cell

Hematological Cancers. *Cancers (Basel)* (2021) 13(21):5418. doi: 10.3390/cancers13215418
55. Allan DSJ, Chakraborty M, Waller GC, Hochman MJ, Poolcharoen A, Reger RN, et al. Systematic Improvements in Lentiviral Transduction of Primary Human Natural Killer Cells Undergoing *Ex Vivo* Expansion. *Mol Ther Methods Clin Dev* (2021) 20:559–71. doi: 10.1016/j.omtm.2021.01.008
56. Bari R, Granzin M, Tsang KS, Roy A, Krueger W, Orentas R, et al. A Distinct Subset of Highly Proliferative and Lentiviral Vector (LV)-Transducible NK Cells Define a Readily Engineered Subset for Adoptive Cellular Therapy. *Front Immunol* (2019) 10:2001. doi: 10.3389/fimmu.2019.02784
57. Joglekar AV, Sandoval S. Pseudotyped Lentiviral Vectors: One Vector, Many Guises. *Hum Gene Ther Methods* (2017) 28(6):291–301. doi: 10.1089/hgtb.2017.084
58. Jensen H, Potempa M, Gotthardt D, Lanier LL. Cutting Edge: IL-2-Induced Expression of the Amino Acid Transporters SLC1A5 and CD98 Is a Prerequisite for NKG2D-Mediated Activation of Human NK Cells. *J Immunol* (2017) 199(6):1967–72. doi: 10.4049/jimmunol.1700497
59. Dreyer K, Pedersen FS, Pedersen L. A 13-Amino-Acid Pit1-Specific Loop 4 Sequence Confers Feline Leukemia Virus Subgroup B Receptor Function Upon Pit2. *J Virol* (2000) 74(6):2926–9. doi: 10.1128/JVI.74.6.2926-2929.2000
60. O'Hara B, Johann SV, Klinger HP, Blair DG, Rubinson H, Dunn KJ, et al. Characterization of a Human Gene Conferring Sensitivity to Infection by Gibbon Ape Leukemia Virus. *Cell Growth Differ* (1990) 1(3):119–27.
61. Rein A, Mirro J, Haynes JG, Ernst SM, Nagashima K. Function of the Cytoplasmic Domain of a Retroviral Transmembrane Protein: P15e-P2e Cleavage Activates the Membrane Fusion Capability of the Murine Leukemia Virus Env Protein. *J Virol* (1994) 68(3):1773–81. doi: 10.1128/jvi.68.3.1773-1781.1994
62. Shah GL, Scordo M, Kosuri S, Herrera DA, Cho C, Devlin SM, et al. Impact of Toxicity on Survival for Older Adult Patients After CD34(+) Selected Allogeneic Hematopoietic Stem Cell Transplantation. *Biol Blood Marrow Transplant* (2018) 24(1):142–9. doi: 10.1016/j.bbmt.2017.08.040
63. Berger MD, Branger G, Leibundgut K, Baerlocher GM, Seipel K, Mueller BU, et al. CD34+ Selected Versus Unselected Autologous Stem Cell Transplantation in Patients With Advanced-Stage Mantle Cell and Diffuse Large B-Cell Lymphoma. *Leuk Res* (2015) 39(6):561–7. doi: 10.1016/j.leukres.2015.03.004
64. Kearney CJ, Ramsbottom KM, Voskoboinik I, Darcy PK, Oliaro J. Loss of DNAM-1 Ligand Expression by Acute Myeloid Leukemia Cells Renders Them Resistant to NK Cell Killing. *Oncoimmunology* (2016) 5(8):e1196308. doi: 10.1080/2162402X.2016.1196308
65. Diermayr S, Himmelreich H, Durovic B, Mathys-Schneeberger A, Siegler U, Langenkamp U, et al. NKG2D Ligand Expression in AML Increases in Response to HDAC Inhibitor Valproic Acid and Contributes to Allorecognition by NK-Cell Lines With Single KIR-HLA Class I Specificities. *Blood* (2008) 111(3):1428–36. doi: 10.1182/blood-2007-07-101311
66. Boerman GH, van Ostaijen-ten Dam MM, Kraal KC, Santos SJ, Ball LM, Lankester AC, et al. Role of NKG2D, DNAM-1 and Natural Cytotoxicity Receptors in Cytotoxicity Toward Rhabdomyosarcoma Cell Lines Mediated by Resting and IL-15-Activated Human Natural Killer Cells. *Cancer Immunol Immunother* (2015) 64(5):573–83. doi: 10.1007/s00262-015-1657-9
67. Du Z, Ng YY, Zha S, Wang S. Piggybac System to Co-Express NKG2D CAR and IL-15 to Augment the *In Vivo* Persistence and Anti-AML Activity of Human Peripheral Blood NK Cells. *Mol Ther Methods Clin Dev* (2021) 23:582–96. doi: 10.1016/j.omtm.2021.10.014
68. Imamura M, Shook D, Kamiya T, Shimasaki N, Chai SM, Coustan-Smith E, et al. Autonomous Growth and Increased Cytotoxicity of Natural Killer Cells Expressing Membrane-Bound Interleukin-15. *Blood* (2014) 124(7):1081–8. doi: 10.1182/blood-2014-02-556837

Conflict of Interest: HH and CW are inventors on a patent describing the CD34 hinge for CAR immune effector cells.

The remaining authors declare that the research was conducted in the absence of any commercial or financial relationships that could be construed as a potential conflict of interest.

Publisher's Note: All claims expressed in this article are solely those of the authors and do not necessarily represent those of their affiliated organizations, or those of the publisher, the editors and the reviewers. Any product that may be evaluated in this article, or claim that may be made by its manufacturer, is not guaranteed or endorsed by the publisher.

12.3 Cover Image: A novel CD34-derived hinge for rapid and efficient detection and enrichment of CAR T cells

Journal: Molecular Therapy: Oncolytics | Volume 23 | December 2021 | [184]

Contribution: My contribution to the cover image is the design of the imaging experiments, the execution of microscopic measurements as well as the image selection and post-processing resulting in the final cover image selected by the journal editors.

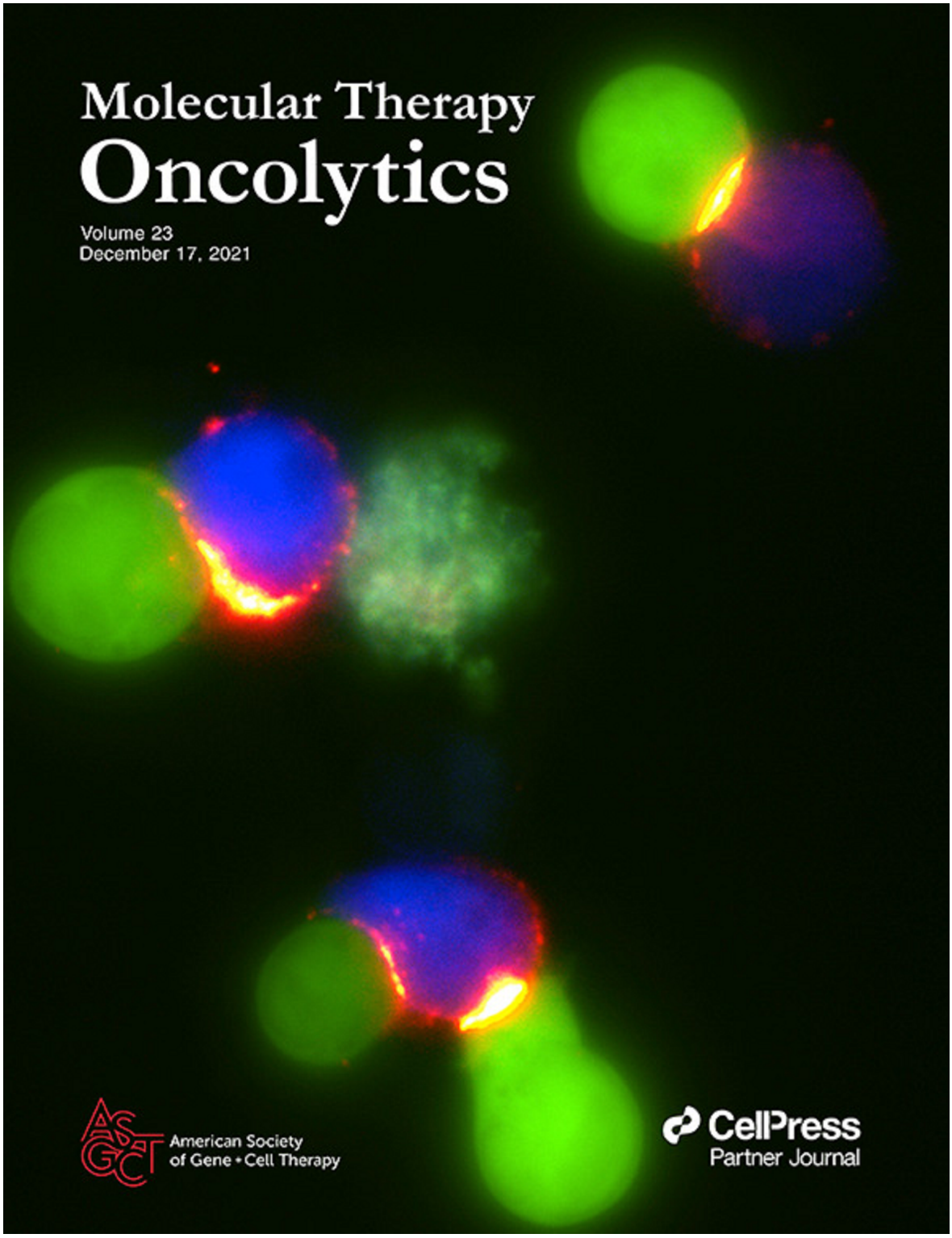

Figure 12.1: On the Cover: Formation of immunological synapses between CD19 CAR T-cells and CD19+ REH ALL (acute lymphocytic leukemia) cells. Three genetically modified T-cells (blue cells) attack via their CD19 CAR construct (red membrane staining) either a single (top), two (middle) or three (bottom) REH cells (green cells). [185]. Untransduced T-cells in the cultures do not express any fluorescence (see bright field image, Figure 12.2).

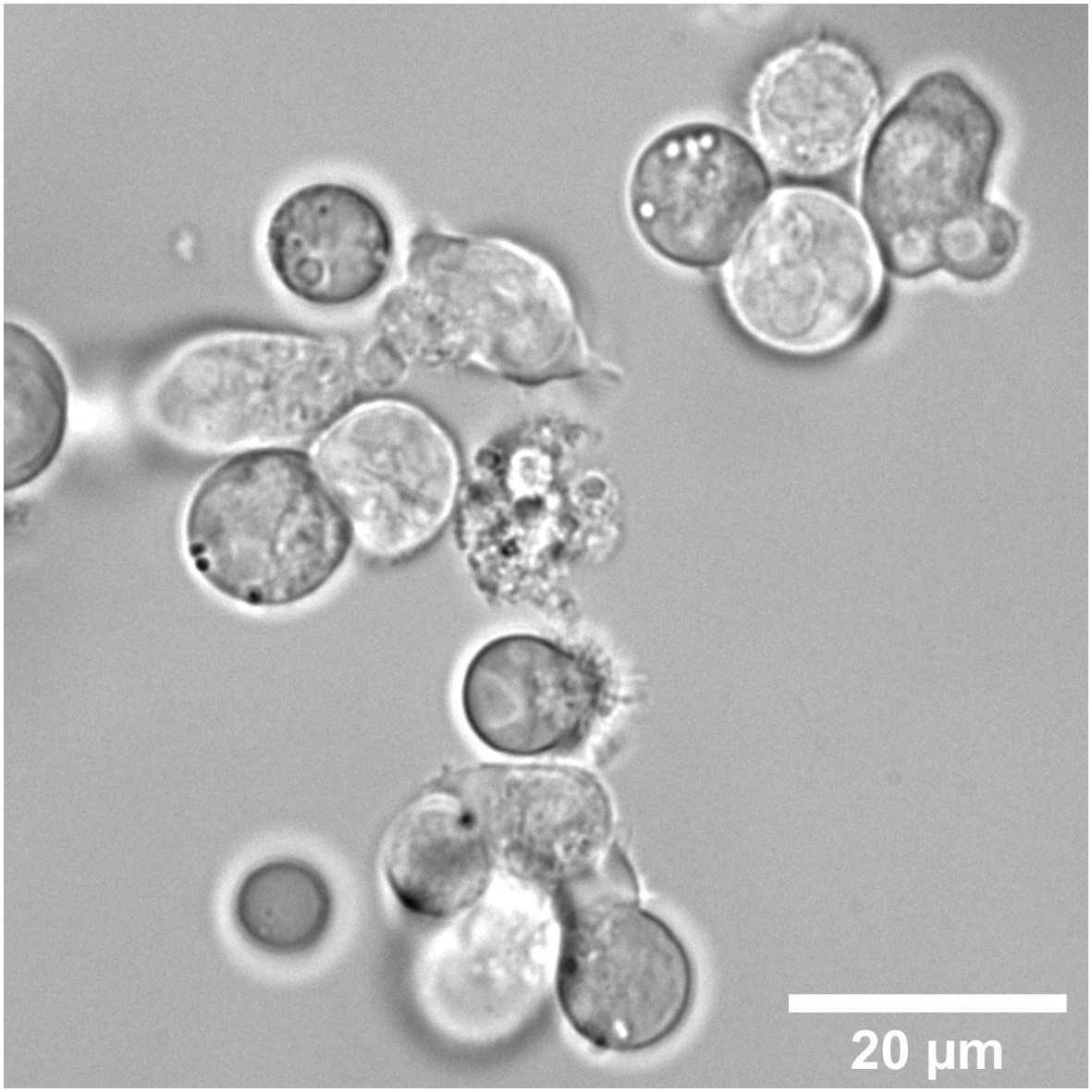

Figure 12.2: Bright field image corresponding to the Journal Cover shown in Figure 12.1.

VI

Final Conclusion

Final Conclusion

In this work, fluorescence microscopy and spectroscopy techniques were utilized and advanced to contribute towards a greater understanding of receptors in the cellular plasma membrane.

In particular, models of signal initiation for cell apoptosis by the death receptor CD95 were challenged and a minimal model of CD95 signal initiation was found, identifying monomers oligomerizing to $6-15\,\%$ dimers and trimers evenly distributed in the membrane as efficient apoptosis signal inducers in live HeLa cells. The absolute number of activated receptors turned out to be a crucial aspect of apoptosis signal initiation, as increased receptor surface concentrations do not show significant changes in receptor oligomer fractions or stoichiometries but induce a remarkable change in signaling dynamics. While crucial for the signal transmission, the death domain was shown to be irrelevant in the CD95 oligomerization.

These novel biological insights on CD95 could only be achieved via an integral approach, combining the complementary results of 6 microscopy and spectroscopy techniques:
Widefield and confocal microscopy were necessary to determine signaling dynamics of CD95 revealing a remarkable acceleration and increased percentage of apoptosis events with increased absolute ligand and receptor numbers up to $>95\,\%$ of apoptotic cells within less than 2 hours.
FCS measurements were required to confirm and determine receptor mobilities with membrane diffusion constants of $0.21-0.24\,{}^{\mu m^2}/_{s}$ sufficient to exhibit dynamic changes in their organization state.
STED enabled the sub-diffraction resolution of receptor distributions over the membrane surface and the detection of small, randomly distributed, isolated spots of CD95 with potential oligomer formation.
cPBSA quantified receptor stoichiometries in spots and revealed a pre-ligand stoichiometry with $>70\,\%$ single bleaching steps in CD95 spots, similar to the monomer control. Ligand addition shifted the distribution towards more dimer and trimer bleaching steps ($+7\,\%$), while no larger step numbers were detected.
An advanced FRET approach confirmed the oligomerization of CD95 after ligand addition with an oligomer fraction of $5-16\,\%$. FRET enabled to cover a broad range

of expression levels in live cells, not indicating any concentration-induced signature of higher oligomer formation.
Each technique exhibits particular spatio-temporal regimes of superior performance, and the synergetic combination allowed to probe the CD95 activation over the whole dynamic range from µs to hours, molecular to cellular scales and with particular focus on molecular concentrations.

In particular, to achieve a quantitative understanding of molecular oligomerization states, substantial technical advancements were implemented during this project.
Despite the well-known limit of molecular counting in STED, a quantitative brightness analysis of STED images was achieved using molecular benchmarks and a polarization-based analysis to control for photophysical effects.
As a second example, time-correlated readouts in PBSA enabled discrimination of blinking from bleaching events and a correct scaling of multi-step traces was realized by comparing calculated occupancy probabilities with the number of bleaching steps. By expanding PBSA to a confocal approach and using conventional fluorescent molecules such as mEGFP, this technique is rendered accessible to all kinds of biological recordings including the intracellular space.
Sophisticated FRET measurements featuring a quantitative interpretation and high precision of FRET-sensitized fluorescence donor decays were achieved by multiple in-depth advancements. A crucial issue was the determination of absolute receptor concentrations on the cell surface. This was achieved deriving a value of the molecular brightness per laser power from precise concentration, confocal volume and intensity determination. Further, using a sample-specific FRET signal calibration by exploiting AV simulations in combination with corrections of non-FRET donor self-interactions, a robust derivation of the real fraction of dimers/oligomers was realized.

The benefit of quantifying fluorescence readouts from single cell recordings was further demonstrated by a clinical study on CAR immunotherapy. The analysis of fluorescence time-lapse data elucidated the killing dynamics of CD44v6 CAR T-cells on malignant head and neck squamous cell carcinoma cells and the effect of effector-to-target cell ratio variations. Resolving the time evolution of therapeutic processes can contribute to an assessment of how and when to expect first reactions in the *in vivo* situation and how to dose the potential drug.
Further, the cellular interactions between CD19 CAR NK or T-cells and their target cells in the form of immunological synapses could be visualized using multi-channel widefield microscopy. Combined with the deployment of negative controls, here an unspecific (CD33) CAR, the presence of specific cellular interactions could be verified. This visual confirmation of the functionality of a novel receptor design was awarded as

a journal cover image, demonstrating the great impact microscopic imaging can have on the representation and outreach of pre-clinical studies.

Overall, this thesis presents general strategies to study signal initiation mechanisms alongside with necessary technical advancements.
The developments presented here enable a more robust unique interpretation of the individual techniques and can be applied to study molecular interactions in a variety of biological systems. Additionally, the importance of high-fidelity monomer and dimer controls as molecular benchmarks to study receptor oligomerization reliably is shown. Further, this work demonstrates the need to acquire information from different angles to extract reliable conclusions and fully elucidate biological processes. Consequently, a generic concept to fully unravel molecular mechanisms and spatio-temporal hallmarks of signal initiation based on the synergy of complementary state-of-the-art fluorescence microscopy and spectroscopy techniques is presented.
Particularly, this generic concept elucidates the minimal requirements for efficient apoptosis signal induction of CD95. These findings are crucial prerequisites to understand a disease-inducing CD95 deregulation and to eventually advance clinical therapy approaches. Due to the structural similarity, this study on CD95 signal initiation might serve as precursor for similar studies of other death receptors or membrane receptors in general.

Supplementary Information

A Protein Sequences

The following chapter includes the complete amino acid sequences for all used constructs in this work. The protein sequences are shown using the 1-letter amino acid code (Table A.1) and the linkers between receptor and fluorescent protein(s) / tags are highlighted in magenta.

One letter code	Three letter code	Amino Acid
A	Ala	Alanine
C	Cys	Cysteine
D	Asp	Aspartic Acid
E	Glu	Glutamic Acid
F	Phe	Phenylalanine
G	Gly	Glycine
H	His	Histidine
I	Ile	Isoleucine
K	Lys	Lysine
L	Leu	Leucine
M	Met	Methionine
N	Asn	Asparagine
O	Pyl	Pyrrolysine
P	Pro	Proline
Q	Gln	Glutamine
R	Arg	Arginine
S	Ser	Serine
T	Thr	Threonine
U	Sec	Selenocysteine
V	Val	Valine
W	Trp	Tryptophan
Y	Tyr	Tyrosine

Table A.1: Protein letter code used to display the amino acid sequences in this thesis.

CD95-mEGFP

MLGIWTLLPLVLTSVARLSSKSVNAQVTDINSKGLELRKTVTTVETQNLEGLH
HDGQFCHKPCPPGERKARDCTVNGDEPDCVPCQEGKEYTDKAHFSSKCRRC
RLCDEGHGLEVEINCTRTQNTKCRCKPNFFCNSTVCEHCDPCTKCEHGIIKEC
TLTSNTKCKEEGSRSNLGWLCLLLLPIPLIVWVKRKEVQKTCRKHRKENQGSH
ESPTLNPETVAINLSDVDLSKYITTIAGVMTLSQVKGFVRKNGVNEAKIDEIKN
DNVQDTAEQKVQLLRNWHQLHGKKEAYDTLIKDLKKANLCTLAEKIQTIILK
DITSDSENSNFRNEIQSLVGGGGGPVPQWEGFAALLATPVGGAVMVSKGEELF
TGVVPILVELDGDVNGHKFSVSGEGEGDATYGKLTLKFICTTGKLPVPWPTL
VTTLTYGVQCFSRYPDHMKQHDFFKSAMPEGYVQERTIFFKDDGNYKTRAE
VKFEGDTLVNRIELKGIDFKEDGNILGHKLEYNYNSHNVYIMADKQKNGIKVN
FKIRHNIEDGSVQLADHYQQNTPIGDGPVLLPDNHYLSTQSKLSKDPNEKRDH
MVLKEFVTAAGITLGMDELYK

CD95-mCherry

MLGIWTLLPLVLTSVARLSSKSVNAQVTDINSKGLELRKTVTTVETQNLEGLH
HDGQFCHKPCPPGERKARDCTVNGDEPDCVPCQEGKEYTDKAHFSSKCRRC
RLCDEGHGLEVEINCTRTQNTKCRCKPNFFCNSTVCEHCDPCTKCEHGIIKEC
TLTSNTKCKEEGSRSNLGWLCLLLLPIPLIVWVKRKEVQKTCRKHRKENQGSH
ESPTLNPETVAINLSDVDLSKYITTIAGVMTLSQVKGFVRKNGVNEAKIDEIKN
DNVQDTAEQKVQLLRNWHQLHGKKEAYDTLIKDLKKANLCTLAEKIQTIILK
DITSDSENSNFRNEIQSLVGGGGGPVPQWEGFAALLATPVATMVSKGEEDNMA
IIKEFMRFKVHMEGSVNGHEFEIEGEGEGRPYEGTQTAKLKVTKGGPLPFAW
DILSPQFMYGSKAYVKHPADIPDYLKLSFPEGFKWERVMNFEDGGVVTVTQD
SSLQDGEFIYKVKLRGTNFPSDGPVMQKKTMGWEASSERMYPEDGALKGEIK
QRLKLKDGGHYDAEVKTTYKAKKPVQLPGAYNVNIKLDITSHNEDYTIVEQY
ERAEGRHSTGGMDELYK

CD95(ΔDD)-mEGFP

MLGIWTLLPLVLTSVARLSSKSVNAQVTDINSKGLELRKTVTTVETQNLEGLH
HDGQFCHKPCPPGERKARDCTVNGDEPDCVPCQEGKEYTDKAHFSSKCRRC
RLCDEGHGLEVEINCTRTQNTKCRCKPNFFCNSTVCEHCDPCTKCEHGIIKEC
TLTSNTKCKEEGSRSNLGWLCLLLLPIPLIVWVKRKEVQKTCRKHRKENQGSH
GGGPVPQWEGFAALLATPVGGAVMVSKGEELFTGVVPILVELDGDVNGHKFS
VSGEGEGDATYGKLTLKFICTTGKLPVPWPTLVTTLTYGVQCFSRYPDHMK

QHDFFKSAMPEGYVQERTIFFKDDGNYKTRAEVKFEGDTLVNRIELKGIDFK
EDGNILGHKLEYNYNSHNVYIMADKQKNGIKVNFKIRHNIEDGSVQLADHYQQ
NTPIGDGPVLLPDNHYLSTQSKLSKDPNEKRDHMVLKEFVTAAGITLGMDELY
K

CD95(ΔDD)-mCherry

MLGIWTLLPLVLTSVARLSSKSVNAQVTDINSKGLELRKTVTTVETQNLEGLH
HDGQFCHKPCPPGERKARDCTVNGDEPDCVPCQEGKEYTDKAHFSSKCRRC
RLCDEGHGLEVEINCTRTQNTKCRCKPNFFCNSTVCEHCDPCTKCEHGIIKEC
TLTSNTKCKEEGSRSNLGWLCLLLLPIPLIVWVKRKEVQKTCRKHRKENQGSH
GGGPVPQWEGFAALLATPVATMVSKGEEDNMAIIKEFMRFKVHMEGSVNGHE
FEIEGEGEGRPYEGTQTAKLKVTKGGPLPFAWDILSPQFMYGSKAYVKHPAD
IPDYLKLSFPEGFKWERVMNFEDGGVVTVTQDSSLQDGEFIYKVKLRGTNFPS
DGPVMQKKTMGWEASSERMYPEDGALKGEIKQRLKLKDGGHYDAEVKTTY
KAKKPVQLPGAYNVNIKLDITSHNEDYTIVEQYERAEGRHSTGGMDELYK

CTLA4-mEGFP

MACLGFQRHKAQLNLATRTWPCTLLFFLLFIPVFCKAMHVAQPAVVLASSRG
IASFVCEYASPGKATEVRVTVLRQADSQVTEVCAATYMMGNELTFLDDSICT
GTSSGNQVNLTIQGLRAMDTGLYICKVELMYPPPYYLGIGNGTQIYVIDPEPC
PDSDFLLWILAAVSSGLFFYSFLLTAVSLSKMLKKRSPLTTGVGGGPVPQWEG-
FAALLATPVGGAVMVSKGEELFTGVVPILVELDGDVNGHKFSVSGEGEGDATY
GKLTLKFICTTGKLPVPWPTLVTTLTYGVQCFSRYPDHMKQHDFFKSAMPEG
YVQERTIFFKDDGNYKTRAEVKFEGDTLVNRIELKGIDFKEDGNILGHKLEYN
YNSHNVYIMADKQKNGIKVNFKIRHNIEDGSVQLADHYQQNTPIGDGPVLLPD
NHYLSTQSKLSKDPNEKRDHMVLKEFVTAAGITLGMDELYK

CTLA4-mCherry

MACLGFQRHKAQLNLATRTWPCTLLFFLLFIPVFCKAMHVAQPAVVLASSRG
IASFVCEYASPGKATEVRVTVLRQADSQVTEVCAATYMMGNELTFLDDSICT
GTSSGNQVNLTIQGLRAMDTGLYICKVELMYPPPYYLGIGNGTQIYVIDPEPC
PDSDFLLWILAAVSSGLFFYSFLLTAVSLSKMLKKRSPLTTGVGGGPVPQWEG-
FAALLATPVATMVSKGEEDNMAIIKEFMRFKVHMEGSVNGHEFEIEGEGEGRP
YEGTQTAKLKVTKGGPLPFAWDILSPQFMYGSKAYVKHPADIPDYLKLSFPE
GFKWERVMNFEDGGVVTVTQDSSLQDGEFIYKVKLRGTNFPSDGPVMQKKT

MGWEASSERMYPEDGALKGEIKQRLKLKDGGHYDAEVKTTYKAKKPVQLPG
AYNVNIKLDITSHNEDYTIVEQYERAEGRHSTGGMDELYK

CD86-mEGFP

MGLSNILFVMAFLLSGAAPLKIQAYFNETADLPCQFANSQNQSLSELVVFWQD
QENLVLNEVYLGKEKFDSVHSKYMGRTSFDSDSWTLRLHNLQIKDKGLYQCII
HHKKPTGMIRIHQMNSELSVLANFSQPEIVPISNITENVYINLTCSSIHGYPEPK
KMSVLLRTKNSTIEYDGIMQKSQDNVTELYDVSISLSVSFPDVTSNMTIFCILET
DKTRLLSSPFSIELEDPQPPPDHIPWITAVLPTVIICVMVFCLILWKWKKKKRP
RNSYKCGTNTMEREESEQTKKREKIHIPERSDETQRVFKSSKTSSCDKSDTCF
GGGPVPQWEGFAALLATPVGGAVMVSKGEELFTGVVPILVELDGDVNGHKFS
VSGEGEGDATYGKLTLKFICTTGKLPVPWPTLVTTLTYGVQCFSRYPDHMK
QHDFFKSAMPEGYVQERTIFFKDDGNYKTRAEVKFEGDTLVNRIELKGIDFK
EDGNILGHKLEYNYNSHNVYIMADKQKNGIKVNFKIRHNIEDGSVQLADHYQQ
NTPIGDGPVLLPDNHYLSTQSKLSKDPNEKRDHMVLKEFVTAAGITLGMDELY
K

CD86-mCherry

MGLSNILFVMAFLLSGAAPLKIQAYFNETADLPCQFANSQNQSLSELVVFWQD
QENLVLNEVYLGKEKFDSVHSKYMGRTSFDSDSWTLRLHNLQIKDKGLYQCII
HHKKPTGMIRIHQMNSELSVLANFSQPEIVPISNITENVYINLTCSSIHGYPEPK
KMSVLLRTKNSTIEYDGIMQKSQDNVTELYDVSISLSVSFPDVTSNMTIFCILET
DKTRLLSSPFSIELEDPQPPPDHIPWITAVLPTVIICVMVFCLILWKWKKKKRP
RNSYKCGTNTMEREESEQTKKREKIHIPERSDETQRVFKSSKTSSCDKSDTCF
GGGPVPQWEGFAALLATPVATMVSKGEEDNMAIIKEFMRFKVHMEGSVNGHE
FEIEGEGEGRPYEGTQTAKLKVTKGGPLPFAWDILSPQFMYGSKAYVKHPAD
IPDYLKLSFPEGFKWERVMNFEDGGVVTVTQDSSLQDGEFIYKVKLRGTNFPS
DGPVMQKKTMGWEASSERMYPEDGALKGEIKQRLKLKDGGHYDAEVKTTY
KAKKPVQLPGAYNVNIKLDITSHNEDYTIVEQYERAEGRHSTGGMDELYK

CD86-mEGFP-mEGFP(-Spot-His)

ASMGLSNILFVMAFLLSGAAPLKIQAYFNETADLPCQFANSQNQSLSELVVFW
QDQENLVLNEVYLGKEKFDSVHSKYMGRTSFDSDSWTLRLHNLQIKDKGLYQ
CIIHHKKPTGMIRIHQMNSELSVLANFSQPEIVPISNITENVYINLTCSSIHGYPEP
KKMSVLLRTKNSTIEYDGIMQKSQDNVTELYDVSISLSVSFPDVTSNMTIFCILE

TDKTRLLSSPFSIELEDPQPPPDHIPWITAVLPTVIICVMVFCLILWKWKKKKR
PRNSYKCGTNTMEREESEQTKKREKIHIPERSDETQRVFKSSKTSSCDKSDTC
GGGPVPQWEGFAALLATPVGGAVMVSKGEELFTGVVPILVELDGDVNGHKFS
VSGEGEGDATYGKLTLKFICTTGKLPVPWPTLVTTLTYGVQCFSRYPDHMKQ
HDFFKSAMPEGYVQERTIFFKDDGNYKTRAEVKFEGDTLVNRIELKGIDFKED
GNILGHKLEYNYNSHNVYIMADKQKNGIKVNFKIRHNIEDGSVQLADHYQQNT
PIGDGPVLLPDNHYLSTQSKLSKDPNEKRDHMVLKEFVTAAGITLGMDELYK
GSSGSSNAAIINAAGSSGSSMVSKGEELFTGVVPILVELDGDVNGHKFSVSGEGE
GDATYGKLTLKFICTTGKLPVPWPTLVTTLTYGVQCFSRYPDHMKQHDFFKS
AMPEGYVQERTIFFKDDGNYKTRAEVKFEGDTLVNRIELKGIDFKEDGNILGH
KLEYNYNSHNVYIMADKQKNGIKVNFKIRHNIEDGSVQLADHYQQNTPIGDGP
VLLPDNHYLSTQSKLSKDPNEKRDHMVLKEFVTAAGITLGMDELYKGSPDRV
RAVSHWSSGGGSSGGSHHHHHH

Bicistronic Plasmid T2A Linkers

The linkers before and after the T2A peptide sequence connecting the above listed protein sequences in bicistronic plasmids are the following:

CD95-mCherry-T2A-CD95-mEGFP

SGLGSGEGRGSLLTCGDVEENPGPRASATGLRSRVAT

CD95(ΔDD)-mCherry-T2A-CD95(ΔDD)-mEGFP

SGLGSGEGRGSLLTCGDVEENPGPRSRVAT

CD86-mCherry-T2A-CD86-mEGFP

SGLGSGEGRGSLLTCGDVEENPGPRASAT

CTLA4-mCherry-T2A-CTLA4-mEGFP

SGLGSGEGRGSLLTCGDVEENPGPRASAT

B Cell Biology Protocols

B.1 Cell Passaging and Seeding Protocol

The cells were cultured in culture medium consisting of DMEM (Dulbecco's Modified Eagle Medium) with high glucose, GlutaMAX™ supplement and pyruvate (Gibco, Life Technologies Inc., Carlsbad, California, USA, #31966021) supplemented with 10 % fetal bovine serum (FBS, Gibco, #10500064) and 1 % Penicillin-Streptomycin (Sigma-Aldrich, Merck KGaA, Darmstadt, Germany, #P0781). The cultivation was maintained in a controlled atmosphere at 37 °C at 5 % CO_2.
For passaging, the cell flask (T25) was first washed once with DPBS (Dulbecco's Phosphate Buffered Saline), no calcium, no magnesium (Gibco, #14190144) (pre-heated to 37 °C) and then incubated with Trypsin-EDTA solution (Sigma-Aldrich, #14190144) (1 ml per 25 cm^2 growth area, not pre-heated) at room temperature for $2-3$ minutes to detach the cells. After detachment, the 5-fold amount of culture medium (pre-heated) was added to inhibit the Trypsin. To remove the Trypsin, the cell suspension was centrifuged at 300 ×g for 5 minutes and the supernatant was discarded. The cell pellet was resuspended in pre-heated culture medium and seeded into the respective vessels.

B.2 Transfection Protocol

The transfection solution was prepared with 50 µl Opti-MEM™ (Gibco, #11058021), 1 µg of plasmid DNA and 4 µl ViaFect™ and incubated for 30 minutes at room temperature (all reagents heated to room temperature, not 37 °C). Following, the cells were incubated with the transfection solution diluted 10-fold in pre-heated 500 µl Opti-MEM™ supplemented with 10 % FBS and 1 % P/S for 3 h at 37 °C. After the incubation, the transfection medium was exchanged to complete cell culture medium (DMEM with 10 % FBSand 1 % P/S) again. The given volumes were used for either two wells of an 8-well imaging slide or one coverslip in a 12-well plate, respectively.

B.3 Fixation and Immunostaining Protocol

As a first step of the fixation, the cells were washed three times using a washing buffer consisting of HBSS (Gibco, #14025050) containing 0.1 M sucrose (Carl Roth GmbH + Co. KG, Karlsruhe, Germany, #57-50-1) and 1 % BSA (ITW Reagents, AppliChem GmbH, Darmstadt, Germany, #A1391). The fixation was obtained using 16 % methanol-free formaldehyde stock (Thermo Scientific, Life Technologies Inc., Carlsbad, USA, #28906) diluted to 4 % in washing buffer for 10 minutes at room temperature on a shaking device. For STED, the fixation buffer additionally contained 0.1 % Glutaraldehyde (0.1 % in H_2O, Sigma-Aldrich, #G5882), which was not used for PBSA in order to reduce the fixation related green autofluorescence of the sample. After the fixation, the cells were washed again three times with the washing buffer. All steps (prior and following) were performed with cold reagents taken directly out of the fridge (4 °C) and all incubations were done at room temperature on a shaker.

For **PBSA**, as a last step, the cells were incubated with 750 mM Tris (Tris(hydroxymethyl)aminomethane, VWR Chemicals, VWR International GmbH, Darmstadt, Germany, #103156X) in DPBS (Gibco, #14190144) to quench the autofluorescence of the formaldehyde. Afterwards, they were washed with DPBS (Gibco, #14190144) three times and covered with DPBS for the measurement.

For **STED** immunostaining of intracellular mEGFP, the next step was the permeabilization with a buffer of similar composition like the washing buffer, complemented by 0.2 % Saponin (Sigma-Aldrich, #47036) as permeabilizing reagent. The buffer was incubated for 10 minutes. Following, the sample was washed twice using the washing buffer and blocked using a blocking buffer (HBSS with 0.1 M sucrose and 4 % BSA) for 1 hour. For the staining step, the GFP-Booster Atto647N (ChromoTek GmbH, Planegg-Martinsried, Germany, #gba647n-100) was diluted 1:200 in the blocking buffer and again incubated for 1 hour. Next, extensive washing was done using the washing buffer at least three times, incubating for a time span > 30 minutes in total. As a last step, the coverslips were mounted upside down on a microscope slide using ProLong™ Diamond Antifade Mountant (Invitrogen, Life Technologies Inc., Carlsbad, California, USA, #P36965) and stored over night before imaging.

C CD95 Imaging and Sample Characterization

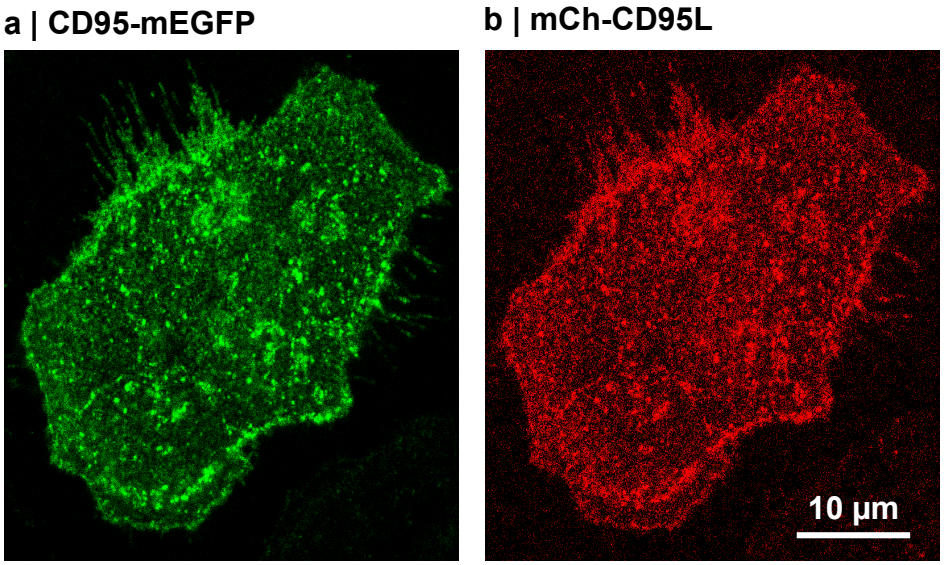

Figure C.1: Soluble CD95L arrives at the bottom cell membrane. To verify if CD95L can induce CD95 signaling via the bottom cell membrane, we tested whether the ligand in solution diffuses underneath the cell using confocal microscopy. An mCherry-labeled trimeric sCD95L was expressed and collected in the supernatant of HEK293T cells, as described before [186]. HeLa $CD95^{KO}$ cells were cultured, seeded and transiently transfected as described in Chapter 4.2 with 25 ng target plasmid DNA of full-length CD95-mEGFP. The cells were incubated with the mCh-sCD95L in medium (not purified) for 2 hours and subsequently washed, fixed and mounted (methods in Chapter 4.3). Confocal images of the fixed cells were recorded on the Abberior setup (Chapter 5.2.1) with the 485 nm and 561 nm laser lines. **a |** mEGFP and **b |** mCherry channel of one exemplary cell, the shown images were corrected for crosstalk using the Huygens Crosstalk Corrector (HuPro Version 21.10.1p2 64b, Scientific Volume Imaging B.V.). The images confirm, that sCD95L is able to diffuse underneath the bottom cell membrane.

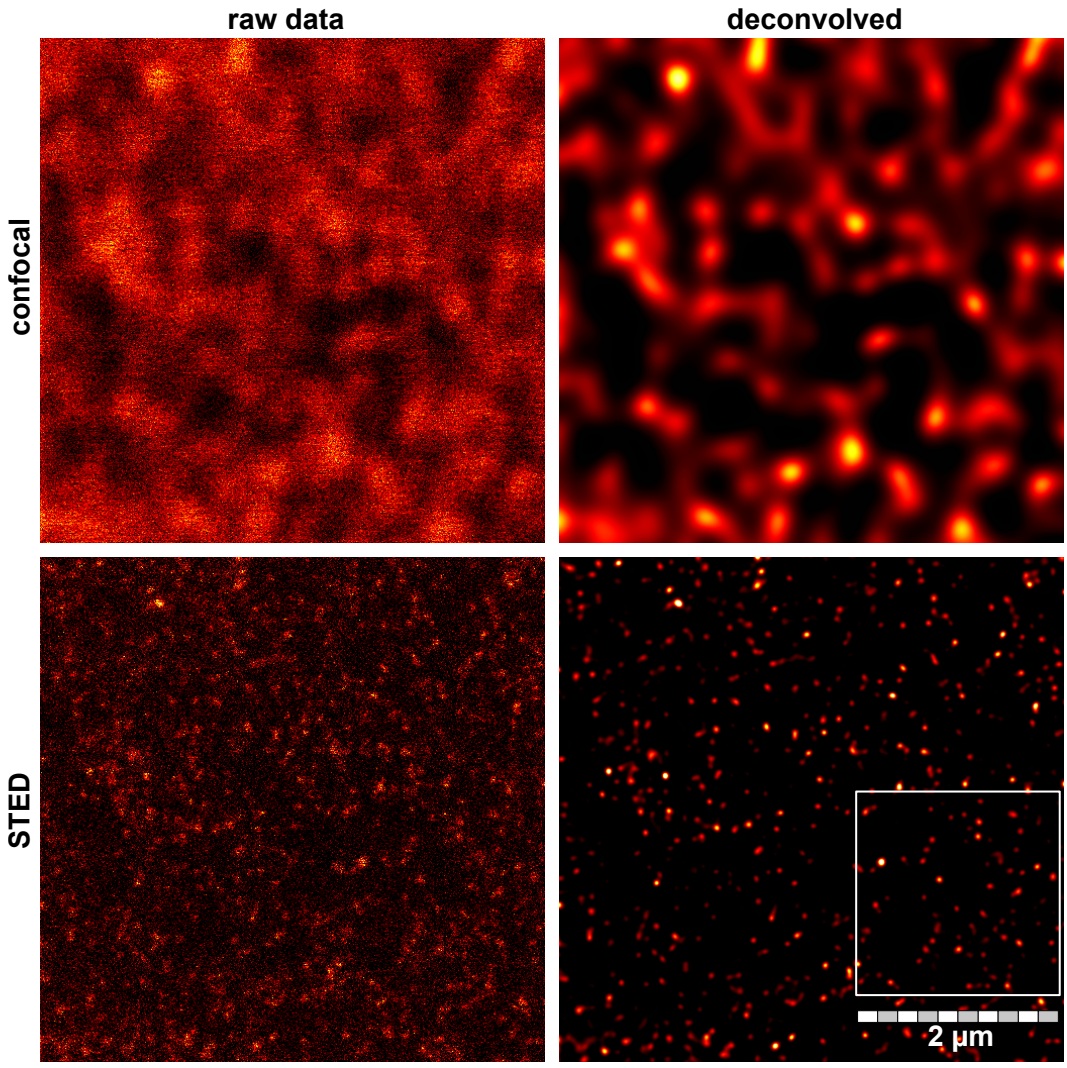

Figure C.2: Comparison of confocal and STED image. The $5 \times 5\,\mu m^2$ ROI shows Hela $CD95^{KO}$ transfected with CD95-mEGFP and stained with an anti-GFP nanobody Atto-647N (compare Chapter 5.3) imaged in confocal and STED mode as comparison. The left column shows the raw data (time-gated) and the right column the deconvolved image (Huygens Professional, Scientific Volume Imaging B.V.). The rectangular box indicates the $2 \times 2\,\mu m^2$ image segment shown in Figure 8.2.

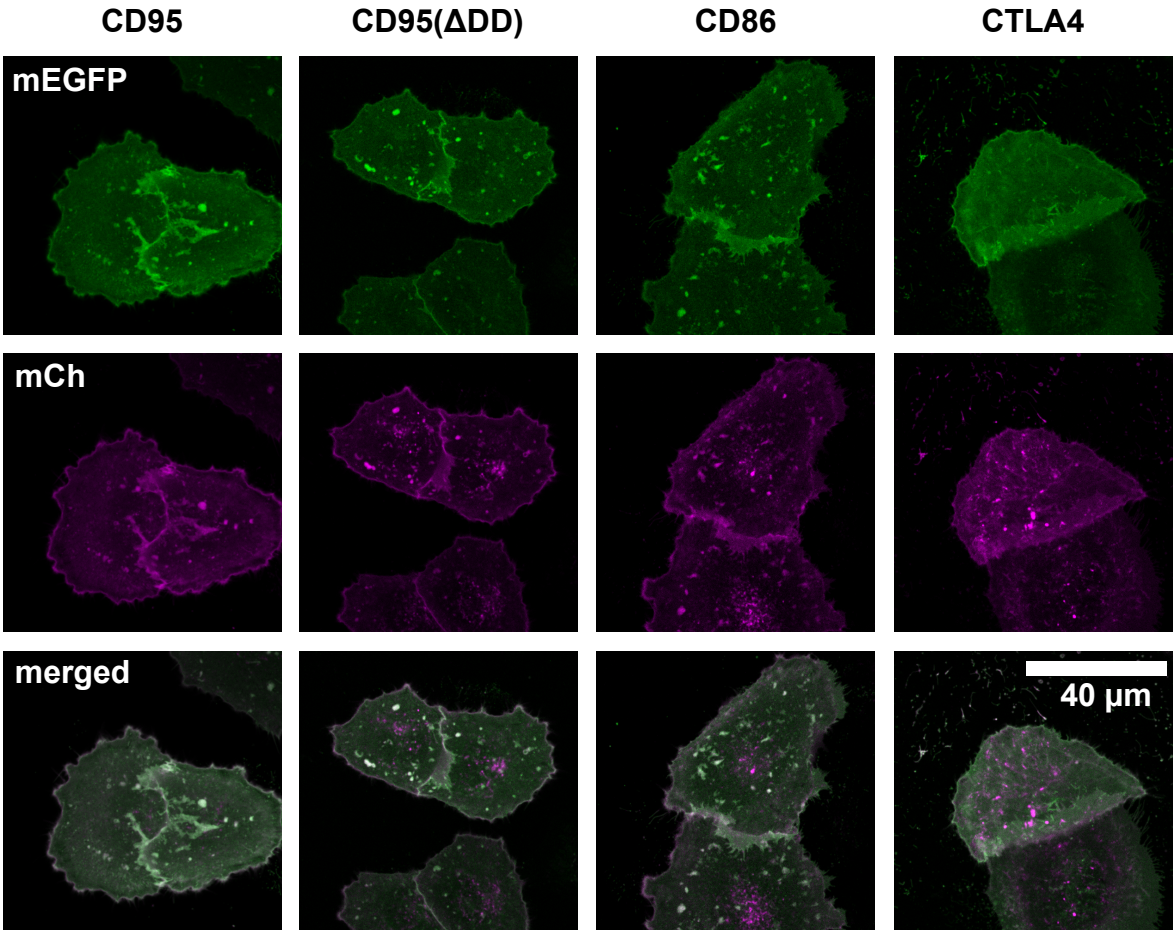

Figure C.3: Confocal images of transfected cells show the protein localization in the membrane during FRET measurements. Images show live HeLa $CD95^{KO}$ cells transfected with bicistronic plasmids coding for donor (mEGFP) and acceptor (mCherry) bound CD95, CD95(ΔDD), CD86 or CTLA4 during FRET measurements, focused on the lower cell membrane. Higher intensities at cell edges and cell-to-cell contact points show the correct integration of the membrane proteins into the outer cell membrane. Scale bar applies for all images.

C.1 QIFIKIT Accuracy Discussion

In order to estimate the method accuracy, we consider the deviation of the measured MFI (mean fluorescent intensity) of the calibration beads. Interestingly, there is a broad spread in the MFI of each bead populations. Albeit the producer describes the quantities of a mouse monoclonal antibody on the surface as "well-defined", they do not give quantitative information on the production-related accuracy [187]. The absolute SD scales with the Antibody-Binding Capacity (ABC) of the beads. Table C.1 shows the MFI with absolute and relative standard deviation determined in the two measurements.

The linear relation to determine the ABC of the sample from the measured MFI is

$$\mathrm{ABC} = a \cdot \mathrm{MFI} + b, \tag{C.1}$$

where a is the calibration coefficient obtained by the linear regression of the calibration beads with well-defined ABC.

Assuming a well-defined, definite number of binding sites (ABC) per bead population (albeit a quantitative information is not provided by the producer), the propagated error of a is only defined by the beads' MFI standard deviation:

$$a = \frac{\mathrm{ABC}}{\mathrm{MFI}} \Rightarrow \Delta a = \left| \frac{\mathrm{d}a}{\mathrm{dMFI}} \cdot \Delta\mathrm{MFI} \right| = \left| \frac{\mathrm{ABC}}{\mathrm{MFI}^2} \cdot \Delta\mathrm{MFI} \right| = \left| \frac{\Delta\mathrm{MFI}}{\mathrm{MFI}} \cdot a \right|. \tag{C.2}$$

Concluding, the error in a directly depends on the relative error of the measured signal $\frac{\Delta\mathrm{MFI}}{\mathrm{MFI}}$. Thus, the relative standard deviation (RSD) of the MFI can be understood as an effective measurement error. This includes technical errors (like device and detector inaccuracies) as well as variations in the degree of labeling. The mean RSD of the two measurement runs for all bead populations was 29.9 %, where the maximum RSD was 38.1 %. This value suggests, that the calibration induces a high error which is directly propagated to the accuracy achievable in the assessment of the ABC of cell measurements. Overall, the QIFIKIT can be used to assess the order of magnitude of receptor numbers on a cell population, but does not allow to determine precise receptor numbers of single cells due to an inaccuracy of the calibration factor of $\sim 30\,\%$.

Of note, in practice a is determined using a linear regression of the MFI vs. the ABC inducing a further, fit-related error which is not considered for this estimation as it is small compared to the RSD of the measurement values.

Bead population ABC	Run 1 MFI±SD	Run 1 RSD	Run 2 MFI±SD	Run 2 RSD
$2 \cdot 10^3$	1.39±0.44	31.7 %	1.36±0.37	27.2 %
$8.1 \cdot 10^3$	7.21±2.37	32.9 %	6.35±1.96	30.9 %
$42 \cdot 10^3$	40.09±15.31	38.1 %	33.81±12.03	35.6 %
$250 \cdot 10^3$	243.99±64.30	26.4 %	194.80±49.49	25.4 %
$787 \cdot 10^3$	618.63±148.96	24.1 %	506.70±133.55	26.4 %

Table C.1: Measurement results of the QIFIKIT calibration beads. The beads were stained and measured as described in Chapter 4.1.1. Mean fluorescent intensity (MFI) and absolute standard deviation (SD) given in arbitrary units.

D FCS

D.1 Optimal Instrument Settings for Live Cell FCS

Live cell FCS measurements on mEGFP remain challenging due to the limited mEGFP photostability and limited mEGFP abundance in a cell. To nevertheless obtain a robust readout, we discuss optimal experimental settings along with a brief description of the photophysical effects governing the observations.

Pinhole Setting

The optimal pinhole setting was determined experimentally to be 200 µm in diameter, or 492 nm backprojected pinhole radius [188], which corresponds to 2.1 Airy Units (AU). This setting optimally balances 1) a high photon collection efficiency, 2) a sharp Point Spread Function (PSF), and 3) the PSF shape to resemble a Gaussian. The tradeoff consists thereof that an open pinhole with high collection efficiency is needed to compensate for the poor photo-stability of mEGFP and resulting low SNR. However, opening the pinhole transforms the shape of the PSF from a sinc^2, which is Gaussian-like, to a sinc function, which in not Gaussian-like. As the FCS theory (see Equation 5.6) models a molecule diffusing through a 3D Gaussian volume, an open pinhole results in a mismatch between model and measurement visible in the fit residuals. As reported by others [131], a 2.1 AU pinhole leads to small but acceptable deviations between model function and data.

Fluorescent Molecule Concentration Fluctuates during Measurement

A change in fluorescent protein concentration is registered by the correlation function at long time scales, which complicates fitting slow membrane diffusion. For solution measurements, the dominant process for concentration decrease is adsorption to the glass surface, which is easily prevented by coating the glass surfaces with BSA (incubate 1 $^{\text{mg}}/_{\text{ml}}$ BSA (Sigma-Aldrich) for 10 minutes). Bleaching does not significantly affect concentrations in solution measurements as the bleaching rate is small compared

to the large fluorophore reservoir. In cells, a change in fluorescent protein concentration cannot be circumvented as photobleaching can readily deplete the reservoir of fluorescent proteins at an organelle or cellular scale. To mitigate the effects of a decreasing mEGFP concentration on the FCS curve, we divide the photon trace in chunks of approximately constant concentration and average these partial results [131].

We are able to gain additional insight by synergistically combining our results. From our FCS measurements we obtain diffusion times τ_{diff} and fluorophore brightness B, which we use to calculate the average number of photons per time the molecule (Mol) diffuses through the focus $B_{\tau_{\text{diff}}}$ to be ~ 1.5 for mEGFP (see Table D.1). From cPBSA we are able to obtain the total photon budget of mEGFP to be ~ 1000 photons. Taken together we conclude that the probability of mEGFP bleaching during a single pass through the detection volume is very low and that the mEGFP concentration decreases because a single molecule passes through the detection volume several times.

Dataset	N_{Mol}	B [Hz/Mol]	B_{norm} [Hz/(Mol·µW)]	τ_{diff} [ms] s1/s2	$B_{\tau_{\text{diff}}}$ [cnts/Mol] s1/s2
CD86-mEGFP v2[1]	6.0	2638	713	0.65 ± 0.06 / 41 ± 1	1.7 / 67
CD86-mEGFP v2[1]	6.1	2298	621	0.9 ± 0.2 / 56 ± 2.6	2.0 / 130
CD86-mEGFP v2[1]	4.1	3014	815	1.3 ± 0.2 / 122 ± 4[2]	4.0 / 366[2]
CD86-mEGFP v2[1]	6.2	2374	642	0.45 ± 0.05 / 34 ± 1	1.1 / 82
CD86-mEGFP v1	12.6	2252	608	0.60 ± 0.04 / 42 ± 1	1.35 / 95
CD86-mEGFP v1	13.0	3066	829	0.56 ± 0.05 / 31 ± 1	1.7 / 95
Average		**2607**	**705**	0.63 / 41	1.6 / 94

Table D.1: FCS mEGFP brightness measurements. Transfected HeLa CD95$^{\text{KO}}$ live cell FCS measurements on Abberior Setup (Chapter 5.2.1) to obtain mEGFP brightness B. Measurement details: excitation power at 485 nm: 3.7 µW, pinhole: 2.1 Airy Units (210 µm), $\kappa^2 = 7.72$. Two diffusion times were fitted for two species s1 and s2 (compare Chapter 5.4 and SI Figure D.1).
[1]: v2 is a 2$^{\text{nd}}$ version of the same plasmid as v1 (original) which was initially used for a failed pseudo dimer cloning approach (verified with multiple techniques).
[2]: outliers ignored for average.

Power Setting & Photon Budget

A higher laser power increases the SNR for the FCS curve at the cost of a higher bleaching rate, which cause unwanted changes in local concentrations (see section above). In

this section, we explain the underlying processes and obtain a trade-off between the SNR level of the FCS curve and the bleaching rate.

Primarily, the SNR of an FCS curve must be sufficient to enable interpretation, which scales with the number of photons detected while a single molecule diffuses through the focus [189]. Interestingly, our results indicate that the average number of photons is ~ 1.5 (see Table D.1). On the condition that molecules diffuse independent from each other, at least two photons are needed to obtain a correlation. This apparent contradiction is resolved by realizing that the number of photons per event follows a distribution with a long tail at higher photon numbers. I.e., while some of the molecules emit zero or one photon, the fraction which emits two or more photons is responsible for the correlation in FCS [190].

To help understand bleaching processes, we introduce the concept of photon budget to mean the total amount of photons emitted by the fluorophore before bleaching. It is inversely proportional to the bleaching probability per excitation cycle. Several studies on decay pathway modelling [191–193] reveal that the photon budget of mEGFP is constant at low irradiance but decreases after a transition regime. The decrease in photon budget is due to an additional photon being absorbed while the molecule is in the excited state, opening up additional photobleaching pathways and increasing the photobleaching probability per cycle. While a laser power lower than the transition irradiance maximizes the photon budget, a definite number could not be found in literature, although an upper limit was reported by Cranfill et al. [191] to be 80 µW using 488 nm excitation in a diffraction limited focus. Based on our own experimental experience we estimate the transition point from mEGFP to be lower than ∼10 µW.

To satisfy all the criteria above, the laser power was experimentally determined to be 5 µW corresponding to $3\,^{\mathrm{kW}}/_{\mathrm{cm}^2}$ for a calibrated 0.165 $\mu\mathrm{m}^2$ focal area.

Recording Time

Longer recording times improve the SNR of the FCS curve. However, to sample sufficient cell-to-cell variation during a measurement day it was limited to 5 minutes.

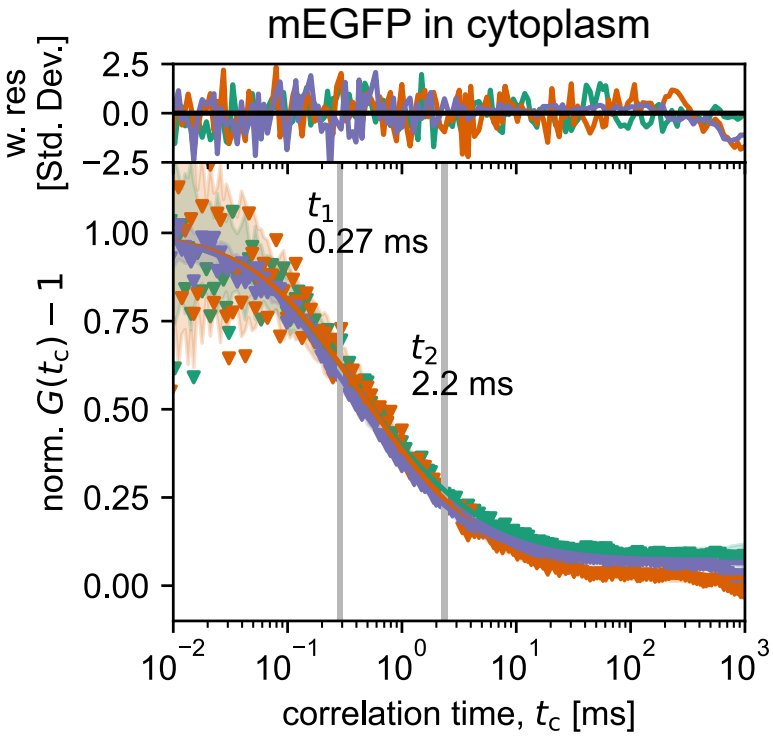

Figure D.1: FCS curves of free mEGFP in cytoplasm. Correlation curve of free mEGFP in cytoplasm expressed in Hela CD95^{KO} was fitted globally with two diffusion terms, with a weighted average of 0.50 ms.

E cPBSA

E.1 cPBSA Exemplary Traces and their Cross-Correlation Analysis

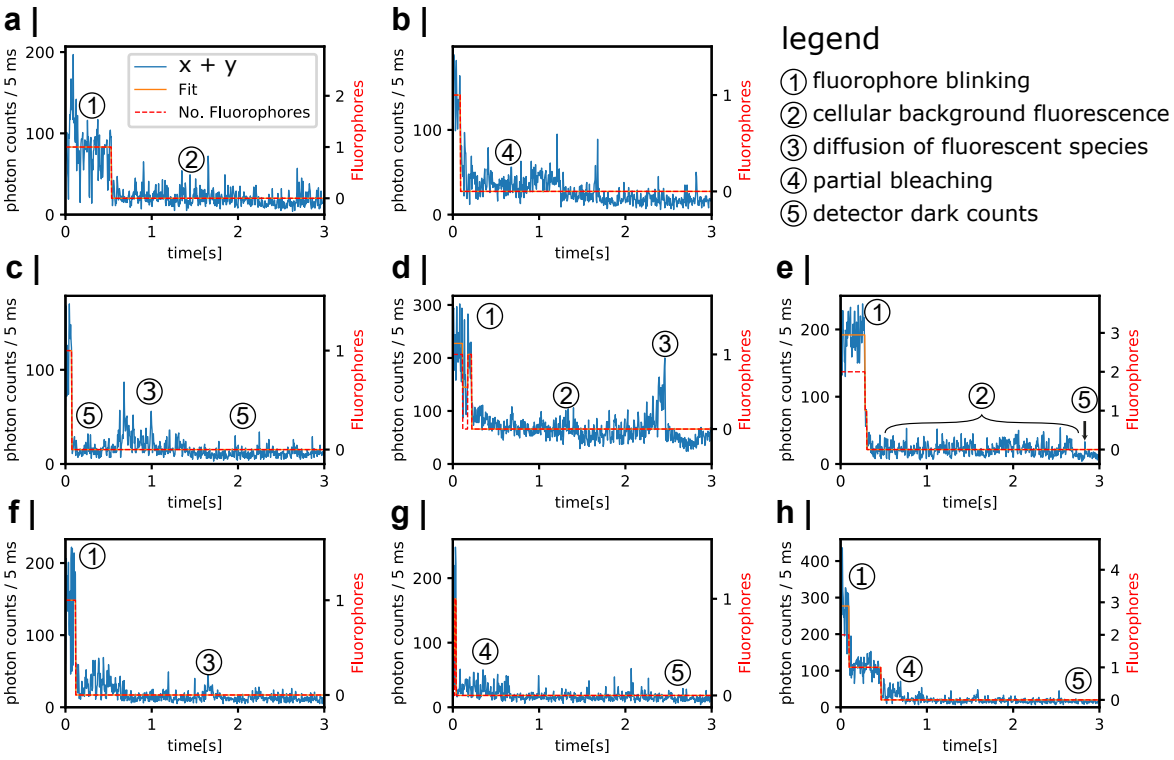

Figure E.1: Exemplary traces for confocal photo bleaching step analysis. **a-h |** Total fluorescent signal and fitted step trace, sources of noise are annotated. The most prominent sources of noise have been labelled in each graph for illustration purposes, although other sources are generally also present. **c-e |** Correlation curves of traces are plotted in Supplementary Figure E.2, panels b-d, respectively. **h |** Two-step bleaching event show variation in step size. Traces were selected to illustrate noise sources and illustrate the overall data quality with little bias.

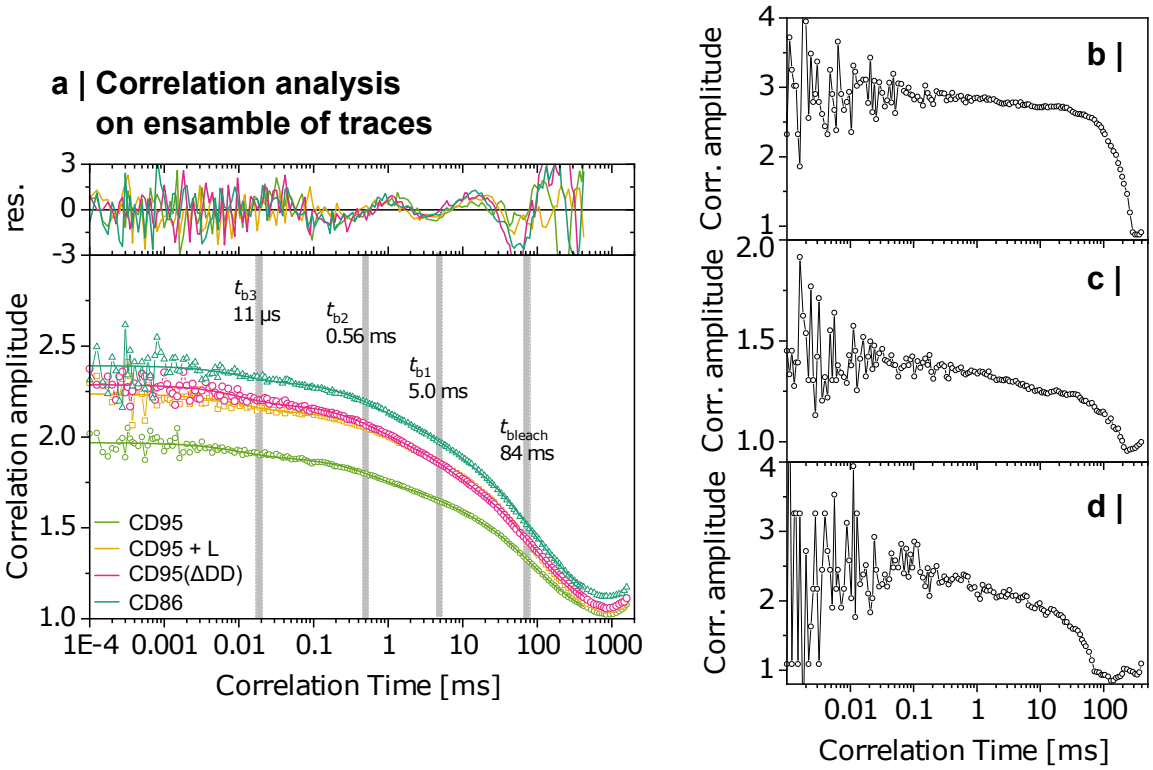

Figure E.2: Correlation analysis on photo bleaching traces. **a |** Cross-correlation curves calculated for the ensemble of traces for each sample. Curves were fitted with 3 bunching terms and 1 3D diffusion term as an approximation to model the bleaching behavior (see Equation 5.10). As the bleaching statistics do not follow 3D diffusion statistics, we see a correlation in the residuals. All time parameters were fitted globally, whereas the fractions were left free (see Methods Table 5.2). We may obtain the parameters α and k_{on} from the bunching fraction and bunching times, respectively, and predict the variance of trace sections (see Supplementary Chapter E.2). Note that the bunching fractions were similar over different samples, indicating that the photophysical properties of mEGFP over different samples were similar as well. **b-d |** CD86 correlation curves correspond to traces c-e respectively of Supplementary Figure E.1. As all photons correlate, a high signal correlation curve can be generated based on only a few photons, allowing single-molecule based correlation fits. Whereas the correlation due to blinking looks similar to the ensemble fits, the bleaching correlation varies per molecular assembly, as also the bleaching time and amplitude varies.

E.2 Predicted Variance from cPBSA Cross-Correlation Curves

We assume a simple model where the mEGFP molecule can enter a dark state with rate k_{off} and return to the bright state with rate k_{on}. The latter can directly be obtained from the cross-correlation fit as it is inversely proportional to t_{on}, the characteristic time from the cross-correlation bunching therm. To obtain k_{off}, we define the fraction of time spent in the on state, α, as

$$\alpha = \frac{k_{\text{on}}}{k_{\text{on}} + k_{\text{off}}}, \tag{E.1}$$

where $(1 - \alpha)$ equals the amplitude of the bunching term. Using the values from the fit listed in Table E.1, we obtain 1/5 ms and 1/30 ms for k_{on} and k_{off} for the slowest transition. To obtain a theoretical description of the variance on a trace segment, we define

$$n = t_{\text{bin}} \left(k_{\text{on}} + k_{\text{off}}\right), \tag{E.2}$$

where n is the average number of transitions in some time period t_{bin}. For a fluorophore with fluorescence rate k_{fl}, the average signal in time period t_{bin} is given by

$$\langle S \rangle = t_{\text{bin}} \langle k_{\text{fl}} \rangle \alpha; \tag{E.3}$$

$$\langle S \rangle = N_{\text{fl}} \alpha, \tag{E.4}$$

where N_{fl} is defined as the average number of photons emitted if there was no dark state. Note that the fluorophore brightness, k_{fl} is understood to include polarization effects, such that it differs per molecule. We may now write the variance of the signal as

$$Var(S) = \left|\frac{\delta S}{\delta \alpha}\right|^2 Var(\alpha) + \left|\frac{\delta S}{\delta N_{\text{fl}}}\right|^2 Var(N_{\text{fl}}), \tag{E.5}$$

where the covariance between α and N_{fl} as a function of excitation power is not considered as the excitation was kept within the range $1.3 \pm 0.2\,\mu\text{W}$ (compare Table 5.1). From Barth et al. [194], we obtain the variance of α:

$$Var(\alpha) = \alpha(1 - \alpha)\frac{2}{n}\left(1 + \frac{e^{-n} - 1}{n}\right). \tag{E.6}$$

To obtain the variance of N_{fl}, we consider that the average number of photons emitted follows a poissonian distribution

$$Var(N_{\mathrm{fl}}) = \frac{N_{\mathrm{fl}}}{\alpha}. \tag{E.7}$$

Combining all formulas, we obtain a direct expression:

$$Var(S) = N_{\mathrm{fl}}^2 \alpha(1-\alpha)\frac{2}{n}\left(1 + \frac{e^{-n}-1}{n}\right) + \alpha N_{\mathrm{fl}}. \tag{E.8}$$

We check that in the limit of very fast fluctuations from the dark state, the variance due to α becomes zero and we obtain a Poisson distribution as expected

$$\lim_{n\to\infty} Var(S) = \alpha N_{\mathrm{fl}}. \tag{E.9}$$

Intuitively, we understand that long dark state times with respect to t_{bin} cause fluctuations in α whose variance dominates the inherent Poisson noise, hence this result confirms that our initial model of considering only the longest dark states captures all essential features. To check our expression, we perform Monte Carlo simulations for all values of α, n and N_{fl} (see Supplementary Figure E.3) confirming that it correctly predicts the variance and showing that the variance per trace fluctuates with the stochastic number of blinks. Simulations were performed by Nicolaas T M van der Voort.

Model no. terms	$\chi^2_{\mathrm{red,avg}}{}^*$	$t_{\mathrm{diff,w}}$	$t_{\mathrm{bunch,1}}$	$t_{\mathrm{bunch,2}}$	$t_{\mathrm{bunch,3}}$	$t_{\mathrm{bunch,4}}$
1 diffusion, 1 bunching[1]	6.7	59.6 ms	0.85 ms	-	-	-
1 diffusion, 2 bunching[1]	2.1	73 ms	2.41 ms	0.09 ms	-	-
1 diffusion, 3 bunching	1.08	83 ms	5.00 ms	0.56 ms	0.011 ms	-
1 diffusion, 4 bunching[2]	0.78	95 ms	13.4 ms	1.4 ms	0.11 ms	0.006 ms

Table E.1: cPBSA trace cross-correlation fitting model. The correct model for fitting cross-correlation of cPBSA traces was determined by best $\chi^2_{\mathrm{red,avg}}$, the reduced χ^2 averaged over the four cross-correlations shown in Supplementary Figure E.2 c. Correlation times were fitted globally over the four correlation curves, the amplitudes were fitted individually.
* Average from global fit of four traces.
[1] Fit has too high χ^2_{red} to describe data well.
[2] $\chi^2_{\mathrm{red}} < 1$ indicates overfitting.

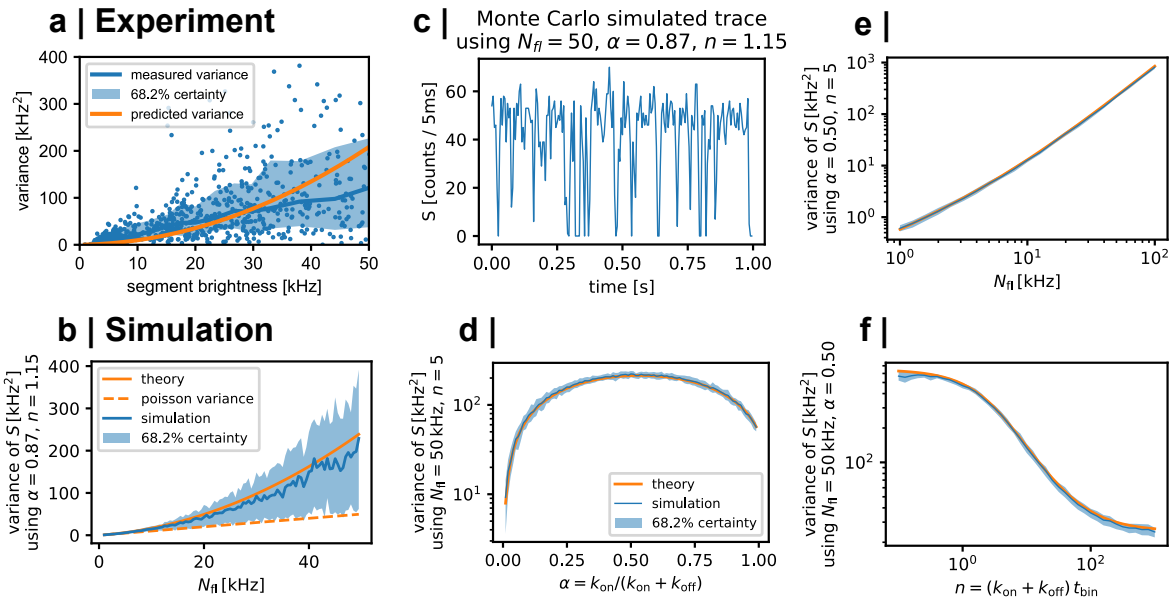

Figure E.3: A single dark state predicts cPBSA trace variance. A theoretical formula for the variance of an emitter under a single dark state (see Supplementary Chapter E.2) is compared to measured and simulated trace variances. **a |** For each trace segment from CD86 traces measured on 22 July 2021 the segment intensity and variance was obtained from PBSA analysis (blue points). For each 50 consecutive intensities the median (blue line) and 15.9 % - 84.1 % quantiles (blue area) are determined to aid visualization. Supplementary Equation E.8 is used to predict the variance for each segment using α and n obtained from FCS [194] and N_{fl} for each segment. For reference the variance based on pure Poisson noise is shown. **b |** Monte Carlo traces using identical α, n , trace duration as in a) match the theoretical prediction. The short trace duration (84 ms, see Supplementary Figure E.2) causes a large spread in the variance due to the varying number of blinks in this period, matching the spread observed in a). **c |** Exemplary Monte Carlo trace under conditions typical to mEGFP measurements. **d-f |** Similar to b, but using a simulation time of 1 second and scanning the whole parameter space. Legend for all as given in d).

F Advanced FRET

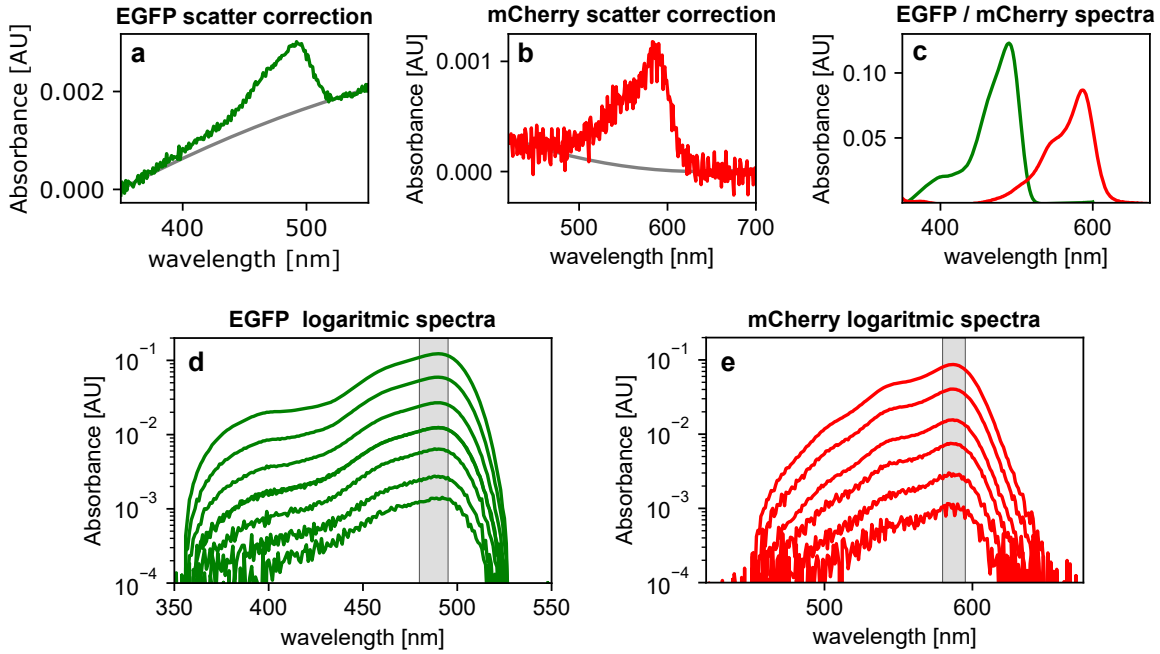

Figure F.1: Accurate fluorophore concentration determination from absorption spectra. a | Raw 0.16 µM EGFP spectra is affected by scatter which cannot be corrected for using a blank. Background signal is fitted outside the absorption peak from 350−360 nm and 520−600 nm with a parabolic function. The scatter contribution is subtracted to yield the corrected absorption curve. **b |** Same as in a) for 0.093 µM mCherry concentration using 350 − 450 nm and 320 − 700 nm for background fitting. **c |** Familiar linear representation of 14.1 µM EGFP and 7.8 µM mCherry absorption spectra. **d |** Logaritmic representation of all corrected EGFP and **e |** mCherry spectra. Concentration C was determined by Lambert-Beer's law $C = A/(\epsilon b)$ using the average dimensionless absorption A in the grey shaded area. b is the pathlength of the cuvette in cm and ϵ is the extinction coefficient.

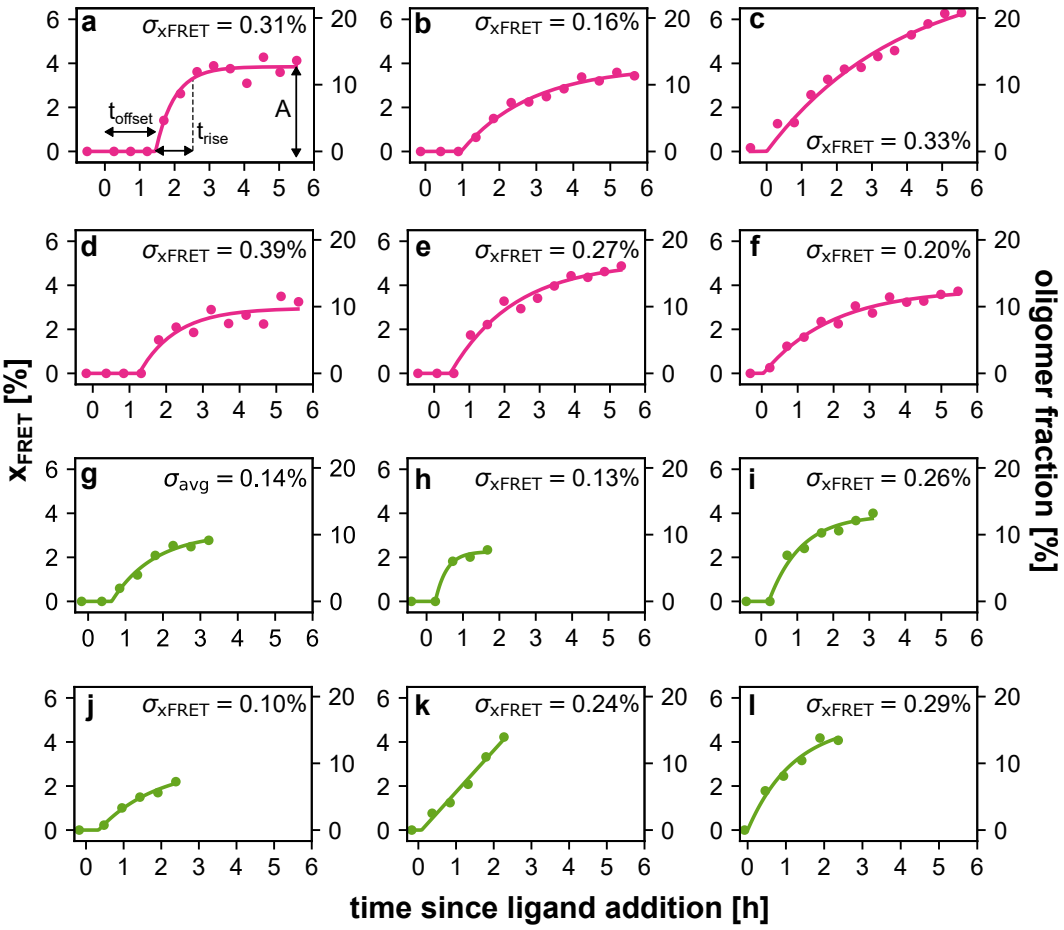

Figure F.2: Time evolution of selected cells show an oligomerization increase reaching a steady-state Time evolution is fitted according to the exponential convergence to a new steady state. Axes labels are valid for all panels, color legend same as in Figure 6.2. **a** | Fitting parameters are illustrated. **a-f** | Time traces of the oligomerization of apoptosis-incompetent Hela CD95^{KO} cells expressing CD95(ΔDD). **g-l** | Apoptosis-competent CD95 cells undergo apoptosis after 2-3 hours. The fit residuals are corrected for the number of fit parameters to obtain the standard deviation of the measurement, σ_{xFRET}, for each cell.

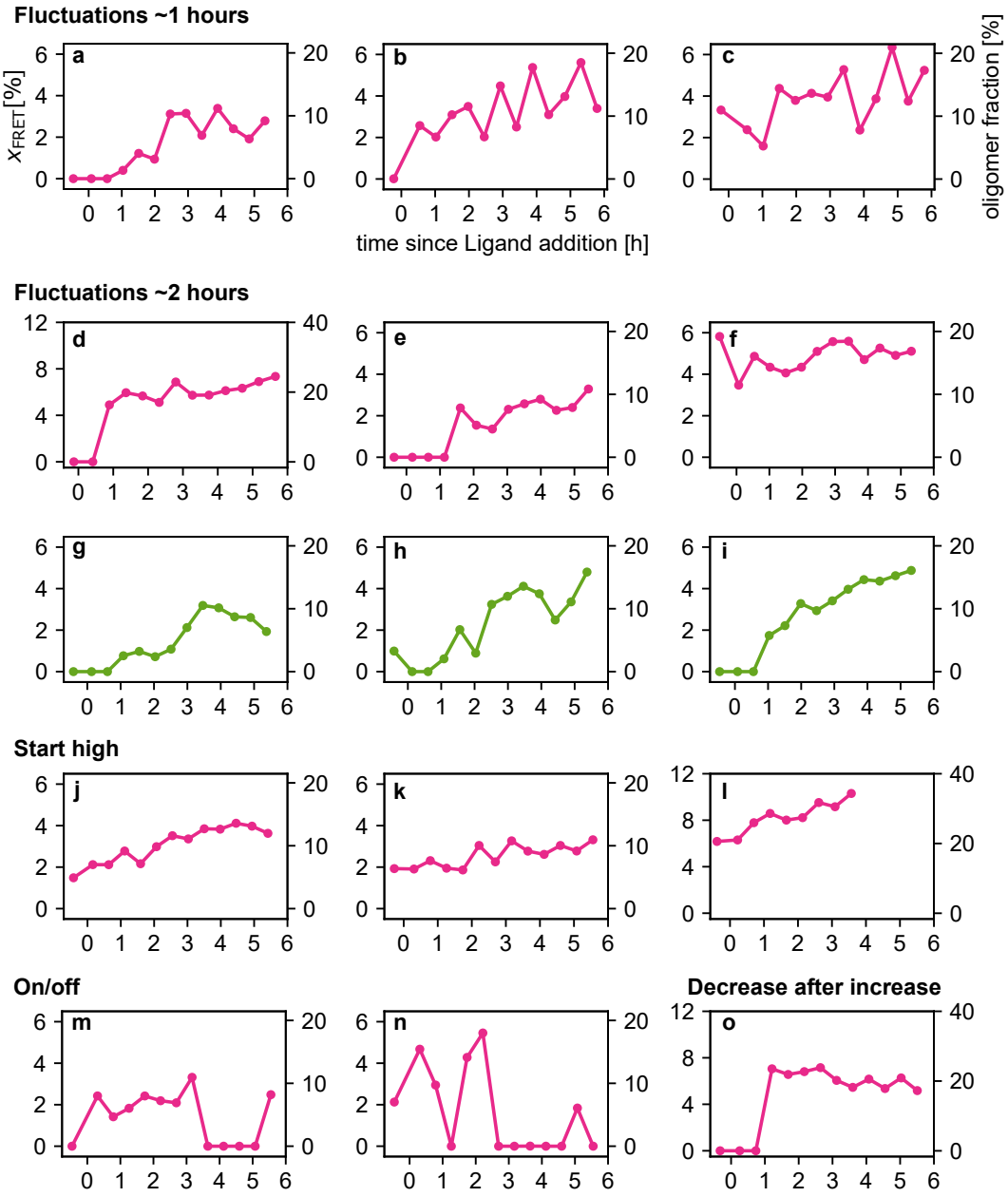

Figure F.3: Oligomer time evolution of selected cells show a variety of modulated responses to ligand stimulation. **a-c |** The oligomer fraction oscillates on the ~ 1 hour timescale. **d-i |** Oligomer fraction shows an oscillation on a ~ 2 hour timescale in addition to an overall increase. **a,e |** Oligomerization is delayed by a certain time. **j-l |** Before ligand addition the oligomer fraction is nonzero and ligand addition still increases the overall oligomer fraction. This was primarily observed for CD95(ΔDD) traces at high expression levels. **m,n |** After ligand addition initially triggered oligomerization, the oligomerization process is reversed showing extended periods of absence of oligomers. Potentially this is an extreme case of the oscillations observed in a-i. **o |** After an initial rapid increase, the oligomer fraction slowly decreases again. Trace colors follows the global color legend (Figure 6.2). Note that the majority of traces come from CD95(ΔDD) transfected cells as the truncation of the DD prevented apoptosis and enabled longer measurement times.

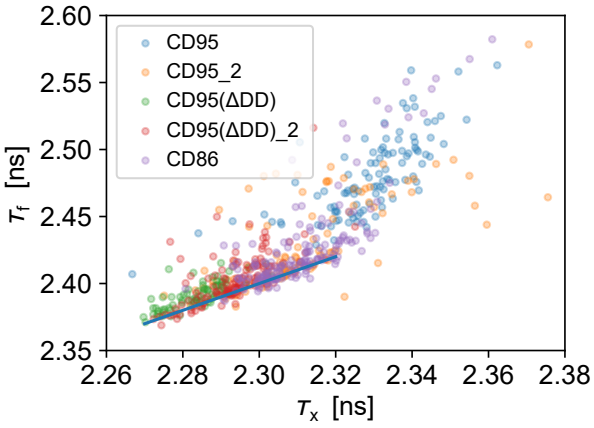

Figure F.4: Donor only lifetimes. The species weighted average lifetime (τ_x) versus the fluorescence weighted average lifetime (τ_f) is shown. Five different control measurements of donor only (D0) proteins expressed in HeLa CD95^{KO} recorded on five different days are shown. A selection criterion for receptor surface concentrations between 150 and 1000 $^{\text{receptors}}/_{\mu m^2}$ was applied to avoid noisy controls on one hand and controls affected by proximity-induced homo-FRET on the other hand. Center and standard deviation for τ_x of each population is 2.335 ± 0.008 ns, 2.304 ± 0.009 ns, 2.282 ± 0.007 ns, 2.290 ± 0.008 ns and 2.307 ± 0.009 ns for CD95, CD95_2, CD95(ΔDD), CD95(ΔDD)_2 and CD86 donor only controls respectively, yielding a standard error of 0.36 % x_{FRET} within a control measurement and 0.79 % between control measurements. Interestingly, we identify a population of constant τ_x/τ_f (blue line), indicating a change in lifetime but not in species fraction. An increased lifetime is consistent with a drop in the dielectric constant due to e.g. an increase in medium temperature. As such, these fluctuations are the consequence of minor temperature fluctuations between measurement days and within a calibration sample. In addition, the population located away from the blue line from mostly CD95 samples indicates a change in species fraction, consistent with a change in the preferred fluorescent state of mEGFP.

List of Figures

List of Tables

Acronyms

aa Amino Acid (also: AA).

AB Antibody.

ABC Antibody-Binding Capacity.

AIDS Acquired Immune Deficiency Syndrome.

ALEX Alternating Line EXcitation.

ALL Acute Lymphocytic (or Lymphoblastic) Leukemia.

APAF1 Apoptotic Protease Activating Factor 1.

APC Allophycocyanin (a fluorescent dye).

ApC Antigen-Presenting Cell.

APD Avalanche Photodiode.

API Application Programming Interface.

ATCC American Type Culture Collection.

AU Airy Units.

AV Accessible Volume.

BAD BCL2-associated Agonist of cell Death protein.

BCL2 B-Cell Lymphoma 2.

BF Bright Field.

BID BH3 Interacting-domain Death agonist.

BSA Bovine Serum Albumin.

CAR Chimeric Antigen Receptor.

CASMER Clusters of Apoptotic Signaling Molecule-Enriched Rafts.

CD Cluster of Differentiation.

CD95 Cluster of Differentiation 95.

CD95L CD95 Ligand, also FasL / Fas Ligand.

CID Calcium-Inducing Domain.

CID Calcium-Inducing Domain.

CMLE Classic Maximum Likelihood Estimation (Deconvolution Algorithm).

CMV human Cytomegalovirus.

cPBSA confocal Photobleaching Step Analysis.

CRC Collaborative Research Center.

CRD Cysteine-Rich Domain.

CTLA4 Cytotoxic T-Lymphocyte-associated Antigen 4.

D0 Donor-only (Plasmid/Sample).

DA Donor-Acceptor (Plasmid/Sample).

DC Dichroic Mirror.

DD Death Domain.

DED Death-Effector Domain.

DFG Deutsche Forschungsgemeinschaft, *english: German Research Foundation.*

DISC Death Inducing Signaling Complex.

DNA Deoxyribonucleic Acid.

DOL Degree Of Labeling.

DR Death Receptor.

ECD Extracellular Domain.

EM Electron Microscopy.

em. emission.

ER Endoplasmic Reticulum.

exc. excitation.

FADD Fas-Associated protein with Death Domain, also Mort-1.

FBS Fetal Bovine Serum.

FCS Fluorescence Correlation Spectroscopy.

FITC Fluorescein (a fluorescent dye).

FLICE FADD-like ICE, or FADD-Homologous ICE/CED-3–like Protease.

FLIM Fluorescence Lifetime Imaging.

FLIP FLICE (caspase-8)-Like Inhibitory Proteins.

FP Fluorescent Protein.

FRET Förster Resonance Energy Transfer.

FWHM Full Width at Half Maximum.

GvHD Graft-versus-Host Disease.

HeLa Human Cervix Carcinoma Cell Line.

HLA Human Leukocyte Antigen.

HNSCC Head and Neck Squamous Cell Carcinoma.

IAP Inhibitor of Apoptosis Proteins.

ICD Intracellular Domain.

IL-2 Interleukin-2.

IRF Instrument Response Function.

ITAM Immunoreceptor Tyrosine-based Activation Motif.

KV Kalafut-Visscher (algorithm).

MAPK Mitogen-Activated Protein Kinases.

mCD95L membrane bound CD95 Ligand.

mEGFP monomeric Enhanced Green Fluorescent Protein.

MFI Mean Fluorescent Intensity.

MHC Major Histocompatibility Complex.

MMP Matrix MetalloProteases.

Mol Molecule.

MOMP Mitochondrial Outer Membrane Permeability.

NA Numerical Aperture.

NF Notch Filter.

NK Natural Killer (cell).

NMR Nuclear Magnetic Resonance.

nTPM normalized Transcripts Per Million.

P/S Penicillin-Streptomycin (solution).

PALM Photoactivated Localization Microscopy.

PBSA Photobleaching Step Analysis.

PDB Protein Data Bank.

PH Phase Contrast.

PI3K Phosphoinositid-3-Kinase.

PIE Pulsed Interleaved Excitation.

PLAD Pre-Ligand Assembly Domain.

PSF Point Spread Function.

pxl Pixel.

QIFIKIT Quantitative Analysis Kit.

Rh101 Rhodamin101.

Rh110 Rhodamin110.

ROI Region Of Interest.

RSD Relative Standard Deviation.

sCD95L soluble form of CD95 Ligand.

scFv Single-Chain Variable Fragment.

SD Standard Deviation.

SDS-PAGE Sodium Dodecyl Sulfate Polyacrylamide Gel Electrophoresis.

SI Supplementary Information.

SMAC (Small Mitochondria-derived Activator of Caspases.

SMLM Single-Molecule Localization Microscopy.

SNR Signal-to-Noise Ratio.

SP Signaling Peptide.

STED Stimulated Emission Depletion.

STORM STochastic Optical Reconstruction Microscopy.

TCR T-Cell Receptor.

TCSPC Time-Correlated Single Photon Counting.

THD TNF Homology Domain.

TIRF Total Internal Reflection Fluorescence.

TM Transmembrane Domain.

TNF Tumor Necrosis Factor.

TNFR Tumor Necrosis Factor Receptor.

TNFSF Tumor Necrosis Factor Superfamily.

TRAF TNF Receptor-Associated Factor.

TRAIL Tumor Necrosis Factor Related Apoptosis Inducing Ligand.

Tris Tris(hydroxymethyl)aminomethane.

WT Wild Type.

Bibliography

[1] Gülce S. Gülcüler Balta, Cornelia Monzel, Susanne Kleber, Joel Beaudouin, Emre Balta, Thomas Kaindl, Si Chen, Liang Gao, Meinolf Thiemann, Christian R. Wirtz, Yvonne Samstag, Motomu Tanaka, and Ana Martin-Villalba. 3D Cellular Architecture Modulates Tyrosine Kinase Activity, Thereby Switching CD95-Mediated Apoptosis to Survival. *Cell Reports*, 29:2295–2306.e6, 11 2019. ISSN 22111247. doi: 10.1016/j.celrep.2019.10.054.

[2] Joan Stiles and Terry L. Jernigan. The Basics of Brain Development. *Neuropsychology Review*, 20:327, 12 2010. ISSN 10407308. doi: 10.1007/s11065-010-9148-4.

[3] Joseph P. Kolb, Thomas H. Oguin, Andrew Oberst, and Jennifer Martinez. Programmed Cell Death and Inflammation: Winter Is Coming. *Trends in Immunology*, 38:705–718, 10 2017. ISSN 1471-4906. doi: 10.1016/j.it.2017.06.009.

[4] Shigekazu Nagata and Masato Tanaka. Programmed cell death and the immune system. *Nature Reviews Immunology*, 17:333–340, 2 2017. ISSN 1474-1741. doi: 10.1038/nri.2016.153.

[5] U. Ziegler and P. Groscurth. Morphological features of cell death. *News Physiol Sci*, 19:124–128, 6 2004. ISSN 0886-1714. doi: 10.1152/nips.01519.2004.

[6] Paul G. Ekert and David L. Vaux. Apoptosis and the immune system. *British medical bulletin*, 53:591–603, 1997. ISSN 0007-1420. doi: 10.1093/oxfordjournals.bmb.a011632.

[7] Peter H Krammer. CD95's deadly mission in the immune system. *Nature*, 407:789–795, 2000.

[8] Jean Luc Bodmer, Pascal Schneider, and Jürg Tschopp. The molecular architecture of the TNF superfamily. *Trends in Biochemical Sciences*, 27:19–26, 2002. ISSN 09680004. doi: 10.1016/s0968-0004(01)01995-8.

[9] Bharat B. Aggarwal. Signalling pathways of the TNF superfamily: a double-edged sword. *Nature Reviews Immunology*, 3:745–756, 2003. ISSN 1474-1741. doi: 10.1038/nri1184.

[10] Éva S. Vanamee and Denise L. Faustman. Structural principles of tumor necrosis factor superfamily signaling. *Science Signaling*, 11, 2018. ISSN 19379145. doi: 10.1126/scisignal.aao4910.

[11] Edwin Bremer. Targeting of the Tumor Necrosis Factor Receptor Superfamily for Cancer Immunotherapy. *ISRN Oncology*, 2013:1–25, 6 2013. doi: 10.1155/2013/371854.

[12] M. E. Peter, A. Hadji, A. E. Murmann, S. Brockway, W. Putzbach, A. Pattanayak, and P. Ceppi. The role of CD95 and CD95 ligand in cancer. *Cell Death & Differentiation*, 22:549–559, 2 2015. ISSN 1476-5403. doi: 10.1038/cdd.2015.3.

[13] Susanne Kleber, Ignacio Sancho-Martinez, Benedict Wiestler, Alexandra Beisel, Christian Gieffers, Oliver Hill, Meinolf Thiemann, Wolf Mueller, Jaromir Sykora, Andreas Kuhn, Nina Schreglmann, Elisabeth Letellier, Cecilia Zuliani, Stefan Klussmann, Marcin Teodorczyk, Hermann Josef Gröne, Tom M. Ganten, Holger Sültmann, Jochen Tüttenberg, Andreas von Deimling, Anne Regnier-Vigouroux, Christel Herold-Mende, and Ana Martin-Villalba. Yes and PI3K Bind CD95 to Signal Invasion of Glioblastoma. *Cancer Cell*, 13:235–248, 2008. ISSN 15356108. doi: 10.1016/j.ccr.2008.02.003.

[14] Naoto Itoh, Shin Yonehara, Ai Ishii, Minako Yonehara, Sei Ichi Mizushima, Masazumi Sameshima, Atsushi Hase, Yoshiyuki Seto, and Shigekazu Nagata. The polypeptide encoded by the cDNA for human cell surface antigen Fas can mediate apoptosis. *Cell*, 66:233–243, 7 1991. ISSN 0092-8674. doi: 10.1016/0092-8674(91)90614-5.

[15] Valérie Edmond, Benoist Ghali, Aubin Penna, Jean Luc Taupin, Sophie Daburon, Jean François Moreau, and Patrick Legembre. Precise Mapping of the CD95 Pre-Ligand Assembly Domain. *PLOS ONE*, 7:e46236, 9 2012. ISSN 1932-6203. doi: 10.1371/journal.pone.0046236.

[16] Francis Ka-Ming Chan. The pre-ligand binding assembly domain: a potential target of inhibition of tumour necrosis factor receptor function. *Annals of the Rheumatic Diseases*, 59:i50, 2000. ISSN 00034967. doi: 10.1136/ard.59.suppl _1.i50.

[17] Giuliana Papoff, Peter Hausler, Adriana Eramo, Maria Grazia Pagano, Giulia Di Leve, Alberto Signore, and Giovina Ruberti. Identification and characterization of a ligand-independent oligomerization domain in the extracellular region of the CD95 death receptor. *Journal of Biological Chemistry*, 274:38241–38250, 12 1999. ISSN 00219258. doi: 10.1074/jbc.274.53.38241.

[18] Richard M. Siegel, John K. Frederiksen, David A. Zacharias, Francis Ka Ming Chan, Michele Johnson, David Lynch, Roger Y. Tsien, and Michael J. Lenardo. Fas preassociation required for apoptosis signaling and dominant inhibition by pathogenic mutations. *Science*, 288:2354–2357, 6 2000. ISSN 00368075. doi: 10.1126/science.288.5475.2354.

[19] Gary C. Starling, Jürgen Bajorath, John Emswiler, Jeffrey A. Ledbetter, Alejandro Aruffo, and Peter A. Kiener. Identification of Amino Acid Residues Important for Ligand Binding to Fas. *The Journal of Experimental Medicine*, 185:1487, 4 1997. ISSN 00221007. doi: 10.1084/jem.185.8.1487.

[20] Nicolas Levoin, Mickael Jean, and Patrick Legembre. CD95 Structure, Aggregation and

Cell Signaling. *Frontiers in Cell and Developmental Biology*, 8, 2020. ISSN 2296634X. doi: 10.3389/fcell.2020.00314.

[21] Jason R. Orlinick, Keith B. Elkon, and Moses V. Chao. Separate Domains of the Human Fas Ligand Dictate Self-association and Receptor Binding. *Journal of Biological Chemistry*, 272:32221–32229, 12 1997. ISSN 0021-9258. doi: 10.1074/jbc.272.51.32221.

[22] Matthias Voss, Marcus Lettau, Maren Paulsen, and Ottmar Janssen. Posttranslational regulation of Fas ligand function. *Cell Communication and Signaling*, 6:1–12, 12 2008. ISSN 1478811X. doi: 10.1186/1478-811x-6-11/figures/5.

[23] R. A. Smith and C. Baglioni. The active form of tumor necrosis factor is a trimer. *Journal of Biological Chemistry*, 262:6951–6954, 5 1987. ISSN 0021-9258. doi: 10.1016/s0021-9258(18)48183-5.

[24] E. Y. Jones, D. I. Stuart, and N. P.C. Walker. Structure of tumour necrosis factor. *Nature*, 338:225–228, 1989. ISSN 1476-4687. doi: 10.1038/338225a0.

[25] M J Eck and S R Sprang. The Structure of Tumor Necrosis Factor-α at 2.6 ÅResolution: Implications for receptor binding. *Journal of Biological Chemistry*, 264:17595–17605, 10 1989. ISSN 0021-9258. doi: 10.1016/s0021-9258(18)71533-0.

[26] M. J. Eck, M. Ultsch, E. Rinderknecht, A. M. De Vos, and S. R. Sprang. The structure of human lymphotoxin (tumor necrosis factor-beta) at 1.9-A resolution. *Journal of Biological Chemistry*, 267:2119–2122, 2 1992. ISSN 0021-9258. doi: 10.1016/s0021-9258(18)45849-8.

[27] D. Berg, M. Lehne, N. Müller, D. Siegmund, S. Münkel, W. Sebald, K. Pfizenmaier, and H. Wajant. Enforced covalent trimerization increases the activity of the TNF ligand family members TRAIL and CD95L. *Cell Death & Differentiation*, 14:2021–2034, 8 2007. ISSN 1476-5403. doi: 10.1038/sj.cdd.4402213.

[28] M Tanaka, T Suda, T Yatomi, N Nakamura, and S Nagata. Lethal effect of recombinant human Fas ligand in mice pretreated with Propionibacterium acnes. *The Journal of Immunology*, 158:2303–2309, m 1997.

[29] Marta Muzio, Arul M. Chinnaiyan, Frank C. Kischkel, Karen O'Rourke, Andrej Shevchenko, Jian Ni, Carsten Scaffidi, James D. Bretz, Mei Zhang, Reiner Gentz, Matthias Mann, Peter H. Krammer, Marcus E. Peter, and Vishva M. Dixit. FLICE, a novel FADD-homologous ICE/CED-3-like protease, is recruited to the CD95 (Fas/APO-1) death–inducing signaling complex. *Cell*, 85:817–827, 6 1996. ISSN 0092-8674. doi: 10.1016/s0092-8674(00)81266-0.

[30] Frank C. Kischkel, Stefan Hellbardt, Iris Behrmann, Matthias Germer, Michael Pawlita, Peter H. Krammer, and Marcus E. Peter. Cytotoxicity-dependent APO-1 (Fas/CD95)-associated proteins form a death-inducing signaling complex (DISC) with the receptor. *The EMBO Journal*, 14:5579–5588, 11 1995. ISSN 1460-2075. doi: 10.1002/j.1460-

2075.1995.tb00245.x.

[31] Carsten Scaffidi, Simone Fulda, Anu Srinivasan, Claudia Friesen, Feng Li, Kevin J Tomaselli, Klaus-Michael Debatin, Peter H Krammer, and Marcus E Peter. Two CD95 (APO-1/Fas) signaling pathways, 1998.

[32] Mrudula Donepudi, Aengus Mac Sweeney, Christophe Briand, and Markus G. Grütter. Insights into the Regulatory Mechanism for Caspase-8 Activation. *Molecular Cell*, 11: 543–549, 2 2003. ISSN 1097-2765. doi: 10.1016/s1097-2765(03)00059-5.

[33] Michelle A. Hughes, Ian R. Powley, Rebekah Jukes-Jones, Sebastian Horn, Maria Feoktistova, Louise Fairall, John W.R. Schwabe, Martin Leverkus, Kelvin Cain, and Marion MacFarlane. Co-operative and Hierarchical Binding of c-FLIP and Caspase-8: A Unified Model Defines How c-FLIP Isoforms Differentially Control Cell Fate. *Molecular Cell*, 61:834, 3 2016. ISSN 10974164. doi: 10.1016/j.molcel.2016.02.023.

[34] Andrew Oberst, Cristina Pop, Alexandre G. Tremblay, Véronique Blais, Jean Bernard Denault, Guy S. Salvesen, and Douglas R. Green. Inducible Dimerization and Inducible Cleavage Reveal a Requirement for Both Processes in Caspase-8 Activation. *Journal of Biological Chemistry*, 285:16632–16642, 5 2010. ISSN 0021-9258. doi: 10.1074/jbc.m109.095083.

[35] Marta Muzio, Brent R. Stockwell, Henning R. Stennicke, Guy S. Salvesen, and Vishva M. Dixit. An Induced Proximity Model for Caspase-8 Activation. *Journal of Biological Chemistry*, 273:2926–2930, 1 1998. ISSN 0021-9258. doi: 10.1074/jbc.273.5.2926.

[36] Mahitosh Mandal, Sanjay B. Maggirwar, Neeta Sharma, Scott H. Kaufmann, Shao Cong Sun, and Rakesh Kumar. Bcl-2 Prevents CD95 (Fas/APO-1)-induced Degradation of Lamin B and Poly(ADP-ribose) Polymerase and Restores the NF-κB Signaling Pathway. *Journal of Biological Chemistry*, 271:30354–30359, 11 1996. ISSN 0021-9258. doi: 10.1074/jbc.271.48.30354.

[37] Noriko Yasuhara, Setsuko Sahara, Shinji Kamada, Yutaka Eguchi, and Yoshihide Tsujimoto. Evidence against a functional site for Bcl-2 downstream of caspase cascade in preventing apoptosis. *Oncogene*, 15:1921–1928, 1997. ISSN 1476-5594. doi: 10.1038/sj.onc.1201370.

[38] Carsten Scaffidi, Ingo Schmitz, Peter H. Krammer, and Marcus E. Peter. The Role of c-FLIP in Modulation of CD95-induced Apoptosis. *Journal of Biological Chemistry*, 274:1541–1548, 1 1999. ISSN 0021-9258. doi: 10.1074/jbc.274.3.1541.

[39] Martin Irmler, Margot Thome, Michael Hahne, Pascal Schneider, Kay Hofmann, Véronique Steiner, Jean Luc Bodmer, Michael Schröter, Kim Burns, Chantal Mattmann, Donata Rimoldi, Lars E. French, and Jürg Tschopp. Inhibition of death receptor signals by cellular FLIP. *Nature*, 388:190–195, 1997. ISSN 1476-4687. doi: 10.1038/40657.

[40] Wen Chen Yeh, Annick Itie, Andrew J. Elia, Michelle Ng, Hong Bing Shu, Andrew Wakeham, Christine Mirtsos, Nobutaka Suzuki, Madeleine Bonnard, David V. Goeddel, and Tak W. Mak. Requirement for Casper (c-FLIP) in Regulation of Death Receptor–Induced Apoptosis and Embryonic Development. *Immunity*, 12:633–642, 6 2000. ISSN 1074-7613. doi: 10.1016/s1074-7613(00)80214-9.

[41] Frederik H. Igney and Peter H. Krammer. Death and anti-death: tumour resistance to apoptosis. *Nature Reviews Cancer*, 2:277–288, 2002. ISSN 1474-1768. doi: 10.1038/nrc776.

[42] Daniela Siegmund, Isabell Lang, and Harald Wajant. Cell death-independent activities of the death receptors CD95, TRAILR1, and TRAILR2. *The FEBS Journal*, 284: 1131–1159, 4 2017. ISSN 1742-4658. doi: 10.1111/febs.13968.

[43] Hisaaki Shinohara, Hideo Yagita, Yoji Ikawa, and Naoki Oyaizu. Fas Drives Cell Cycle Progression in Glioma Cells via Extracellular Signal-regulated Kinase Activation. *Cancer Research*, 60(6):1766–1772, 03 2000. ISSN 0008-5472.

[44] George Jarad, Bingcheng Wang, Shenaz Khan, Jay DeVore, Hui Miao, Karen Wu, Stephen L. Nishimura, Barbara A. Wible, Martha Konieczkowski, John R. Sedor, and Jeffrey R. Schelling. Fas Activation Induces Renal Tubular Epithelial Cell β_8 Integrin Expression and Function in the Absence of Apoptosis. *Journal of Biological Chemistry*, 277:47826–47833, 12 2002. ISSN 0021-9258. doi: 10.1074/jbc.m204901200.

[45] Sebastian Kreuz, Daniela Siegmund, Jost Julian Rumpf, Dierk Samel, Martin Leverkus, Ottmar Janssen, Georg Häcker, Oliver Dittrich-Breiholz, Michael Kracht, Peter Scheurich, and Harald Wajant. NFκB activation by Fas is mediated through FADD, caspase-8, and RIP and is inhibited by FLIP. *The Journal of Cell Biology*, 166:369, 8 2004. ISSN 00219525. doi: 10.1083/jcb.200401036.

[46] M. Grunert, K. Gottschalk, J. Kapahnke, S. Gündisch, A. Kieser, and I. Jeremias. The adaptor protein FADD and the initiator caspase-8 mediate activation of NF-κB by TRAIL. *Cell Death & Disease*, 3:e414–e414, 10 2012. ISSN 2041-4889. doi: 10.1038/cddis.2012.154.

[47] Eugene Varfolomeev, Heather Maecker, Darcie Sharp, David Lawrence, Mark Renz, Domagoj Vucic, and Avi Ashkenazi. Molecular Determinants of Kinase Pathway Activation by Apo2 Ligand/Tumor Necrosis Factor-related Apoptosis-inducing Ligand. *Journal of Biological Chemistry*, 280:40599–40608, 12 2005. ISSN 0021-9258. doi: 10.1074/jbc.m509560200.

[48] John M. Kyriakis and Joseph Avruch. Mammalian MAPK signal transduction pathways activated by stress and inflammation: A 10-year update. *Physiological Reviews*, 92:689–737, 4 2012. ISSN 00319333. doi: 10.1152/physrev.00028.2011.

[49] Ignacio Sancho-Martinez and Ana Martin-Villalba. Tyrosine phosphorylation and

CD95: a FAScinating switch. *Cell cycle*, 8:838–842, 3 2009. ISSN 1551-4005. doi: 10.4161/cc.8.6.7906.

[50] Richard M. Locksley, Nigel Killeen, and Michael J. Lenardo. The TNF and TNF Receptor Superfamilies: Integrating Mammalian Biology. *Cell*, 104:487–501, 2 2001. ISSN 0092-8674. doi: 10.1016/s0092-8674(01)00237-9.

[51] Fiona L. Scott, Boguslaw Stec, Cristina Pop, Małgorzata K. Dobaczewska, Jeongeun J. Lee, Edward Monosov, Howard Robinson, Guy S. Salvesen, Robert Schwarzenbacher, and Stefan J. Riedl. The Fas-FADD death domain complex structure unravels signalling by receptor clustering. *Nature*, 457:1019–1022, 2009. ISSN 00280836. doi: 10.1038/nature07606.

[52] Éva S. Vanamee, Gábor Lippner, and Denise L. Faustman. Signal Amplification in Highly Ordered Networks Is Driven by Geometry. *Cells*, 11:272, 1 2022. ISSN 2073-4409. doi: 10.3390/cells11020272.

[53] Pierre Golstein. FasL binds preassembled Fas. *Science*, 288:2328–2329, 6 2000. ISSN 00368075. doi: 10.1126/science.288.5475.2328.

[54] Francis Ka Ming Chan. Three is Better Than One: Pre-Ligand Receptor Assembly in the Regulation of TNF Receptor Signaling. *Cytokine*, 37:101, 2 2007. ISSN 10434666. doi: 10.1016/j.cyto.2007.03.005.

[55] J. H. Naismith, T. Q. Devine, B. J. Brandhuber, and S. R. Sprang. Crystallographic Evidence for Dimerization of Unliganded Tumor Necrosis Factor Receptor. *Journal of Biological Chemistry*, 270:13303–13307, 6 1995. ISSN 0021-9258. doi: 10.1074/jbc.270.22.13303.

[56] Lynn E. Rodseth, Barbara Brandhuber, Tracey Q. Devine, Michael J. Eck, Karin Hale, James H. Naismith, and Stephen R. Sprang. Two Crystal Forms of the Extracellular Domain of Type I Tumor Necrosis Factor Receptor. *Journal of Molecular Biology*, 239: 332–335, 6 1994. ISSN 0022-2836. doi: 10.1006/jmbi.1994.1371.

[57] James H Naismith, Barbara J Brandhuber, Tracey Q Devine, and Stephen R Sprangs. Seeing Double: Crystal Structures of the Type I TNF Receptor. *Journal of Molecular Recognition*, 9:113–114, 1996. doi: 10.1002/(sici)1099-1352(199603)9:2.

[58] David W. Banner, Allan D'Arcy, Wolfgang Janes, Reiner Gentz, Hans Joachim Schoenfeld, Clemens Broger, Hansruedi Loetscher, and Werner Lesslauer. Crystal structure of the soluble human 55 kd TNF receptor-human TNFβ complex: Implications for TNF receptor activation. *Cell*, 73:431–445, 5 1993. ISSN 0092-8674. doi: 10.1016/0092-8674(93)90132-a.

[59] Juthathip Mongkolsapaya, Jonathan M. Grimes, Nan Chen, Xiao Ning Xu, David I. Stuart, E. Yvonne Jones, and Gavin R. Screaton. Structure of the TRAIL-DR5 complex reveals mechanisms conferring specificity in apoptotic initiation. *Nature Structural*

Biology, 6:1048–1053, 1999. ISSN 1072-8368. doi: 10.1038/14935.

[60] Sarah G. Hymowitz, Hans W. Christinger, Germaine Fuh, Mark Ultsch, Mark O'Connell, Robert F. Kelley, Avi Ashkenazi, and Abraham M. De Vos. Triggering Cell Death: The Crystal Structure of Apo2L/TRAIL in a Complex with Death Receptor 5. *Molecular Cell*, 4:563–571, 10 1999. ISSN 1097-2765. doi: 10.1016/s1097-2765(00)80207-5.

[61] Yohei Mukai, Teruya Nakamura, Mai Yoshikawa, Yasuo Yoshioka, Shin Ichi Tsunoda, Shinsaku Nakagawa, Yuriko Yamagata, and Yasuo Tsutsumi. Solution of the structure of the TNF-TNFR2 complex. *Science Signaling*, 3, 11 2010. ISSN 19450877. doi: 10.1126/scisignal.2000954.

[62] Hyun Jung An, Young Jin Kim, Dong Hyun Song, Beom Suk Park, Ho Min Kim, Ju Dong Lee, Sang Gi Paik, Jie Oh Lee, and Hayyoung Lee. Crystallographic and Mutational Analysis of the CD40-CD154 Complex and Its Implications for Receptor Activation. *Journal of Biological Chemistry*, 286:11226–11235, 4 2011. ISSN 0021-9258. doi: 10.1074/jbc.m110.208215.

[63] Sun Shin Cha, Byung Je Sung, Young A. Kim, Young Lan Song, Hyun Ju Kim, Sunshin Kim, Myung Shik Lee, and Byung Ha Oh. Crystal Structure of TRAIL-DR5 Complex Identifies a Critical Role of the Unique Frame Insertion in Conferring Recognition Specificity. *Journal of Biological Chemistry*, 275:31171–31177, 10 2000. ISSN 0021-9258. doi: 10.1074/jbc.m004414200.

[64] Qingshan Fu, Tian Min Fu, Anthony C. Cruz, Prabuddha Sengupta, Stacy K. Thomas, Shuqing Wang, Richard M. Siegel, Hao Wu, and James J. Chou. Structural Basis and Functional Role of Intramembrane Trimerization of the Fas/CD95 Death Receptor. *Molecular Cell*, 61:602–613, 2 2016. ISSN 10974164. doi: 10.1016/j.molcel.2016.01.009.

[65] Liqiang Pan, Tian Min Fu, Wenbin Zhao, Linlin Zhao, Wen Chen, Chixiao Qiu, Wenhui Liu, Zhijun Liu, Alessandro Piai, Qingshan Fu, Shuqing Chen, Hao Wu, and James J. Chou. Higher-Order Clustering of the Transmembrane Anchor of DR5 Drives Signaling. *Cell*, 176:1477–1489.e14, 3 2019. ISSN 0092-8674. doi: 10.1016/j.cell.2019.02.001.

[66] Arul M. Chinnaiyan, Karen O'Rourke, Muneesh Tewari, and Vishva M. Dixit. FADD, a novel death domain-containing protein, interacts with the death domain of fas and initiates apoptosis. *Cell*, 81:505–512, 5 1995. ISSN 0092-8674. doi: 10.1016/0092-8674(95)90071-3.

[67] B. J. Ferguson, D. Esposito, J. Jovanovic, A. Sankar, P. C. Driscoll, and H. Mehmet. Biophysical and cell-based evidence for differential interactions between the death domains of CD95/Fas and FADD. *Cell death and differentiation*, 14:1717–1719, 9 2007. ISSN 1350-9047. doi: 10.1038/sj.cdd.4402191.

[68] Liwei Wang, Jin Kuk Yang, Venkataraman Kabaleeswaran, Amanda J. Rice, An-

thony C. Cruz, Ah Young Park, Qian Yin, Ermelinda Damko, Se Bok Jang, Stefan Raunser, Carol V. Robinson, Richard M. Siegel, Thomas Walz, and Hao Wu. The Fas–FADD death domain complex structure reveals the basis of DISC assembly and disease mutations. *Nature Structural & Molecular Biology*, 17:1324–1329, 10 2010. ISSN 1545-9985. doi: 10.1038/nsmb.1920.

[69] Diego Esposito, Andrew Sankar, Nina Morgner, Carol V. Robinson, Katrin Rittinger, and Paul C. Driscoll. Solution NMR Investigation of the CD95/FADD Homotypic Death Domain Complex Suggests Lack of Engagement of the CD95 C Terminus. *Structure*, 18:1378–1390, 10 2010. ISSN 0969-2126. doi: 10.1016/j.str.2010.08.006.

[70] Mark P. Boldin, Igor L. Mett, Eugene E. Varfolomeev, Irina Chumakov, Yonat Shemer-Avni, Jacques H. Camonis, and David Wallach. Self-association of the "Death Domains" of the p55 Tumor Necrosis Factor (TNF) Receptor and Fas/APO1 Prompts Signaling for TNF and Fas/APO1 Effects. *Journal of Biological Chemistry*, 270:387–391, 1 1995. ISSN 0021-9258. doi: 10.1074/jbc.270.1.387.

[71] Carlos R. Reis, Aart H.G. Van Assen, Wim J. Quax, and Robbert H. Cool. Unraveling the Binding Mechanism of Trivalent Tumor Necrosis Factor Ligands and Their Receptors. *Molecular & Cellular Proteomics*, 10, 1 2011. ISSN 15359476. doi: 10.1074/mcp.m110.002808.

[72] Jagan R. Muppidi and Richard M. Siegel. Ligand-independent redistribution of Fas (CD95) into lipid rafts mediates clonotypic T cell death. *Nature Immunology*, 5:182–189, 1 2004. ISSN 1529-2916. doi: 10.1038/ni1024.

[73] Isabell Lang, Andrea Fick, Viktoria Schäfer, Tina Giner, Daniela Siegmund, and Harald Wajant. Signaling Active CD95 Receptor Molecules Trigger Co-translocation of Inactive CD95 Molecules into Lipid Rafts. *Journal of Biological Chemistry*, 287:24026–24042, 7 2012. ISSN 0021-9258. doi: 10.1074/jbc.m111.328211.

[74] Adriana Eramo, Massimo Sargiacomo, Lucia Ricci-Vitiani, Matilde Todaro, Giorgio Stassi, Carlo G.M. Messina, Isabella Parolini, Fiorenza Lotti, Giovanni Sette, Cesare Peschle, and Ruggero De Maria. CD95 death-inducing signaling complex formation and internalization occur in lipid rafts of type I and type II cells. *European Journal of Immunology*, 34:1930–1940, 7 2004. ISSN 1521-4141. doi: 10.1002/eji.200324786.

[75] Consuelo Gajate and Faustino Mollinedo. Lipid raft-mediated Fas/CD95 apoptotic signaling in leukemic cells and normal leukocytes and therapeutic implications. *Journal of Leukocyte Biology*, 98:739–759, 11 2015. ISSN 1938-3673. doi: 10.1189/jlb.2mr0215-055r.

[76] Faustino Mollinedo and Consuelo Gajate. *Fas/CD95, Lipid Rafts, and Cancer*, pages 187–227. Springer International Publishing, Cham, 2017. ISBN 978-3-319-56805-8. doi: 10.1007/978-3-319-56805-8_9.

[77] A. Jablonski. Über den Mechanismus der Photolumineszenz von Farbstoffphosphoren. *Zeitschrift für Physik*, 94:38–46, 1 1935. ISSN 14346001. doi: 10.1007/bf01330795.

[78] Tal M. Dankovich and Silvio O. Rizzoli. Challenges facing quantitative large-scale optical super-resolution, and some simple solutions. *iScience*, 24:102134, 3 2021. ISSN 2589-0042. doi: 10.1016/j.isci.2021.102134.

[79] Stefan W. Hell and Jan Wichmann. Breaking the diffraction resolution limit by stimulated emission: stimulated-emission-depletion fluorescence microscopy. *Optics letters*, 19:780, 6 1994. ISSN 0146-9592. doi: 10.1364/ol.19.000780.

[80] Waja Wegner, Peter Ilgen, Carola Gregor, Joris Van Dort, Alexander C. Mott, Heinz Steffens, and Katrin I. Willig. In vivo mouse and live cell STED microscopy of neuronal actin plasticity using far-red emitting fluorescent proteins. *Scientific Reports*, 7:1–10, 2017. ISSN 20452322. doi: 10.1038/s41598-017-11827-4.

[81] Steffen J. Sahl, Stefan W. Hell, and Stefan Jakobs. Fluorescence nanoscopy in cell biology. *Nature Reviews Molecular Cell Biology*, 18:685–701, 9 2017. ISSN 1471-0080. doi: 10.1038/nrm.2017.71.

[82] Till Stephan, Axel Roesch, Dietmar Riedel, and Stefan Jakobs. Live-cell STED nanoscopy of mitochondrial cristae. *Scientific Reports*, 9:1–6, 12 2019. ISSN 20452322. doi: 10.1038/s41598-019-48838-2.

[83] Alexander Stockhammer and Francesca Bottanelli. Appreciating the small things in life: STED microscopy in living cells. *Journal of Physics D: Applied Physics*, 54:033001, 10 2020. ISSN 0022-3727. doi: 10.1088/1361-6463/abac81.

[84] Haisen Ta, Jan Keller, Markus Haltmeier, Sinem K. Saka, Jürgen Schmied, Felipe Opazo, Philip Tinnefeld, Axel Munk, and Stefan W. Hell. Mapping molecules in scanning far-field fluorescence nanoscopy. *Nature Communications*, 6:1–7, 8 2015. ISSN 2041-1723. doi: 10.1038/ncomms8977.

[85] Jan Keller-Findeisen, Steffen J. Sahl, and Stefan W. Hell. *Quantifying Molecule Numbers in STED/RESOLFT Fluorescence Nanoscopy*, pages 205–226. Springer International Publishing, Cham, 2020. ISBN 978-3-030-34413-9. doi: 10.1007/978-3-030-34413-9_7.

[86] Nike Walther and Jan Ellenberg. Quantitative live and super-resolution microscopy of mitotic chromosomes. *Methods in Cell Biology*, 145:65–90, 1 2018. ISSN 0091-679X. doi: 10.1016/bs.mcb.2018.03.014.

[87] Maximilian H. Ulbrich and Ehud Y. Isacoff. Subunit counting in membrane-bound proteins. *Nature Methods*, 4:319–321, 3 2007. ISSN 1548-7105. doi: 10.1038/nmeth1024.

[88] Ryan J. Arant and Maximilian H. Ulbrich. Deciphering the Subunit Composition of Multimeric Proteins by Counting Photobleaching Steps. *ChemPhysChem*, 15:600–605, 3 2014. ISSN 1439-7641. doi: 10.1002/cphc.201301092.

[89] Johan Hummert, Klaus Yserentant, Theresa Fink, Jonas Euchner, Yin Xin Ho, Stanimir Asenov Tashev, and Dirk Peter Herten. Photobleaching step analysis for robust determination of protein complex stoichiometries. *Molecular Biology of the Cell*, 32, 11 2021. ISSN 19394586. doi: 10.1091/mbc.e20-09-0568.

[90] Samuel Clarke, Fabien Pinaud, Oliver Beutel, Changjiang You, Jacob Piehler, and Maxime Dahan. Covalent monofunctionalization of peptide-coated quantum dots for single-molecule assays. *Nano Letters*, 10:2147–2154, 6 2010. ISSN 15306984. doi: 10.1021/nl100825n.

[91] Theodor Förster. Energiewanderung und Fluoreszenz. *Naturwissenschaften*, 33:166–175, 6 1946. ISSN 1432-1904. doi: 10.1007/bf00585226.

[92] Theodor Förster. Zwischenmolekulare Energiewanderung und Fluoreszenz. *Annalen der Physik*, 437:55–75, 1 1948. ISSN 1521-3889. doi: 10.1002/andp.19484370105.

[93] Brian A. Pollok and Roger Heim. Using GFP in FRET-based applications. *Trends in Cell Biology*, 9:57–60, 2 1999. ISSN 0962-8924. doi: 10.1016/s0962-8924(98)01434-2.

[94] Robert M. Clegg. *The History of Fret*, pages 1–45. Springer US, Boston, MA, 2006. ISBN 978-0-387-33016-7. doi: 10.1007/0-387-33016-x_1.

[95] Annemarie Greife, Suren Felekyan, Qijun Ma, Christoph G.W. Gertzen, Lina Spomer, Mykola Dimura, Thomas O. Peulen, Christina Wöhler, Dieter Häussinger, Holger Gohlke, Verena Keitel, and Claus A.M. Seidel. Structural assemblies of the di- and oligomeric G-protein coupled receptor TGR5 in live cells: An MFIS-FRET and integrative modelling study. *Scientific Reports*, 6:1–16, 2016. ISSN 20452322. doi: 10.1038/srep36792.

[96] Stefanie Weidtkamp-Peters, Suren Felekyan, Andrea Bleckmann, Rüdiger Simon, Wolfgang Becker, Ralf Kühnemuth, and Claus A.M. Seidel. Multiparameter fluorescence image spectroscopy to study molecular interactions. *Photochemical & Photobiological Sciences*, 8:470–480, 3 2009. ISSN 1474-9092. doi: 10.1039/b903245m.

[97] Elisabeth Kravets, Daniel Degrandi, Qijun Ma, Thomas Otavio Peulen, Verena Klümpers, Suren Felekyan, Ralf Kühnemuth, Stefanie Weidtkamp-Peters, Claus Am Seidel, and Klaus Pfeffer. Guanylate binding proteins directly attack toxoplasma gondii via supramolecular complexes. *eLife*, 5, 1 2016. ISSN 2050084X. doi: 10.7554/elife.11479.001.

[98] Lirong Chen, Lawrence Novicky, Mikhail Merzlyakov, Tihomir Hristov, and Kalina Hristova. Measuring the energetics of membrane protein dimerization in mammalian membranes. *Journal of the American Chemical Society*, 132:3628–3635, 3 2010. ISSN 00027863. doi: 10.1021/ja910692u.

[99] Sarvenaz Sarabipour, Nuala Del Piccolo, and Kalina Hristova. Characterization of Membrane Protein Interactions in Plasma Membrane Derived Vesicles with Quantita-

tive Imaging Förster Resonance Energy Transfer. *Accounts of Chemical Research*, 48: 2262–2269, 8 2015. ISSN 15204898. doi: 10.1021/acs.accounts.5b00238.

[100] Christopher King, Michael Stoneman, Valerica Raicu, and Kalina Hristova. Fully quantified spectral imaging reveals in vivo membrane protein interactions. *Integrative Biology*, 8:216–229, 2 2016. ISSN 17579708. doi: 10.1039/c5ib00202h.

[101] Jan-Hendrik Budde, Nicolaas van der Voort, Suren Felekyan, Julian Folz, Ralf Kühnemuth, Paul Lauterjung, Markus Köhler, Andreas Schönle, Julian Sindram, Marius Otten, Matthias Karg, Christian Herrmann, Anders Barth, and Claus A. M. Seidel. FRET nanoscopy enables seamless imaging of molecular assemblies with sub-nanometer resolution. *arXiv preprint arXiv:2108.00024*, 2021. doi: 10.48550/arxiv.2108.00024.

[102] Alan M. Szalai, Bruno Siarry, Jerónimo Lukin, Sebastián Giusti, Nicolás Unsain, Alfredo Cáceres, Florian Steiner, Philip Tinnefeld, Damián Refojo, Thomas M. Jovin, and Fernando D. Stefani. Super-resolution Imaging of Energy Transfer by Intensity-Based STED-FRET. *Nano Letters*, 21:2296–2303, 3 2021. ISSN 15306992. doi: 10.1021/acs.nanolett.1c00158.

[103] Nina S. Deußner-Helfmann, Alexander Auer, Maximilian T. Strauss, Sebastian Malkusch, Marina S. Dietz, Hans Dieter Barth, Ralf Jungmann, and Mike Heilemann. Correlative Single-Molecule FRET and DNA-PAINT Imaging. *Nano Letters*, 18:4626–4630, 7 2018. ISSN 15306992. doi: 10.1021/acs.nanolett.8b02185.

[104] Martin Weigert, Uwe Schmidt, Tobias Boothe, Andreas Müller, Alexandr Dibrov, Akanksha Jain, Benjamin Wilhelm, Deborah Schmidt, Coleman Broaddus, Siân Culley, Mauricio Rocha-Martins, Fabián Segovia-Miranda, Caren Norden, Ricardo Henriques, Marino Zerial, Michele Solimena, Jochen Rink, Pavel Tomancak, Loic Royer, Florian Jug, and Eugene W. Myers. Content-aware image restoration: pushing the limits of fluorescence microscopy. *Nature Methods*, 15:1090–1097, 11 2018. ISSN 1548-7105. doi: 10.1038/s41592-018-0216-7.

[105] Jagadish Sankaran and Thorsten Wohland. Fluorescence strategies for mapping cell membrane dynamics and structures. *APL Bioengineering*, 4:020901, 5 2020. ISSN 24732877. doi: 10.1063/1.5143945.

[106] Jagadish Sankaran, Harikrushnan Balasubramanian, Wai Hoh Tang, Xue Wen Ng, Adrian Röllin, and Thorsten Wohland. Simultaneous spatiotemporal super-resolution and multi-parametric fluorescence microscopy. *Nature Communications*, 12:1–14, 3 2021. ISSN 2041-1723. doi: 10.1038/s41467-021-22002-9.

[107] C. Liesche, L. Venkatraman, S. Aschenbrenner, S. Grosse, D. Grimm, R. Eils, and J. Beaudouin. Death receptor-based enrichment of Cas9-expressing cells. *BMC Biotechnology*, 16:1–13, 2 2016. ISSN 14726750. doi: 10.1186/s12896-016-0250-4.

[108] C. Liesche, J. Berndt, F. Fricke, S. Aschenbrenner, M. Heilemann, R. Eils, and J. Beau-

douin. CD95 receptor activation by ligand-induced trimerization is independent of its partial pre-ligand assembly. *bioRxiv*, 2018. doi: 10.1101/293530.

[109] Nicolai Fricker, Joel Beaudouin, Petra Richter, Roland Eils, Peter H. Krammer, and Inna N. Lavrik. Model-based dissection of CD95 signaling dynamics reveals both a pro- and antiapoptotic role of c-FLIPL. *Journal of Cell Biology*, 190:377–389, 8 2010. ISSN 00219525. doi: 10.1083/jcb.201002060.

[110] Omar S. Qureshi, Satdip Kaur, Tie Zheng Hou, Louisa E. Jeffery, Natalie S. Poulter, Zoe Briggs, Rupert Kenefeck, Anna K. Willox, Stephen J. Royle, Joshua Z. Rappoport, and David M. Sansom. Constitutive Clathrin-mediated Endocytosis of CTLA-4 Persists during T Cell Activation. *The Journal of Biological Chemistry*, 287:9429, 3 2012. ISSN 00219258. doi: 10.1074/jbc.m111.304329.

[111] Franziska Fricke, Joel Beaudouin, Roland Eils, and Mike Heilemann. One, two or three? Probing the stoichiometry of membrane proteins by single-molecule localization microscopy. *Scientific Reports*, 5, 2015. ISSN 20452322. doi: 10.1038/srep14072.

[112] Brendan P. Cormack, Raphael H. Valdivia, and Stanley Falkow. FACS-optimized mutants of the green fluorescent protein (GFP). *Gene*, 173:33–38, 1 1996. ISSN 0378-1119. doi: 10.1016/0378-1119(95)00685-0.

[113] David A. Zacharias, Jonathan D. Violin, Alexandra C. Newton, and Roger Y. Tsien. Partitioning of lipid-modified monomeric GFPs into membrane microdomains of live cells. *Science*, 296:913–916, 5 2002. ISSN 00368075. doi: 10.1126/science.1068539.

[114] Nathan C. Shaner, Robert E. Campbell, Paul A. Steinbach, Ben N.G. Giepmans, Amy E. Palmer, and Roger Y. Tsien. Improved monomeric red, orange and yellow fluorescent proteins derived from Discosoma sp. red fluorescent protein. *Nature Biotechnology*, 22:1567–1572, 11 2004. ISSN 1546-1696. doi: 10.1038/nbt1037.

[115] Mathias Uhlén, Linn Fagerberg, Bjö M. Hallström, Cecilia Lindskog, Per Oksvold, Adil Mardinoglu, Åsa Sivertsson, Caroline Kampf, Evelina Sjöstedt, Anna Asplund, Ing Marie Olsson, Karolina Edlund, Emma Lundberg, Sanjay Navani, Cristina Al Khalili Szigyarto, Jacob Odeberg, Dijana Djureinovic, Jenny Ottosson Takanen, Sophia Hober, Tove Alm, Per Henrik Edqvist, Holger Berling, Hanna Tegel, Jan Mulder, Johan Rockberg, Peter Nilsson, Jochen M. Schwenk, Marica Hamsten, Kalle Von Feilitzen, Mattias Forsberg, Lukas Persson, Fredric Johansson, Martin Zwahlen, Gunnar Von Heijne, Jens Nielsen, and Fredrik Pontén. Tissue-based map of the human proteome. *Science*, 347, 1 2015. ISSN 10959203. doi: 10.1126/science.1260419.

[116] ChromoteK. Better images with Nanobodies - Nano-Secondaries, Nano-Boosters, Nano-Labels, Chromobodies, and Nanobody-Fc fusions for immunofluorescence. Brochure, 2022. URL https://www.ptglab.com/products/pictures/pdf/chromotek-nanobodies-brochure.PDF.

[117] F. Zernike. Phase contrast, a new method for the microscopic observation of transparent objects. *Physica*, 9:686–698, 7 1942. ISSN 0031-8914. doi: 10.1016/s0031-8914(42)80035-x.

[118] H. Siedentopf and R. Zsigmondy. Über Sichtbarmachung und Größenbestimmung ultramikoskopischer Teilchen, mit besonderer Anwendung auf Goldrubingläser. *Ann Phys*, 315(1):1–39, 1902.

[119] Oskar Heimstaedt. Das Fluoreszenzmikroskop. *Z Wiss Mikrosk*, 28:330–337, 1911.

[120] Karl Reichert. Das Fluoreszenzmikroskop. *Phys Z*, 12:1010, 1911.

[121] Johannes Schindelin, Ignacio Arganda-Carreras, Erwin Frise, Verena Kaynig, Mark Longair, Tobias Pietzsch, Stephan Preibisch, Curtis Rueden, Stephan Saalfeld, Benjamin Schmid, Jean Yves Tinevez, Daniel James White, Volker Hartenstein, Kevin Eliceiri, Pavel Tomancak, and Albert Cardona. Fiji: an open-source platform for biological-image analysis. *Nature Methods*, 9:676–682, 6 2012. ISSN 1548-7105. doi: 10.1038/nmeth.2019.

[122] Marvin Minsky. Microscopy apparatus, 1961. US patent 3,013,467.

[123] Desmond V. O'Connor and David Phillips. Basic Principles of the Single Photon Counting Lifetime Measurement. *Time-Correlated Single Photon Counting*, pages 36–54, 1 1984. doi: 10.1016/b978-0-12-524140-3.50006-x.

[124] Dietrich Stoyan and Helga Stoyan. Estimating pair correlation functions of planar cluster processes. *Biometrical Journal*, 38:259–271, 1996. ISSN 03233847. doi: 10.1002/bimj.4710380302.

[125] D Stoyan, U Bertram, and H Wendrock. Estimation variances for estimators of product densities and pair correlation functions of planar point processes. *Ann. Inst. Statist. Math*, 45:211–221, 1993. doi: 10.1007/bf00775808.

[126] Thomas Fiksel. Edge-corrected density estimators for point processes. *Statistics*, 19: 67–75, 1988. ISSN 1029-4910. doi: 10.1080/02331888808802072.

[127] Diana B. Peckys, Ulrike Korf, and Niels De Jonge. Local variations of HER2 dimerization in breast cancer cells discovered by correlative fluorescence and liquid electron microscopy. *Science Advances*, 1, 2015. ISSN 23752548. doi: 10.1126/sciadv.1500165.

[128] Douglas Magde, Elliot Elson, and W. W. Webb. Thermodynamic Fluctuations in a Reacting System—Measurement by Fluorescence Correlation Spectroscopy. *Physical Review Letters*, 29:705, 9 1972. ISSN 00319007. doi: 10.1103/physrevlett.29.705.

[129] S. Felekyan, R. Kühnemuth, V. Kudryavtsev, C. Sandhagen, W. Becker, and C. A.M. Seidel. Full correlation from picoseconds to seconds by time-resolved and time-correlated single photon detection. *Review of Scientific Instruments*, 76:083104, 7 2005. ISSN 0034-6748. doi: 10.1063/1.1946088.

[130] P. O. Gendron, F. Avaltroni, and K. J. Wilkinson. Diffusion coefficients of several rhodamine derivatives as determined by pulsed field gradient-nuclear magnetic resonance and fluorescence correlation spectroscopy. *Journal of Fluorescence*, 18:1093–1101, 11 2008. ISSN 10530509. doi: 10.1007/s10895-008-0357-7.

[131] Thorsten Wohland, Rudolf Rigler, and Horst Vogel. The Standard Deviation in Fluorescence Correlation Spectroscopy. *Biophysical Journal*, 80:2987–2999, 6 2001. ISSN 0006-3495. doi: 10.1016/s0006-3495(01)76264-9.

[132] Bennett Kalafut and Koen Visscher. An objective, model-independent method for detection of non-uniform steps in noisy signals. *Computer Physics Communications*, 179:716–723, 11 2008. ISSN 0010-4655. doi: 10.1016/j.cpc.2008.06.008.

[133] Jan Willem Borst, S. P. Laptenok, A. H. Westphal, R. Kühnemuth, H. Hornen, N. V. Visser, S. Kalinin, J. Aker, A. Van Hoek, C. A.M. Seidel, and A. J.W.G. Visser. Structural Changes of Yellow Cameleon Domains Observed by Quantitative FRET Analysis and Polarized Fluorescence Correlation Spectroscopy. *Biophysical Journal*, 95:5399–5411, 12 2008. ISSN 0006-3495. doi: 10.1529/biophysj.107.114587.

[134] Caroline A. Schneider, Wayne S. Rasband, and Kevin W. Eliceiri. NIH Image to ImageJ: 25 years of image analysis. *Nature Methods*, 9:671–675, 6 2012. ISSN 1548-7105. doi: 10.1038/nmeth.2089.

[135] D.R. Lide R. C. Weast. *CRC Handbook of Chemistry and Physics*, volume 65. CRC press, 1985. ISBN 9780849304651.

[136] Peter Kapusta. Absolute diffusion coefficients: compilation of reference data for FCS calibration, 2010. URL `https://www.picoquant.com/images/uploads/page/files/7353/appnote_diffusioncoefficients.pdf`.

[137] G. Majer and J. P. Melchior. Characterization of the fluorescence correlation spectroscopy (FCS) standard Rhodamine 6G and calibration of its diffusion coefficient in aqueous solutions. *The Journal of Chemical Physics*, 140:094201, 3 2014. ISSN 0021-9606. doi: 10.1063/1.4867096.

[138] George H. Patterson, Susan M. Knobel, Wallace D. Sharif, Steven R. Kain, and David W. Piston. Use of the green fluorescent protein and its mutants in quantitative fluorescence microscopy. *Biophysical Journal*, 73:2782–2790, 11 1997. ISSN 0006-3495. doi: 10.1016/s0006-3495(97)78307-3.

[139] Mykola Dimura, Thomas Otavio Peulen, Hugo Sanabria, Dmitro Rodnin, Katherina Hemmen, Christian A. Hanke, Claus A.M. Seidel, and Holger Gohlke. Automated and optimally FRET-assisted structural modeling. *Nature Communications*, 11:1–14, 10 2020. ISSN 2041-1723. doi: 10.1038/s41467-020-19023-1.

[140] Qingshan Fu and James J. Chou. Transmembrane domain of human Fas/CD95 death receptor. 2016. doi: 10.2210/pdb2na7/pdb.

[141] Christopher King, Sarvenaz Sarabipour, Patrick Byrne, Daniel J. Leahy, and Kalina Hristova. The FRET Signatures of Noninteracting Proteins in Membranes: Simulations and Experiments. *Biophysical Journal*, 106:1309–1317, 3 2014. ISSN 0006-3495. doi: 10.1016/j.bpj.2014.01.039.

[142] Valentin Dunsing, Madlen Luckner, Boris Zühlke, Roberto A. Petazzi, Andreas Herrmann, and Salvatore Chiantia. Optimal fluorescent protein tags for quantifying protein oligomerization in living cells. *Scientific Reports*, 8:1–12, 7 2018. ISSN 2045-2322. doi: 10.1038/s41598-018-28858-0.

[143] Enrique Balleza, J. Mark Kim, and Philippe Cluzel. Systematic characterization of maturation time of fluorescent proteins in living cells. *Nature Methods*, 15:47–51, 11 2017. ISSN 1548-7105. doi: 10.1038/nmeth.4509.

[144] C. Monzel, D. Schmidt, C. Kleusch, D. Kirchenbüchler, U. Seifert, A. S. Smith, K. Sengupta, and R. Merkel. Measuring fast stochastic displacements of bio-membranes with dynamic optical displacement spectroscopy. *Nature Communications*, 6:1–8, 10 2015. ISSN 2041-1723. doi: 10.1038/ncomms9162.

[145] Eric O. Potma, Wim P. De Boeij, Leonard Bosgraaf, Jeroen Roelofs, Peter J.M. Van Haastert, and Douwe A. Wiersma. Reduced Protein Diffusion Rate by Cytoskeleton in Vegetative and Polarized Dictyostelium Cells. *Biophysical Journal*, 81:2010–2019, 10 2001. ISSN 0006-3495. doi: 10.1016/s0006-3495(01)75851-1.

[146] Jérôme Wenger, Fabien Conchonaud, José Dintinger, Laure Wawrezinieck, Thomas W. Ebbesen, Hervé Rigneault, Didier Marguet, and Pierre François Lenne. Diffusion Analysis within Single Nanometric Apertures Reveals the Ultrafine Cell Membrane Organization. *Biophysical Journal*, 92:913–919, 2 2007. ISSN 0006-3495. doi: 10.1529/biophysj.106.096586.

[147] Jared Hennen, Kwang Ho Hur, Cosmo A. Saunders, G. W.Gant Luxton, and Joachim D. Mueller. Quantitative Brightness Analysis of Protein Oligomerization in the Nuclear Envelope. *Biophysical Journal*, 113:138–147, 7 2017. ISSN 0006-3495. doi: 10.1016/j.bpj.2017.05.044.

[148] Hugo McGuire, Mark R.P. Aurousseau, Derek Bowie, and Rikard Bluncks. Automating Single Subunit Counting of Membrane Proteins in Mammalian Cells. *Journal of Biological Chemistry*, 287:35912–35921, 10 2012. ISSN 0021-9258. doi: 10.1074/jbc.m112.402057.

[149] Konstantinos Tsekouras, Thomas C. Custer, Hossein Jashnsaz, Nils G. Walter, and Steve Pressé. A novel method to accurately locate and count large numbers of steps by photobleaching. *Molecular Biology of the Cell*, 27:3601–3615, 11 2016. ISSN 19394586. doi: 10.1091/mbc.e16-06-0404.

[150] Jon Garry, Yuchong Li, Brandon Shew, Claudiu C. Gradinaru, and Andrew D. Ruten-

berg. Bayesian counting of photobleaching steps with physical priors. *The Journal of Chemical Physics*, 152:024110, 1 2020. ISSN 0021-9606. doi: 10.1063/1.5132957.

[151] Andrew H.A. Clayton and Amitabha Chattopadhyay. Taking care of bystander FRET in a crowded cell membrane environment. *Biophysical Journal*, 106:1227–1228, 2014. ISSN 15420086. doi: 10.1016/j.bpj.2014.02.004.

[152] Christos Karathanasis, Juliane Medler, Franziska Fricke, Sonja Smith, Sebastian Malkusch, Darius Widera, Simone Fulda, Harald Wajant, Sjoerd J.L. van Wijk, Ivan Dikic, and Mike Heilemann. Single-molecule imaging reveals the oligomeric state of functional TNFα-induced plasma membrane TNFR1 clusters in cells. *Science Signaling*, 13, 1 2020. ISSN 19379145. doi: 10.1126/scisignal.aax5647.

[153] Verena Boschert, Anja Krippner-Heidenreich, Marcus Branschädel, Jessica Tepperink, Andrew Aird, and Peter Scheurich. Single chain TNF derivatives with individually mutated receptor binding sites reveal differential stoichiometry of ligand receptor complex formation for TNFR1 and TNFR2. *Cellular Signalling*, 22:1088–1096, 7 2010. ISSN 0898-6568. doi: 10.1016/j.cellsig.2010.02.011.

[154] Frank Henkler, Eva Behrle, Kevin M. Dennehy, Andreas Wicovsky, Nathalie Peters, Clemens Warnke, Klaus Pfizenmaier, and Harald Wajant. The extracellular domains of FasL and Fas are sufficient for the formation of supramolecular FasL-Fas clusters of high stability. *Journal of Cell Biology*, 168:1087–1098, 3 2005. ISSN 0021-9525. doi: 10.1083/jcb.200501048.

[155] Ricarda M L Berger, Johann M Weck, Simon M Kempe, Oliver Hill, Tim Liedl, Joachim O Rädler, Cornelia Monzel, Amelie Heuer-Jungemann, R M L Berger, S M Kempe, T Liedl, J O Rädler, J M Weck, A Heuer-Jungemann, O Hill, and C Monzel. Nanoscale FasL Organization on DNA Origami to Decipher Apoptosis Signal Activation in Cells. *Small*, 17:2101678, 7 2021. ISSN 1613-6829. doi: 10.1002/smll.202101678.

[156] Richard M. Siegel, David A. Martin, Lixin Zheng, Samuel Y. Ng, John Bertin, Jeffrey Cohen, and Michael J. Lenardo. Death-effector Filaments: Novel Cytoplasmic Structures that Recruit Caspases and Trigger Apoptosis. *Journal of Cell Biology*, 141: 1243–1253, 6 1998. ISSN 0021-9525. doi: 10.1083/jcb.141.5.1243.

[157] Kolja Schleich, Uwe Warnken, Nicolai Fricker, Selcen Öztürk, Petra Richter, Kerstin Kammerer, Martina Schnölzer, Peter H. Krammer, and Inna N. Lavrik. Stoichiometry of the CD95 Death-Inducing Signaling Complex: Experimental and Modeling Evidence for a Death Effector Domain Chain Model. *Molecular Cell*, 47:306–319, 7 2012. ISSN 1097-2765. doi: 10.1016/j.molcel.2012.05.006.

[158] Laura S. Dickens, Robert S. Boyd, Rebekah Jukes-Jones, Michelle A. Hughes, Gemma L. Robinson, Louise Fairall, John W.R. Schwabe, Kelvin Cain, and Marion MacFarlane. A Death Effector Domain Chain DISC Model Reveals a Crucial Role for Caspase-8 Chain Assembly in Mediating Apoptotic Cell Death. *Molecular Cell*, 47:

291–305, 7 2012. ISSN 1097-2765. doi: 10.1016/j.molcel.2012.05.004.

[159] Nitu Singh, Ali Hassan, and Kakoli Bose. Molecular basis of death effector domain chain assembly and its role in caspase-8 activation. *The FASEB Journal*, 30:186–200, 1 2016. ISSN 1530-6860. doi: 10.1096/fj.15-272997.

[160] Peter S. Linsley, Steven G. Nadler, Jürgen Bajorath, Robert Peach, Helios T. Leung, Julie Rogers, Jeff Bradshaw, Mark Stebbins, Gina Leytze, William Brady, Alison R. Malacko, Hans Marquardt, and Shyh Yu Shaw. Binding stoichiometry of the cytotoxic T lymphocyte-associated molecule-4 (CTLA-4): A disulfide-linked homodimer binds two CD86 molecules. *Journal of Biological Chemistry*, 270:15417–15424, 6 1995. ISSN 00219258. doi: 10.1074/jbc.270.25.15417.

[161] Peter S. Linsley, Jeff Bradshaw, Jo Anne Greene, Robert Peach, Kelly L. Bennett, and Robert S. Mittler. Intracellular trafficking of CTLA-4 and focal localization towards sites of TCR engagement. *Immunity*, 4:535–543, 1996. ISSN 1074-7613. doi: 10.1016/s1074-7613(00)80480-x.

[162] Peter J. Darlington, Mark G. Kirchhof, Gabriel Criado, Jitin Sondhi, and Joaquín Madrenas. Hierarchical Regulation of CTLA-4 Dimer-Based Lattice Formation and Its Biological Relevance for T Cell Inactivation. *The Journal of Immunology*, 175: 996–1004, 7 2005. ISSN 0022-1767. doi: 10.4049/jimmunol.175.2.996.

[163] Sumeena Bhatia, Michael Edidin, Steven C. Almo, and Stanley G. Nathenson. Different cell surface oligomeric states of B7-1 and B7-2: Implications for signaling. *Proceedings of the National Academy of Sciences of the United States of America*, 102:15569–15574, 10 2005. ISSN 00278424. doi: 10.1073/pnas.0507257102.

[164] Yvonne Stahl, Stephanie Grabowski, Andrea Bleckmann, Ralf Kühnemuth, Stefanie Weidtkamp-Peters, Karine Gustavo Pinto, Gwendolyn K. Kirschner, Julia B. Schmid, René H. Wink, Adrian Hülsewede, Suren Felekyan, Claus A.M. Seidel, and Rüdiger Simon. Moderation of Arabidopsis Root Stemness by CLAVATA1 and ARABIDOPSIS CRINKLY4 Receptor Kinase Complexes. *Current Biology*, 23:362–371, 3 2013. ISSN 0960-9822. doi: 10.1016/j.cub.2013.01.045.

[165] Kenneth L. Rock, Eric Reits, and Jacques Neefjes. Present Yourself! By MHC Class I and MHC Class II Molecules. *Trends in immunology*, 37:724, 11 2016. ISSN 14714981. doi: 10.1016/j.it.2016.08.010.

[166] Luís Almeida, Matthias Lochner, Luciana Berod, and Tim Sparwasser. Metabolic pathways in T cell activation and lineage differentiation. *Seminars in Immunology*, 28: 514–524, 10 2016. ISSN 1044-5323. doi: 10.1016/j.smim.2016.10.009.

[167] Marco Vitale, Giuseppe Pelusi, Beatrice Taroni, Giuliana Gobbi, Cristina Micheloni, Rita Rezzani, Francesco Donato, Xinhui Wang, and Soldano Ferrone. HLA Class I Antigen Down-Regulation in Primary Ovary Carcinoma Lesions: Association with Disease

Stage. *Clinical Cancer Research*, 11:67–72, 1 2005. ISSN 1078-0432. doi: 10.1158/1078-0432.67.11.1.

[168] Drew M. Pardoll. The blockade of immune checkpoints in cancer immunotherapy. *Nature Reviews Cancer*, 12:252–264, 3 2012. ISSN 1474-1768. doi: 10.1038/nrc3239.

[169] Yoshihiro Ohue and Hiroyoshi Nishikawa. Regulatory T (Treg) cells in cancer: Can Treg cells be a new therapeutic target? *Cancer Science*, 110:2080, 7 2019. ISSN 13497006. doi: 10.1111/cas.14069.

[170] Michael Hudecek, Maria Teresa Lupo-Stanghellini, Paula L. Kosasih, Daniel Sommermeyer, Michael C. Jensen, Christoph Rader, and Stanley R. Riddell. Receptor affinity and extracellular domain modifications affect tumor recognition by ROR1-specific chimeric antigen receptor T-cells. *Clinical cancer research : an official journal of the American Association for Cancer Research*, 19:3153, 6 2013. ISSN 10780432. doi: 10.1158/1078-0432.ccr-13-0330.

[171] Rebecca C. Larson and Marcela V. Maus. Recent advances and discoveries on the mechanisms and functions of CAR T cells. *Nature reviews. Cancer*, 21:145, 3 2021. ISSN 14741768. doi: 10.1038/s41568-020-00323-z.

[172] Gianpietro Dotti, Stephen Gottschalk, Barbara Savoldo, and Malcolm K. Brenner. Design and Development of Therapies using Chimeric Antigen Receptor-Expressing T cells. *Immunological reviews*, 257:107–126, 1 2014. ISSN 01052896. doi: 10.1111/imr.12131.

[173] David L. Porter, Bruce L. Levine, Michael Kalos, Adam Bagg, and Carl H. June. Chimeric Antigen Receptor–Modified T Cells in Chronic Lymphoid Leukemia. *The New England Journal of Medicine*, 365:725, 8 2011. ISSN 0028-4793. doi: 10.1056/nejmoa1103849.

[174] Renier J. Brentjens, Isabelle Rivière, Jae H. Park, Marco L. Davila, Xiuyan Wang, Jolanta Stefanski, Clare Taylor, Raymond Yeh, Shirley Bartido, Oriana Borquez-Ojeda, Malgorzata Olszewska, Yvette Bernal, Hollie Pegram, Mark Przybylowski, Daniel Hollyman, Yelena Usachenko, Domenick Pirraglia, James Hosey, Elmer Santos, Elizabeth Halton, Peter Maslak, David Scheinberg, Joseph Jurcic, Mark Heaney, Glenn Heller, Mark Frattini, and Michel Sadelain. Safety and persistence of adoptively transferred autologous CD19-targeted T cells in patients with relapsed or chemotherapy refractory B-cell leukemias. *Blood*, 118:4817, 11 2011. ISSN 15280020. doi: 10.1182/blood-2011-04-348540.

[175] Martin A. Pulè, Karin C. Straathof, Gianpietro Dotti, Helen E. Heslop, Cliona M. Rooney, and Malcolm K. Brenner. A chimeric T cell antigen receptor that augments cytokine release and supports clonal expansion of primary human T cells. *Molecular Therapy*, 12:933–941, 11 2005. ISSN 1525-0016. doi: 10.1016/j.ymthe.2005.04.016.

[176] Markus Chmielewski and Hinrich Abken. CAR T cells transform to trucks: Chimeric antigen receptor-redirected T cells engineered to deliver inducible IL-12 modulate the tumour stroma to combat cancer. *Cancer Immunology, Immunotherapy*, 61, 2012. ISSN 03407004. doi: 10.1007/s00262-012-1202-z.

[177] Mohamed Reda Benmebarek, Clara Helke Karches, Bruno Loureiro Cadilha, Stefanie Lesch, Stefan Endres, and Sebastian Kobold. Killing Mechanisms of Chimeric Antigen Receptor (CAR) T Cells. *International Journal of Molecular Sciences*, 20, 3 2019. ISSN 14220067. doi: 10.3390/ijms20061283.

[178] Lee K. Hong, Yuhui Chen, Christof C. Smith, Stephanie A. Montgomery, Benjamin G. Vincent, Gianpietro Dotti, and Barbara Savoldo. CD30-Redirected Chimeric Antigen Receptor T Cells Target CD30+ and CD30– Embryonal Carcinoma via Antigen-dependent and Fas/FasL Interactions. *Cancer immunology research*, 6:1274, 10 2018. ISSN 23266074. doi: 10.1158/2326-6066.cir-18-0065.

[179] Nathan Singh, Yong Gu Lee, Olga Shestova, Pranali Ravikumar, Katharina E. Hayer, Seok Jae Hong, Xueqing Maggie Lu, Raymone Pajarillo, Sangya Agarwal, Shunichiro Kuramitsu, Elena J. Orlando, Karen Thudium Mueller, Charly R. Good, Shelley L. Berger, Ophir Shalem, Matthew D. Weitzman, Noelle V. Frey, Shannon L. Maude, Stephan A. Grupp, Carl H. June, Saar Gill, and Marco Ruella. Impaired death receptor signaling in leukemia causes antigen-independent resistance by inducing CAR T cell dysfunction. *Cancer discovery*, 10:552, 4 2020. ISSN 21598290. doi: 10.1158/2159-8290.cd-19-0813.

[180] Maelig G. Morvan and Lewis L. Lanier. NK cells and cancer: you can teach innate cells new tricks. *Nature Reviews Cancer*, 16:7–19, 12 2015. ISSN 1474-1768. doi: 10.1038/nrc.2015.5.

[181] Ying Gong, Roel G.J. Klein Wolterink, Jianxiang Wang, Gerard M.J. Bos, and Wilfred T.V. Germeraad. Chimeric antigen receptor natural killer (CAR-NK) cell design and engineering for cancer therapy. *Journal of Hematology & Oncology*, 14:1–35, 5 2021. ISSN 1756-8722. doi: 10.1186/s13045-021-01083-5.

[182] Corinna Haist, Elena Schulte, Nina Bartels, Arthur Bister, Zoe Poschinski, Tabea C. Ibach, Katja Geipel, Constanze Wiek, Martin Wagenmann, Cornelia Monzel, Kathrin Scheckenbach, and Helmut Hanenberg. CD44v6-targeted CAR T-cells specifically eliminate CD44 isoform 6 expressing head/neck squamous cell carcinoma cells. *Oral oncology*, 116, 5 2021. ISSN 1879-0593. doi: 10.1016/j.oraloncology.2021.105259.

[183] Maren Soldierer, Arthur Bister, Corinna Haist, Anitha Thivakaran, Sevgi Can Cengiz, Stephanie Sendker, Nina Bartels, Antonia Thomitzek, Denise Smorra, Maryam Hejazi, Markus Uhrberg, Kathrin Scheckenbach, Cornelia Monzel, Constanze Wiek, Dirk Reinhardt, Naghmeh Niktoreh, and Helmut Hanenberg. Genetic Engineering and Enrichment of Human NK Cells for CAR-Enhanced Immunotherapy of Hema-

tological Malignancies. *Frontiers in Immunology*, 13, 4 2022. ISSN 1664-3224. doi: 10.3389/fimmu.2022.847008.

[184] Arthur Bister, Tabea Ibach, Corinna Haist, Denise Smorra, Katharina Roellecke, Martin Wagenmann, Kathrin Scheckenbach, Norbert Gattermann, Constanze Wiek, and Helmut Hanenberg. A novel CD34-derived hinge for rapid and efficient detection and enrichment of CAR T cells. *Molecular Therapy - Oncolytics*, 23:534–546, 12 2021. ISSN 23727705. doi: 10.1016/j.omto.2021.11.003.

[185] *Cover Image: Molecular Therapy - Oncolytics Volume 23*. Cell Press, 12 2021. URL https://www.cell.com/cms/asset/atypon:cms:attachment:img:d85e6:rev:1646448727909-2822:pii:S2372770521X00058/cover.tif.jpg.

[186] Clarissa Liesche, Kristin S. Grußmayer, Michael Ludwig, Stefan Wörz, Karl Rohr, Dirk Peter Herten, Joël Beaudouin, and Roland Eils. Automated Analysis of Single-Molecule Photobleaching Data by Statistical Modeling of Spot Populations. *Biophysical Journal*, 109:2352–2362, 2015. ISSN 15420086. doi: 10.1016/j.bpj.2015.10.035.

[187] Dako Denmark ApS Agilent. QIFIKIT®, Code K0078. Brochure, 2020. URL https://www.agilent.com/cs/library/packageinsert/public/SSK0078RUO-E_02.pdf.

[188] Scientific Volume Imaging B.V. Backprojected Pinhole Calculator., 2021. URL https://svi.nl/Olympus_FV1000.

[189] Dennis E. Koppel. Statistical accuracy in fluorescence correlation spectroscopy. *Physical Review A*, 10:1938, 12 1974. ISSN 10502947. doi: 10.1103/physreva.10.1938.

[190] C. Eggeling, S. Berger, L. Brand, J. R. Fries, J. Schaffer, A. Volkmer, and C. A.M. Seidel. Data registration and selective single-molecule analysis using multi-parameter fluorescence detection. *Journal of Biotechnology*, 86:163–180, 4 2001. ISSN 0168-1656. doi: 10.1016/s0168-1656(00)00412-0.

[191] Paula J. Cranfill, Brittney R. Sell, Michelle A. Baird, John R. Allen, Zeno Lavagnino, H. Martijn De Gruiter, Gert Jan Kremers, Michael W. Davidson, Alessandro Ustione, and David W. Piston. Quantitative assessment of fluorescent proteins. *Nature Methods*, 13:557–562, 5 2016. ISSN 1548-7105. doi: 10.1038/nmeth.3891.

[192] Joanna Oracz, Volker Westphal, Czesław Radzewicz, Steffen J. Sahl, and Stefan W. Hell. Photobleaching in STED nanoscopy and its dependence on the photon flux applied for reversible silencing of the fluorophore. *Scientific Reports*, 7:1–14, 9 2017. ISSN 2045-2322. doi: 10.1038/s41598-017-09902-x.

[193] Chenxi Duan, Virgile Adam, Martin Byrdin, Jacqueline Ridard, Sylvie Kieffer-Jaquinod, Cécile Morlot, Delphine Arcizet, Isabelle Demachy, and Dominique Bourgeois. Structural evidence for a two-regime photobleaching mechanism in a reversibly switchable fluorescent protein. *Journal of the American Chemical Society*, 135:15841–15850, 10 2013. ISSN 15205126. doi: 10.1021/ja406860e.

[194] Anders Barth, Oleg Opanasyuk, Thomas Otavio Peulen, Suren Felekyan, Stanislav Kalinin, Hugo Sanabria, and Claus A.M. Seidel. Unraveling multi-state molecular dynamics in single-molecule FRET experiments. I. Theory of FRET-lines. *The Journal of Chemical Physics*, 156:141501, 4 2022. ISSN 0021-9606. doi: 10.1063/5.0089134.

Danksagung

An dieser Stelle möchte ich mich bei allen bedanken, die mich während der Zeit meiner Doktorarbeit begleitet und unterstützt haben.

Mein besonderer Dank gilt Prof. Dr. Cornelia Monzel. Cornelia, danke für deine Betreuung, die zuverlässige Unterstützung und dein beeindruckendes Engagement für unsere Arbeit – wissenschaftlich und darüber hinaus!

Vielen Dank an Prof. Dr. Claus Seidel. Danke, Claus, für die große fachliche Unterstützung und alle methodischen Feinheiten, die ich durch deine Betreuung lernen durfte.

Nicolaas, danke für die großartige Zusammenarbeit, konstruktive Kritik und lange Diskussionen, um das Beste aus allem herauszuholen.

Daniel, vielen Dank für deine ständige Diskussions- und Hilfsbereitschaft und deine aufbauenden Worte.

Danke an alle Mitglieder meiner Arbeitsgruppe. Andi, Philipp, Xiaoyue und Daniel, danke für ironisch-witzige Mittagspausen, die tolle Zusammenarbeit und das aufwendige Korrekturlesen!

Danke an alle Mitglieder der AG Seidel - für den wissenschaftlichen Input kombiniert mit schönen Grillabenden.

Danke an unsere Kollaborationspartner der HNO. Es hat mir große Freude bereitet durch euch über klinische Forschung zu lernen und daran mitzuwirken.

Danke an den SFB1208 – für die großen Herausforderungen und Weiterentwicklungsmöglichkeiten, die die Zusammenarbeit mit anderen Fachbereichen bringt.

Danke an alle Freunde, die mich in der Zeit meines Studiums begleitet haben. Danke für euer Interesse, das Zuhören, und die nötigen Ablenkungen.

Beni, ich danke dir für unendliche Geduld in den letzten vier Jahren, für deine Unterstützung bei allem und für die Kraft und Stärke, die du mir gibst. Von Herzen Danke!

Danke an meine Familie für die uneingeschränkte, liebevolle und vielseitige Unterstützung - ohne euch wäre ich nicht da, wo ich jetzt bin.